

Thermomechanical Fatigue Behavior of a Near Alpha Titanium Alloy

A THESIS

SUBMITTED FOR THE DEGREE OF

DOCTOR OF PHILOSOPHY

IN THE FACULTY OF MATERIALS ENGINEERING

BY

KARTIK PRASAD

(REGISTRATION NO: 11ETPM05)



Department of Materials Engineering

School of Engineering Science and Technology

University of Hyderabad, Hyderabad - 500046

(OCTOBER 2015)

Dedicated

to

My Beloved Late Father

List of Publications/Conference Proceedings

Peer-Reviewed Technical Papers:

1. Fatigue Crack Growth Behaviour of a near α Titanium Alloy Timetal 834 at 450°C and 600°C
Kartik Prasad, S. Abhaya, G. Amarendra, Vikas Kumar, K. V. Rajulapati, K. Bhanu Sankara Rao
Engineering Fracture Mechanics, 102 (2013) 194-206
2. Electron Back Scattered Diffraction Characterization of Thermomechanical Fatigue Crack Propagation of a Near α Titanium alloy Timetal 834
Kartik Prasad, Phani S. Karamched, A. Bhattacharjee, Vikas Kumar, K. Bhanu Sankara Rao, M. Sundararaman
Materials & Design, 65 (2015) 297-311
3. Experimental evidence for segregation of interstitial impurities to defects in a near α titanium alloy during dynamic strain aging using energy filtered transmission electron microscopy
Kartik Prasad, S. Amrithapandian, B. K. Panigrahi, Vikas Kumar, K. Bhanu Sankara Rao, M. Sundararaman
Material Science & Engineering, 638 (2015) 90-96
4. Effects of crack closure and cyclic deformation on thermomechanical fatigue crack growth of a near α titanium alloy
Kartik Prasad, Vikas Kumar, K. Bhanu Sankara Rao, M. Sundararaman
Under review - Metallurgical & Materials Transactions A

Conference Proceedings:

1. Characterization of oxide and roughness induced crack closure in a near alpha titanium alloy at 450°C and 600°C

Kartik Prasad, S. Abhaya, G. Amarendra, V. Kumar, K. Bhanu Sankara Rao
Proceedings of Annual Technical Meeting of Indian Institute of Metals,
14th -16th November, 2012, Jamshedpur

2. Microstructural Characterization of crack growth micro-mechanisms under thermomechanical fatigue loading of a near alpha Ti-alloy through electron back scattered diffraction

Kartik Prasad, Phani S. Karamched, P. Ghosal, V. Kumar, M. Sundararaman, K. Bhanu Sankara Rao,
Proceedings of Annual Technical Meeting of Electron Microscopy Society of India,
06th-08th July, 2013, Kolkata

3. Characterization of fatigue crack growth behaviour under thermomechanical loading of a near alpha Ti-alloy through EBSD

Kartik Prasad, Phani S. Karamched, P. Ghosal, V. Kumar, M. Sundararaman, K. Bhanu Sankara Rao,
Proceedings of Annual Technical Meeting of Indian Institute of Metals,
14th -16th November, 2013, Varanasi

4. Influence of extrinsic crack tip shielding on fatigue crack growth behaviour of a near alpha Ti-alloy at elevated temperature

Kartik Prasad, S. Abhaya, G. Amarendra, V. Kumar, M. Sundararaman, K.

Bhanu Sankara Rao,

Proceedings of First International Conference on Structural Integrity,

04th-07th February, 2014, Kalpakkam

5. Thermomechanical Fatigue Behavior of a Near α Titanium Alloy

Kartik Prasad, P. Ghosal, R. Sarkar, V. Kumar, M. Sundararaman, K.

Bhanu Sankara Rao,

Communicated to Annual Technical Meeting of Indian Institute of Metals,

13th-16th November, 2015, Coimbatore

Acknowledgements

I express my deep gratitude to my thesis supervisors Professor Rajendra Singh, Professor Sundararaman Mahadevan and Dr. Vikas Kumar for giving me the opportunity to work on this topic and their excellent supervision, continuous support and constant encouragement. I recall with deep gratitude the valuable inspiration and meticulous care received from Professor Sundararaman Mahadevan in several stages of this thesis work.

I have received support in several stages of this thesis work from my workplace (DMRL) as well as from other research organizations. Firstly, I would like to thank the financial support and sanctioning of study leave for pursuing the PhD coursework of Defence Research and Development Organization. I would like to thank the doctoral committee members: Dr. K. V. Rajulapati, Dr. Dibakar Das, Prof. K. P. N. Murthy and Prof. K. Padmanabhan for their kind understanding and encouragement during half yearly progress reviews.

I recall the valuable inspiration received from Dr. V. K. Varma who taught me how to play 'safe' with servohydraulic test systems. I owe many thanks to Shri E. Hari Krishna for his skills and patience in carrying out long term fatigue and fracture related mechanical testing. Thanks are due to Shri G. B. Vikram for rendering support in tensile testing.

I am gratefully obliged to Dr. Amit Bhattacharjee and Mr. V. K. Chandravanshi for their help in processing one of the alloys used in this thesis work. I would like to thank Mr. Srinivas Rao Nandam and members of mechanical engineering group for their help in machining the blanks for mechanical testing. Special thanks to Mr. Ram Kumar for preparing the ‘not so easy’ tubular specimens for thermomechanical fatigue testing. I sincerely acknowledge the kind assistance of members of structures and failure analysis group in help with the metallography. I heartily thank Dr. P. Ghosal for voluntarily lending the TEM and SEM facilities for microscopy related studies. I am deeply indebted to Dr. T. K. Nandy whole principles of simplicity and transparency with brilliant understanding on ‘dislocations’ inspired me in analyzing TEM results. My fondest gratitude to Dr. Rajdeep Sarkar for his whole-hearted support in TEM studies and teaching me the operation of ‘scanning electron microscope’. I sincerely acknowledge the kind assistance and help rendered by Mr. Ravi Teja in cross checking the TEM results. I wish to thank Dr. Phani S. Karamched for fruitful discussions on many issues concerned with electron back scattered diffraction which proved great help in writing one of the chapter of this thesis. I thank Mr. Rajnish Goyel for help with the stylus base profilometer. I particularly thank Shri J. Sudhama for preparing the TEM foils with immense care. I would also like to thank Mr. Venkat and Mr. Deepak for the help with the scanning electron microscope.

I am thankful to senior scientists as well as my colleagues at DMRL for their valuable suggestions. My thanks are due to Dr. K. Gopinath, Dr. D. V. V

Satyanarayana, Mr. B. Gopalkrishna, Dr. A. K. Singh, Dr. D. K. Das and Dr. Mithun Palit. Thanks are also due to Dr. N. Eshwara Prasad (Former Regional Director, RCMA (Mat.)) for his energetic support during numerous occasions. I acknowledge the understanding and support I enjoyed from my friends, especially Mrs. Vindia Prasoon (GTRE), Mr. Bipin (ADE) and Mr. Kiran Govind (NPOL).

I wish to thank Prof. J.-L. Strudel (France) for stimulating discussions on dynamic strain aging. I am grateful to Prof. M. D. Kulkarni (Former Head of Department, Institute of Armament Technology, Pune) and Prof. M. Ramulu (Department of Mechanical Engineering, University of Washington) for teaching me the basics of fracture mechanics. Their efforts in providing me the technical inputs in the form of reports, lecture and study materials are gratefully acknowledged. I sincerely thank Dr. B. K. Panigrahi (Head, Materials Physics Division, IGCAR, Kalpakkam) for allowing tension free access to HR-TEM and Auger Spectrometer at IGACR, Kalpakkam. I warmly remember Dr. S. Amrithapandian for his scientific support in energy filtered transmission electron microscopy. Thanks to Dr. S. Abhaya for her help in Auger spectroscopy. I thank Dr. A. Nagesha and Dr. G. V. K. Prasad Reddy of IGCAR for their friendly support and care during my visits to IGCAR.

I cherish my stay at University of Hyderabad (UoH) for the coursework during which I had the opportunity to interact and learn from many new friends. I treasure the continuous support that I have received from Mr. P. Pardhu, Mrs. U. Savitha and Chandrakala during subsequent visits to UoH. My sincere

thanks to them for their help during half yearly registration process. I place on record my deep appreciation and gratitude to Prof. K. Bhanu Sankara Rao (Former Dean, SEST, UoH) for his keen interest in this thesis work, constant encouragement and help during my stay at UoH.

Needless to say, I am deeply grateful to Dr. G. Malakondaiah (Former Director, DMRL), who set me on my current path, and provided immense support over the years. I express my deep appreciation to him. I am grateful to Dr. S. V. Kamat (Director, DMRL) for being kind, understanding, reassuring and trusting my abilities. I warmly remember him for his support during unusual times.

I am eternally grateful to my wife, Sonu for unmatched support, care, patience and affection. While the company of my sweet little daughter Kanchan has preserved me well within the elastic limit during long concentrated working hours, the naughtiness of my little son Karan has helped me in building enough patience to treat the experimental results with extreme care. I express my deepest gratitude to my mother, brother and in-laws for their unconditional love and prayers throughout this thesis work.

Finally, I wish to dedicate this thesis to my beloved late father Gopal Ram on the occasion of his 1st death anniversary. His counterless sacrifices for the sake of my education are gratefully acknowledged.

SYNOPSIS

Background and Objective

Titanium alloys have been the undisputed choice for compressor discs in gas turbine aeroengines as they exhibit the best available combination of strength to weight ratio and resistance to fatigue, which are essential for a disc alloy. Timetal 834 is a near alpha titanium alloy developed for high pressure compressor disc application and exhibit superior elevated temperature tensile strength, fatigue and creep properties. It is distinct from contemporary disc alloys because of its chemistry (especially Sn, Zr, Si and C contents), processing and heat treatment. However, literature available in open domain to develop an understanding of mechanical properties in intermediate temperature regime, which are quite often experienced by high pressure compressor disc modules, is rather limited. The information available in the literature with respect to structure property correlation in this alloy will be described in this chapter. Moreover, in an aeroengine, depending upon the type of the applications it is being used, there will be situations where large thermal gradients may be generated in high temperature components. Thermal gradient causes thermal stresses which may eventually initiate and propagate fatigue cracks. While thermal fatigue, as a damaging process per se, is more realistic for internally air cooled high pressure turbine blades and vanes, its prevalence with relatively lesser degree of internal constraint around stress concentration sites in high pressure titanium compressor module which can see temperature $\sim 600^{\circ}\text{C}$ during service cannot be ruled out. This study was

taken up in this background with an objective of assessing the tensile, low cycle fatigue (LCF) and thermomechanical fatigue (TMF) properties exhibited by Timetal 834 alloy within the temperature regime of interest and also to understand the structure-property correlations behind it.

Tensile Behavior

The effect of temperature and strain rate on monotonic tensile properties were assessed at different temperature in the range of 300°C – 600°C at a strain rate of 10^{-4} s^{-1} and strain rate effects were explored in detail at 300, 350, 400, 450 and 500°C at different strain rates between 10^{-6} to 10^{-3} s^{-1} . Yield and ultimate tensile strength of the alloy remains unaffected by temperature till about 400°C, beyond which both showed a plateau up to 500°C. Negative strain rate sensitivity exhibited by the alloy in the temperature range between 400°C-475°C indicated that flow stress is a strong function of strain hardening rather than strain rate hardening. The fracture mode remained quasi-cleavage at almost all the test conditions. Timetal 834 exhibits jerky flow in monotonic tension at intermediate temperatures ranging from 400°C-475°C. After considering all known mechanisms for serrated flow in materials, the instability in flow (Portevin-LeChatelier (PLC) effect) is attributed to dynamic strain aging (DSA), arising from interactions between diffusing solute atoms and mobile dislocations during plastic flow. While Si is known to cause DSA in this alloy, in order to understand the influence of interstitial solutes on DSA, if any, a modified alloy without Si has been studied. So far, all the data reported in literature is generally concerned with

the influence of only one solute - either interstitial or substitutional on DSA. Hardly any literature is available on the effect of different interstitials diffusing simultaneously in the same temperature range at different rates to dislocations. Electron microscopic investigation of tensile tested samples in an energy filtered transmission electron microscopy provided direct experimental evidence for segregation of interstitial elements like carbon (C) and nitrogen (N) to lath boundaries and dislocation pile ups. On the basis of these results and the comparison of lattice strain generated by different interstitials in α -Ti, it was concluded that segregation of carbon and nitrogen and not oxygen to defects is responsible for DSA in this alloy. As the temperature range of occurrence of DSA coincided with typical bore and web temperatures of high pressure compressor discs, its possible influence on tensile properties is considered in detail. Significant change in flow stress, ductility, and work hardening exponent is observed.

LCF Behavior

LCF studies were carried out under fully reversed constant strain amplitude conditions at 300°C, 450°C and 600°C with strain amplitudes ranging from 0.4 to 1.2%. The alloy exhibits an anomalous peak at 450°C in the variation of peak tensile stress versus test temperatures which was attributable to the occurrence of dynamic strain aging. The alloy softens at 300°C and 600°C in which the cyclic stress-strain (CSS) curves lies below the monotonic curves and it hardens at 450°C thereby showing CSS curve above than that of monotonic curve. Different cyclic stress responses observed

depending on the imposed conditions are correlated to the substructures that evolved. TEM studies show that Ti_3Al precipitates that are degraded through repeated shearing are responsible for the continuous softening at all test temperatures. Studies at 450°C show manifestation of DSA on LCF behavior in the form of increased work hardening which tends to offset softening effects. Plastic strain dependence of fatigue lives exhibited single slope behavior at all test temperatures. TEM substructures revealed that planar slip with deformation concentrated on slip bands is the major deformation mode under all the conditions examined. However, homogeneity of deformation increases at 600°C .

TMF Behavior

TMF studies were carried out under fully reversed constant strain amplitude conditions at two temperature intervals viz. $300^\circ\text{C} \leftrightarrow 450^\circ\text{C}$ and $450^\circ\text{C} \leftrightarrow 600^\circ\text{C}$ with strain amplitudes ranging from 0.6 to 1.2%. The influence of phasing (In-phase (IP) and Out-of-Phase (OP)) on thermomechanical fatigue lives were assessed at a heating and cooling rate of $5^\circ\text{C}/\text{sec}$. The cyclic stress response of the alloy at 450°C under $300^\circ\text{C} \leftrightarrow 450^\circ\text{C}$ TMF loading was observed to be initial cyclic softening followed by hardening. However, in the temperature interval of $450^\circ\text{C} \leftrightarrow 600^\circ\text{C}$ TMF loading, the alloy did not show cyclic softening at 450°C . In this test temperature interval, the alloy exhibits gradual cyclic hardening till failure. Considering the hardening response of the alloy at 450°C , under the conditions of thermal transients, this study showed the uncertainties associated

using isothermal stress – strain curves for design. The cyclic stress – strain curves under IP and OP-TMF loading in the temperature interval of 450°C↔600°C lies above than that of isothermal stress – strain curves. TEM substructure revealed that the severity of planar slip is higher under TMF loading as compared to isothermal test conditions. The fatigue lives are observed to be lower under OP-TMF loading as compared to IP-TMF loading and was attributable to development of mean stresses during OP-TMF loading.

Fatigue Crack Growth Behavior under Isothermal Test Conditions

Fatigue crack growth (FCG) studies were carried out at three temperatures viz., 300°C, 450°C, 600°C under constant load amplitude cycling. Amongst the temperature studied, the alloy exhibited higher crack growth rate at 450°C as compared to 300°C and 600°C. Cyclic hardening occurring at the crack tip, as revealed by microhardness measurements, was attributed to increase in the crack growth rate at 450°C. Surface roughness induced crack closure as a predominant crack closure mechanism influences the stage I crack growth rates at all temperatures. However, the effect of oxide induced crack closure as revealed by Auger electron spectroscopy was found to be significant at 600°C as compared to 300°C and 450°C. It is surmised that the oxide induced crack closure leads to significant increase in average surface roughness which eventually retards the crack growth rate at 600°C. In this investigation, it has been concluded that the alloy exhibits highest level of crack closure at 600°C than that of 300°C and 450°C.

Thermomechanical Fatigue Crack Growth Behavior

Fatigue crack growth studies under thermomechanical fatigue loading were carried out at two temperature intervals viz., 300°C↔450°C and 450°C↔600°C. In both the temperature intervals, thermomechanical fatigue crack growth rate was observed to be higher under OP-TMF loading as compared to IP-TMF loading. Fatigue crack growth (FCG) mechanisms have been studied in the light of the interaction of a propagating crack with local crystallographic orientations of primary alpha (α_p) and secondary alpha (α_s) colonies in a near α Timetal 834 Ti-alloy under thermomechanical fatigue (TMF) loading using electron backscattered diffraction (EBSD). EBSD analysis and microhardness measurements have confirmed that larger cyclic plastic zone size at the crack tip leads to lower crack propagation under IP-TMFCG loading as compared to OP-TMFCG loading. EBSD analysis has also confirmed that crack dissipates more energy to propagate when it passes from a soft grain oriented with its c-axis normal to the loading direction and encounters a hard grain with its c-axis parallel with the loading direction. It was also found that closure mechanisms significantly influence the stage I crack growth behavior. Surface roughness induced crack closure (RICC) predominantly modifies the crack growth rate of near threshold region at 300°C↔450°C test conditions. However, oxide induced crack closure (OICC) further strengthens RICC at 450°C↔600°C TMF loading. In stage II crack growth behavior, the alloy shows higher crack growth rates at 450°C↔600°C OP-TMF loading which is attributed to the combined effect of cyclic hardening occurring at the crack tip and weakening of interlamellar regions due to oxidation. In this investigation, it was concluded that thermomechanical

fatigue crack growth behavior can be accounted by combining crack closure effects and crack tip opening displacement (CTOD) per cycle.

Conclusions and Scope for Future Work

This chapter provides a brief summary of the salient results obtained in this study. While the properties and behavior of Timetal 834 under monotonic and cyclic loading conditions over a range of temperatures and temperature intervals could be rationalized on the basis of deformation substructures as well as intrinsic (slip character) and extrinsic factors (crack closure mechanisms), the thesis opens up the door for further in-depth studies on deformation mechanisms in Timetal 834 as well as other disc alloys of similar microstructure.

List of Figures

Chapter II: Literature Survey

- Fig. 2.1 Trends in jet engine material usage [Driver et al. 1981]
- Fig. 2.2 Unit cell of (a) α and (b) β phase [Lütjering and Williams 2007].
- Fig. 2.3 Slip planes and slip directions in hexagonal α phase [Lütjering and Williams 2007].
- Fig. 2.4 Schematic illustration of influence of alloying elements on phase diagrams of titanium alloys [Lütjering and Williams 2007].
- Fig. 2.5 Classification of phase diagram based on 3D phase diagram [Peters et al. 2003].
- Fig. 2.6 Microstructural constituents in a near α Ti alloy [Rugg et al. 2007]
- Fig. 2.7 Timetal 834 originally named as IMI 834 showing improved creep resistance as compared to other Ti alloys [Smallman and Bishop 1999].
- Fig. 2.8 Schematic illustration of the influence of DSA on various mechanical properties [Rodriguez 1984].

- Fig. 2.9 A schematic illustration of load train of a tensile test system. The spring represents the elastic properties of the machine and specimen [Hull and Bacon 1984].
- Fig. 2.10 Load drop in conventional hydraulic machine (a) and rigid machine (b to f) [Pink et al. 1984]
- Fig. 2.11 A schematic illustration of equally stressed material replicating constrained deformation near the vicinity of notch [Bannantine, Comer, Handrock 1998]
- Fig. 2.12 A schematic illustration of strain controlled LCF testing showing (a) cyclic hardening and (b) softening [Bannantine, Comer, Handrock 1998]. The variation of stress range versus cycles to illustrate the cyclic softening, hardening and stable behaviour is shown in (c) [Manson and Halford 2006].
- Fig. 2.13 Generation of cyclic stress – strain curves from the transient response of the material under strain controlled LCF loading [Francois, Pineau and Zaoui 2013].
- Fig. 2.14 Schematic illustration of inspection interval between crack lengths higher and lower than initial and critical crack sizes, respectively.
- Fig. 2.15 Schematic illustration of fatigue crack growth curve showing various regions and factors influencing crack growth behaviour [Ritchie 1999]
- Fig. 2.16 Schematic illustration of crack opening while loading and crack closing while unloading in load (S) versus COD plot [Schijve 2009]

- Fig. 2.17 A schematic illustration of the mechanisms which promote retardation of fatigue crack growth. (a) plasticity induced crack closure; (b) oxide induced crack closure; (c) roughness induced crack closure; (d) fluid induced crack closure; (e) transformation induced crack closure; (f) crack deflection; (g) crack bridging by fibers; (h) crack bridging by particles [Suresh 2004].
- Fig. 2.18 Waveforms and resulting hysteresis loops under Out-of-Phase and In-Phase TMF loading [Viswanathan 1993].
- Fig. 2.19 A schematic illustration showing the various steps in carrying out thermomechanical fatigue test.

Chapter III: Material Processing and Microstructural Characterization

- Fig. 3.1 SEM microstructure of Timetal 834 showing volume fraction of α_p ~15% in transformed β matrix.
- Fig. 3.2 TEM microstructure of Timetal 834 showing (a) α_p and transformed β matrix (b) several secondary α colonies in transformed β matrix (c) secondary α laths within α colonies and (d) extra superlattice diffraction spots revealing the presence of α_2 (Ti_3Al) inside α_p grains.
- Fig. 3.3 Bright field TEM micrograph of Timetal 834 showing (a) spherical particles in transformed β matrix and (b) EDS spectrum taken from the spherical particle showing preferential enrichment of Zr, Si and Al into them.
- Fig. 3.4 Various types of microstructural constituents in near α Timetal 834 Ti-alloy

- Fig. 3.5 SEM microstructures of alloy 834 without Si showing bimodal microstructure up to 1000°C and fully transformed β at 1020°C.
- Fig. 3.6 Bright field TEM micrographs of alloy 834 without Si showing (a) secondary α colonies of transformed β matrix and (b) secondary α laths inside α colonies.
- Fig. 3.7 Bright field TEM micrographs of Timetal 834 showing (a) straight dislocation segments inside primary α grain in $g=0002$ reflection and (b) limited dislocation activity in $g=0002$ reflection in secondary α laths.
- Fig. 3.8 Bright field TEM micrographs of alloy 834 without Si showing (a) few isolated dislocations in $g=01\bar{1}1$ reflection inside primary α grain and (b) limited dislocation activity in $g=0\bar{1}1\bar{1}$ reflection in secondary α laths.

Chapter IV: Tensile Behaviour

- Fig. 4.1 Schematic illustration of orientation of test coupon extraction for tensile testing from heat treated plates.
- Fig. 4.2 (a) Geometry of cylindrical specimens used for tensile testing and (b) photograph of round threaded type tensile specimen
- Fig. 4.3 Photograph of electromechanical test system (Walter + Bai ag) for tensile testing. Split type three zone resistance furnace and high temperature extensometer are shown in the inset.
- Fig. 4.4 (a) True stress-strain curves of Timetal 834 as a function of temperature at strain rate 10^{-5} s^{-1} and (b) various types of serrations in the plastic regime of stress-strain curves.

- Fig. 4.5 Plastic region of true stress-strain curves showing effect of strain rate at (a) 400°C and (b) 450°C.
- Fig. 4.6 Serration map of Timetal 834 showing the classification of serrations as a function of temperature and strain rate.
- Fig. 4.7 Engineering stress-strain curves of Timetal 834 as a function of temperature at 500°C.
- Fig. 4.8 Plastic region of true stress-strain curves of alloy 834 without Si showing (a) effect of temperature at strain rate of 10^{-5} s^{-1} and (a) effect of strain rate at 450°C.
- Fig. 4.9 Serration map of alloy 834 without Si showing the classification of serrations as a function of temperature and strain rate.
- Fig. 4.10 (a) Variation of 0.2% yield strength and ultimate tensile strength and (b) ductility in terms of total elongation as a function of temperature of Timetal 834.
- Fig. 4.11 (a) Result of fit flow relationship of log true stress-strain at 10^{-5} s^{-1} (b) variation of strain hardening exponent as a function of temperature of Timetal 834.
- Fig. 4.12 Variation of (a) 0.2% yield strength and ultimate tensile strength (b) total elongation and (c) strain hardening exponent as a function of temperature at 10^{-5} s^{-1} .
- Fig. 4.13 Nature of transients during strain rate jump tests at (a) 450°C, serrated region and (b) 300°C, non-serrated region of Timetal 834.
- Fig. 4.14 Variation of strain rate sensitivity as a function of temperature of (a) Timetal 834 and (b) alloy 834 without Si.

Fig. 4.15 Bright field TEM micrographs of alloy 834 without Si deformed at room temperature. These images are taken along $[2\bar{1}\bar{1}0]$ zone axis showing a slip band of 'a₃' dislocations with burger vector, $b=1/3[11\bar{2}0]$ in the (1101) pyramidal plane. Common locations marked by arrow in all micrographs.

(a) $g = 0002$, showing complete visibility of straight dislocation segments

(b) $g = 01\bar{1}1$, showing visibility of straight and curved dislocation segments

(c) $g = 0\bar{1}11$, showing complete visibility of curved dislocation segments

(d) $g = 0\bar{1}10$, showing a fringe contrast running along the band

Fig. 4.16 TEM micrographs of alloy 834 without Si deformed at room temperature taken along $[1\bar{1}01]$ zone axis. Common locations marked by arrow in all micrographs.

(a) $g = 1\bar{1}0\bar{2}$, showing complete invisibility.

(b) $g = 11\bar{2}0$, showing complete visibility.

Fig. 4.17 Bright field TEM micrographs of alloy 834 without Si deformed at room temperature taken along $[4\bar{2}\bar{2}3]$ zone axis. Common locations marked by arrow in all micrographs.

(a) $g = 01\bar{1}0$, showing residual visibility

(b) $g = 1\bar{1}0\bar{2}$, showing complete invisibility

(c) $g = \bar{1}012$, showing complete invisibility

Fig. 4.18 Stereographic projection showing the orientations and trace analysis of Figs. 4.15-4.17.

Fig. 4.19 Bright field TEM micrographs of deformed specimen of Timetal 834 at room temperature taken along $[2\bar{1}\bar{1}0]$ zone axis showing a dislocation pile up of 'a₃' dislocations ($b=1/3[11\bar{2}0]$)

slip band in the (0002) basal plane. Common locations marked by arrow in all micrographs.

- (a) $g = 0\bar{1}11$, showing complete visibility
- (b) $g = 01\bar{1}0$, showing complete visibility
- (c) $g = 0\bar{1}1\bar{1}$, showing residual visibility
- (d) $g = 000\bar{2}$, showing complete invisibility

Fig. 4.20 Bright field TEM micrographs of tensile interrupted specimen of Timetal 834 at ambient temperature taken along $[1\bar{2}10]$ zone axis showing complete visibility of dislocations at $g = 10\bar{1}1$.

Fig. 4.21 Bright field TEM micrographs of tensile interrupted specimen of Timetal 834 at room temperature taken along $[4\bar{2}\bar{2}3]$ zone axis showing (a) complete invisibility, $g = \bar{1}01\bar{2}$ and (b) complete visibility, $g = 0\bar{1}10$.

Fig. 4.22 Bright field TEM micrographs of deformed specimen of Timetal 834 at ambient temperature. These images are taken along $[2\bar{4}2\bar{3}]$ zone axis.

- (a) $g = \bar{1}10\bar{2}$, showing complete invisibility
- (b) $g = 0\bar{1}12$, showing complete visibility
- (c) $g = \bar{1}010$, showing residual visibility

Fig. 4.23 Stereographic projection showing the orientations and trace analysis of Figs. 4.19-4.22.

Fig. 4.24 Bright field TEM micrographs of deformed specimen of Alloy 834 without Si at 450°C taken along $[0001]$ zone axis showing two dislocation pile ups of 'a₁' dislocations ($b=1/3[2\bar{1}\bar{1}0]$) in pyramidal (0111) plane and 'a₃' dislocations ($b=1/3[11\bar{2}0]$) in basal plane. Common locations marked by arrow in all micrographs.

- (a) $g = \bar{1}010$, showing complete visibility

(b) $g = 01\bar{1}0$, showing complete visibility for a_3 type dislocations.

Fig. 4.25 Bright field TEM micrographs of tensile interrupted specimen of alloy 834 without Si at 450°C taken along $[11\bar{2}3]$ zone axis. Common locations marked by arrow in all micrographs.

(a) $g = 0\bar{1}11$, showing complete visibility of a_3 type of dislocations

(b) $g = \bar{1}011$, showing residual visibility

(c) $g = \bar{1}100$, showing complete invisibility

Fig. 4.26 Bright field TEM micrographs of tensile interrupted specimen of Alloy 834 without Si at 450°C taken along $[1\bar{2}13]$ zone axis. Common locations marked by arrow in all micrographs.

(a) $g = 1\bar{1}01$, showing residual visibility of a_1 dislocations and complete invisibility of a_3 type of dislocations

(b) $g = 0\bar{1}1\bar{1}$, showing complete invisibility of a_1 dislocations and residual visibility of a_3 type of dislocations

Fig. 4.27 Stereographic projection showing the orientations and trace analysis of Figs. 4.24-4.26.

Fig. 4.28 Bright field TEM micrographs of tensile interrupted specimen of Timetal 834 at 450°C taken along $[\bar{1}2\bar{1}3]$ zone axis showing two dislocation pile ups of ' a_3 ' dislocations ($b=1/3[11\bar{2}0]$) in the $(1\bar{1}01)$ pyramidal and (0001) basal plane. Common locations marked by arrow in all micrographs.

(a) $g = 0\bar{1}11$, showing complete visibility

(b) $g = 1\bar{1}01$, showing complete invisibility

(c) $g = 10\bar{1}0$, showing residual visibility

- Fig. 4.29 Bright field TEM micrographs of tensile interrupted specimen of Timetal 834 at 450°C taken along $[\bar{2}4\bar{2}3]$ zone axis. Common locations marked by arrow in all micrographs.
 (a) $g = 01\bar{1}\bar{2}$, showing complete invisibility
 (b) $g = 1\bar{1}02$, showing complete invisibility
- Fig. 4.30 Bright field TEM micrographs of tensile interrupted specimen of Timetal 834 at 450°C taken along $[0001]$ zone axis. Common locations marked by arrow in all micrographs.
 (a) $g = 1\bar{1}00$, showing complete invisibility
 (b) $g = \bar{1}2\bar{1}0$, showing residual visibility
 (c) $g=0\bar{1}10$, showing residual visibility
- Fig. 4.31 Stereographic projection showing the orientations and trace analysis of Figs. 4.28-4.30.
- Fig. 4.32 Dislocation substructure taken with $g = 0111$ in two beam orientation in Timetal 834 tensile tested up to 0.2% plastic strain at room temperature.
- Fig. 4.33 Dislocation substructure taken with multi beam orientation showing dislocation pile-ups in Timetal 834 tensile tested up to 0.2% plastic strain at room temperature.
- Fig. 4.34 (a) Dislocation substructure in Timetal 834 tensile tested at 450°C showing two types of dislocation pile-ups (Type I is indicated by A and type II is indicated by B) as shown in insets. Two types of dislocation pile ups are shown schematically in (b) and with high magnification micrographs in (c).
- Fig. 4.35 (a) Dislocation substructure in Timetal 834 tensile tested up to 0.2% plastic strain at 450°C showing (a) pinned dislocation segments and (b) random tangles of dislocations.

- Fig. 4.36 Dislocation substructure in alloy 834 without Si tensile tested up to 0.2% plastic strain at room temperature showing (a-b) dislocation pile-ups (c) dislocation tangles and (d) cusped dislocations.
- Fig. 4.37 Dislocation substructure in alloy 834 without Si tensile tested up to 0.2% plastic strain at 450°C showing (a) dislocation tangles (b-c) sub-boundaries and isolated dislocations and (d) long curved dislocations.
- Fig. 4.38 Dislocation substructure in alloy 834 without Si tensile tested up to 0.2% plastic strain at 450°C showing (a) relatively straight dislocations with $g = 0002$ and (b) curved dislocations with $g = 01\bar{1}1$. The visibility/invisibility of these dislocations is shown also shown schematically in (c).
- Fig. 4.39 Low and high magnification SEM fractographs of (a) Timetal 834 and (b) alloy 834 without Si at 300°C at 10^{-5} s^{-1} .
- Fig. 4.40 Low and high magnification SEM fractographs of (a) Timetal 834 and (b) alloy 834 without Si at 400°C at 10^{-5} s^{-1} .
- Fig. 4.41 Low and high magnification SEM fractographs of (a) Timetal 834 and (b) alloy 834 without Si at 450°C at 10^{-5} s^{-1} .
- Fig. 4.42 Low and high magnification SEM fractographs of (a) Timetal 834 and (b) alloy 834 without Si at 500°C at 10^{-5} s^{-1} .
- Fig. 4.43 Low and high magnification SEM fractographs of Timetal 834 at (a) lowest and (b) highest strain rates at 300°C.
- Fig. 4.44 Low and high magnification SEM fractographs of alloy 834 without Si at (a) lowest and (b) highest strain rates at 300°C.

- Fig. 4.45 Low and high magnification SEM fractographs of Timetal 834 at (a) lowest and (b) highest strain rates at 350°C.
- Fig. 4.46 Low and high magnification SEM fractographs of alloy 834 without Si at (a) lowest and (b) highest strain rates at 350°C.
- Fig. 4.47 Low and high magnification SEM fractographs of Timetal 834 at (a) lowest and (b) highest strain rates at 450°C.
- Fig. 4.48 Low and high magnification SEM fractographs of alloy 834 without Si at (a) lowest and (b) highest strain rates at 450°C.
- Fig. 4.49 SEM fractographs showing (a) entire fracture surface (20 X) and (b) central region (500 x) of base and modified alloy at 600 °C at strain rate of 10^{-3} s^{-1} .
- Fig. 4.50 Variation of critical true plastic strain with strain rate for the onset of serrations in (a) Timetal 834 and (b) alloy 834 without Si.
- Fig. 4.51 Variation of critical true plastic strain with (a) strain rate and (b) temperature for the determination of activation energy by McCormick's method for Timetal 834.
- Fig. 4.52 Variation of critical true plastic strain with (a) strain rate and (b) temperature for the determination of activation energy by intercept method for Timetal 834.
- Fig. 4.53 Variation of (a) stress increments with strain rate and (b) strain rate with temperature using intercepts from (a) at various stress increments for Timetal 834.

- Fig. 4.54 Plots of (a) log (strain rate) vs log (critical plastic strain) and (b) log (critical plastic strain) vs. reciprocal temperature for the determination of activation energy for alloy 834 without Si.
- Fig. 4.55 Variation of (a) stress increments with strain rate and (b) strain rate with temperature using intercepts from (a) at various stress increments for alloy 834 without Si.
- Fig. 4. 56 (a) Zero loss image, (b and e) Carbon, (c and f) Nitrogen and (d and g) Oxygen elemental maps taken along [2-1-10] zone axis of 300°C tensile interrupted sample using EFTEM. Electron energy loss spectrum (EELS) of Fig. 4f is shown in Fig. 4h showing N and Ti edges.
- Fig. 4.57 (a) Zero loss image (b and e) Carbon (c and f) Nitrogen and (d and g) Oxygen elemental maps taken along [2-1-10] zone axis of 450°C tensile interrupted sample using EFTEM of alloy 834 without Si.
- Fig. 4.58 (a) Zero loss image taken in [2-1-10] zone axis orientation from a specimen tensile tested (interrupted test) carried out at ambient temperature: (b) Carbon,(c) Nitrogen and (d) Oxygen elemental maps of alloy 834 without Si. Symbol of elements are indicated in the respective micrographs.
- Fig. 4.59 Variation of activation volume as a function of temperature for alloy 834 without Si and Timetal 834.

Chapter V: Low Cycle Fatigue Behavior

- Fig. 5.1 Geometry of cylindrical specimens used for low cycle fatigue (LCF) testing [ASTM Standard E 606/E606-12] and (b) photograph of LCF specimen
- Fig. 5.2 Photographs of (a) MTS servohydraulic test system and (b) mounting arrangement of high temperature extensometer for LCF testing
- Fig. 5.3 Cyclic stress response curves of Timetal 834 at (a) 300°C (b) 450°C and (c) 600°C
- Fig. 5.4 Variation of peak tensile stress vs. test temperature to illustrate the strain aging peak at 450°C.
- Fig. 5.5 Cyclic stress – strain curves at (a) 300°C (b) 450°C and (c) 600°C
- Fig. 5.6 (a) Dependence of fatigue life on imposed total strain amplitude and (b) Coffin-Manson plots of plastic strain amplitude ($\Delta\epsilon_p/2$) versus number of strain reversals to failure ($2N_f$) at three test temperatures.
- Fig. 5.7 TEM micrographs of deformation substructure in specimens fatigued up to half life at 300°C and $\Delta\epsilon_T/2 = 1.0\%$. General bright-field image of dislocation substructures showing (a) dislocation pile-ups inside primary α grains (b) superlattice diffraction spots and (c) isolated slip bands across α laths of transformed β grains.
- Fig. 5.8 TEM micrographs showing the dislocation substructures during initial cyclic softening ($N=3$) at 450°C. (a) planar slip bands inside primary α grains (b) paired dislocations inside a pile up in secondary α laths and (c) α_2 superlattice reflections in diffraction pattern corresponding to the region of paired dislocation as shown in (b) can be seen in the micrographs.
- Fig. 5.9 TEM micrographs showing the dislocation substructures at the end of cyclic softening at 450°C. (a) planar slip bands (b) high magnification micrograph of encircled region showing anchored dislocations (c) cellular substructure inside primary α

grains and (d) planar slip bands in secondary α laths can be seen in the micrographs.

- Fig. 5.10 TEM micrographs showing the dislocation substructures during cyclic hardening ($N=100$) at 450°C . Intense planar slip bands can be seen inside (a) primary α grains and (b) secondary α laths.
- Fig. 5.11 TEM micrographs of deformation substructure in specimens fatigued up to half life at 600°C and $\Delta\epsilon_T/2 = 1.0\%$. General bright-field image of dislocation substructures showing (a) multiple slip bands and (b-c) bowing out of dislocation segments inside primary α grains (d) planar slip bands with threaded dislocations in secondary α laths of transformed β grains.
- Fig. 5.12 Schematic illustration showing the (a) mutual competition between cyclic softening and cyclic hardening and (b) loading and unloading segments of a hysteresis loop.
- Fig. 5.13 Variation of peak stress with cumulative plastic strain at 450°C showing the onset of cyclic hardening at cumulative plastic strain ~ 0.1 .
- Fig. 5.14 Variation of peak tensile stress vs. elapsed cycles at $\Delta\epsilon_T/2 = 1.0\%$ at 450°C showing instantaneous increase in stress response at lower strain rate .
- Fig. 5.15 Plastic strain amplitude developed at half-life as a function of imposed total strain amplitude at the three temperature studied
- Fig. 5.16 SEM fractographs at strain amplitude of 0.4% for specimens tested at (a) 300°C (b) 450°C (c) 600°C .

Chapter VI: Thermomechanical Fatigue Behaviour

- Fig. 6.1 (a) Tubular specimen geometry (all dimensions are in mm) and (b) photograph of tubular specimen used for TMF testing.

- Fig. 6.2 (a) Induction heating based thermomechanical fatigue test system and (b-c) showing specimen mounting arrangement and fixing of thermocouples.
- Fig. 6.3 Waveform showing variation of temperature and mechanical strain vs. time during (a) IP-TMF and (b) OP-TMF test conditions in the temperature interval of $450^{\circ}\text{C} \leftrightarrow 600^{\circ}\text{C}$.
- Fig. 6.4 Cyclic stress response curves in the temperature interval of (a) $300^{\circ}\text{C} \leftrightarrow 450^{\circ}\text{C}$ IP-TMF (b) $300^{\circ}\text{C} \leftrightarrow 450^{\circ}\text{C}$ OP-TMF (c) $450^{\circ}\text{C} \leftrightarrow 600^{\circ}\text{C}$ IP-TMF and (d) $450^{\circ}\text{C} \leftrightarrow 600^{\circ}\text{C}$ OP-TMF loading.
- Fig. 6.5 Hysteresis loops (stress vs. mechanical strain) recorded at (a) IP-TMF and (b) OP-TMF test conditions in the temperature interval of $450^{\circ}\text{C} \leftrightarrow 600^{\circ}\text{C}$.
- Fig. 6.6 Variation of mean stress with elapsed cycles in the temperature interval of (a) $300^{\circ}\text{C} \leftrightarrow 450^{\circ}\text{C}$ IP-TMF (b) $300^{\circ}\text{C} \leftrightarrow 450^{\circ}\text{C}$ OP-TMF (c) $450^{\circ}\text{C} \leftrightarrow 600^{\circ}\text{C}$ IP-TMF and (d) $450^{\circ}\text{C} \leftrightarrow 600^{\circ}\text{C}$ OP-TMF loading.
- Fig. 6.7 Variation of mechanical strain amplitude with thermomechanical fatigue lives at two temperature intervals and phase relationships.
- Fig. 6.8 Bright field TEM micrographs of $300^{\circ}\text{C} \leftrightarrow 450^{\circ}\text{C}$ TMF loading showing planar slip bands under (a-b) IP-TMF and (c-d) OP-TMF test conditions.
- Fig. 6.9 Bright field TEM micrographs of $450^{\circ}\text{C} \leftrightarrow 600^{\circ}\text{C}$ IP-TMF loading showing (a) planar slip bands (b) additional slip systems inside α_{p} grains and (c) stacking fault fringes in secondary alpha colonies of T_{β} grains.
- Fig. 6.10 Bright field TEM micrographs of $450^{\circ}\text{C} \leftrightarrow 600^{\circ}\text{C}$ OP-TMF loading showing (a) planar slip bands (b) intense slip bands inside α_{p} grains and (c) stacking fault fringes in secondary alpha colonies of T_{β} grains.
- Fig. 6.11 (a) SEM fractograph of a failed TMF tested tubular sample. Crack initiation region identified by tracking the radial pattern to its origin is encircled. (b-c) Increase in striation spacing can be seen with increase in crack length.

- Fig. 6.12 SEM fractographs at relatively low and high strain amplitudes for specimens tested at 300°C↔450°C IP-TMF loading.
- Fig. 6.13 SEM fractographs at relatively low and high strain amplitudes for specimens tested at 300°C↔450°C OP-TMF loading.
- Fig. 6.14 SEM fractographs at relatively low and high strain amplitudes for specimens tested at 450°C↔600°C IP-TMF loading.
- Fig. 6.15 SEM fractographs at relatively low and high strain amplitudes for specimens tested at 450°C↔600°C OP-TMF loading.
- Fig. 6.16 EDAX plots from the striated area showing dominant peak of oxygen at (a) OP-TMF loading as compared to (b) IP-TMF loading in the temperature interval of 450°C↔600°C.
- Fig. 6.17 Variation of peak stress with cumulative plastic strain at 450°C during (a) TMF and (b) isothermal loading.
- Fig. 6.18 Cyclic stress response curves initially run isothermally at 300°C and 600°C for 50 cycles and subsequently switched to 450°C↔600°C IP-TMF test.
- Fig. 6.19 Cyclic stress response curves of Timetal 834 Ti alloy in (a) aged and solution treated condition during 450°C↔600°C IP-TMF test (b) cyclic stress response of the alloy only at 450°C for aged and solution treated condition of the alloy.

Chapter VII: Fatigue Crack Growth Behaviour under Isothermal Loading

- Fig. 7.1 Geometry of CT specimens used for fatigue crack growth testing.
- Fig. 7.2 (a) Schematic illustration of orientation of specimen extraction from plates and (b) photograph of CT specimen with knife-edge, fatigue starter notch and scribed marks used for fatigue crack growth testing.

- Fig. 7.3 Photographs of (a) Instron 8500 plus servohydraulic test system used for FCG testing and mounting arrangement of high temperature COD gauge (b) before and (b) after closing the resistance furnace.
- Fig. 7.4 Photographs of fatigue crack growth tested specimen at (a) 300°C (b) 450°C and (c) 600°C
- Fig. 7.5 Fatigue crack growth curves of Timetal 834 Ti-alloy at various test temperatures.
- Fig. 7.6 SEM fractographs showing microstructurally sensitive crystallographic mode of stage I crack propagation at near threshold region at (a) 300°C (b) 400°C and (c) 600°C. EDS plot taken from encircled region of figure 7.6c is shown in figure 7.6d.
- Fig. 7.7 SEM fractographs showing striated mode of crack propagation at (a) 300°C (b) 450°C and (c) 600°C
- Fig. 7.8 Surface roughness profiles along the crack length direction at low ΔK region at (a) 300°C (b) 450°C (c) 600°C.
- Fig. 7.9 Variation of microhardness as a function of distance from the crack tip at various fatigue crack growth test conditions. Solid and dashed arrows indicate the cyclic and monotonic plastic zone size, respectively.
- Fig. 7.10 Auger spectrum of tested specimens in near threshold region.
- Fig. 7.11 (a) da/dN versus $\Delta K/E$ and (b) da/dN versus $\Delta K^2/\sigma_y E$ at various test conditions
- Fig. 7.12 Closure corrected fatigue crack growth curves at various test temperatures.
- Fig. 7.13 Closure corrected fatigue crack growth curves as a function of (b) modulus and (c) CTOD at various test temperatures
- Fig. 7.14 Schematic plot of K_{cl} versus K_{max} illustrating various types of crack closure mechanisms [Allison 1988]
- Fig. 7.15 Variation of (b) K_{cl} versus K_{max} and (c) K_{cl}/K_{max} versus K_{max} at various test temperatures

- Fig. 7.16 SEM microstructures at low ΔK region showing different extent of crack branching at (a) 300°C (b) 450°C and (c) 600°C.
- Fig. 7.17 SEM microstructures at higher ΔK region showing different extent of crack branching at (a) 300°C (b) 450°C and (c) 600°C.
- Fig. 7.18 Schematic illustration of cyclic softening and hardening behaviour at the crack tip

Chapter VIII: Thermomechanical Fatigue Crack Growth Behavior

- Fig. 8.1 Single edge notch tensile (SENT) specimen geometry used for TMFCG tests (all dimensions are in mm).
- Fig. 8.2 A schematic illustration of orientation of test coupon with respect to rolling direction of plate.
- Fig. 8.3 Schematic illustration showing the positioning of various thermocouples (TC₁, TC₂, TC₃ and TC₄) around fatigue starter notch for measurement of temperature gradient.
- Fig. 8.4 Photographs of (a) TMF test facility for carrying out fatigue crack growth testing under TMF loading (b) mounting arrangement of SENT specimen inside the infra-red furnace and (b) an ongoing test in the temperature interval of 450°C↔600°C.
- Fig. 8.5 Potential curves with temperature cycling between 300°C↔450°C under (a) zero load and (b) with load cycling.
- Fig. 8.6 Photograph of a SENT specimen interrupted during testing for crack length measurement.
- Fig. 8.7 Variation of optically measured crack length vs. $(V_1 - V_0)/-V_0$ for determination of coefficients A_0 , A_1 and A_2 under (a) IP-TMFCG loading and (b) OP-TMFCG loading at 300°C↔450°C temperature interval. $(V_1 - V_0)/-V_0$ vs. time, crack length vs. time and crack length vs. elapsed cycles under

(c-e) IP-TMFCG loading and (f-h) OP-TMFCG loading at the same temperature interval.

- Fig. 8.8 Fractures surface of the tested specimen in the temperature interval of 300°C↔450°C temperature interval.
- Fig. 8.9 Fatigue crack growth resistance curve (da/dN vs. ΔK) of Timetal 834 Ti-alloy under TMF loading.
- Fig. 8.10 SEM fractographs showing microstructurally sensitive crystallographic mode of stage I crack propagation at near threshold region at 300°C↔450°C IP (b) 300°C↔450°C OP (c) 450°C↔600°C IP and (d) 450°C↔600°C OP –TMFCG test conditions.
- Fig. 8.11 SEM fractographs showing striated mode of stage II crack propagation at (a) 300°C↔450°C IP (b) 300°C↔450°C OP (c) 450°C↔600°C IP and (d) 450°C↔600°C OP –TMFCG test conditions. Fig. 8.11e is the high magnification micrograph of encircled region of Fig. 8.11d.
- Fig. 8.12 EDS plots taken from Fig. 8.11d showing (a) dominant peak of oxygen in the encircled region and (c) weak oxygen peak from the matrix.
- Fig. 8.13 Fracture surface roughness profiles along the direction of crack propagation at near threshold region at (a) 300°C↔450°C IP (b) 300°C↔450°C OP (c) 450°C↔600°C IP and (d) 450°C↔600°C OP –TMFCG test conditions.
- Fig. 8.14 Auger spectrum of tested specimens in near threshold region at (a) 300°C↔450°C IP (b) 300°C↔450°C OP (c) 450°C↔600°C IP and (d) 450°C↔600°C OP – TMFCG test conditions.
- Fig. 8.15 Variation of microhardness as a function of distance from the crack tip under (a)) 300°C↔450°C and (b) 450°C↔600°C TMFCG loading. Solid and dashed arrows indicate the cyclic and monotonic plastic zone size, respectively.
- Fig. 8.16 Local hcp pole figures around crack wake of (a) 300°C↔450°C (b) 450°C↔600°C IP-TMFCG loading interrupted sample at 30 MPa.m^{1/2}.

- Fig. 8.17 Local hcp pole figures around crack wake of (a) 300°C↔450°C (b) 450°C↔600°C OP-TMFCG loading interrupted sample at 30 MPa.m^{1/2} .
- Fig. 8.18 Distribution maps showing the percentage of (a-c) α_p grains and (d-f) secondary α colonies deformed under prismatic, basal and pyramidal slip from the observation of 0.5 x 0.3 mm² under. 300°C↔450°C IP-TMFCG loading, respectively
- Fig. 8.19 Distribution maps showing the percentage of (a-c) α_p grains and (d-f) secondary α colonies deformed under prismatic, basal and pyramidal slip from the observation of 0.5 x 0.3 mm² under. 300°C↔450°C OP-TMFCG loading, respectively
- Fig. 8.20 Distribution maps showing the percentage of (a-c) α_p grains and (d-f) α – colonies deformed under prismatic, basal and pyramidal slip from the observation of 0.5 x 0.3 mm² under. 450°C↔600°C IP-TMF loading, respectively
- Fig. 8.21 Distribution maps showing the percentage of (a-c) α_p grains and (d-f) α – colonies deformed under prismatic, basal and pyramidal slip from the observation of 0.5 x 0.3 mm² under. 450°C↔600°C OP-TMFCG loading, respectively
- Fig. 8.22 (a) High resolution FEG-SEM images and corresponding (b) EBSD map and (c) misorientation between grains. SEM images and EBSD maps shows the local interaction of growing crack with primary α grains and secondary α – colonies. CP and LD represent direction of crack propagation and loading, respectively. These images are representative of 300°C↔450°C IP-TMFCG test condition.
- Fig. 8.23 (a) High resolution FEG-SEM images and corresponding (b) EBSD map and (c) misorientation between grains. SEM images and EBSD maps shows the local interaction of growing crack with two secondary α – colonies. CP and LD represent direction of crack propagation and loading, respectively. These images are representative of 450°C↔600°C IP-TMFCG test condition.
- Fig. 8.24 (a) High resolution FEG-SEM images and corresponding (b) EBSD maps and (c) misorientation between adjacent secondary α colonies. SEM images and EBSD maps show the local interaction of growing crack with secondary α colonies. CP and

LD represent direction of crack propagation and loading, respectively. These images are representative of 300°C↔450°C OP-TMFCG test condition.

Fig. 8.25 (a) High resolution FEG-SEM image and corresponding (b) EBSD map and (c) misorientation between adjacent grains. SEM image and EBSD map shows the local interaction of growing crack with primary α grains and secondary α colonies. CP and LD represent direction of crack propagation and loading, respectively. These images are representative of 300°C↔450°C OP-TMFCG test condition.

Fig. 8.26 (a) High resolution FEG-SEM images and corresponding (b) EBSD map and (c) misorientation between adjacent secondary α colonies. SEM images and EBSD maps show the local interaction of growing crack with secondary α colonies. CP and LD represent direction of crack propagation and loading, respectively. These images are representative of 450°C↔600°C OP-TMFCG test condition.

Fig. 8.27 (a) High resolution FEG-SEM image and corresponding (b) EBSD map and (c) misorientation between adjacent grains. SEM image and EBSD map shows the local interaction of growing crack with primary α grains and secondary α colonies. CP and LD represent direction of crack propagation and loading, respectively. These images are representative of 450°C↔600°C OP-TMFCG test condition.

Fig. 8.28 (a) da/dN versus $\Delta K/E$ and (b) da/dN versus $\Delta K^2/\sigma_y E$ at various TMFCG test conditions

Fig. 8.29 Local misorientation maps of (a) 300°C↔450°C (b) 450°C↔600°C IP-TMF loading interrupted sample, (c) 300°C↔450°C (d) 450°C↔600°C OP-TMF loading interrupted sample, respectively at 30 MPa. $m^{1/2}$ and (e) showing histogram of local average misorientation for the four tested samples.

Fig. 8.30 Variation of potential versus applied load in the temperature interval of 450°C↔600°C OP –TMFCG test condition.

Fig. 8.31 (a) da/dN versus effective ΔK . Closure corrected fatigue crack growth curves as a function of (b) modulus and (c) CTOD at various TMFCG test conditions.

- Fig. 8.32 Variation of (a) K_{cl} versus K_{max} and (b) K_{cl}/K_{max} versus K_{max} at various TMFCG test conditions.
- Fig. 8.33 A schematic plot of da/dN vs. ΔK illustrating the influence of oxidation in stage I and stage II TMFCG behaviour.
- Fig. 8.34 Hysteresis loops at 1st and 100th cycle showing significant increase in peak tensile stress at 450°C as compared to 600°C.

Chapter IX: Comparative Assessment of Fatigue and Fracture Behavior

- Fig. 9.1 (a) Comparison of hardening response of Timetal 834 at 450°C under isothermal and 450°C↔600°C OP-TMF loading and (b) comparison of stress – strain curves at 450°C under monotonic, isothermal and 450°C↔600°C OP-TMF loading
- Fig. 9.2 Variation of fatigue lives of Timetal 834 under isothermal (LCF) and non-isothermal (TMF) loading.
- Fig. 9.3 (a) da/dN vs. ΔK curves and (b) da/dN versus $\Delta K^2/\sigma_y E$ at isothermal and TMF test conditions.
- Fig. 9.4 Comparison of da/dN vs. ΔK curves of Timetal 834 under identical crack growth rates for both the modes of loading.
- Fig. 9.5 Comparison of closure curves in (a) K_{cl} versus K_{max} and (b) K_{cl}/K_{max} versus K_{max} plots under isothermal and thermomechanical fatigue test conditions.
- Fig. 9.6 Comparison of closure load determined using COD and ACPD at 600°C. ACPD based technique gives small reduction in closure load as compared to COD technique

Fig. 9.7 Comparision of characteristic values of crack closure mechanisms under isothermal and thermomechanical fatigue test condition.

List of Tables

Chapter II: Literature Survey

Table 2.1	Characteristics of different types of serrations [Rodriguez 1984]
-----------	---

Chapter III: Material Processing and Microstructural Characterization

Table 3.1	Nominal chemical composition of Timetal 834
Table 3.2	Nominal chemical composition of alloy 834 without Si.
Table 3.3	Microstructural parameters of Timetal 834
Table 3.4	Microstructural parameters of alloy 834 without Si.

Chapter IV: Tensile Behavior

Table 4.1	Monotonic strain hardening exponent (n) and coefficient (K) at various temperatures
Table 4.2	g vectors and zone axis for the tensile tested specimen of alloy 834 without Si at ambient temperature.
Table 4.3	g vectors and zone axis for the tensile tested specimen at ambient temperature for Timetal 834.
Table 4.4	g vectors and zone axis for the tensile tested specimen at 450°C for alloy 834 without Si.
Table 4.5	g vectors and zone axis for the tensile tested specimen at 450°C for Timetal 834.
Table 4.6	Activation energy of various elements in α -Titanium [Doner and Conrad 1973, Conrad 1981].
Table 4.7	Diffusivity of interstitial solute elements in α -Titanium.

Chapter V: Low Cycle Fatigue Behavior

Table 5.1	Cyclic and monotonic strain hardening exponent at various temperatures
Table 5.2	Values of fatigue ductility coefficient and fatigue ductility exponent at three test temperatures.
Table 5.3	Values of cumulative plastic strain at various strain amplitudes at 450°C.

Chapter VI: Thermomechanical Fatigue Behavior

Table 6.1	Average striation spacing at a distance of 25 μm (approximately) from the crack initiation region at various TMF loading conditions.
Table 6.2	Cumulative plastic strain amplitude for the onset of secondary cyclic hardening during 300°C \leftrightarrow 450°C TMF and 450°C LCF.

Chapter VII: Fatigue Crack Growth Behavior under Isothermal Loading

Table 7.1	Parameters (Paris constants, maximum and cyclic crack tip opening displacement, average surface roughness, thickness of the oxide layer and cyclic plastic zone size) at various test conditions.
-----------	---

Chapter VIII: Thermomechanical Fatigue Crack Growth Behavior

Table 8.1	Parameters (Paris constants, maximum and cyclic crack tip opening displacement, average surface roughness, thickness of the oxide layer and cyclic plastic zone size) at various test conditions.
-----------	---

Chapter IX: Comparative Assessment of Fatigue & Fracture Behaviour

Table 9.1 Paris constants under isothermal and non-isothermal test conditions.

Contents

List of Publications/Conference Proceedings.....	I
Acknowledgements.....	IV
Synopsis.....	VIII
List of Figures	XV
List of Tables.....	XXXVIII

Chapter I

Introduction

1.1 Titanium Alloys and Gas Turbines	1
1.2 High Pressure Compressor Discs	3
1.3 Thesis Objective	4
1.4 Thesis Outlay	5

Chapter II

Literature Survey

2.1 Titanium Alloys: An Introduction	8
2.1.1 Classification of Ti Alloys	10
2.1.2 Microstructural Constituents of Near α Ti Alloys	12
2.1.3 Timetal 834	14
2.2 Mechanical Properties of Timetal 834	17
2.2.1 Dynamic Strain Aging (DSA)	19
2.2.1.1 Manifestations of DSA	20

2.2.1.2	Principle Involved in Load Drop Phenomenon	21
2.2.1.3	Serrations	24
2.2.1.4	Various Models of DSA	26
2.2.1.5	Plastic Instabilities Associated with DSA	30
2.2.1.6	DSA in Timetal 834	34
2.2.2	Low Cycle Fatigue (LCF)	35
2.2.2.1	LCF Behavior of Timetal 834	40
2.2.3	Fatigue Crack Growth	41
2.2.3.1	Fatigue Crack Closure	45
2.2.3.1.1	Plasticity Induced Crack Closure	49
2.2.3.1.2	Oxide Induced Crack Closure	49
2.2.3.1.3	Fracture Surface Induced Crack Closure	50
2.2.3.2	Fatigue Crack Growth Behavior of Timetal 834	50
2.2.4	Thermomechanical Fatigue	51
2.2.4.1	Thermomechanical Fatigue Behavior of Timetal 834	55
2.3	Aim of the Thesis	56

Chapter III

Material Processing and Microstructural Characterization

3.1	Introduction	58
3.2	Materials and Experimental Procedure	60
3.2.1	Materials and their Processing	60
3.3	Results	60
3.3.1	Microstructural Constituents of Timetal 834 and Alloy 834 without silicon	63
3.3.2	Dislocation substructure of Timetal 834 and alloy 834 without silicon	72
3.4	Discussion	73
3.5	Summary	76

Chapter IV

Tensile Behavior

4.1	Introduction	77
4.2	Experimental Procedure	81
4.3	Results	85
4.3.1	Serrated Flow	85
4.3.2	Tensile Properties	91
4.3.3	Dislocation Behavior in Tensile Deformation	96
4.3.3.1	Dislocation Behavior at Room Temperature (Non-Serrated Regime)	97
4.3.3.2	Dislocation Behavior at 450°C (Serrated Regime)	109
4.3.3.3	Dislocation Substructure at Room	120

Temperature and at 450°C

4.3.4	Tensile Fracture Behavior	128
4.4	Discussion	133
4.4.1	Determination of Activation Energy for the Occurrence of DSA	134
4.4.2	Identification of solute atmosphere around Dislocations in Alloy 834 without Si	141
4.4.3	Mechanism of Solute Segregation at Different Test Temperatures	146
4.4.4	Nature of Serrations	149
4.4.5	Tensile Deformation Behavior	152
4.4.6	Activation Volume	155
4.5	Summary	158

Chapter V

Low Cycle Fatigue Behavior

5.1	Introduction	160
5.2	Experimental Procedure	161
5.2.1	Low Cycle Fatigue Testing	161
5.2.2	Characterization for Cyclic Deformation Behavior	163
5.3	Results	165
5.3.1	Cyclic Stress Response Curves	165
5.3.2	Cyclic Stress-Strain Response	167
5.3.3	Low Cycle Fatigue Lives	169
5.3.4	Dislocation Substructures	171
5.4	Discussion	178

5.4.1	Characteristics of Cyclic Deformation	178
5.4.1.1	Cyclic Stress Response	178
5.4.1.2	Monotonic and Cyclic Stress-Strain Behavior	188
5.4.1.3	Fatigue lives and Deformation Substructures	189
5.5	Summary	192

Chapter VI

Thermomechanical Fatigue (TMF) Behavior

6.1	Introduction	193
6.2	Experimental Procedure	195
6.2.1	Thermomechanical Fatigue Test Procedure	195
6.2.2	Characterization of Deformation and Fracture Behavior	195
6.3	Results	200
6.3.1	Cyclic Stress Response Curves	200
6.3.2	Development of Mean Stress during Thermomechanical Fatigue	202
6.3.3	Thermomechanical Fatigue Lives	203
6.3.4	Dislocation Substructures	204
6.3.5	Fracture Behavior under Thermomechanical Loading	208
6.4	Discussion	216
6.4.1	Characterization of Cyclic Deformation	216
6.4.4.1	Cyclic Stress Response and Fatigue Lives	216
6.5	Summary	223

Chapter VII

Fatigue Crack Growth Behavior under Isothermal Loading

7.1	Introduction	225
7.2	Experimental Procedure	226
7.2.1	Extraction and Preparation of Specimens	226
7.2.2	Fatigue Pre-Cracking	229
7.2.3	Fatigue Crack Growth Experiments	231
7.2.4	Fractography and Measurement of Fracture Surface Roughness	234
7.2.5	Measurement of Plastic Zone Size using Microhardness	235
7.2.6	Auger Electron Spectroscopy	235
7.3	Results	236
7.3.1	Fatigue Crack Growth Rates	238
7.3.2	Fracture Behavior	238
7.3.3	Fracture Surface Roughness Profile	241
7.3.4	Estimation of Plastic Zone Size	242
7.3.5	Auger Electron Spectroscopy	243
7.4	Discussion	245
7.4.1	Effects of Yield Strength and Modulus	246
7.4.2	Characterization of Crack Closure	247
7.4.3	Fatigue Crack Growth Based on Micro Crack Tip Low Cycle Fatigue Process	255
7.5	Summary	259

Chapter VIII

Thermomechanical Fatigue Crack Growth Behavior

8.1	Introduction	260
8.2	Experimental Procedure	261
8.2.1	Extraction and Preparation of Specimens	261
8.2.2	Fatigue Pre-Cracking	263
8.2.3	Measurement of Temperature Gradient and	264
	Thermomechanical Fatigue Crack Growth Procedure	266
8.2.4	Generation of Calibration Curves for the Measurement	273
	of Crack Length	
8.2.5	Fractography and Measurement of Fracture surface	273
	Roughness	
8.2.6	Measurement of Plastic Zone Size using Microhardness	274
8.2.7	Electron Back Scattered Diffraction	275
8.3	Results	
8.3.1	Thermomechanical Fatigue Crack Growth Rates	276
8.3.2	Fracture Behavior	276
8.3.3	Fracture Surface Roughness Profile	280
8.3.4	Auger Electron Spectroscopy	281
8.3.5	Estimation of Plastic Zone Size	284
8.3.6	Microstructural Characterization using Electron Back	285
	Scattered Diffraction	
8.3.6.1	IP-TMF Loading (300°C↔450°C)	301
8.3.6.2	IP-TMF Loading (450°C↔600°C)	302
8.3.6.3	OP-TMF Loading (300°C↔450°C)	302
8.3.6.4	OP-TMF Loading (450°C↔600°C)	303

8.4	Discussion	305
8.4.1	Effects of Yield Strength and Modulus	305
8.4.2	Role of Local Crystallographic Orientation on TMFCG Behavior	306
8.4.3	Characterization of Crack Closure	313
8.4.4	TMFCG Behavior Based on Micro Crack Tip TMF Process	321
8.5	Summary	323

Chapter IX

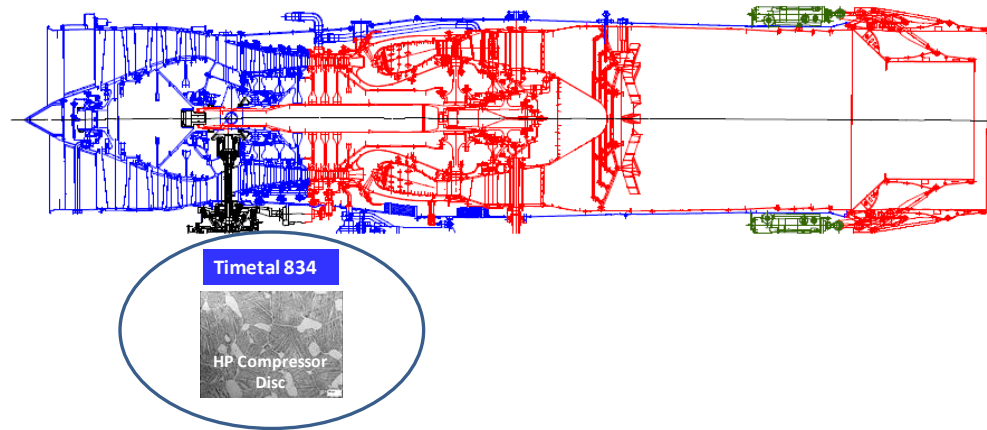
Comparative Assessment of Fatigue and Fracture Behavior

9.1	Introduction	324
9.1.1	Comparative Assessment of Fatigue Behavior under Isothermal and Non-Isothermal Test Conditions	324
9.2.2	Comparative Assessment of Fracture Behavior under Isothermal and Non-Isothermal Test Conditions	327
9.2	Summary	334

Chapter X

Conclusions and Suggestions for Future Work

10.1	Monotonic Tensile Behavior	335
10.2	Cyclic Deformation Behavior	337
10.3	Fatigue Crack Growth Behaviour	341
10.4	Suggestions for Future Work	346
	Bibliography	348
	Appendix A	374



■ Ti-base alloys ■ Ni-base alloys ■ Fe-base alloys ■ Other alloys

Chapter I

Introduction

1.1 Titanium Alloys and Gas Turbines

Titanium base alloys exhibit superior ratio of endurance limit to tensile strength and hence high fatigue strength at a given stress level, high ratio of strength to density and hence high specific strength, high passivation potential for getting corroded and hence high corrosion resistance. Primarily these properties have driven the usage of Ti base alloys in most sectors of the industries. Although the production of Titanium (Ti) is highly capital and energy intensive in nature due to its chemical reactivity, Ti has now acquired the name of a “well behaved material” due to its reliable performance in most of the demanding applications. The demands of Ti base alloys have, almost entirely, been driven by the requirement to improve the reliability and efficiency of gas turbine aero engines. The constant drive for development of newer and newer gas turbine aero engines with improved thrust and efficiency has commercially exploited the Ti and Ti-base alloys. This has been successfully exploited so much so that Ti base intermetallic alloy which was earlier neglected primarily due to its limited ductility is now finding its place in newer generation of gas turbine aero engines. Apart from this class of alloy, better control of high temperature deformation behaviour of Ti base alloys such as $\alpha+\beta$ and near α Ti alloys has paved the way of their usage by as much as 50% in most of the newer versions of military gas turbine aero engines. Specific gas turbine compressor module parts manufactured using Ti base alloys include discs and blades of compressor, casings, rings and fasteners. The differing requirements in specific parts of the engine have led to the development of various classes of Ti

base alloys with varying balances of mechanical properties such as yield strength, fatigue (low as well as high cycle fatigue), fatigue crack growth resistance, fracture toughness, and oxidation resistance especially at high temperatures.

As highlighted above, development of modern gas turbine aero engines, military engines in particular demands generation of higher thrust and efficiency at low specific fuel consumption without increasing the weight or size of the jet engine. While it primarily depends on the ability to increase the turbine entry temperature (TET), the maximum temperature up to which the compressed air is increased in rear stages of compressor is limited by the high temperature capabilities of the materials used for high pressure compressor blades/vanes and discs [Lütjering and Williams 2007]. In most of the engines, while the best possible combination of high temperature mechanical properties as mentioned above and reliability in performance of these components are attained through Ni-base superalloys, near α titanium alloys have emerged as a potential candidate material to be used as a high pressure compressor discs. Although the high pressure compressor discs encounters a synergistic interaction of various damaging modes, the usable service life of stators/rotors is governed by creep strength and oxidation resistance. Likewise, in case of discs, tensile strength and low cycle fatigue resistance are the life limiting damaging modes. In view of the relevance of near α Ti base alloys developed and used for high pressure compressor discs of military gas turbine aero engines, the requirements of this alloy and its characteristics for this application are elaborated below.

1.2 High Pressure Compressor Discs

High pressure compressor discs in a gas turbine aero engines is classified as a 'critical component', failure of which will result in loss of the engine and hence the aircraft. These discs are subjected to higher stresses and temperature which varies as per the sortie of the aircraft. As a support structure for the rotor blades and stator vanes, it rotates at very high speeds (~10,000 rpm) and hence are subjected to centrifugal loads associated with high rotational speed. Unlike airfoils, compressor discs, being geometrically large component, are subjected to a spectrum of temperature which varies as per the various regions of the disc. The rim region due to its close proximity to hot gases attains high temperature as compared to the bore region, as a result of which temperature gradient develops across these regions. The temperature gradient leads to the development of thermal stresses and eventually the amalgamation of centrifugal load and thermal stresses results in low cycle fatigue (LCF) of compressor discs. However, it is imperative to note that these discs are designed to remain in elastic regime of the material, however, the mechanical/geometrical stress concentration sites/raisers such as bolt holes near the bore region and fir-trees near the rim region causes local plastic deformation in case of over speeding of aircraft. In recent times, when designers aim to use blisks (integrated discs) or blings (removal of bore region) in place of discs to further reduce the weight penalty on the engine, the temperature gradient is expected to be much higher than that of discs. This in turn will lead to the

generation of thermal stresses of higher magnitude and hence thermomechanical fatigue (details of which has been discussed in chapter 2) instead of low cycle fatigue becomes the life limiting damaging modes for such components. Design of such components are based either on safe-life approach in which the crack initiation life is converted to service life of the component or the damage tolerant approach where the sub critical crack propagation period in addition to crack initiation is considered as the service life of the component. Therefore, crack initiation as well as propagation both should be considered in design in order to use a disc to its fullest capability. The objective of the thesis covers both the aspects of design and will be discussed in detail in section 1.3.

1.3 Objective and Motivation of the Thesis

Investigations on structure – property correlations on near α titanium alloys can lead to better understanding to suitably tailor the microstructure for a desired application. In context to high pressure compressor discs as outlined in section 1.2, as an input to safe-life design approach, the primary objective of the thesis is to examine in detail the cyclic deformation behaviour of a near α titanium alloy in isothermal (low cycle fatigue) as well as under non-isothermal conditions (thermomechanical fatigue) using smooth cylindrical specimens. Subsequently, in order to complement the damage tolerant design approach, fatigue crack growth behaviour under isothermal and non-isothermal (thermomechanical) conditions have been studied. However, studies on fatigue behaviour always demand some

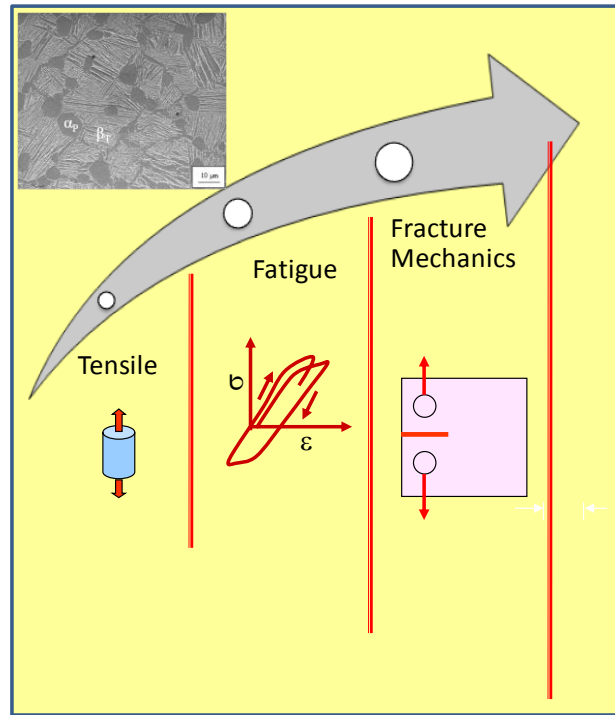
parametric input from the tensile behaviour of a material. Hence, monotonic tensile behaviour has also been studied in detail. Amongst the family of near α titanium alloy, Timetal 834 is an advanced near α titanium alloy specifically developed for high pressure compressor module of gas turbine aero engines [Neal 1988]. While many aspects of this alloy related to melt processing, optimization of microstructure and mechanical properties (detailed in chapter II, literature survey) have been addressed in past. However, systematic studies on the micro-mechanisms related to monotonic tensile deformation as well as cyclic deformation in the intermediate temperature range have not been reported in open literature. Moreover, the intrinsic and extrinsic behaviour of fatigue crack growth under isothermal as well non-isothermal conditions of Timetal 834 have also not been reported in open literature. The detailed understanding on these aspects is the primary objective of the thesis.

1.3 Outlay of the Thesis

The flow of this thesis is organized in the following manner. This introductory chapter is followed by chapter II which succinctly reviews the relevant scientific literature on different aspects of Titanium alloys and, in particular, Timetal 834 alloy. Chapter III presents the material processing and microstructural characterization of Timetal 834. The tensile behaviour of Timetal 834 as a function of temperature and strain rate ranging from 250°C – 750°C and 10^{-6} s^{-1} to 10^{-3} s^{-1} , respectively, is presented in chapter IV. Micro-mechanisms of tensile deformation

behaviour and fracture modes within the temperature – strain rate regime studied are also assessed and discussed in this chapter. In analyzing the tensile behaviour of Timetal 834, it was found that this alloy exhibits ‘inverse’ as well as ‘normal’ Portevin LeChatelier (PLC) effect which is considered as a sub-domain of dynamic strain aging. The characteristics of serrated flow and possible reasons behind it and its influence on tensile properties such as 0.2% yield strength, % elongation, strain rate sensitivity, and activation volume are discussed in chapter IV. As an input for safe-life design approach, fatigue behaviour of Timetal 834 under isothermal test conditions (low cycle fatigue) at three test temperatures viz., 300°C, 400°C and 650°C under fully reversed constant strain amplitude conditions is presented in chapter V. Cyclic stress response, plastic strain dependence of low cycle fatigue lives and micro-mechanisms involved during cyclic deformation are interpreted and discussed in light of deformation substructures obtained. Fatigue behaviour of the alloy under non-isothermal test conditions (Thermomechanical fatigue) behaviour was assessed in two temperature intervals viz., 300°C↔450°C and 450°C↔600°C under fully reversed constant mechanical strain amplitudes ($\Delta\epsilon_m/2$) ranging from 0.6% to 1.2% in chapter VI. Cyclic stress response, thermomechanical fatigue lives and micro-mechanisms involved during cyclic deformation are interpreted and discussed in light of deformation substructures, development of mean stresses and fracture modes obtained. Few unconventional fatigue tests have been conducted under LCF as well as under TMF loading to emphasize the occurrence of dynamic strain aging. These studies were conducted on smooth cylindrical specimens. As an input to damage tolerant based design

approach, fatigue crack growth studies using fracture mechanics type specimens under isothermal test conditions is presented in chapter VII, whereas, chapter VIII is based on thermomechanical crack growth behaviour. Temperature ranges as well as temperature intervals under isothermal and non-isothermal conditions, respectively, were kept same as that of chapter V and VII, respectively. In these chapters, the effects of tensile properties, intrinsic factors such as slip character and extrinsic factor such as crack closure on fatigue crack growth behaviour is suitably characterized. The influence of local crystallographic orientation on thermomechanical fatigue crack growth behaviour is studied using electron back scattered diffraction technique. Chapter IX is based on the comparison of fatigue behaviour (low cycle fatigue as well as fatigue crack growth) under isothermal and non-isothermal test conditions. Chapter X describes the conclusion obtained in this thesis and also the insights gained into the monotonic tensile, cyclic deformation behaviour as well as fatigue crack growth behaviour under isothermal and non-isothermal conditions of Timetal 834 alloy. Suggestion for future work is also included in this chapter.



Chapter II

Literature Survey

2.1 Titanium Alloys: An Introduction

In the early 50's, the emergence of titanium (Ti) as a 'wonder metal' enthused titanium industries to produce a variety of Ti alloys [Driver et al. 1981]. The advantages of Ti is primarily associated with high strength to weight ratio, good resistance to corrosion and low thermal conductivity as well as low thermal expansion [Lütjering and Williams 2007]. These properties contribute to the superiority of titanium alloys for aerospace applications in both engine and airframe components. Appreciation of Ti has led the gradual reduction in consumption of Al and steel by engine developers as shown in Fig. 2.1 [Driver et al. 1981].

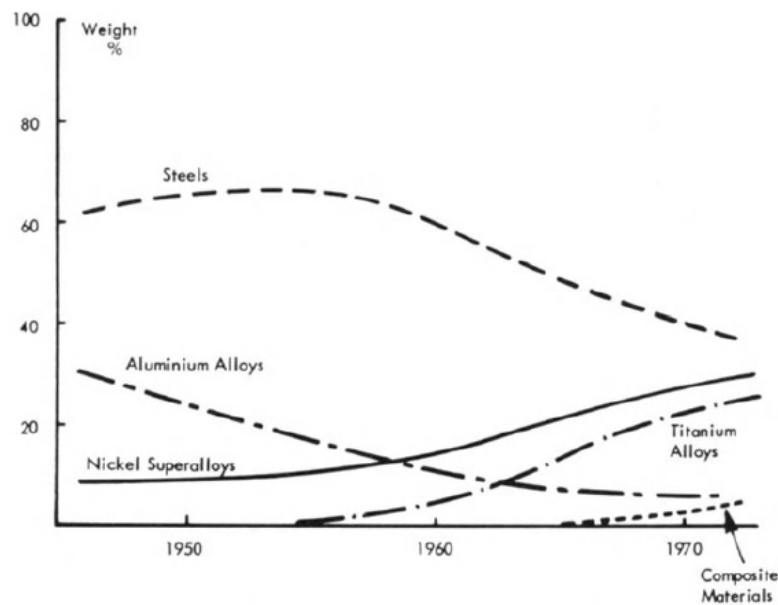


Fig. 2.1 Trends in jet engine material usage [Driver et al. 1981]

As a gas turbine material, the maximum service temperature up to which a titanium alloy can be used is 600°C beyond which oxidation takes away all the advantages associated with Ti alloys [Lütjering and Williams 2007]. Similar to that of steels, Ti exhibits allotropic phase transformations. It exists in close packed hexagonal phase (α) to about 882°C beyond which it changes to body centered cubic phase (β) up to its melting temperature. This phase transformation temperature is also known as β – transus temperature and it plays an important role in thermomechanical processing of Ti alloys. The corresponding unit cells of α and β phases are shown in Fig. 2.2 [Lütjering and Williams 2007].

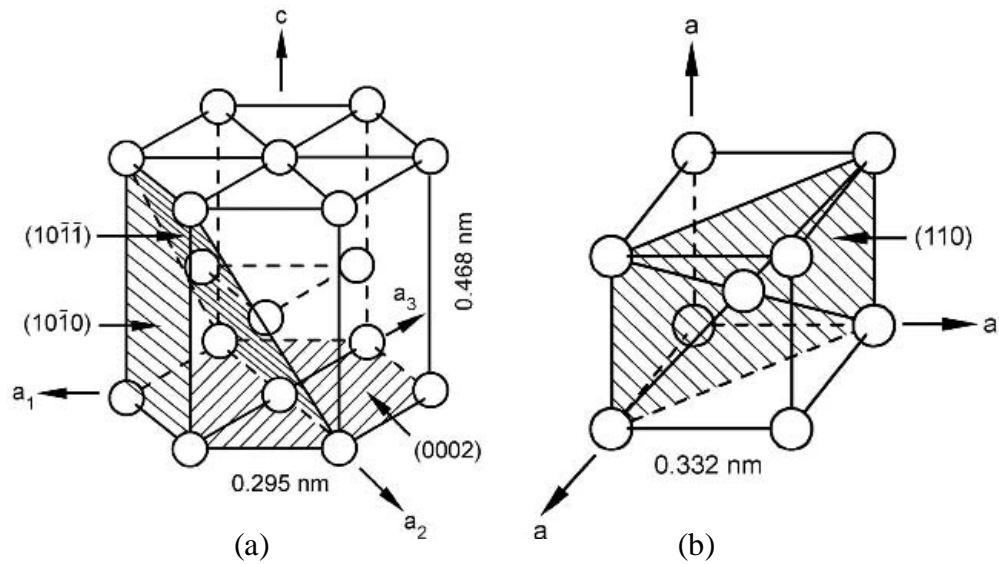


Fig. 2.2 Unit cell of (a) α and (b) β phase [Lütjering and Williams 2007].

Basal (0002), prismatic $\{10\bar{1}0\}$ and first order pyramidal $\{10\bar{1}1\}$ planes are the three close densely packed planes in α titanium as shown in Fig. 2.3. $\langle a \rangle$ type directions of indices $\langle 11\bar{2}0 \rangle$ are the close packed direction in α titanium. As per Von Mises criterion, minimum 5 independent slip systems are required for homogeneous plastic deformation in polycrystalline alloys. While α titanium has

total 12 slip systems, only 4 numbers of independent slip systems favors the activation of $\langle c \rangle$ type burger vector which could be either of pure $\langle c \rangle$ or $\langle c+a \rangle$ character [Lütjering and Williams 2007]. Limited capacity of strain hardening in Ti alloys is primarily attributed to these aspects of slip systems.

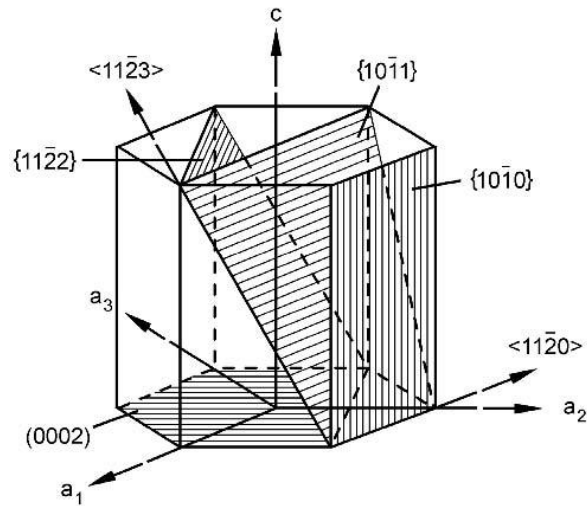


Fig. 2.3 Slip planes and slip directions in hexagonal α phase [Lütjering and Williams 2007].

2.1.1 Classification of Ti Alloys

The alloying additions strongly influence the β – transus temperature as shown in Fig. 2.4 [Lütjering and Williams 2007]. This has laid down the foundation of classification of Ti alloys.

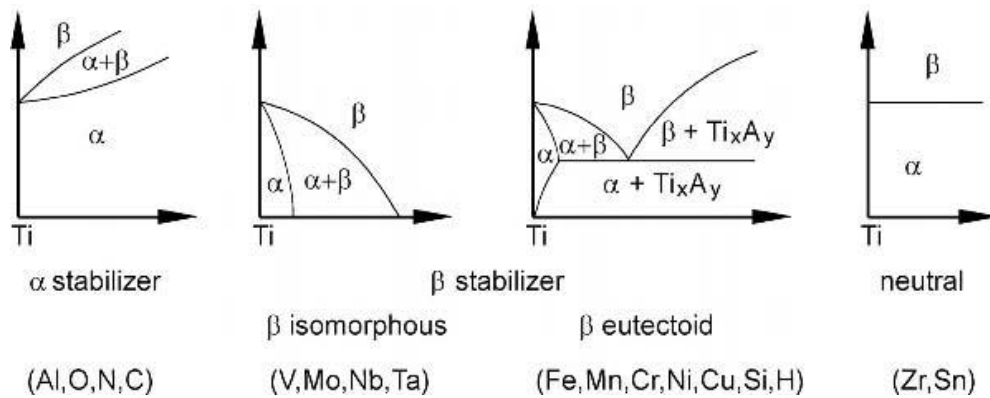


Fig. 2.4 Schematic illustration of influence of alloying elements on phase diagrams of titanium alloys [Lütjering and Williams 2007].

While β – transus temperature is raised by α stabilizers, β stabilizers lowers it (Fig. 2.4, Lütjering and Williams 2007). The various alloying elements which raises or lowers the β – transus temperature is also included in Fig. 2.4 [Lütjering and Williams 2007]. In conventional terms, Ti alloys are classified in three main family of alloys based on microstructural phases which are α , $\alpha + \beta$ and β . While α alloys are non heat treatable alloys, the other two categories respond to heat treatment. As strengthening mechanisms, these alloys are predominantly strengthened by solid solution and precipitation hardening. Near α and metastable β Ti alloys belongs to the families of $\alpha + \beta$ and β Ti alloys, respectively. The classification of these alloys in 3D space is shown in Fig. 2.5 [Peters et al. 2003]. As high temperature Ti alloys, $\alpha + \beta$ and near α Ti alloys are used up to 400°C and 600°C, respectively. In addition to oxidation as a primary damaging mode, ‘creep’

also dominates the maximum usable temperature of these alloys. While the alloy of interest in this thesis is a near α Ti alloy, the various aspects on this alloy are discussed in the next few sections.

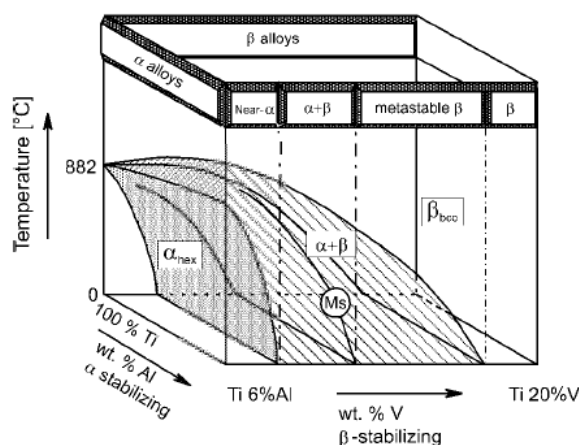


Fig. 2.5 Classification of phase diagram based on 3D phase diagram [Peters et al. 2003].

2.1.2 Microstructural Constituents of Near α Ti Alloys

Continual studies on structure – properties correlations have paved the way for incremental improvements in mechanical properties of near α Ti alloys. The family of near α Ti alloys with respect to progressive stages of development is IMI 679, IMI 685, IMI 829 and IMI 834. While alloys prior to Timetal 834 (originally named as IMI 834) were used in application in fully lamellar microstructure, Timetal 834 is developed with a bimodal microstructure. The bimodal microstructure is also referred as duplex microstructure. It consists of various microstructural parameters which are difficult to identify using a common

characterization tool. In response to external load, the partitioning of strain into α and β phases varies which results in heterogeneous plasticity and it strongly influences the mechanical properties. In conventional terms, these microstructure parameters are sizes of prior β grain, secondary α colony, primary α , α lath in α colony and grain boundary α which forms along prior β grain boundaries. These are shown schematically in Fig. 2.6 [Rugg et al. 2007].

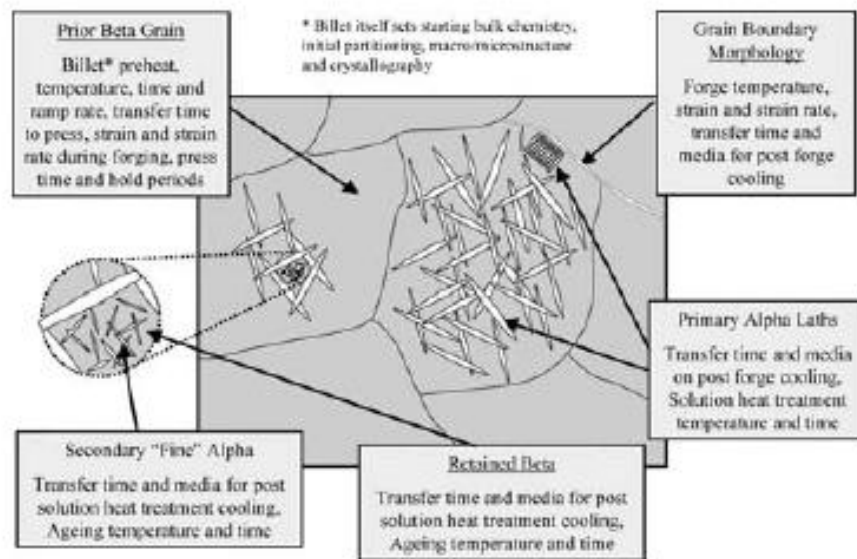


Fig. 2.6 Microstructural constituents in a near α Ti alloy [Rugg et al. 2007]

While sizes of prior β grain, primary α and α laths influence tensile (mainly yield strength and ductility) and fatigue (low cycle fatigue and high cycle fatigue) properties, secondary α colony size strongly influence fracture related mechanical properties [Lütjering and Williams 2007]. Apart from microstructure parameters, one of the factors which also strongly affect the tensile and fatigue properties is the

alloy partitioning effect. During annealing in $\alpha + \beta$ phase region, α stabilizers (Al, O and Sn) preferentially partitions to primary α from secondary α colonies. This promotes the precipitation of very fine and coherent α_2 (Ti_3Al) precipitation in primary α grains thereby increases the strength of primary α grains as compared to secondary α colonies. Therefore, in case of high volume fraction of primary α grains, crack under HCF loading preferentially initiates from weaker secondary α colonies. However, under the same circumstances, crack under LCF loading forms inside primary α grains [Lütjering and Williams 2007]. In LCF loading, repeated shearing of α_2 precipitates by mobile dislocations results in planar slip and strain localization in few of these dense bands promotes crack initiation [Lütjering and Williams 2007]. Finer α laths and coarser prior β grains favours improvement in creep resistance [Lütjering and Williams 2007]. In recent past, the importance of microtexture in influencing mechanical properties has been examined and it transpires that microtexture plays a larger role in governing mechanical properties due to anisotropic nature of α titanium in near α titanium alloys [Banerjee and Williams 2013].

2.1.3 Timetal 834

As discussed in section 2.1.1, creep and oxidation resistance are the life limiting damaging modes which governs the upper service temperature of Ti alloys as an aeroengine component. The family of near α Ti alloys were envisioned and developed in progressive years to meet the required combination of creep and

fatigue properties. However, oxidation resistance is still an issue for most of the advanced near α Ti alloys. In the family of near α Ti alloys, systematic research studies in several stages has resulted in development of Timetal 834 [Neal 1988, Cope and Hill 1988, Neal and Fox 1993]. The improved creep resistance of Timetal 834 as compared to other Ti alloys is shown in Fig. 2.7 [Smallman and Bishop 1999].

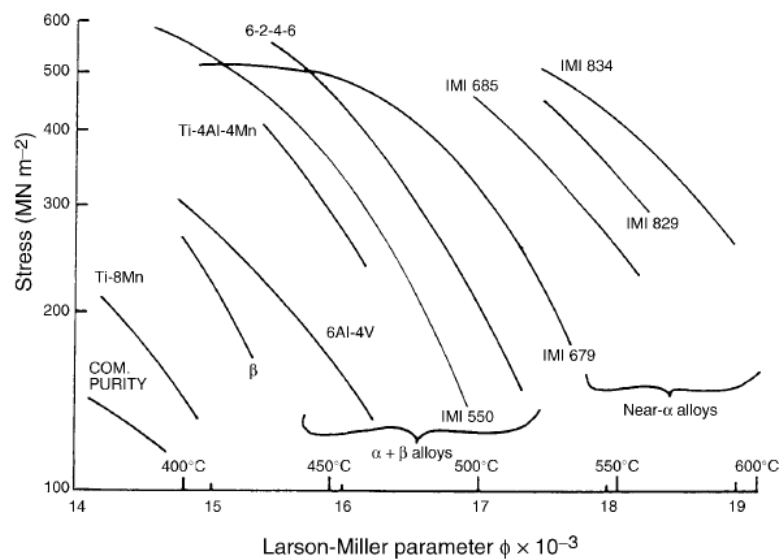


Fig. 2.7 Timetal 834 originally named as IMI 834 showing improved creep resistance as compared to other Ti alloys [Smallman and Bishop 1999].

It is a chemically complex alloy which is not easy to produce in industrial scale. Although it can be produced with ranges of microstructures, a bimodal microstructure with less volume fraction of primary α (around 15% vol%) in transformed β matrix is optimized for balanced creep and fatigue properties as an high temperature aeroengine component [Neal 1988]. It is already in application as

rear stages compressor modules of civil (Trent 700) and Military (EJ 200) gas turbine aero engines [Lütjering and Williams 2007]. Chemistry of Timetal 834 is established over stages of developmental research. Controlling aluminum equivalent $[Al_{eq} = Al + Sn/3 + Zr/6 + (10 \times O_2)]$ below 9 and total content of β stabilizing elements below 2.0 wt.% has resulted in improved mechanical properties [Lütjering and Williams 2007]. The content of β stabilizing elements is low enough to make this alloy amenable for heat treatment. In addition, while the diffusion rates of β phase is two times higher than α phase, the lower content of β stabilizers ensures optimum creep resistance. The combined approach of using (a) slower diffusing β stabilizing elements such as Mo and Nb as compared to relatively fast diffusing elements like V (b) optimum level of Sn and Zr and (c) very low level of Fe (<0.05 wt.%) has resulted in very less volume fraction of β (<5%). Precise control of α stabilizers is a challenging task where slight change in interstitials content (mainly oxygen) can alter the strength of the alloy [Lütjering and Williams 2007]. Timetal 834 contains two types of precipitates viz., very fine and coherent α_2 (Ti_3Al) [Donlon et al. 1993, Cope and Hill 1988, Ghosal et al. 1995, Renner et al. 1996, Lütjering and Williams 2007] and relatively coarser and incoherent silicide particles [Ramchandra et al. 1993, Ghosal et al. 1995]. These precipitates restrict dislocation glide in different phases of Timetal 834 and increases strength as well as creep resistance, however, fatigue properties are compromised as these particles acts as a source of strain localization. While α_2 precipitates acts as obstacles to dislocation glide in primary α grains, silicides of type $(Ti,Zr)_5Si_3$ [Ramchandra et al. 1993] blocks the slip transfer across α/α lath

boundaries in transformed β matrix. In order to take the maximum benefit of precipitation strengthening, the solution treatment temperature and the aging temperature is always maintained above than that of solvus temperature of these precipitates [Neal and Fox 1993]. In addition to contributing strength as silicides, Si also acts as an effective solute solution strengthener. Carbon (C) as an alloying element helps in realizing Timetal 834 as a large scale aeroengine component such as compressor discs in industrial scale. Addition of C leads to the widening of annealing heat treatment window with which these components can be thermomechanically processed in industrial scale [Lütjering and Williams 2007].

2.2 Mechanical Properties of Timetal 834

Timetal 834 originally named as IMI 834 was developed in the early 80's as a British alloy [Neal 1988]. Since then mechanical properties of this alloy is studied by many researchers. Mechanical properties on tensile [Borchert and Daeubler 1988, Singh et al. 1999, Sai Srinadh et al. 2007, Singh and Singh 2008, Prasad and Varma 2008, Prasad and Kamat 2008, Prasad and Kamat 2009, Prasad 2010], hot compression [Bate and Blackwell 1988, Wang et al. 2006], creep [Borchert and Daeubler 1988, Evans and Hull 1995, Andres et al. 1997, Mishra et al. 2005, Mishra et al. 2008, Sounim 2001, Omprakash et al. 2011], creep-fatigue interaction [Kordisch et al. 1995, Prasad and Kumar 2012], low cycle fatigue [Kestler et al. 1995, Torster et al. 1995, Albrecht et al. 1999, Hardt et al. 1999, Baxter et al. 1996, Singh et al. 2002, Kumar et al. 2003, Singh et al. 2007, Biallas

and Maier 2004, Biallas and Maier 2007, Prasad et al. 2008, Prasad et al. 2010, Prasad et al. 2011], thermomechanical fatigue [Pototzky et al. 1999, Pototzky et al. 1998, Christ 2007, Maier and Christ 1997], multiaxial fatigue [Evans and Bache 1995], fracture toughness under mode I [Prasad and Kamat 2009, Chandra Rao et al. 2009, Prasad and Kamat 2010] and mixed mode [Chandra Rao et al. 2008, Chandra Rao et al. 2009], notch fatigue [Evans et al. 2001], creep crack growth [Omprakash et al. 2011, Satyanarayana et al. 2008], fatigue crack growth [Evans 1995, Cope and Hill 1988, Specht 1988, Neal 1988, Lenets and Nicholas 1998, Dowsen et al. 1992, Spence et al. 1997] have been reported in open literature. While influence of range of microstructures on mechanical properties were reported in past, recent studies are focusing on effect of macrostructure and microtexture on mechanical properties [Germain et al. 2003, Uta et al. 2007, Germain et al. 2008]. While the focus of this thesis is on thermomechanical fatigue as an input for safe life and damage tolerant design methodologies, it is complemented by systematic studies on tensile and low cycle fatigue. Therefore, these aspects of mechanical behavior are reviewed in this section.

Studies on tensile behavior of Timetal 834 have been reported by many researchers [Borchert and Daeubler 1988, Singh et al. 1999, Sai Srinadh et al. 2007, Singh and Singh 2008, Prasad and Varma 2008, Prasad and Kamat 2008, Prasad and Kamat 2009, Prasad 2010]. Key papers on tensile behavior, though not detailed in tensile properties and deformation mechanisms, have highlighted the advantages of Timetal 834 over other Ti alloys. The anomalous tensile behavior in

intermediate temperature range (350°C to 550°C) has established the occurrence of dynamic strain aging (DSA) in this alloy [Singh et al. 1999, Singh and Singh 2008, Prasad and Varma 2008, Prasad and Kamat 2008, Prasad 2010]. The phenomenon of DSA is discussed in the next section before presenting its effects on various properties of Timetal 834.

2.2.1 Dynamic Strain Aging

Dynamic Strain Aging (DSA) occurs during straining which involves the interaction of moving dislocation and mobile point defects [Robinson and Shaw 1994, Rodriguez 1984]. This phenomenon is termed as ‘Portevin LeChatelier (PLC) effect. In a crystal lattice containing solute atoms and dislocations both of which are source of misfit strains, interaction of strain fields in response to external force is bound to take place to reduce the overall energy of the lattice [Reed Hill and Abbaschian 2003]. In this process, when solute atoms (s) are sufficiently mobile to diffuse and interact with the mobile dislocations, it results in strengthening. This occurs in a specific combination of temperature and strain rate. Hence, the phenomena of DSA may be considered as a macroscopic manifestation of ease of solute (s) mobility in a crystal lattice which results in inhomogeneous plastic deformation [Cottrell 1953, Mulford and Kocks 1979, Ananthkrishna 2007]. The plastic instability which sets during this process causes plastic oscillations in form of either serrations/load drops (in displacement controlled test) or strain increments (in load controlled tests) [Estrin and Kubin 1991, McCormick

1988]. In dynamic strain aging, material shows anomalous behavior thereby showing manifestations of various types in most of the mechanical properties.

2.2.1.1 Manifestations of Dynamic Strain Aging

A material can exhibit several manifestations during inhomogeneous plastic deformation. The response of material to monotonic tensile or compressive loading is generally studied to understand the various manifestations of DSA. It is important to note that a commonality considering manifestations of DSA in various alloy systems based on fcc, bcc and hcp crystal lattice is difficult to establish. In other words, the manifestation of DSA varies depending on the alloy system investigated. However, the schematic illustration considering most widely reported manifestation of DSA is shown in Fig. 2.8 [Rodriguez 1984, Robinson and Shaw 1994].

These manifestations are as follows:

- A peak or plateau in the variation of flow stress (σ) with test temperature (T).
- Jerky or serrated flow in the plastic region of stress-strain curve
- A peak in the variation of the work hardening rate $\theta = d\sigma/d\varepsilon$ with test temperature (T)
- A peak in the variation of Hall-Petch slope K_ε with test temperature (T)
(while studying the influence of grain size on DSA)

- A minimum in the variation of ductility with test temperature (T)
- A minimum in the strain rate sensitivity $\gamma = \frac{d\sigma}{d \ln \dot{\epsilon}}$ with γ going negative in the temperature region of serrated flow.
- Increase in strain hardening exponent (n) with deformation temperature.
- Fine uniform dispersion of dislocation substructure with very high dislocation density in the dynamic strain aging region.

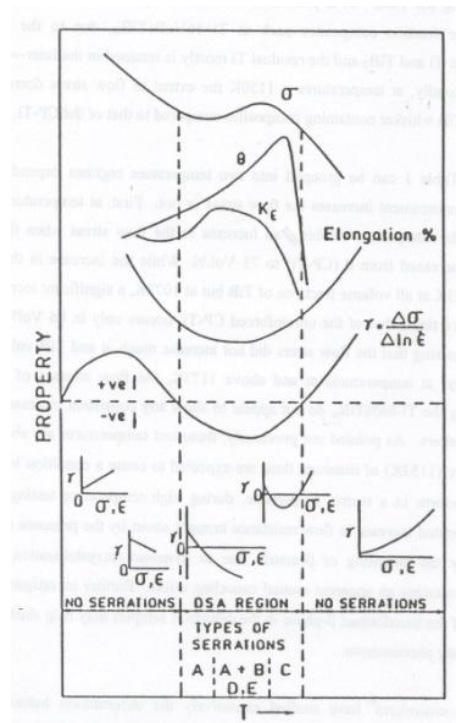


Fig. 2.8 Schematic illustration of the influence of DSA on various mechanical properties [Rodriguez 1984].

2.2.1.2 Principle Involved in Load Drop Phenomenon

The microscopic origin of serrations in stress- strain curve is the load drop due to pinning and unpinning of dislocations by diffusing solute atoms [Cuddy and Leslie 1972]. During uniaxial tensile test, the imposed strain rate $\dot{\epsilon}$ is equal to the sum of plastic strain rate ($\dot{\epsilon}_p$) and the elastic strain (σ/E_s) of the specimen-machine system which can be written as [Rodriguez 1984]:

$$\dot{\epsilon} = \dot{\epsilon}_p + (\sigma/E_s) \quad (2.1)$$

The condition for load drops is when plastic strain rate ($\dot{\epsilon}_p$) exceeds the imposed strain rate $\dot{\epsilon}$ i.e. whenever there is a sudden increase in $\dot{\epsilon}_p$, a load drop occurs [Rodriguez 1984]. Further, a more systematic representation was presented considering the elasticity of the machine (including load cell) and specimen [Hull and Bacon 1984]. These are considered as an imaginary spring as shown in Fig. 2.9. The crosshead moves at a constant speed $S = dl/dt$, so that the crosshead displacement at time t is St . The total elastic displacement of the spring is KF where F is the applied force and K is the spring constant. The plastic elongation of the elongation is $\epsilon_p l_0$ where ϵ_p the plastic strain and l_0 is the original gauge length.

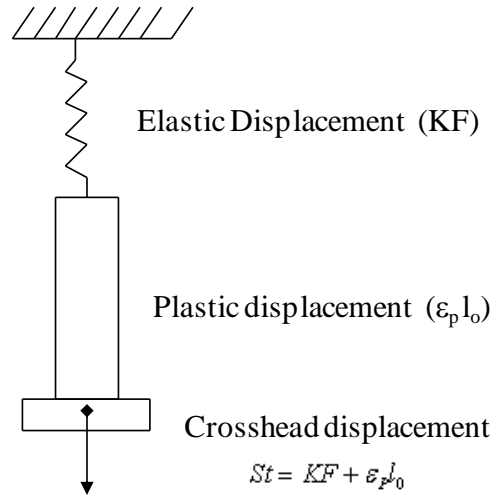


Fig. 2.9 A schematic illustration of load train of a tensile test system. The spring represents the elastic properties of the machine and specimen [Hull and Bacon 1984].

It can be expressed as:

$$St = KF + \varepsilon_p l_0 \quad (2.2)$$

The plastic strain of the specimen is given by:

$$\varepsilon_p = \frac{St - KF}{l_0} \quad (2.3)$$

And the plastic strain rate is given by:

$$\dot{\varepsilon}_p = \frac{S - K \frac{dF}{dt}}{l_0} \quad (2.4)$$

Considering resolved shear stress τ as $F/2A_0$, where A_0 is the original cross sectional area of the specimen and $S = dl/dt$, the measured hardening rate is given by:

$$\frac{d\tau}{dl} = \frac{1}{2A_0 K} \left(1 - \frac{\dot{\epsilon}_p l_0}{S} \right) \quad (2.5)$$

Equation (5) shows that the measured hardening rate depends on the elastic properties of the machine and specimen and the instantaneous plastic strain rate of the specimen. During temporal instability region, mobile dislocation density is large as compared to spatial instability region where forest dislocation density is large. Therefore, the spatial instability region increases the instantaneous plastic strain value as compared to imposed strain rate ($b\rho_m \bar{v} > Sl_0$) which results in load drop.

2.2.1.3 Serrations

As discussed earlier, the inhomogeneous deformation due to plastic strain accumulation in dynamic strain aging leads to the formation of serrations in plastic region of stress- strain curve. Depending upon the interaction between dislocations and interstitial/substitutional solute atoms, nature of serration changes from random (irregular) to well defined serrations. Various types of serrations are

reported in open literature [Pink et al. 1984, Rodriguez 1984]. During 1950's, due to unavailability of rigid machine, tests were carried out in conventional hydraulic machines. These hydraulic machines were not able to register the load drops as shown in Fig. 2.10. Fig 2.10b to f shows plastic region of a stress strain curve obtained from use of a rigid machine.

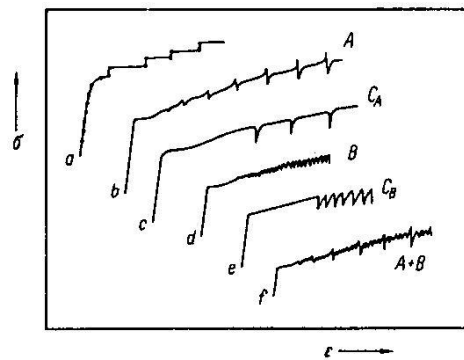


Fig. 2.10 Load drop in conventional hydraulic machine (a) and rigid machine (b to f) [Pink et al. 1984]

However, the characteristics of different types of serrations are listed in Table 2.1 [Rodriguez 1984]. The amplitude of serrations is influenced by magnitude of deformation, temperature and strain rate [Cuddy and Leslie 1972]. However, dynamic strain aging without serrations in Al-Cu eutectic alloy has also been reported [Kale and Kashyap 1992].

Table 2.1: Characteristics of different types of serrations [Rodriguez 1984]

Types of serrations	Characteristics
Type A	Periodic & locking serrations, Low temperature (High $\dot{\epsilon}$)
Type B	Oscillations in σ - ϵ curve, High temperature (Low $\dot{\epsilon}$)
Type C	Dislocations unlocking, High temperature (Low $\dot{\epsilon}$)
Type D	Plateaus in curve σ - ϵ (No work hardening), High temperatures
Type E	At high ϵ , High temperatures

2.2.1.4 Various Models of Dynamic Strain Aging

The very first model [Cottrell 1953] is based on the fact that serrated yielding will start when the velocity of dislocations equals the drift velocity of solute atoms in the stress field of the dislocations. The occurrence of serrated flow in the plastic region of stress-strain curve depends on the attainment of a critical plastic strain (ϵ_c). The critical speed of a dislocation, V_c , is given by [Cottrell 1953]:

$$V_c = \frac{4D}{l} \quad (2.6)$$

where,

D – Diffusion co-efficient of impurity atoms.

l – Effective radius of impurity atmosphere.

Since the dislocation velocity is related to the strain rate through the density of mobile dislocations [Ham and Jaffrey 1967]:

$$\dot{\epsilon}_c = b\rho V_c = \left(\frac{4b\rho}{l} \right) D \quad (2.7)$$

where, ρ is mobile dislocation density and b is the burgers vector.

This relation seems to hold good for interstitial solutes (C and N) in bcc crystal lattice [Keh, Nakada and Leslie 1968]. However, D is too small for this relation to fit the observed temperature – strain rate domain for substitutional solutes. For this reason, it was proposed that deformation induced vacancies may enhance the diffusion sufficiently to satisfy equation (2) [Cottrell 1953]. It was also pointed out that the change in mobile dislocation density during plastic deformation must also be considered in $\dot{\epsilon}_c - D$ relation [Ham and Jaffrey 1967].

In early 1970's, a model is developed to identify the role of interstitial and substitutional solutes causing DSA based on the relationship between critical true plastic strain (ϵ_c) and temperature [McCormick 1972]. This model is widely used by many researchers to identify the role of interstitial and substitutional solutes causing DSA. This model is based on the three assumptions which are (a) increase in mobile dislocation density with increase in strain, (b) enhancement of diffusion coefficient by deformation induced vacancies and (c) aging of mobile dislocations

during the waiting time at the obstacles. This model can be expressed using relation [McCormick 1972]:

$$\dot{\varepsilon} = A.C^n \varepsilon_C^{m+\beta} . \exp(-Q_M/RT) \quad (2.8)$$

where,

$\dot{\varepsilon}$ = Plastic strain rate

C = Solute concentration (Wt%)

Q_M = Effective activation energy for the thermally activated process responsible for serrated flow

ε_C = Critical strain for the onset of serration

$K, n, \text{ and } m$ are empirical constants

Since ε_C is related through the rates of vacancy generation and mobile dislocation segments generation, the exponent m is associated with the vacancy generation and β is associated with the mobile dislocation generation. In this equation, $\dot{\varepsilon}, C, T$ and ε_C are known, and Q_M, n and m must be determined. This can be accomplished by keeping all variables constant except two and plotting one variable against the other. Thus, taking the logarithm of both sides of equation,

$$\log \dot{\varepsilon} = \log A + n \log C - 2.3 \frac{Q_M}{RT} + m \log \varepsilon_c \quad (2.9)$$

By plotting, $\log \dot{\varepsilon}$ versus $\log \varepsilon_c$ and $\log \varepsilon_c$ versus $1/T$ gives m and $2.3 Q_M/m$ respectively. Since Q_M is known now, the exponent m can then be obtained by plotting $\log C$ versus $1/T$ and measuring slope of the resulting curve. Quantitative interpretation of these values can be used to find out the role of interstitial or substitutional solutes in the mechanism of dynamic strain aging. While $m+\beta$ values in the range of 2 – 3 indicates the role of substitutional solute (s), 0.5 to 1 indicates the role of interstitial solute (s) for causing DSA in alloys [Beukel 1980]. While eqn. (2.9) is largely used for determination of activation energy for serrated flow, there are other methods which also attracted attention for determining activation energy for serrated flow. These two methods are (a) stress drop [Pink and Grinberg 1982] and (b) intercept method [Bhanu or Rodriguez]. In stress drop and intercept methods, the amplitude of serrations and intercepts in the variation of critical true plastic strain versus temperature, respectively, are used as an input to the analysis. These methods overcome the limitation associated with McCormick's model in selecting critical true plastic strain which corresponds to the appearance of first load drop/serration in the stress-strain data. The details of these methods are explained in chapter IV. The 'cross-core' mechanism [Curtin et al. 2006] has revealed the physical justification of most of the models where considering the core of dislocations, mechanism of negative SRS is explained based on the single atomic jumps of solutes directly across the slip plane. Further, the mechanism of DSA considering both forest and mobile dislocations was proposed [Soare and Curtin 2008].

2.2.1.5 Plastic Instabilities Associated with Dynamic Strain Aging

The regimes of dynamic strain aging can be studied considering plastic instabilities which induces strain localization in the form of various bands during inhomogeneous deformation. There are mainly two types of plastic instabilities temporal Instability (early stage of deformation of small strain range) and spatial instability (Intermediate stage of plastic deformation of considerable strain range) [Estrin and Kubin 1999]. Two important phenomenological parameters are considered to describe these aspects, work hardening rate, $\theta = d\sigma/d\varepsilon$ and strain rate sensitivity, $\gamma = \partial\sigma/\partial(\ln \dot{\varepsilon})$ which are discussed in detail the following sections:

(A) Work Hardening Rate

In temperature range of occurrence of dynamic strain aging regime, work hardening rate (θ) increases with increase in temperature. It has been explained that increase in density of dislocation leads to increase in work hardening rate [Cheng and Nemat-Nasser 2000]. The flow stress is usually assumed to be proportional to the square root of the total dislocation density:

$$\tau = \tau_0 + \alpha' \mu b \sqrt{\rho_t} \quad (2.10)$$

where, τ is the flow stress, τ_0 and α' are constants and μ and ρ_t are shear modulus and total dislocation density, respectively.

Due to pinning of dislocations by solute atoms, it exerts extra resistance to the motion of dislocation. This leads to increase in applied stress to further plastically deform the material at constant imposed strain rate. Increase of the applied stress results in the activation of the dislocation sources that are inactive at lower stresses. Therefore, an increased multiplication of dislocations causes an increase in work hardening rate in the DSA regime [Cheng and Nemat-Nasser 2000].

(B) Strain Rate Sensitivity (γ)

Strain rate sensitivity is the change in stress required to produce a certain change in strain rate at constant temperature and is a good indicator of changes in deformation behavior [Dieter 1988]. The general relationship between flow stress (σ) and strain rate ($\dot{\epsilon}$), at constant strain (ϵ) and temperature (T) can be written as

$$\sigma = C(\dot{\epsilon})^\gamma \Big|_{\epsilon, T} \quad (2.11)$$

Measurement of γ (strain rate sensitivity) provides a key link between dislocation characteristics of plastic deformation and the macroscopic measurements made in the monotonic tension test. The best way to measure γ is to

carry out a strain rate jump test [Dieter 1988] and to measure the change in flow stress brought about by a change in $\dot{\varepsilon}$ at a constant ε and T , which can be written as,

$$m = \frac{\log\left(\frac{\sigma_2}{\sigma_1}\right)}{\log\left(\frac{\dot{\varepsilon}_2}{\dot{\varepsilon}_1}\right)} \quad (2.12)$$

Strain rate sensitivity of metals is quite low (<0.1) at room temperature and it increases with temperature [Dieter 1988]. However, during aging process, as per the DSI model (Dislocation – Solute interaction) [Beukal et al. 1983], t_w is inversely related to strain rate:

$$t_w \propto 1/\dot{\varepsilon} \quad (2.13)$$

It is the increased waiting time of mobile dislocations at obstacles (solute atoms or forest dislocations) which causes negative strain rate sensitivity in the dynamic strain regime [Korbel and Dybiec 1981]. In an another model [Kubin and Estrin 1990], strain rate sensitivity was assumed as the sum of two additive contributions, γ_o and γ_{aging} . The total SRS can be written as:

$$\gamma(\varepsilon) = \gamma_o + \gamma_{aging}(\varepsilon) \quad (2.14)$$

where, γ_o is the term for the activation of dislocation motion in the absence of DSA and γ_{aging} gives the contribution from DSA.

Contribution of dynamic strain aging to the total SRS is given by

$$\gamma_{aging} = \left(\frac{\partial f}{\partial \ln \dot{\epsilon}} \right)_{\epsilon} = - \frac{df}{d \ln t_w} \quad (2.15)$$

where,

$f(t_w)$ can be expressed as $f(\Omega, \dot{\epsilon})$. Ω is the elementary incremental strain, a strain dependent quantity which corresponds to the deformation obtained when all mobile dislocations accomplish a successful activation event.

Hence, equation (14) becomes:

$$\gamma(\epsilon) = \gamma_o - \frac{df}{d \ln \left[\frac{\Omega(\epsilon)}{\dot{\epsilon}} \right]} \quad (2.16)$$

This shows that mainly it is the waiting time of dislocation which makes strain rate sensitivity negative in the dynamic strain aging region.

At this point, dynamic strain aging can be distinguished from PLC effect by considering above mentioned two parameters. The condition of instability is expressed as:

$$\frac{\theta - \sigma}{\gamma} < 0 \quad (2.17)$$

where, σ is the flow stress. Two types of instability condition can be written as:

1) During temporal instability region:

$$\gamma > 0, \theta \ll \sigma : \theta \text{ type of instability (DSA with No PLC effect)}$$

2) During spatial instability region

$$\gamma < 0, \theta > \sigma : S \text{ type of instability (DSA with PLC Effect)}$$

h-type of instability is associated with positive strain rate sensitivity, which occurs during early phase of deformation (temporal region). One can observe mild jerky flow without negative strain rate sensitivity in this region which could be attributed to anomalous behavior of dynamic strain aging. Negative strain rate sensitivity is the most important criteria for the onset of PLC [Hahner 1996]. *S* type of plastic instability which considers *a) Jerky Flow and b) Negative strain rate sensitivity* is termed as PLC effect [Schlipf 1991, McCormick 1988, Beukel 1982, Penning 1972]. Therefore, PLC effect is a subdomain of dynamic strain aging.

2.2.1.6 Dynamic Strain Aging in Timetal 834

Ample reports exist in open literature which indicates the occurrence of dynamic strain aging Timetal 834 [Singh et al. 1999, Singh and Singh 2008, Prasad et al. 2008, Prasad and Kamat 2008, Prasad et al., 2008, Prasad and Kumar 2010]. The alloy exhibited manifestations of DSA in tensile [Singh et al. 1999,

Singh and Singh 2008, Prasad et al. 2008, Prasad and Kamat 2008,] and low cycle fatigue [Prasad et al. 2008, Prasad and Kumar 2010] deformation. While the temperature range of occurrence of DSA was reported in a wider temperature interval in coarser grain microstructure [Singh et al. 1999, Singh and Singh 2008], a relatively finer microstructure has showed narrower temperature range of occurrence of DSA [Prasad et al. 2008]. It has been confirmed that DSA influences the tensile properties and the ductility drops by nearly 30% in maximum temperature of occurrence of DSA [Prasad et al. 2008]. In LCF studies, the alloy showed reduced fatigue lives in the DSA regime as compared to non-DSA regime [Prasad et al. 2008]. The solute element responsible for causing DSA could not be identified in these studies and based on limited results reported so far, it appeared that Si is playing a dominant role in causing DSA in this alloy [Singh and Singh 2008].

2.2.2 Low Cycle Fatigue

In many published literature, the definition of low cycle fatigue is made based on the number of cycles to failure citing the distinction with high cycle fatigue. In fact, it is tempting to do so due to the term ‘cycle’ in both low cycle and high cycle fatigue. However, it should be defined, explained, and discussed based on the mechanisms involved. Considering the mechanisms of low cycle fatigue reported in open literature [Mughrabi 2009, Mitchell 1979, Suresh 2004], low cycle fatigue can be defined as ‘the accumulation of damage in terms of plastic strain due to externally imposed cyclic plastic flow’. While it is the strain range

which governs the utility of various safe life design methodologies as discussed in detail in next paragraph, high strain range fatigue may be considered as synonymous with low cycle fatigue.

In many applications, engineering components generally undergo some degree of structural constraint and localised plastic flow near stress concentration sites [Bannantine, Comer, Handrock 1998]. In other words, although most engineering components are designed such that the nominal loads remain elastic, stress raisers or concentration sites often causes plastic strains to develop in the vicinity of these sites. This process of development of plastic strains gets aggravated at high temperature. Deformation near the vicinity of these sites is considered strain controlled due to the effect of constraint imposed by the surrounding elastic stressed material. Therefore, strain controlled low cycle fatigue testing carried out on smooth specimens simulates the fatigue damage (accumulation of plastic strain) near the stress concentration sites of a structure [Bannantine, Comer, Handrock 1998]. It is schematically illustrated in Fig. 2.11 [Bannantine, Comer, Handrock 1998] that the laboratory tested smooth specimen simulate an equally stressed volume of a material at the notch root which is also a stress concentration site. It is imperative to note that low cycle fatigue involves the stages of crack initiation as well as crack propagation. However, in practical engineering, it is considered as an estimation of ‘crack initiation life’ under high strain fatigue [Suresh 2004]. The crack propagation life can be estimated by

fracture mechanics methods [Broek 1984] details of which are discussed in section 2.2.3.

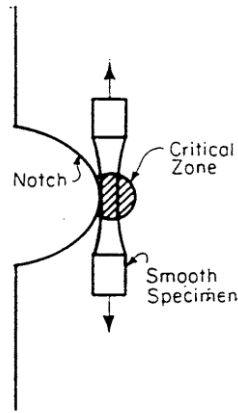


Fig. 2.11 A schematic illustration of equally stressed material replicating constrained deformation near the vicinity of notch [Bannantine, Comer, Handrock 1998]

The strain controlled low cycle fatigue tests are carried out by subjecting a smooth specimen to constant amplitude strain cycling (Fig. 2.12a and b). The variation in stress amplitude ($\Delta\sigma/2$) or maximum stress (σ_{\max}) to maintain the imposed total strain amplitude ($\Delta\epsilon_t/2$) constant and the corresponding number of elapsed cycles, N is recorded. The resulted data is generally presented in a plot of $\Delta\sigma/2$ or $\Delta\sigma$ (stress range) versus N (Fig. 2.12c).

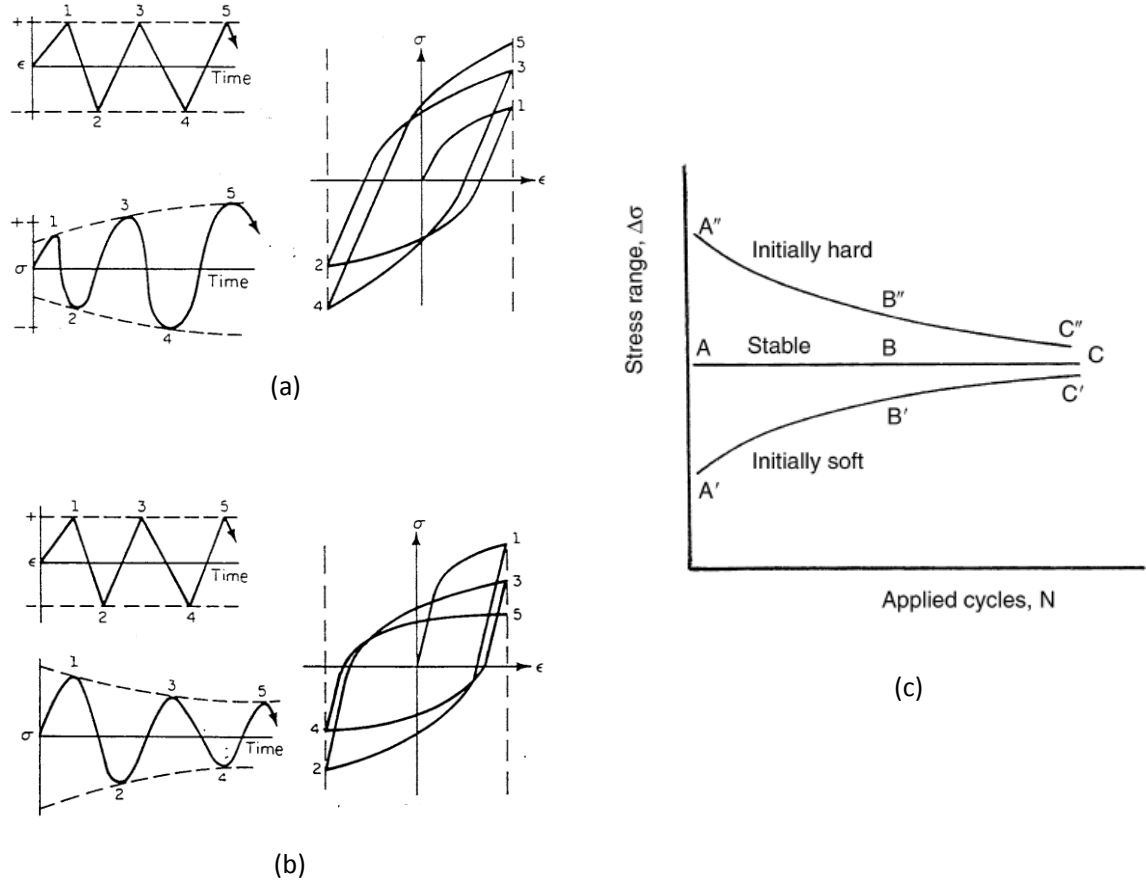


Fig. 2.12 A schematic illustration of strain controlled LCF testing showing (a) cyclic hardening and (b) softening [Bannantine, Comer, Handrock 1998]. The variation of stress range versus cycles to illustrate the cyclic softening, hardening and stable behavior is shown in (c) [Manson and Halford 2006].

This plot reveals the response of the material to external straining in form of (a) cyclic softening, $\Delta\sigma/2$ decreases with each cycle of strain, (b) cyclic hardening, $\Delta\sigma/2$ increases with each cycle of strain, (c) cyclically stable, $\Delta\sigma/2$ remains nearly same with each cycle of strain and (d) mixed behavior comprising of (a), (b) or (c). Studies on the evolution of dislocation substructure on fatigued specimens reveals the micro-mechanisms involved for the transient behavior (cyclic softening,

hardening or stable) of metallic materials. The output of strain controlled LCF testing, cyclic stress strain curves (CSS) are usually established and are compared with the monotonic stress-strain curves for assessing the durability of components subjected to high strain fatigue [Suresh 2004]. Two examples on 304 stainless steel and 4340 high strength steel are shown in Fig. 2.13 [Francois, Pineau and Zaoui 2013].

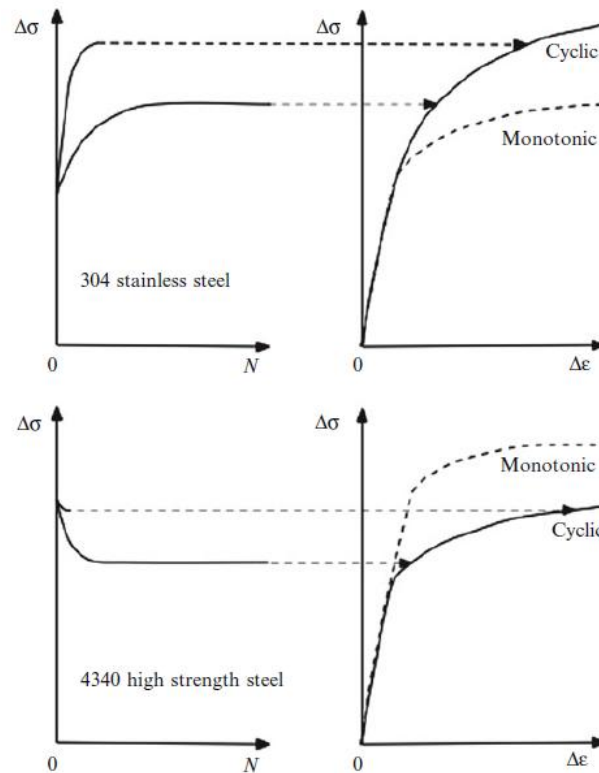


Fig. 2.13 Generation of cyclic stress – strain curves from the transient response of the material under strain controlled LCF loading [Francois, Pineau and Zaoui 2013].

While cyclic softening leads to cyclic yield strength lower than monotonic, cyclic hardening leads to cyclic yield strength higher than monotonic. Hence, for components which undergo cyclic straining, cyclic stress strain curves (CSS) serves as the valuable input for obtaining design parameters.

2.2.2.1 Low Cycle Fatigue Behavior of Timetal 834

Low cycle fatigue behavior of Timetal 834 has been widely studied by many researchers [Kestler et al. 1995, Torster et al. 1995, Albrecht 1999, Hardt et al. 1999, Baxter et al. 1996, Singh et al. 2002, Kumar et al. 2003, Singh et al. 2007, Biallas and Maier 2004, Biallas and Maier 2007, Prasad et al. 2008, Prasad et al. 2010, Prasad et al. 2011]. Most of these studies have revealed that the slip character remains planar in nature up to 600°C and it changes to wavy beyond 600°C. While the alloy exhibited cyclic softening at room temperature and 600°C [Kumar et al. 2003, Singh et al. 2007], initial cyclic softening followed by cyclic hardening was observed at intermediate temperatures [Kestler et al. 1995, Prasad et al. 2008, Prasad et al. 2010]. The micro-mechanism for cyclic softening was attributed to precipitate (Ti_3Al) shearing [Singh et al. 2002, Kumar et al. 2003]. The onset of secondary hardening was attributed to saturation of planar slip bands [Bania and Antolovich 1985] and dynamic strain aging [Prasad et al. 2008, Prasad et al. 2010, Prasad et al. 2011]. In terms of fatigue lives, it has been reported that the alloy exhibits higher fatigue lives at 600°C as compared to room temperature [Singh et al. 2007], reduced fatigue lives were reported in intermediate

temperatures [Prasad et al. 2008]. It has been reported that microstructural changes during cyclic deformation is a function of temperature [Hardt et al. 1999]. Coarsening of silicide particles and disintegration of lamellae boundaries in fatigued specimens were observed with increase in temperature. Comparing the response of lamellar and bimodal microstructure to LCF loading [Albrecht 1999], it was reported that bimodal microstructure with finer prior β grain size exhibits superior LCF resistance as compared to lamellar microstructure. Effect of environment on LCF behavior of Timetal 834 has been reported by few researchers [Biallas and Maier 2004, Biallas and Maier 2007]. By carrying out controlled experiments at different partial pressure of water vapour and different levels of vacuum, it has been shown that the crack initiation mechanism is different at 400°C and at 600°C. While crack preferentially initiated at slip bands at 600°C, crack initiation at slip bands could not be observed at 400°C despite the presence of high density of dislocations in primary α grains. Detailed TEM studies on cyclic deformation mechanism at ambient temperature [Baxter et al. 1996] has shown that fatigue damage accumulation occurs primarily by $\langle a \rangle$ slip on basal planes.

2.2.3 Fatigue Crack Propagation

The life of structural components which contain cracks or that develop in early period of life may be governed from the rate of sub-critical crack propagation by applying the concepts of fracture mechanics [Broek 1984, Suresh 2004, Wei

2010, Schijve 2009]. In these cases, it is very important to establish and validate the initial (minimum) as well as final (critical) crack size that structure can tolerate in service. While non-destructive testing procedures and proof-testing can provide valuable informations regarding relative sizes and distribution of initial crack size, fracture toughness testing yields the information on critical crack size. Most importantly, the rate at which the crack grows from initial to critical size (sub-critical crack growth) decides the useful service life of a structure. By establishing these aspects of fracture mechanics, one can then establish how often should a structure be inspected so that the crack should not reach the critical crack size in service. This is also shown as safety inspection intervals in Fig. 2.14.

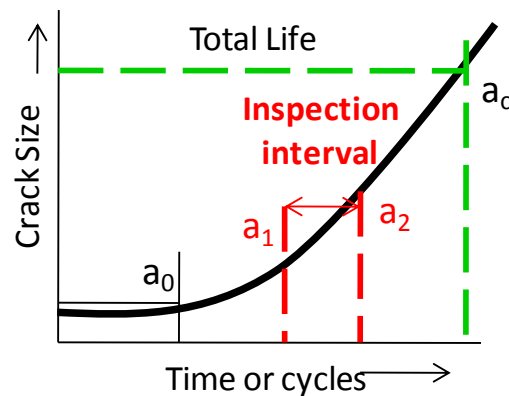


Fig. 2.14 Schematic illustration of inspection interval between crack lengths higher and lower than initial and critical crack sizes, respectively.

The fatigue crack growth tests are carried out by subjecting a fatigue pre-cracked specimen to constant amplitude load cycling. The incremental increase in crack length is measured either by using contact or non-contact based techniques, and the corresponding number of elapsed cycles is recorded. The resulted data is

generally presented in a plot of crack length, a , versus total number of elapsed cycles, N (as shown schematically in Fig. 2.14). Differentiating this curve with respect to N yields crack growth rate per cycle i.e. da/dN and the change in stress intensity factor, ΔK , a single term stress field parameter that incorporates the effects of changing crack length and load results in sigmoidal shaped da/dN versus ΔK curve as shown in Fig. 2.15. This curve is generally plotted in log-log scale and is divided into three regions as per the behavior of the fatigue crack propagation [Viswanathan 1993]. At low ΔK , Region A is associated with threshold effects & hence termed as threshold region. This region is also known as stage I sub-critical crack growth region. In this region, challenge lies in determining the value of threshold stress intensity factor, ΔK_{th} , below which either the crack growth does not occur or occurs at a rate of few atomic spacing which is very difficult to measure. The mid-region, Region B is popularly known as Paris region where the curve can be predicted using Paris-Erdogan equation [Paris and Erdogan 1963]:

$$da/dN = C (\Delta K)^m \quad (2.18)$$

where C and m are the material constants. The constant m which is also termed as Paris exponent varies in the range of 2 – 4 for most of the metallic materials [Dieter 1988]. This region is also known as stage II sub-critical crack growth region. While Region B is associated with stable crack growth, unstable crack growth occurs in Region C where the rate of crack propagation occurs rapidly

leading to catastrophic failure [Viswanathan 1993, Ritchie 1999]. The various factors which influences the crack growth curve is also shown in Fig. 2.15.

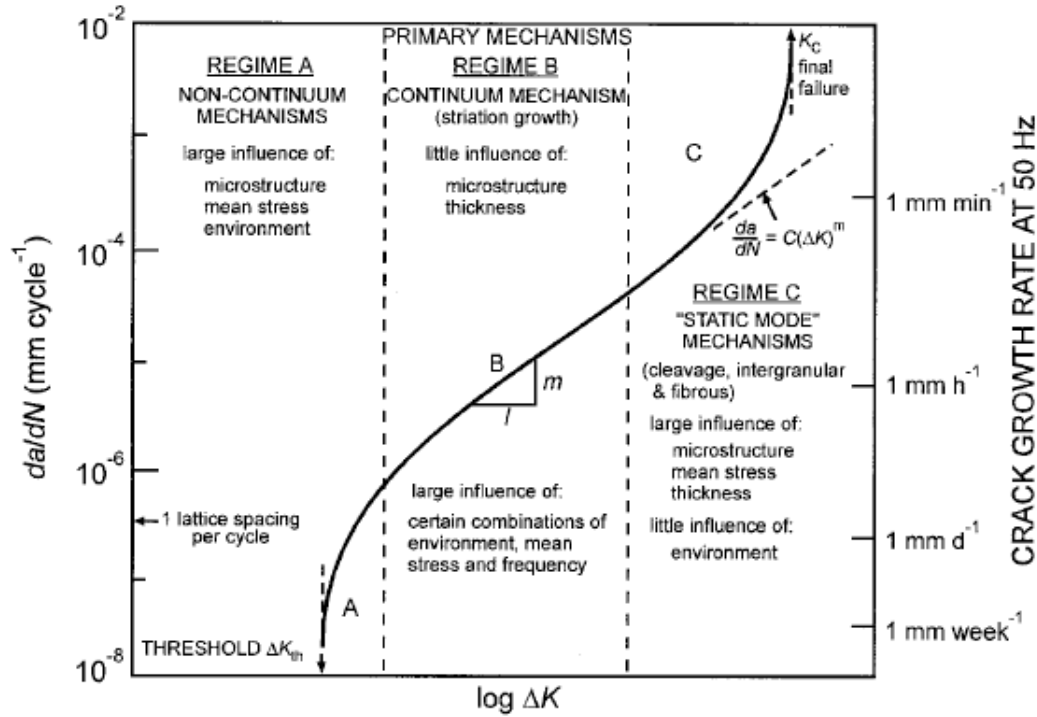


Fig. 2.15 Schematic illustration of fatigue crack growth curve showing various regions and factors influencing crack growth behavior [Ritchie 1999]

The practical interest lies in studying the threshold as well as stable sub-critical fatigue crack growth regions. While most of the thick structures operates in stable crack growth region, characterizing threshold region using proper characterization tools is important as it strongly affect the onset of stable sub-critical crack growth region. In threshold region, while the magnitude of cyclic crack tip opening displacement remains significantly small, several factors

influences the crack growth behavior. One such phenomenon is called as fatigue crack closure and is discussed in detail in section 2.2.3.1.

2.2.3.1 Fatigue Crack Closure

Fatigue crack closure has been recognized as major factor in governing fatigue crack growth rate [Suresh 2004, Suresh and Ritchie 1984, Newman and Piaschik 2004]. In general, the phenomena of pre-mature contact of the crack surfaces while unloading from maximum load level of a applied load cycle even when the far field stresses remains tensile in nature is termed as *crack closure*. It has been reported [Elber 1970] by measuring the crack opening behavior that upon applying tensile load the fatigue crack do no open immediately and it remains closed during some fraction of the loading cycle. In other words, the phenomenon of crack closure occurs when two surfaces of a crack (upper and lower surface) contacts each other at a load level different than the minimum applied load level and load is transmitted through the contact area. However, it is very important to recognize that the role of fatigue crack closure is dominant in threshold region as compared to Paris region in sigmoidal shaped fatigue crack growth curve [Suresh 2004]. While the method of investigating the crack closure phenomena is cumbersome in practice, non-linearity in load – COD plot as shown in Fig. 2.16 indicates the presence of crack closure [Suresh 2004]. In such fatigue crack growth studies, while the opening and closing of crack occurs at a load level different than the minimum load level, it obviates the consideration of minimum load in the

determination of stress intensity factor. Hence, once the existence of crack closure is proven, the next level challenge arises as how to find out the crack driving force as the concept of change in stress intensity factor based on minimum load loses its identity as a crack driving force. The resulting crack driving force lower than the applied stress intensity factor change is popularly known as the “effective stress intensity factor”.

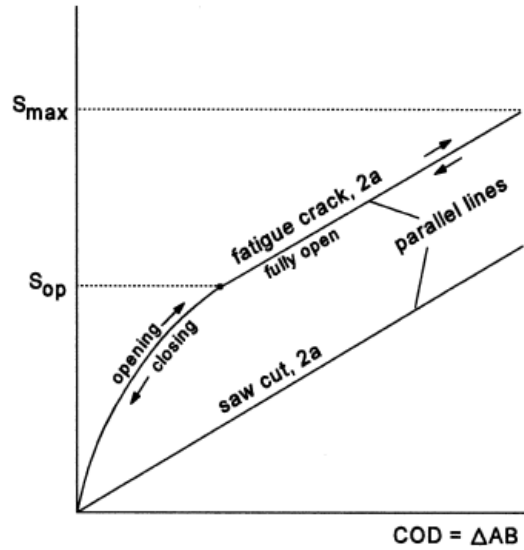


Fig. 2.16 Schematic illustration of crack opening while loading and crack closing while unloading in load (S) versus COD plot [Schijve 2009]

As pointed out earlier, the indication of the stress level at which the crack tip opening or closing occurs is identified for the determination of effective stress intensity factor (ΔK_{eff}) as per the following formulae [Suresh 2004]:

$$\Delta K_{eff} = K_{max} - K_{op} \quad (2.19)$$

However, in spite of dedicated efforts in characterizing crack closure phenomena in last four decades, the identification of ‘load’ value at which the crack remains fully open or fully close remain an ambiguous field of research. Notwithstanding these ambiguities, researchers thrived on to the various experimental techniques [Schijve 1988] for successful interpretation of crack closure phenomenon as well as mechanisms which leads to the earlier mating of crack surfaces. Active research in early 1980’s in the field of crack closure has resulted in identification of several closure mechanisms such as plasticity, oxide debris, fracture surface roughness, fluid, and transformation induced crack closure (Fig. 2.17) [Suresh 2004, Ritchie 1999]. The other mechanisms which also impede crack growth are crack deflection, crack bridging by fibers and crack bridging by particles (Fig. 2.17). However, it is suffice here to mention that three crack closure mechanisms have widely been reported in the open literature viz., plasticity, fracture surface roughness and oxide induced crack closure mechanisms.

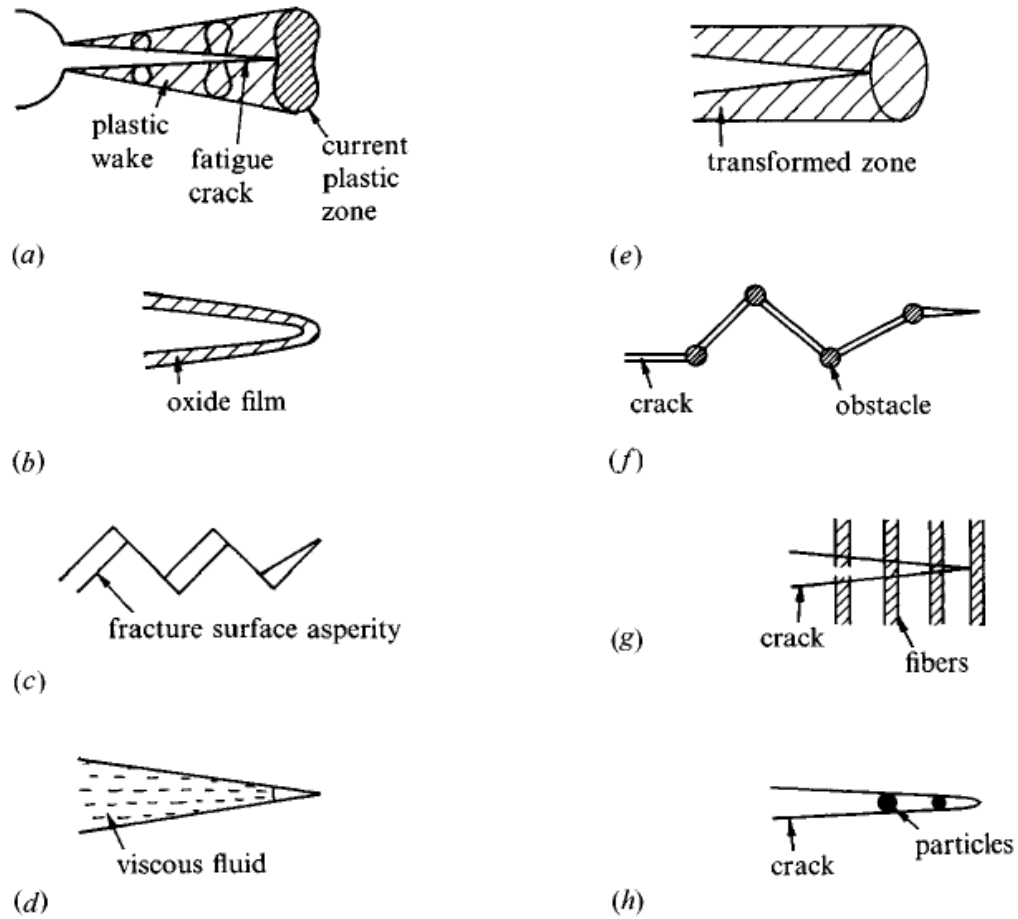


Fig. 2.17 A schematic illustration of the mechanisms which promote retardation of fatigue crack growth. (a) plasticity induced crack closure; (b) oxide induced crack closure; (c) roughness induced crack closure; (d) fluid induced crack closure; (e) transformation induced crack closure; (f) crack deflection; (g) crack bridging by fibers; (h) crack bridging by particles [Suresh 2004].

These mechanisms are briefly introduced and discussed in subsequent sections.

2.2.3.1.1 *Plasticity Induced Crack Closure*

A detailed study on centre cracked aluminum alloy has laid down the concept of plasticity induced crack closure [Elber 1970]. It was reported that a plastic wake which comprises of envelope of prior plastic zones develops around an advancing fatigue crack and when the specimen unloads from the maximum load level, this plastic wake causes the crack surfaces to contact each other before minimum load is reached. In this way, crack tip plasticity promotes plasticity induced crack closure.

2.2.3.1.2 *Oxide Induced Crack Closure*

A fatigue crack has two surfaces which can easily get oxidized when they are exposed to oxidizing (moisture containing) environments while opening in tensile direction. However, the freshly formed oxide film can subsequently rupture during the compressive portion of fatigue cycle. In addition, the mixed mode displacements at the crack tip also promote the local fracturing of the oxide film. Therefore, the continual re-forming and breaking of oxide film can lead to the build-up of oxide layers of some thickness [Suresh et al. 1981]. When the thickness of this oxide layer remains higher or even comparable to the cyclic crack tip opening displacements, the oxide layer can completely wedge the crack tip and eventually leads to retardation of crack growth. This phenomenon is termed as oxide induced crack closure which is promoted by elevated temperature, moisture

containing environments, low load ratios, low ΔK levels, high cyclic frequencies and lower strength materials [Suresh 2004].

2.2.3.1.3 Fracture Surface Roughness Induced Crack Closure

The crack initiation and early stages of crack propagation (micro-crack propagation) is a crystallographic rupture process where the cyclic plastic zone size remains smaller than the characteristic microstructural dimension such as grain size of the material. This causes the faceted or serrated nature of crack surface morphology. Moreover, the associate crack tip plasticity and the strong mode II component at the crack tip cause the mismatch between the fractured surface asperities [Suresh 2004]. This in turn causes the two surfaces of the crack to come in contact to each other prior reaching the point of minimum load of the fatigue cycle. This gives rise to a phenomenon which is termed as fracture surface roughness induced crack closure (RICC). The various factors that promote oxide induced crack closure also promote fracture surface roughness induced crack closure [Suresh 2004].

2.2.3.2 Fatigue Crack Growth Behavior of Timetal 834

Studies on fatigue crack growth behavior in Timetal 834 alloy are limited in literature [Dowsen et al. 1992, Spence et al. 1997, Lenets and Nicholas 1998, Evans 95, Cope and Hill 1988, Specht 1988]. While few reports have emphasized

the importance of crack closure on FCG behavior [Dowsen et al. 1992, Spence et al. 1997, Evans 95], other reports remained either silent or could not bring out the influence of crack closure [Lenets and Nicholas 1998, Cope and Hill 1988, Specht 1988]. Based on the comparison of short and long crack growth behavior at ambient temperature at different R ratio ranging from 0.1 to 0.7 [Dowsen et al. 1992], a high degree of interaction between the growing crack tip and the surrounding microstructure has been revealed. Fatigue crack growth behavior under variable amplitude loading by varying R ratio from 0 to 0.7 at 350°C showed dominant interaction of major and minor fatigue cycles in determining the overall crack growth rate [Spence et al. 1997]. Both these studies emphasized the need for using closure corrected data for empirical design purpose. The importance of crack closure was also emphasized in fatigue crack growth retardation at low ΔK region at three temperature viz., 20°C, 350°C and 630°C. In contrast, retardation of fatigue crack growth at room temperature was attributed to crack blunting or secondary cracking and not to closure effects in determining fatigue crack growth threshold of Timetal 834 [Lenets and Nicholas 1998]. In other high temperature fatigue crack growth experiment, it has been shown that fatigue crack growth resistance is improved at 550°C as compared to room temperature [Specht 1988].

2.2.4 Thermomechanical Fatigue

As discussed in section 2.2.2, in low cycle fatigue (LCF) as a damaging process per se, internal constraint leads to the development of plastic strain near the vicinity of stress concentration sites in engineering components. LCF tests are generally conducted at constant temperature i.e. under isothermal conditions. In thermomechanical fatigue, external constraint under non-isothermal conditions which involves the cycling of temperature in addition to cycling of strain (to be very precise, mechanical strain) causes the development of plastic strain near the vicinity of stress concentration sites in engineering components [Spera 1975, Sehitoglu 1985]. Similar to that of high temperature low cycle fatigue, TMF involves a synergistic interaction of several damaging modes such as creep and oxidation [Neu and Sehitoglu 1989]. When significant temperature gradient develops in a component, the resulting thermal strain gets converted to plastic strain. Let us consider few theoretical cases which highlight the development of temperature gradient. These are; (a) a structure consisting of two materials of different coefficient of thermal expansion bonded with each other and are subjected to a higher temperature (b) a structure consisting of two materials of different coefficient of thermal expansion bonded with each other and both the materials are subjected to different temperature and (c) a structure of a single material which undergo heating from one side and cooling from another side.

While TMF involves simultaneous variation of mechanical strain and temperature, independent control of these parameters is essential in carrying out TMF tests [ASTM Standard E 2368-10]. It is desirable to carry out TMF tests

using random waveforms which simulates the service loading condition of a material, however, two fundamental type of waveforms namely; In-phase (IP), where maximum temperature coincides with maximum value of mechanical strain and out-of-phase (OP) in which maximum temperature and minimum value of mechanical strain occurs at the same time are generally preferred in routine TMF testing. Due to the difference in strength and modulus at maximum and minimum temperature of a temperature interval, the resulting hysteresis loops are unsymmetrical in TMF. The two types of waveforms and the resulted hysteresis loops are shown in Fig. 2.18 [Viswanathan 1993].

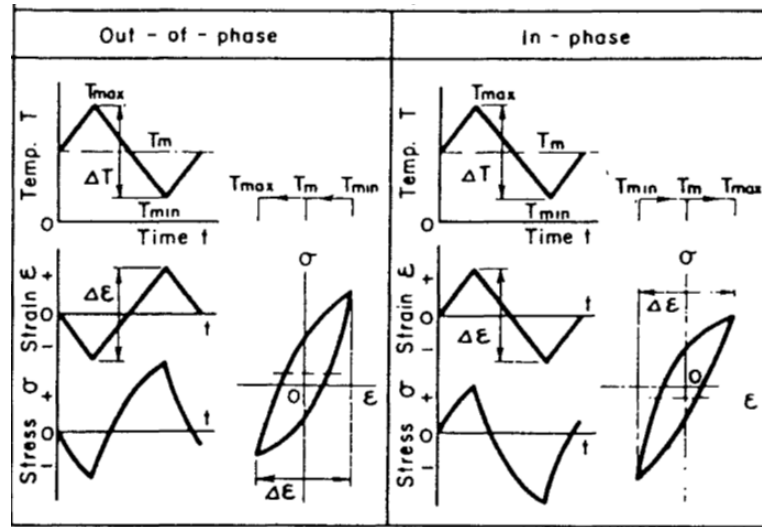


Fig. 2.18 Waveforms and resulting hysteresis loops under Out-of-Phase and In-Phase TMF loading [Viswanathan 1993].

In many ways, laboratory testing practice in TMF loading is different than that of LCF loading. It is the cycling of temperature which brings out the challenges in carrying out TMF testing. Considering two mechanical testing

standards [Hahner et al.2006 and ASTM E- 2368-10], a detailed flow chart is presented in Fig. 2.19 showing the various steps involved TMF testing.

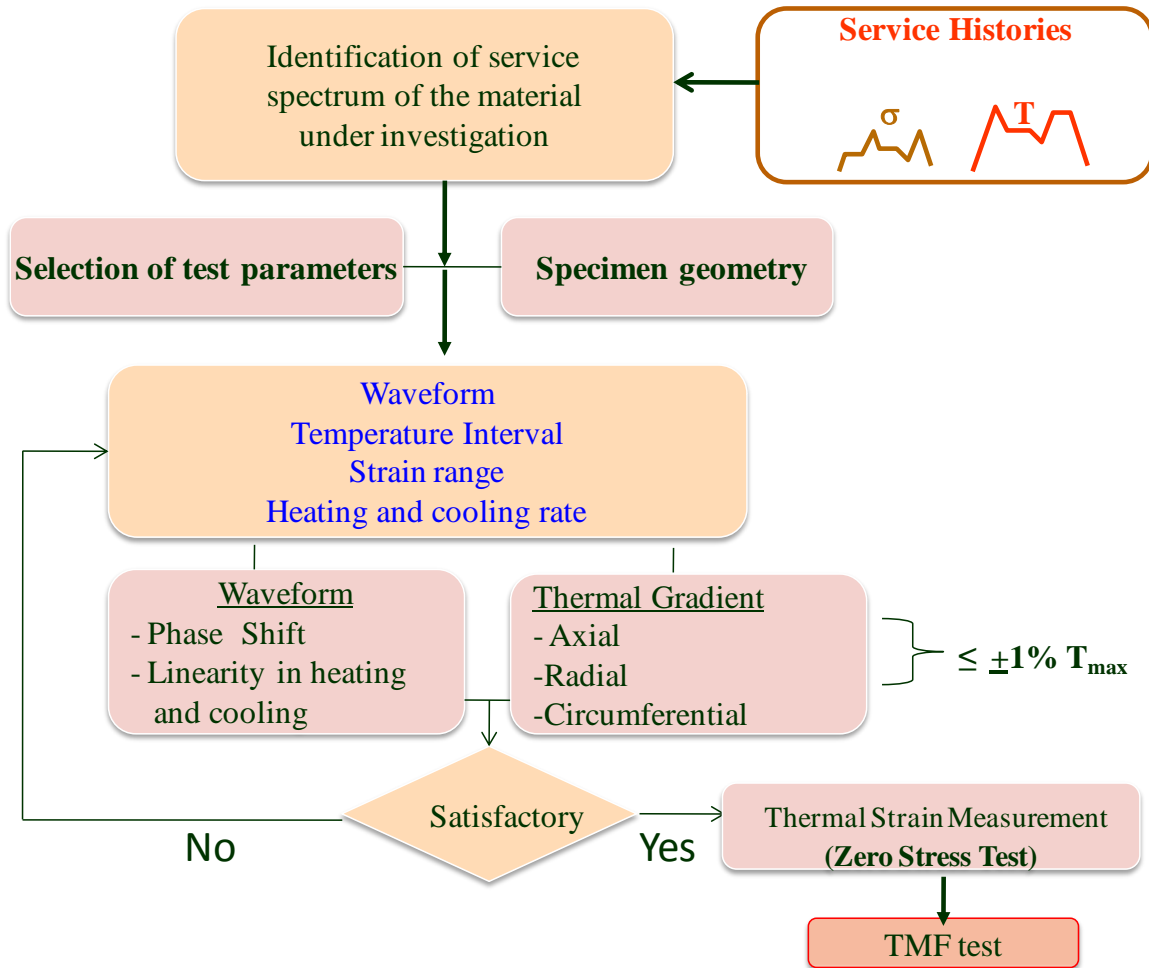


Fig. 2.19 A schematic illustration showing the various steps in carrying out thermomechanical fatigue test.

While the non-uniform temperature field over the gauge section of smooth specimen leads to the development of significant temperature gradient, tubular

(hollow) specimen which reduces the temperature gradient are used for carrying out TMF testing [Hahner et al. 2006]. One has to achieve the desired waveform (IP or OP) by proper positioning of induction heating coils (in case of induction heating based TMF test system) or quartz based halogen bulbs (in case of infrared heating based TMF test system) with respect to the central region of the specimen. A dedicated volume of journal [Int. J. Fatigue, vol. 30, 2008] is published which shows the effects of various testing parameters on TMF results.

2.2.4.1 Thermomechanical Fatigue Behavior of Timetal 834

As discussed in section 2.1.3, near titanium alloys are being used in the rear stages of compressor section. As a disc alloy, studying LCF behavior draws much attention from design perspective; however as a bling alloy, TMF behavior should be studied. TMF behavior using smooth specimens can serve as an input for safe – life design methodology, however, damage tolerant design methodology requires the input from thermomechanical fatigue crack growth studies using fracture mechanics type specimens.

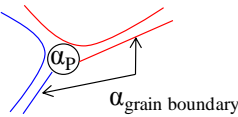
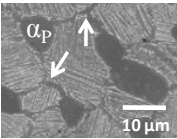

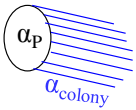
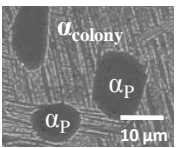
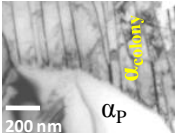
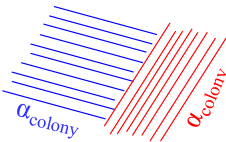
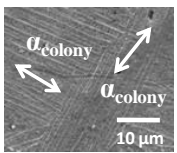
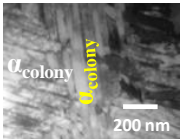
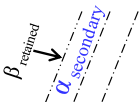
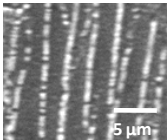
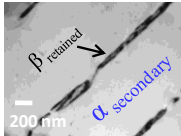
Timetal 834, despite being a high temperature titanium alloy used in gas turbine, literature on TMF behavior is rather scanty [Pototzky et al. 2008, Pototzky et al. 2009, Christ 2007, Maier and Christ 1997]. TMF behavior of Timetal 834 has been reported in two temperature intervals namely $400^{\circ}\text{C} \leftrightarrow 600^{\circ}\text{C}$ and $400^{\circ}\text{C} \leftrightarrow 650^{\circ}\text{C}$ [Pototzky et al. 2008]. The microstructural changes occurring in

these temperature intervals revealed by transmission electron microscopy (TEM) studies have been reported. It has been reported that the maximum temperature (T_{\max}) of a temperature interval ($T_{\max} \leftrightarrow T_{\min}$) governs the establishment of microstructure in fatigued specimens. No significant difference has been observed in stress-strain response between isothermal and $400^{\circ}\text{C} \leftrightarrow 600^{\circ}\text{C}$ TMF tests as deformation characteristics remained same (planar) in both modes of loading. However, marked difference has been observed between isothermal and $400^{\circ}\text{C} \leftrightarrow 650^{\circ}\text{C}$ TMF tests due to slip character changes to wavy beyond 650°C . The fatigue lives of the alloy were observed to be reduced in OP-TMF loading as compared to IP-TMF loading in laboratory air and in vacuum [Pototzky et al. 2008, Pototzky et al. 2009, Maier and Christ 1997]. These studies were conducted using solid specimens and the temperature gradients established in these specimens were not reported. Moreover, the role of dynamic strain aging could not be brought out in these studies.

2.3 Aim of the Thesis

As mentioned in the previous sections, although a significant number of studies have been reported on mechanical properties of Timetal 834, most of them focused either at elevated temperature ($> 550^{\circ}\text{C}$) or at ambient temperature. Few studies reported the structure-property correlations in intermediate temperature ($300\text{--}450^{\circ}\text{C}$). It appears that detailed analysis on the characteristics of DSA in Timetal 834 has not been carried out. It would be of prime importance to reveal

the complete serration map (DSA) comprising the types of serrations in temperature versus strain rate space and to identify the most likely solute which causes DSA in this alloy. Detailed studies on these aspects are reported in chapter IV. Further, its implications on fatigue and fracture behavior under isothermal and non-isothermal conditions is worthwhile to study as it may influence the fatigue and fracture related properties. In spite of the preponderance of literature available in low cycle behavior of Timetal 834, no LCF studies at intermediate and high temperatures with emphasis on establishment of cyclic stress – strain behavior have been reported. Moreover, assessment of deformation characteristics by examining the evolution of dislocation substructures in intermediate temperature range is also rather limited in literature. These aspects are reported in chapter V. Little work was done on thermomechanical fatigue behavior of Timetal 834. Detailed study on thermomechanical fatigue behavior is reported in chapter VI. In all of the studies on fatigue crack growth, no reports on the influence of intrinsic factors (mainly slip character) on fatigue crack growth behavior have been reported. Moreover, although the effects of crack closure on fatigue crack growth have been reported, mechanisms of crack closure as discussed in section 2.2.3.1 were not studied. As an input to damage tolerant design methodology, no report on thermomechanical fatigue crack growth behavior of this alloy seems to have been reported in open literature. The fatigue crack growth behavior under isothermal and non-isothermal loadings is presented in chapters VII and VIII, respectively.

Types of grain boundaries	Schematic layout of grain boundaries	Microstructure	
		Secondary electron SEM images	Bright field TEM images
Prior β grain boundary ($\alpha_{\text{grain boundary}}/\alpha_{\text{colonies}}$)			
$\alpha_{\text{Primary}}/T_{\beta}$			
$\alpha_{\text{colony}}/\alpha_{\text{colony}}$			
$\beta_{\text{retained}}/\alpha_{\text{secondary}}$			

Chapter III

Material Processing and Microstructural Characterization

3.1 Introduction

In the family of near α titanium alloy, Timetal 834 is a chemically complex alloy which is difficult to process in an industrial scale and hence poses a great challenge for the titanium alloy developers [Neal 1988]. As brought out in section 2.1 of chapter II (literature survey) that like steels, the allotropic phase transformation at $\sim 1045^{\circ}\text{C}$ in this alloy facilitates to achieve a range of microstructures by tailoring the various parameters of heat treatment cycle [Lütjering and Williams 2007]. A variety of microstructures can be produced by altering the solution treatment temperature and the subsequent cooling rate. In addition, the aging treatment is generally being carried out after cooling cycle to equilibrate (stabilize) the microstructure and to impart strength to the alloy [Neal and Fox 1992]. As an engine material, the alloy developers tailor the microstructure of Timetal 834 as per the service loading and prevailing conditions of the engine. For example, as a compressor disc material, a fully transformed β microstructure with enhanced creep resistance is desirable for the rim section which encounters maximum temperature during operation [Cope and Hill 1988]. In contrast, the bore section of the disc which experiences high stresses demands a bimodal microstructure for an optimized creep-fatigue type of loading. In the present thesis work, the microstructure chosen consist of primary alpha (α_p) with

~15% volume fraction distributed in lamellar matrix produced from transformed β matrix (β_T) with less than 5% retained β and it is an optimized microstructure for both fatigue and creep dominated applications [Neal 1988].

The influence of various parameters in a heat treatment cycle of near α titanium alloys have been reported [Cope and Hill 1988, Daeubler et al. 1995, Madsen and Ghonem 1995, Sounim 2001, Neal and Fox 1993]. Based on these reports, it can be summarized that as the cooling rate decreases the size of the secondary α laths increases and the morphology changes from basket weave to an aligned colony microstructure. Hence, cooling rate plays a crucial role in altering the thickness/average size of α laths as well as morphology of secondary α colonies. However, one should be very careful in heat treating Silicon containing near α titanium alloys as these should be heat treated above the silicide solvus temperature to derive the full potential of solute drag effect for improving creep resistance. The silicide solvus temperature of Timetal 834 is $\sim 990^\circ\text{C}$ [Neal and Fox 1992].

In one of the objective of the thesis, in order to understand the effect of Silicon on dynamic strain aging, one ingot of composition similar to Timetal 834 but without Silicon is processed and heat treated to achieve a microstructure similar to that obtained in Timetal 834. The alloy 834 without Si is studied only under monotonic loading and the results of this investigation are discussed in detail in section 4.4 of chapter IV (tensile behaviour).

This chapter describes the processing and standard heat treatment given to the Timetal 834 alloy and the alloy 834 without Si. The resulted microstructural features are examined and analyzed using scanning and transmission electron microscopy.

3.2 Materials and Experimental Procedures

3.2.1 Materials and their processing

The nominal chemical composition of near α Timetal 834 titanium alloy is shown in Table 3.1. Timetal 834 was received as 172 mm diameter billets from Imperial Metal Industries, UK. These as-cast ingots were forged at 1100°C to 32 mm thick billets in β region to break the cast structure because of lower forging loads [Lütjering and Williams 2007]. Since the β transus temperature of Timetal 834 is 1045°C [Brandes and Brook 1998], these ingots were subsequently rolled in the α - β region at a temperature of ($\beta_T - 25^\circ\text{C}$) to 18 mm thick plates. 18 mm thick plates of Timetal 834 were solutionized and aged. Solutionizing was carried out at $1025 \pm 2^\circ\text{C}$ for 2 hrs followed by oil quenching. Aging was carried out at 700°C for 2 hrs followed by air cooling. Small size rectangular cross section samples of the heated treated alloy were machined, hot mounted and mechanically polished using emery papers with grit sizes ranging from 220, 600, 800 and 1200, respectively. The samples were subsequently polished on velvet cloth using

diamond paste with particle size of 9 μm down to less than 1 μm . The polished surface was then etched by using Kroll's reagent (15% HF: 15% HNO_3 :70% water) for microstructural observations.

Table 3.1: Nominal chemical composition of Timetal 834

Elements	Al	Sn	Zr	Mo	Nb	Si	O	N	C	Ti
Wt.%	5.75	4.02	3.54	0.71	0.50	0.30	<0.09	0.007	<0.06	Bal.

The nominal chemical composition of the melted alloy 834 without Silicon is shown in Table 3.2. This alloy was prepared by consumable vacuum arc melting. While Ti, Al, Zr, and Sn were added in elemental form, Mo and Nb were added as Mo/Al and Nb/Al master alloys. The raw materials were blended and compacted to 50 x 50 x 500 mm³ rectangular compacts (each weighing 5 kg) using a 1000 ton hydraulic press. Two such compacts welded together inside the furnace, formed the electrode for primary melting, which was carried out in a water cooled copper crucible under a dynamic vacuum of 10^{-3} mbar to obtain an ingot of 110 mm diameter weighing about 10 kg. In order to remove the contaminated layer, the ingots were machined. In addition, the top and bottom portions of the ingot which were usually defective were also cut. Two primary ingots were welded for secondary melting, which yielded a 140 mm diameter ingot weighing about 20 kg.

The ingot was skin machined and radiographed to locate and discard the defective portions. Beta transus temperature (β_T) of the alloy were determined by solution treating specimens in a range of temperature from (975°C to 1105°C) followed by oil quenching and examination of the microstructure.

Table 3.2: Nominal chemical composition of alloy 834 without Si.

Elements	Al	Sn	Zr	Mo	Nb	Si	O	N	C	Ti
Wt. %	5.82	3.97	3.61	0.68	0.55	-	<0.08	<0.008	<0.06	Bal.

As discussed above, these as-cast ingots were subsequently forged at 1100°C to 32 mm thick billets. Small specimens were solution heat treated for 2 hrs at temperatures ranging from 950°C to 1100°C, water quenched and examined metallographically to observe the microstructure. Beta transus (β_T) temperature of the alloy was determined to be ~ 1015°C. This temperature is 30°C less than the β_T temperature of Timetal 834 Ti-alloy with Si which is 1045°C. This is in line with the earlier study on Ti-6Al-4V [Flower et al. 1982] that Si increases the β_T temperature. The ingots were subsequently rolled in $\alpha - \beta$ region at a temperature of $\beta_T - 25^\circ\text{C}$ to 18 mm thick plates. A series of heat treatments, involving solution treatment and aging, were employed to optimize the microstructure as that of Timetal 834.

The microstructures after heat treatment of both the alloys were examined using a FEI quanta 400 scanning electron microscope (SEM). In addition, in order to examine the fine transformed β microstructure and the dislocation sub-structure in as-heat treated condition, if any, the heat treated specimens was studied using a FEI Tecnai G² transmission electron microscopy (TEM). Sample preparation for TEM studied involved sectioning of thin discs from the small sized heat treated samples. The thin discs thus obtained were mechanically polished to 100 μm thickness using a SiC paper and electropolished in twin jet electropolisher (Fischione Instruments). Electropolishing was done using 5% H_2SO_4 and methanol as electrolyte at -50°C and the voltage was maintained at 20V.

3.3 Results

3.3.1 Microstructural Constituents of Timetal 834 and alloy 834 without Si

The heat treated SEM microstructure of Timetal 834 alloy is shown in Fig. 3.1. Fig. 3.1 shows various microstructural constituents which are akin to near α titanium alloys.

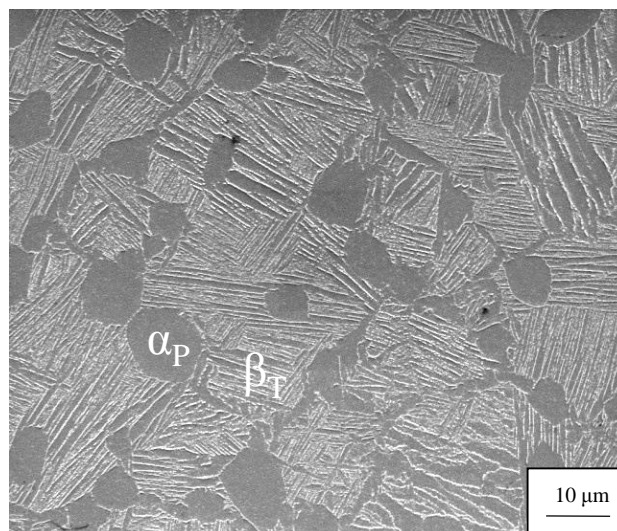


Fig. 3.1 SEM microstructure of Timetal 834 showing volume fraction of primary alpha (α_P) ~15% in transformed β matrix (β_T).

Fig. 3.1 reveals globular & equiaxed morphology of primary alpha (α_P) which are mainly decorated along prior β grain (β_T) boundaries. Grain boundary alpha (α_{GB}) which delineates one transformed β to the other can be seen in Fig. 3.1. Lamellar morphology of transformed β consisting of many secondary alpha (α_S) colonies is also revealed in Fig. 3.1. However, secondary alpha laths (α_{laths}) within secondary alpha (α_S) colonies could not be examined legibly in SEM microstructures. TEM microstructures of the alloy as shown in Fig. 3.2 clearly shows (a) interface of α_P and β_T grains (Fig. 3.2a) (b) secondary alpha (α_S) colonies which are aligned differently to each other (Fig. 3.2b) (c) α_{laths} within a α_S colony and (d) superlattice diffraction spots which corresponds to α_2 (Ti_3Al) type of precipitates inside α_P grains.

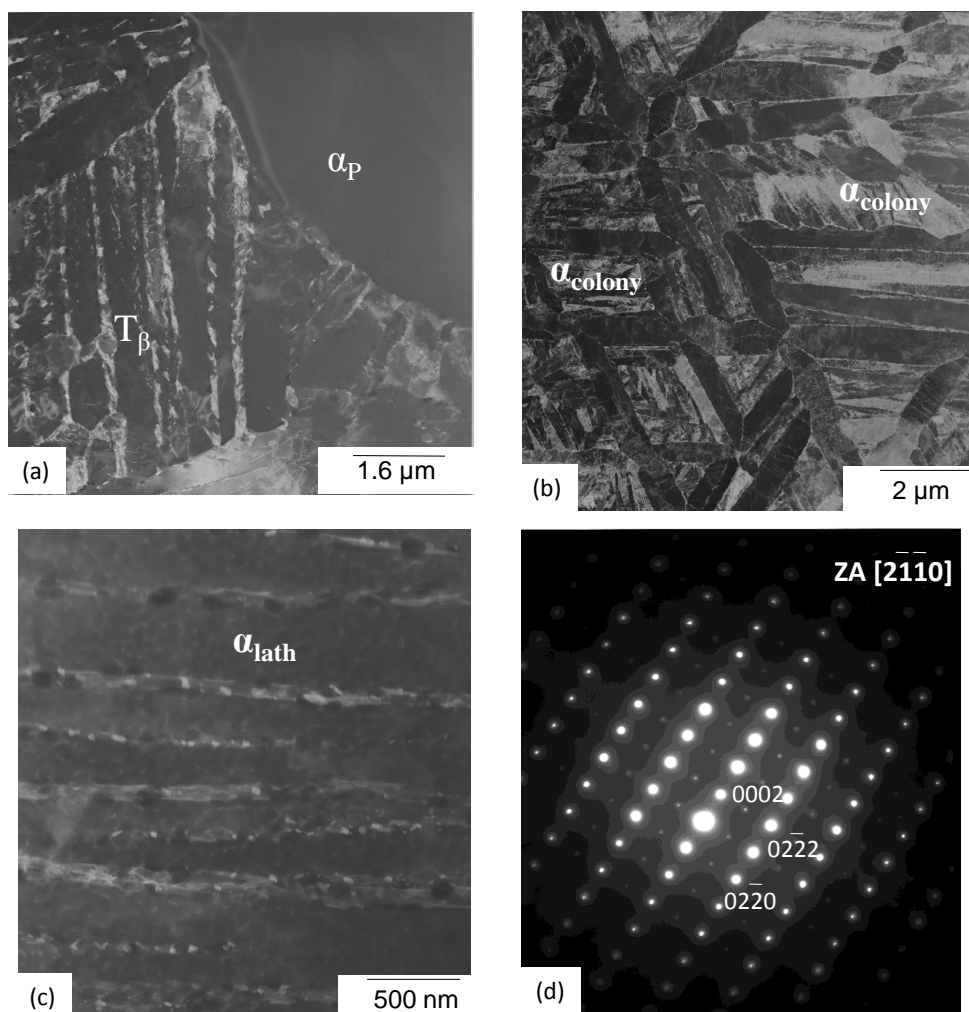


Fig. 3.2 TEM microstructure of Timetal 834 showing (a) α_P and transformed β matrix (b) several secondary α colonies in transformed β matrix (c) secondary α laths within α colonies and (d) extra superlattice diffraction spots revealing the presence of α_2 (Ti_3Al) inside α_P grains.

It can also be seen that the transformed β matrix consisting of α laths are separated by thin β films. TEM studies have also revealed the presence of spherical particles decorated along α_{lath} boundaries (Fig. 3.3).

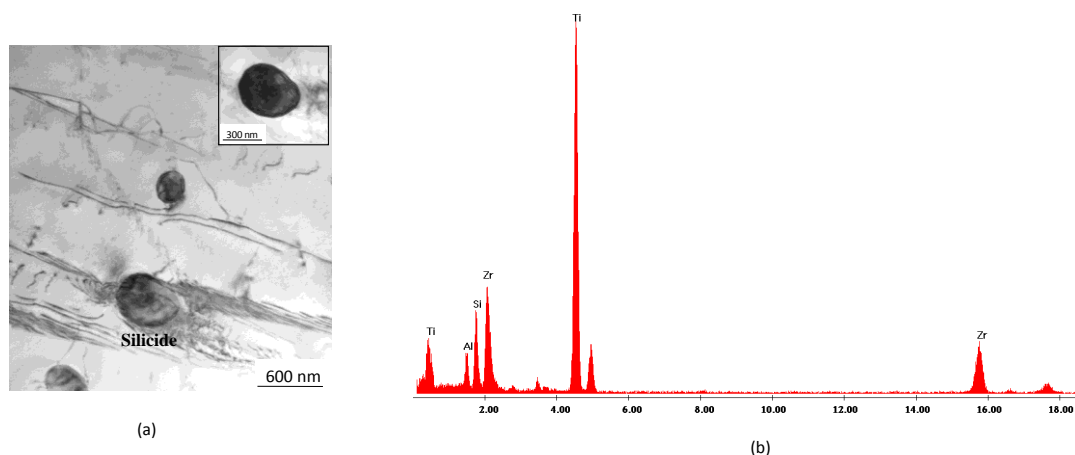


Fig. 3.3 Bright field TEM micrograph of Timetal 834 showing (a) spherical particles in transformed β matrix and (b) EDS spectrum taken from the spherical particle showing preferential enrichment of Zr, Si and Al into them.

EDS analysis has confirmed that these particles contain Zr, Si and Al. As per the reports available in open literature [Ramchandra et al. 1993, Ghosal et al. 1995], these particles are considered as $(\text{Ti,Zr})_5\text{Si}_5$ type of silicide particles. Considering all the microstructural constituents of Timetal 834, a schematic diagram including the SEM and TEM microstructures is illustrated in Fig. 3.4. Various types of grain boundaries/interfaces can be seen in Fig. 3.4.

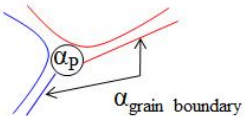
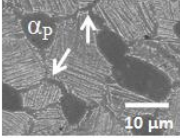

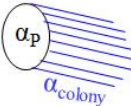
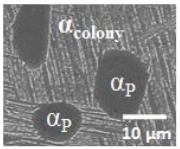
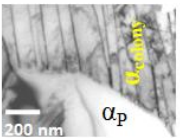
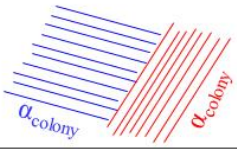
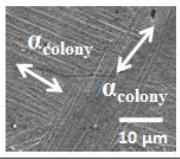
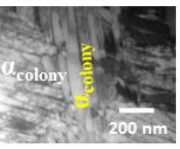

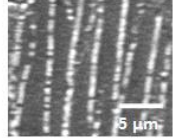
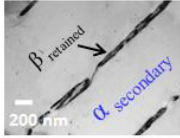
Types of grain boundaries	Schematic layout of grain boundaries	Microstructure	
		Secondary electron SEM images	Bright field TEM images
Prior β grain boundary ($\alpha_{\text{grain boundary}}/\alpha_{\text{colonies}}$)			
$\alpha_{\text{Primary}}/T_{\beta}$			
$\alpha_{\text{colony}}/\alpha_{\text{colony}}$			
$\beta_{\text{retained}}/\alpha_{\text{secondary}}$			

Fig. 3.4 Various types of microstructural constituents in near α Timetal 834 Ti-alloy

Quantitative assessment of microstructural constituents in terms of volume fraction of α_p and average size of α_p grains, β_T grains and α_s laths has been carried out in the present investigation. Volume fraction of primary α was measured using quantitative image analysis using 15 micrographs. The average size of α_p grains was measured using linear intercept method. The average size of β_T grains was measured by tracking the grain boundary α_{GB} using 15 micrographs. The microstructural parameters thus measured including average size of α_p , β_T grains and α laths and volume fraction of α_p are listed in Table 3.3. It is thus clear from Table 3.3 that the Timetal 834 alloy has finer microstructure and less volume fraction of α_p as required for desired application as a disc material.

Table 3.3: Microstructural parameters of Timetal 834

α_p grain size (μm)	Prior β grain size (μm)	Volume fraction of α_p (%)	α_{lath} thickness (μm)
10 ± 1.3	40 ± 2.4	~ 15	1.7 ± 0.4

As mentioned in section 3.2, the microstructure of alloy 834 without Si was optimized to achieve a similar microstructure as that of Timetal 834. Microstructures of alloy 834 without Si under different heat treatment conditions are shown in Fig. 3.5. Similar procedure was adopted to reveal the microstructure of this alloy as that of Timetal 834. It can be observed from Fig. 3.5 that the morphology of microstructural constituents is observed to be similar as that of Timetal 834 for comparable heat treatments. While the alloy exhibits equiaxed α_p grains in a transformed β matrix in $\alpha - \beta$ heat treated condition (Figs. 3.5a-d), a fully transformed β structure is seen in β heat treated condition (Fig. 3.5d).

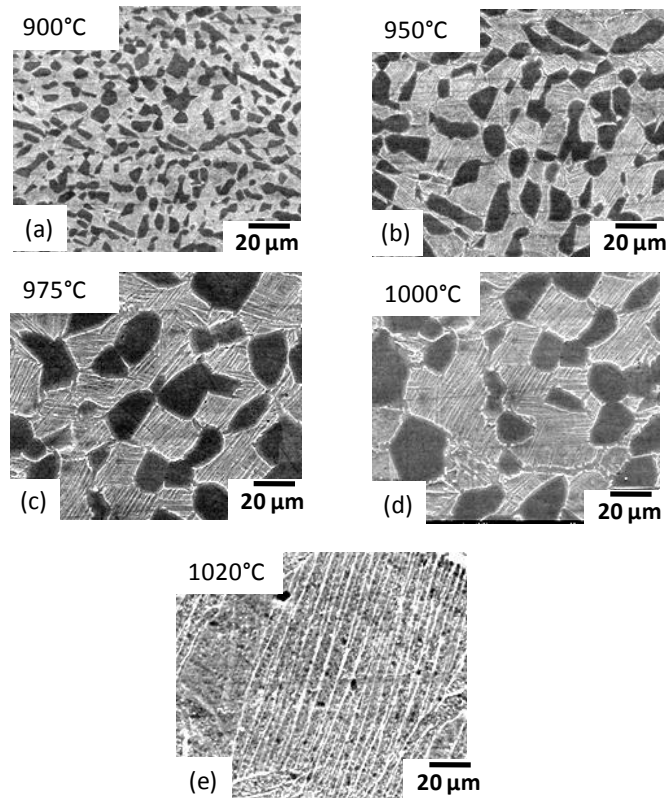


Fig. 3.5 SEM microstructures of alloy 834 without Si showing bimodal microstructure up to 1000°C and fully transformed β at 1020°C.

The microstructural parameters including α lath thickness, volume fraction of α_p , grains sizes of α_p and prior β are measured and are listed in Table 3.4. It can be observed that increase in the solution treatment temperature leads to decrease in the volume fraction of α_p . Also, the prior β grain size increases with increase in solution treatment temperature whereas α lath spacing remains more or less unchanged.

Table 3.4: Microstructural parameters of alloy 834 without Si.

Solution Heat Treatment Temperature (°C)	Volume fraction of α_p (%)	α_p grain size (μm)	Prior β grain size, μm	α lath thickness, μm
900	70 ± 7.8	-	-	-
950	32 ± 5.3	08 ± 1.2	-	-
975	23 ± 4.2	10 ± 1.1	40 ± 3.2	2.1 ± 0.7
1000	17 ± 4.8	11 ± 1.5	55 ± 3.2	2.4 ± 0.7
1020	0	0	324	2.7 ± 0.7

Comparing the microstructural parameters of Timetal 834 (Table 3.3) and alloy 834 without Si (Table 3.4), it has been confirmed that the heat treatment cycle which consists of solution treatment at $\beta_T - 15^\circ\text{C}$ (1000°C) for 2 hrs, oil quenching and subsequent aging at 700°C for 2 hours and air cooled resulted in comparable

microstructural parameters as that of Timetal 834 and the same is displayed in Table 3.4. Hence, alloy 834 without Si with the comparable microstructural constituents is selected for studying tensile properties along with Timetal 834.

Bright field TEM micrographs taken from secondary α colonies as well as α laths of alloy 834 without Si are shown in Fig. 3.7. Colonies oriented differently with respect to each other and fine β film (also termed as retained β layer) separating α laths can be seen legibly in these micrographs.

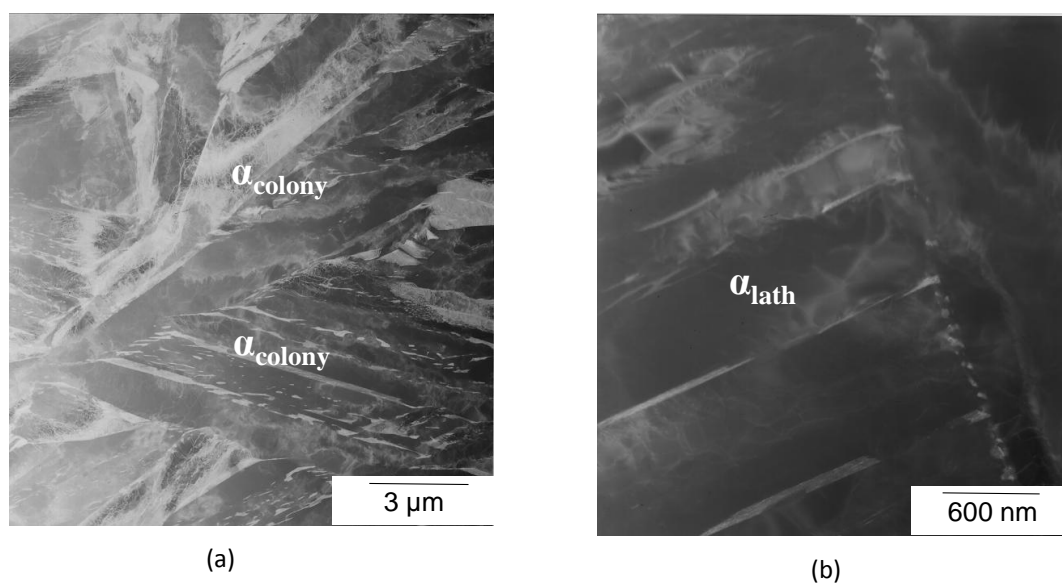


Fig. 3.6 Bright field TEM micrographs of alloy 834 without Si showing (a) secondary α colonies of transformed β matrix and (b) secondary α laths inside α colonies.

3.3.2 Dislocation Substructure of Timetal 834 and alloy 834 without Si

In order to examine the presence of dislocations as a result of heat treatment, few heat treated samples were examined under TEM. The bright field TEM micrographs of α_P grains and α laths of β_T grains of Timetal 834 are shown in Fig. 3.7. TEM micrographs revealed that the microstructure consists of limited dislocation activity inside both the grains. While relatively straight dislocation segments were observed inside α_P grains (Fig. 3.7a), few dislocations along the α lath boundaries can be seen in Fig. 3.7b.

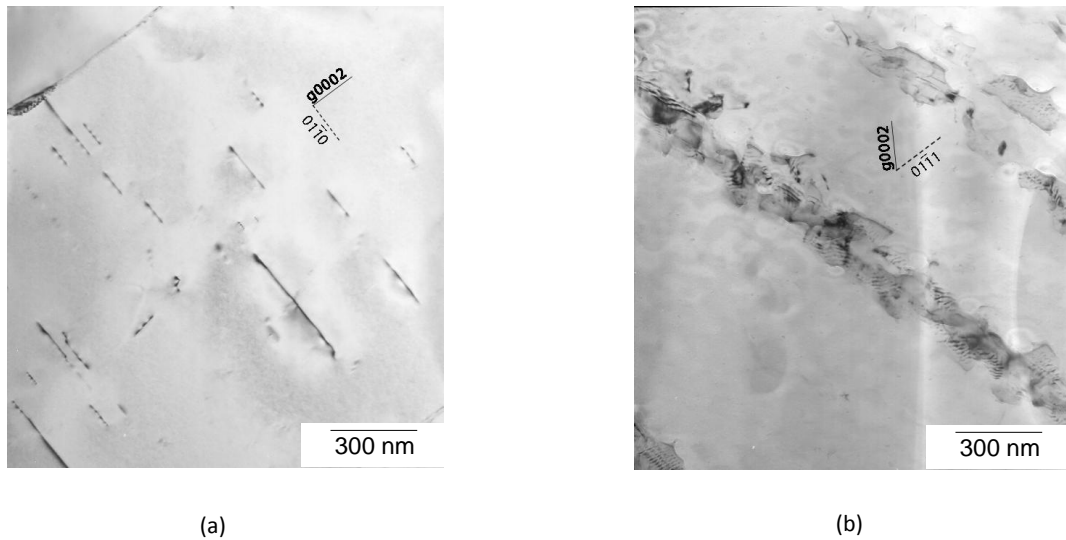


Fig. 3.7 Bright field TEM micrographs of Timetal 834 showing (a) straight dislocation segments inside primary α grain in $g=0002$ reflection and (b) limited dislocation activity in $g=0002$ reflection in secondary α laths.

High magnification TEM micrographs are captured in different regions of the microstructure of alloy 843 without Si to reveal the presence of dislocations, if any. Few isolated dislocations can be seen in α_p grains (Fig. 3.8a) and dislocations of shorter segments but very limited in activity can be seen near α_{lath} boundaries (Fig. 3.8b).

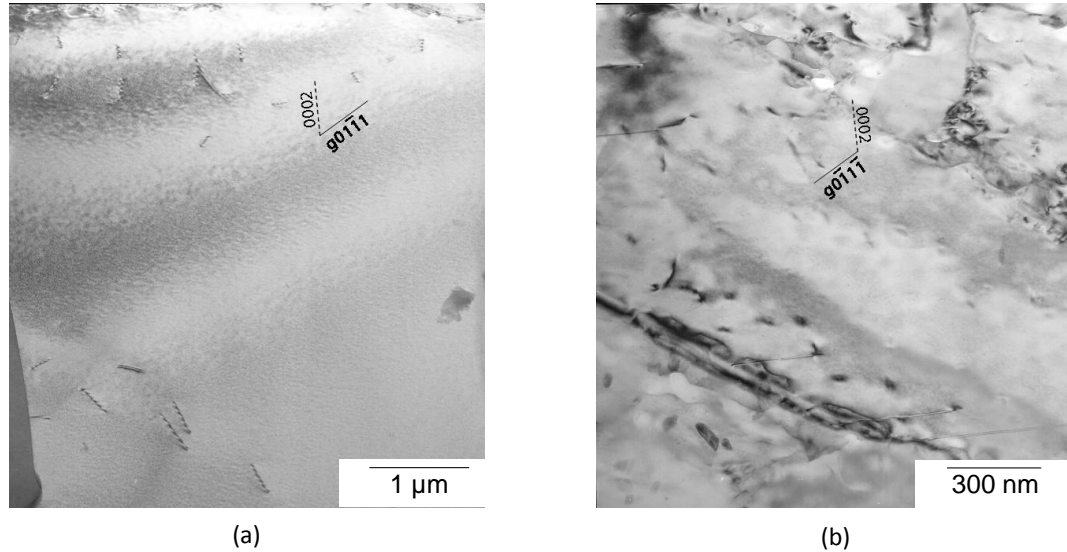


Fig. 3.8 Bright field TEM micrographs of alloy 834 without Si showing (a) few isolated dislocations in $g=01\bar{1}1$ reflection inside primary α grain and (b) limited dislocation activity in $g=01\bar{1}1$ reflection in secondary α laths.

3.4 Discussion

As an undisputed choice of material for high pressure compressor module of advanced gas turbine aeroengines, although Timetal 834 has emerged as a potential candidate material, its maximum use can be realized if one achieves the desired microstructure as per the prevailing service loading conditions.

Metallurgical stress concentration sites such as needle shaped particles should be avoided for premature crack initiation and hence reduced fatigue life [Dieter 1988]. Similarly, equiaxed shaped grains relieves the stress building at the interfaces and improves the fatigue life [Dieter 1988]. In the present study, the optimized microstructure consisting of equiaxed morphology of α_P grains and near spherical shaped silicide particles is obtained to meet these property requirements. Moreover, the finer grain sizes of both α_P and β_T grains is expected to delay the period of crack initiation. Further, as discussed in chapter II (Literature survey), volume fraction of ~15% α_P grains in transformed β matrix as well as finer size of α_{laths} is expected to show improved creep resistance without compromising the fatigue resistance.

In Ti-Al binary alloy system, precipitation of coherent and ordered Ti_3Al phase (D0_{19} structure) depends primarily on the concentration of Al [Blackburn 1967, Crossley 1970, Shamblen and Redden 1972] and aging heat treatment cycle (temperature - soaking time - cooling rate) and partly on processing history and oxygen content [Truax and McMahon 1974]. As per modified Blackburn's Ti-Al binary phase diagram [Namboodhiri et al. 1973], precipitation of Ti_3Al is possible, albeit sluggish in nature, above 400°C for 6.0 wt%. Al. Based on these studies, it is clear that lower aging temperatures ($\geq 400^\circ\text{C}$) and high cooling rate (water and oil quenching) should produce low volume fraction of Ti_3Al which can be identified through weak and diffuse extra super-lattice diffraction spots in TEM. However, being very small in size, imaging of this phase depends on the resolution limit of

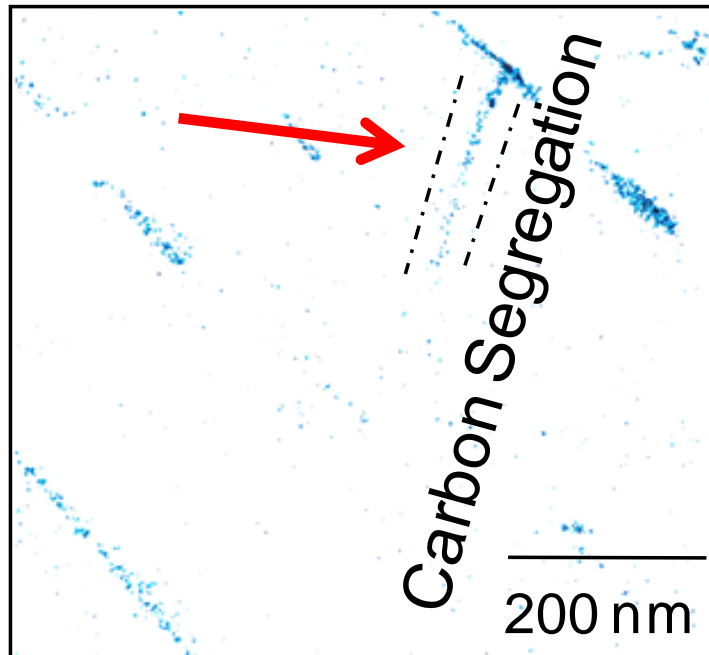
the TEM. The intensity and sharpness of α_2 reflections increases with increase in aging temperature, higher soaking time and lesser cooling rate. In Timetal 834, the solvus temperature of α_2 phase for α/β processed and aged microstructure (700°C for 2 hr and air cooled to ambient temperature) is 795°C \pm 15°C for α_p grains and 735 \pm 15°C for β_T grains, respectively [Donlon et al. 1993]. The observation of Ti_3Al in as-aged microstructure of Timetal 834 in the present investigation is in line with the studies reported in open literature [Donlon et al. 1993, Cope and Hill 1988]. The average diameter and interparticle spacing of Ti_3Al was reported to be ~ 20 Å and ~ 100 Å, respectively [Cope and Hill 1988]. Since the processing condition, aging treatment and oxygen content in the present study is similar to that of this report, it is assumed that these values holds true for the present investigation. Precipitation of Ti_3Al particles in as aged microstructure of titanium alloys have been reported by several researchers [Woodfield et al. 1988, Madsen et al. 1993, Zhang et al. 1998, Gysler and Weissmann 1977, Lütjering and Weissmann 1970].

The observation of limited dislocation activity in α_p grains in transformed β matrix in both the alloys is attributed to accommodation of lattice mismatch generated by the stresses arising from the transformation of β to α phase. In HCP crystal lattice, strain can be accommodated in $\langle a \rangle$, $\langle c \rangle$ or $\langle c + a \rangle$ type dislocations or a combination of any of them in absence of twinning [Lütjering and Williams 2007]. While detailed trace analysis has not been conducted to identify the type of dislocations, it can be inferred from Figs. 3.7a and b which is taken

along $g = 0002$ reflection that 'c' type of dislocations are involved in accommodating the strain during phase transformation. The dislocation substructure of heat treated samples are in close agreement to other heat treated (solution treated, oil quenched and aged) near α titanium alloys [Baxter et al. 1996, Cope and Hill 1988, Ramchandra et al. 1993, Woodfield et al. 1988, White et al. 1985]. While the microstructure of alloy 834 without Si is marginally coarser than Timetal 834 (Table 3.1), it is considered comparable as far as evaluation of tensile properties is concerned.

3.5 Summary

Two near α titanium alloys i.e. Timetal 834 and alloy 834 without Si are processed and heat treated were characterized to understand the microstructural constituents. The microstructural constituents (primary α grain and grain boundary α , secondary α laths, secondary α colonies, retained β layer, prior β grains of transformed β matrix) are characterized using scanning and transmission electron microscopy. The shape, size and morphology of these microstructural constituents are achieved as per the desired application as 'disc' alloy. TEM studies revealed two types of precipitates i.e. Si, Zr and Al rich coarser silicide precipitates and very fine Ti_3Al type precipitates. Dislocation activity in as-heat treated conditions is observed to be minimal in both the alloys.



Chapter IV

Tensile Behavior

4.1 Introduction

The tensile of metallic material constitutes the foundation block for load bearing structural applications. The performance of these materials is generally being assessed by determining three basic properties viz. 0.2% yield strength, ultimate tensile strength (UTS), and ductility (% total elongation or reduction in area). While these properties are routinely studied at the quasi – static strain rates of either 10^{-4} s^{-1} or 10^{-3} s^{-1} , the “strain rate effect” is studied to understand the response of the material at an increased level of applied stress for a given deformation [Dieter 1988]. Similarly, while the tensile properties are generally assessed at room temperature to obtain the first hand information, the “temperature effect” is studied to find out the maximum temperature which limits the performance of the alloy [Meyers and Chawala 2009]. The micro-mechanisms which contribute to the strength of the alloy are largely studied in either “strain rate” or “temperature” effect or a combination of both.

While tensile properties of Timetal 834 in specific test conditions are available in open literature [Cope and Hill 1988, Neal and Fox 1992, Daeubler et al. 1995, Singh et al. 1999, Prasad et al. 2008, Prasad and Kamat 2008, Prasad et al. 2008], limited information on effect of strain rate and temperature on tensile properties are reported [Singh and Singh 2008, Prasad and Kamat 2009]. While the bore and hub regions of high pressure compressor discs are subjected to temperature range

250°C - 450°C, studying tensile properties of Timetal 834 as a function of temperature is of paramount importance.

The phenomena of dynamic strain aging (DSA) in titanium alloys have been extensively studied by earlier investigators [Rosi and Perkins 1953, Kiessel and Sinnott 1953, Santhanam and Reed-Hill 1971, Garde et al. 1972, Doner and Conrad 1973, Moskalenko and Pusptsova 1974, Singh et al. 1999, Singh and Singh 2008, Prasad et al. 2008, Prasad and Kamat 2008, Prasad et al., 2008, Prasad and Kumar 2010]. It has been concluded from an extensive catalogue of material database that the interstitial solute elements responsible for causing DSA in Ti is carbon (C) and oxygen (O) in the temperature ranges 227 to 377°C and 427 to 627°C, respectively [Doner and Conrad 1973]. Later researchers have established, based on calculations of activation energy and activation volume, the role of oxygen [Moskalenko and Pusptsova 1974, Hong 1985] for the occurrence of DSA in Ti alloys. Direct experimental evidence for interstitial ordering in Ti-O alloys [Hirabayashi et al. 1974] has been observed through dark field transmission electron microscopy and neutron diffraction. Based on these results, it has been further emphasized that the preferential direction of oxygen ordering is $\langle 11\bar{2}3 \rangle$ in α Ti [Naka et al. 1988]. However, no microstructural experimental evidence for segregation of interstitial elements (C or N) to dislocations has so far been reported in open literature though nitrogen has been reported to be responsible for DSA in many steels [Petara and Beshers 1965, Reed-Hill and Abbaschian 1977].

The first experimental confirmation of segregation of any element to a defect has been reported using auger electron spectroscopy (AES) [Joshi and Stein 1971]. Thereafter, due to remarkable progress in improvement of characterization tools, this field of identifying “solute segregation” has attracted significant attention primarily in the research area of biology and material science. The techniques employed are X-ray photoelectron spectroscopy (XPS) [Hintz et al. 1983], secondary ion mass spectroscopy (SIMS) [Govrilov et al. 1999], x-ray energy dispersive spectroscopy (XEDS) [Keast and Williams 1999], analytical transmission electron microscope (either in energy filtered EFTEM [Verbeeck et al. 2004] or scanning STEM mode [Wen et al. 2013]) and atom probe field ion microscopy (APFIM) [Hono 1999]. Recently, direct experimental evidence for oxygen segregation in nanocrystalline Al using TEM and atom probe tomography has been reported [Tang et al. 2012]. It has been shown that Si addition increases the creep resistance of Ti alloys containing Al, Mo and Sn either by occurrence of DSA or silicide precipitation on moving dislocations [Assadi et al. 1979] while in binary Ti-Si alloys, Si addition was shown to enhance the DSA effect and also reduce the temperature for occurrence of DSA [Winstone et al. 1973]. It was attributed to the interaction of mobile dislocations with Si-O pairs (solute interstitial complex) which enhances lattice distortion. In Ti-Al alloys, enhancement of DSA effect was associated to Al-interstitial pairs similar to that observed in Ti-Si alloys [Harrison et al. 1975].

It has been reported that Timetal 834 with bi-modal microstructure (α_P grain size and T_β grain size as 28 μm and 126 μm , respectively) exhibits dynamic strain aging in the wider temperature range 350°C to 550°C [Singh et al. 1999, Singh and Singh 2008] and a narrower temperature range 400°C to 475°C in a different bi-modal microstructure (α_P grain size and T_β grain size as 08 μm and 70 μm , respectively) [Prasad et al. 2008]. Si as a substitutional solute is held responsible for causing DSA in Timetal 834 [Singh et al. 2008]. Therefore, in the present chapter, in order to understand the influence of interstitial solutes on DSA, if any, alloy 834 without Si is used in this study. The tensile properties viz. 0.2% YS, UTS, ductility and strain hardening exponent (n) is studied as a function of temperature for both the alloys. In addition, strain rate sensitivity and activation volume are determined from strain rate jump tests to characterize the change in deformation, if any. The influence of strain rate is also studied from 10^{-6} to 10^{-3} s^{-1} in both the alloys to determine the activation energy of solute element/elements which causes dynamic strain aging.

So far, all the data reported in literature is generally concerned with the influence of only one solute - either interstitial or substitutional on DSA. Hardly any literature is available on the effect of different interstitials diffusing simultaneously in the same temperature range at different rates to dislocations. This alloy contains three interstitial solutes namely, C, N and O. In the present work, energy filtered transmission electron microscopy (EFTEM) has been used to examine the tensile tested specimens with a view to identify the solutes segregating to dislocations and

on that basis identify the mechanism responsible for DSA in this alloy. In addition, detailed TEM analysis of deformed tensile specimens to 0.2% plastic strain at selected test temperatures is also carried out to understand the operative slip systems.

4.2 Experimental Procedures

The specimens for tensile testing of Timetal 834 alloy were machined from rectangular blanks that were extracted in T – L orientation (Transverse-Longitudinal) from heated treated plates (Fig. 4.1).

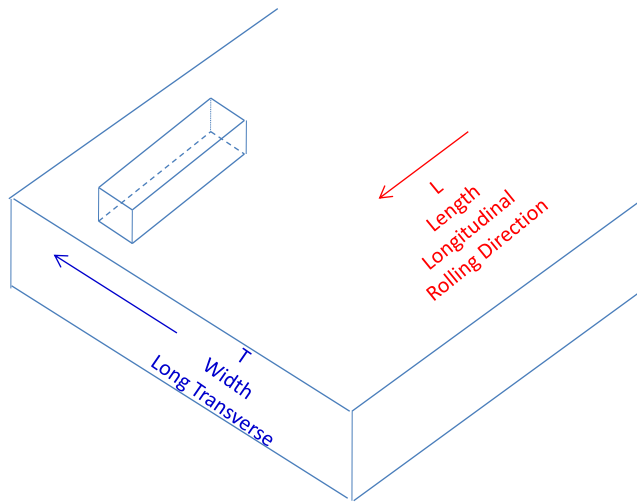


Fig. 4.1 Schematic illustration of orientation of test coupon extraction for tensile testing from heat treated plates.

Tensile tests were conducted on round threaded specimens of gauge diameter 4 mm and gauge length 25 mm as shown in Fig. 4.2. These tests were conducted as



82



Fig. 4.3 Photograph of electromechanical test system (Walter + Bai ag) for tensile testing. Split type three zone resistance furnace and high temperature extensometer are shown in the inset.

As discussed in section 4.1, in order to understand the role of interstitial solute elements on DSA, Alloy 834 near α Ti-alloy without Si (10.38%Al-0.16%Sn-1.86%Zr-0.37%Nb-0.25%Mo-0.27%C-0.30%O-0.006%N, all in at.%), prepared by consumable vacuum arc melting, has been used in the present investigation. Tensile properties of this alloy were evaluated employing the same strain rates and temperature range as that of Timetal 834. However, an additional tensile test was conducted at 250°C.

Few tensile tests were interrupted at a pre-defined strain level (0.2% plastic strain) for transmission electron microscopy (TEM) studies. The tensile tests were interrupted at room temperature for both the alloys. However, tensile tests were interrupted at 300°C and 450°C for alloy 834 without Si and at 450°C for Timetal 834 alloy. In case of specimens deformed at elevated temperatures, specimens were cooled to room temperature by maintaining the same stress as that at test interruption. The specimens interrupted at room temperature and at 450°C were examined for deformation substructure. These studies were carried out using a FEI Techni 20T microscope operating at 200 kV. In addition, microstructure of samples interrupted at room temperature, 300°C and 450°C in alloy 834 without Si were examined in Energy Filtered Transmission Electron Microscopy (EFTEM-LIBRA 200FE, Carl Zeiss make) equipped with Schottky field emission gun and in-column omega filter operating at 200 kV. In EFTEM, compositional images can be obtained from the sample with a resolution better than that in the case of energy dispersive spectrometer attached to TEM. The interstitial elements (C, N and O)

EFTEM maps were obtained by acquiring three images through an energy filter window of 15 eV for 20 s each. This arrangement is expected to give a spatial resolution of about 0.8 nm. One image taken as post-edge and two pre-edge images were used for background subtraction. Thin foils were prepared from 3 mm discs taken from the gauge section of the tensile tested specimens. Thin discs were mechanically polished to 100 μm thickness using SiC paper and electro-polished in twin jet electro polisher (FISCHIONE Instruments). Electro-polishing was done using 5% H_2SO_4 and methanol as electrolyte at -50°C and the voltage was maintained at 20 V.

In order to study the tensile fracture, the fractured end of the tensile tested specimens was cut using an ISOMET low speed saw. Subsequently, specimens were thoroughly cleaned using an ultrasonic cleaner for 5 min and then dried under infrared lamp. The fractured surface was examined using scanning electron microscope model FEI Quanta 400.

4.3 Results

4.3.1 Serrated Flow

The plastic region of true stress-strain curves at various temperatures and at the strain rate of 10^{-5}s^{-1} of Timetal 834 alloy is shown in Fig. 4.4. The plastic region (Fig. 4.4a) is shown to emphasize the load drops or serrated flow observed in this

region in the temperature range between 375°C to 475°C. However, the plastic region is observed to be smooth at 300, 350°C and 500°C (Fig. 4.4a).

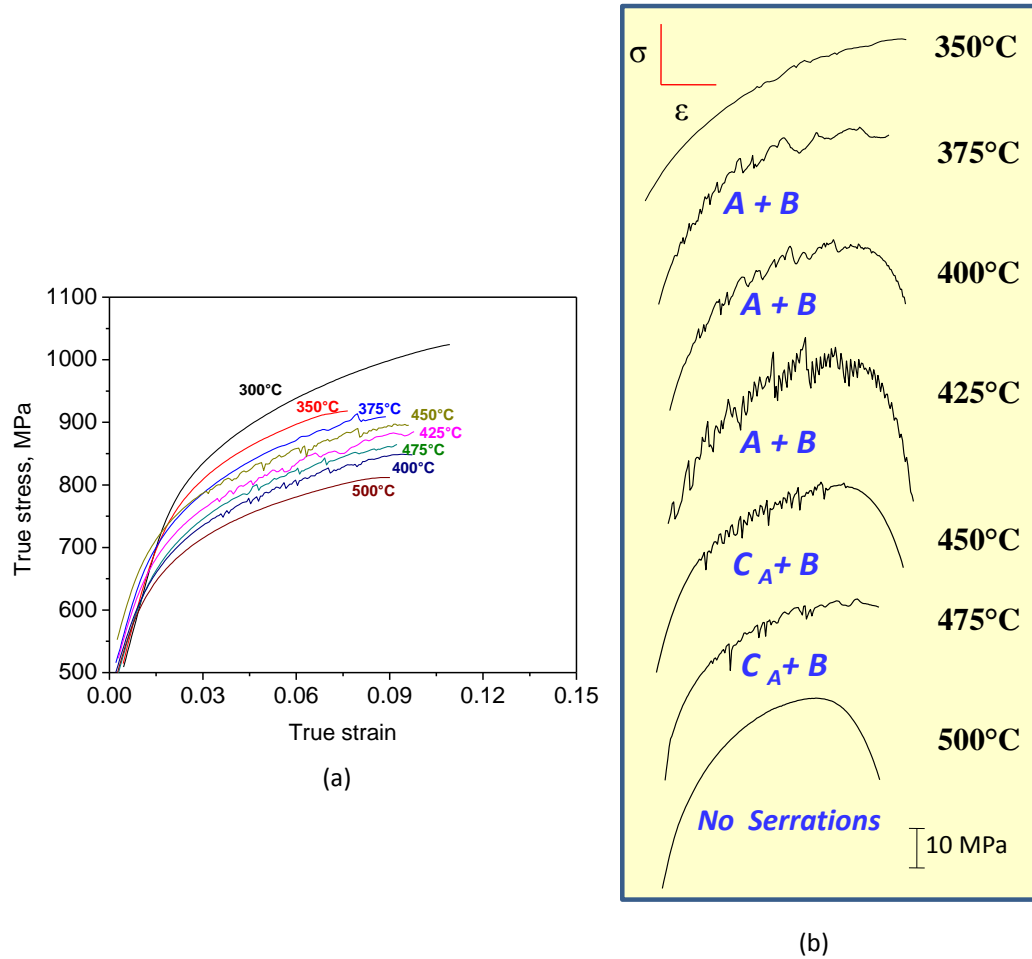


Fig. 4.4 (a) True stress-strain curves of Timetal 834 as a function of temperature at strain rate 10^{-5} s^{-1} and (b) various types of serrations in the plastic regime of stress-strain curves.

It is evident from this figure that the level of flow curves at 450, 425 and 475°C are observed to be marginally above than that of 400°C. It is also clear from these plots that the alloy exhibited a critical plastic strain, ϵ_C , prior to the onset of serrated flow from 375°C to 475°C. The various types of serrations are identified as per the nomenclature reported [Rodriguez 1984] and is shown in Fig. 4.4b. At the strain rate of order of 10^{-5} s^{-1} , the alloy exhibits locking type of serration up to 425°C. Predominantly A type of serrations can be seen at 375 and 400°C which changes to predominantly B type at 425°C. Predominantly unlocking type of serrations (C type) is observed at temperatures 450 and 475°C.

Influence of strain rate on plastic regions of flow curves at two temperatures (400°C and 450°C) is shown in Fig. 4.5. It is evident from Fig. 4.5 that the serrated flow was observed at all strain rates at 450°C employed in this study, however, it could not be manifested at the strain rate of order of 10^{-3} s^{-1} at 400°C.

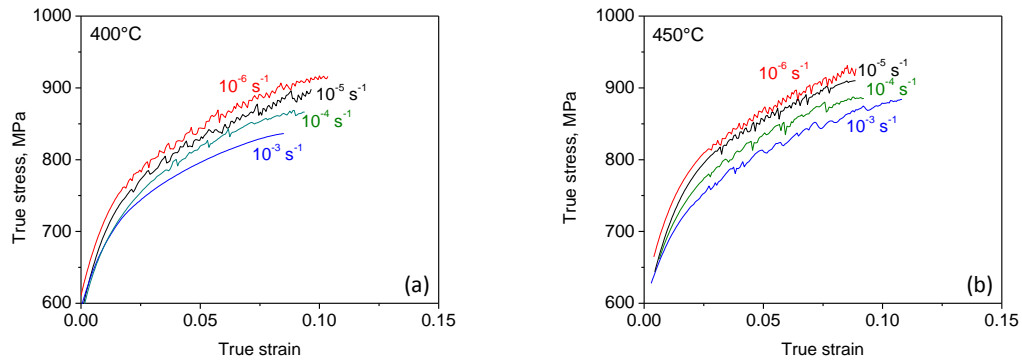


Fig. 4.5 Plastic region of true stress-strain curves showing effect of strain rate at (a) 400°C and (b) 450°C.

The complete serration map covering the temperature range from 300 to 500°C and strain rate from 10^{-6} to 10^{-3} s^{-1} of Timetal 834 is shown schematically in Fig. 4.6.

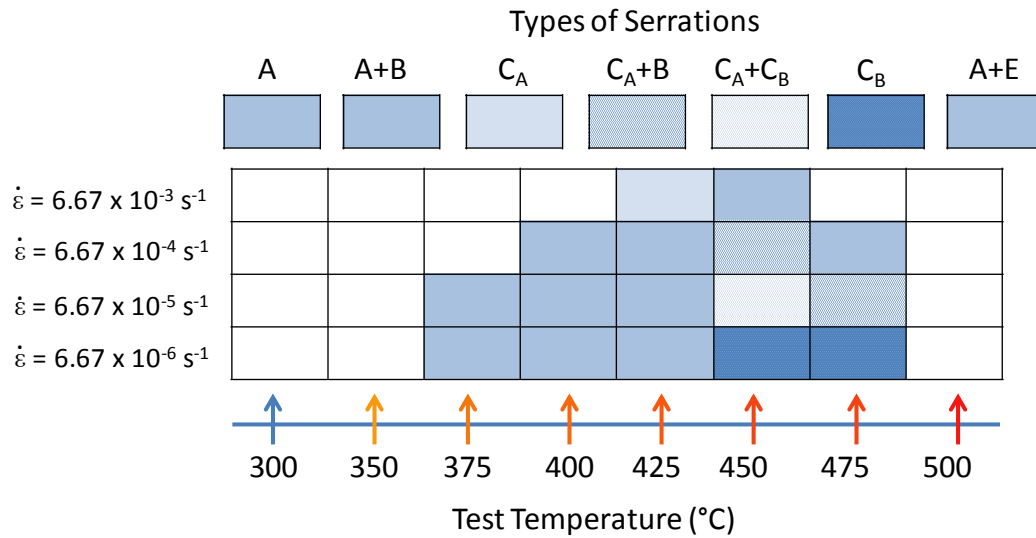


Fig. 4.6 Serration map of Timetal 834 showing the classification of serrations as a function of temperature and strain rate.

In order to show the entire stress-strain curves comprising of elastic and plastic region, four curves showing the engineering stress-strain at 500°C at four different strain rates are shown in Fig. 4.7. It can be inferred from Fig. 4.7 that unlike the influence of strain rates on flow curves at 400 and 450°C (Figs. 4.5a-b), the level of the curve increases with increase in strain rate from 10^{-6} to 10^{-4} s^{-1} , however, it remained nearly same with increase in strain rate from 10^{-4} to 10^{-3} s^{-1} . All curves at this test temperature are observed to be smooth.

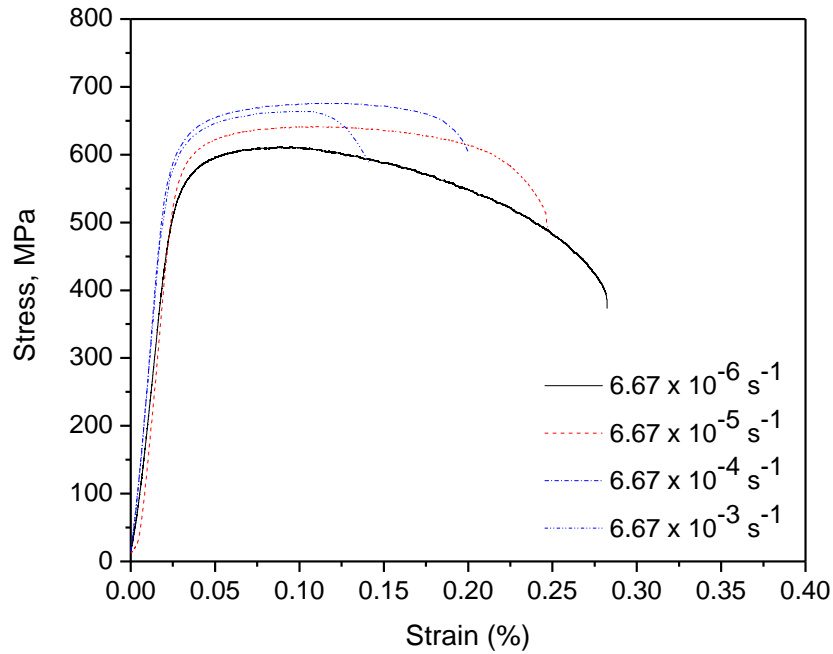


Fig. 4.7 Engineering stress-strain curves of Timetal 834 as a function of temperature at 500°C.

One set of representative plastic region of stress-strain plot at the strain rate of 10^{-5} s^{-1} from 250°C – 500°C of alloy 834 without Si is shown in Fig. 4.8a. It is clear from Fig. 4.8a that the alloy exhibits the manifestation of serrations (load drops) which are mainly A-type at 300°C and 350°C, C-type at 400°C and C+A type at 450°C [Rodriguez 1984]. Fig. 4.8a also shows that the alloy exhibited higher level of flow curve at 350°C than that of 300°C. It is clear from these plots that the alloy exhibited a critical plastic strain, ϵ_C , same as that of Timetal 834 prior to the onset of serrated flow from 300°C to 500°C. The strain corresponding to the peak of the first A or C type serrations were taken as the critical true plastic strain, ϵ_C , for onset of serrations [McCormick 1972]. This value of ϵ_C corresponds to minimum 5

MPa stress drop or rise of the stress strain plot of tested samples. Influence of strain rate on flow curve of the alloy is shown in Fig. 4.8b. It can be seen that the type of serration changes with change in strain rate.

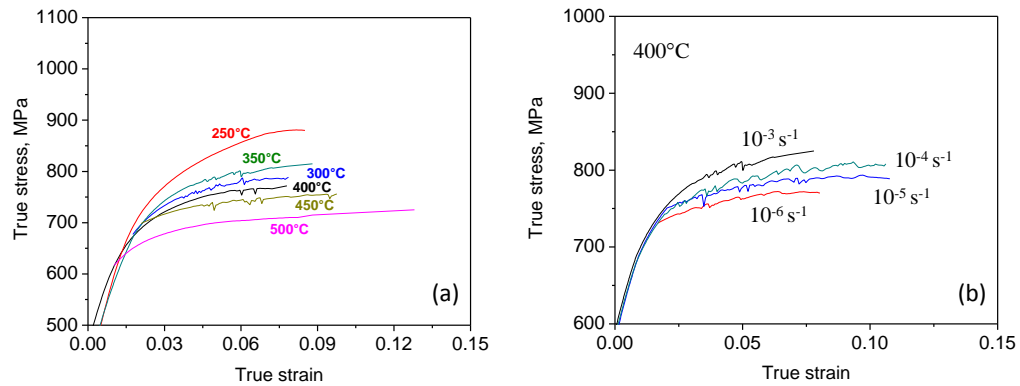


Fig. 4.8 Plastic region of true stress-strain curves of alloy 834 without Si showing (a) effect of temperature at strain rate of 10^{-5} s^{-1} and (a) effect of strain rate at 400°C.

The complete serration map of the alloy 834 without Si is shown in Fig. 4.9. It is clear from Fig. 4.8a and Fig. 4.9 that the temperatures range of the occurrence of serrated flow is wider in alloy 834 without Si as compared to Timetal 834.

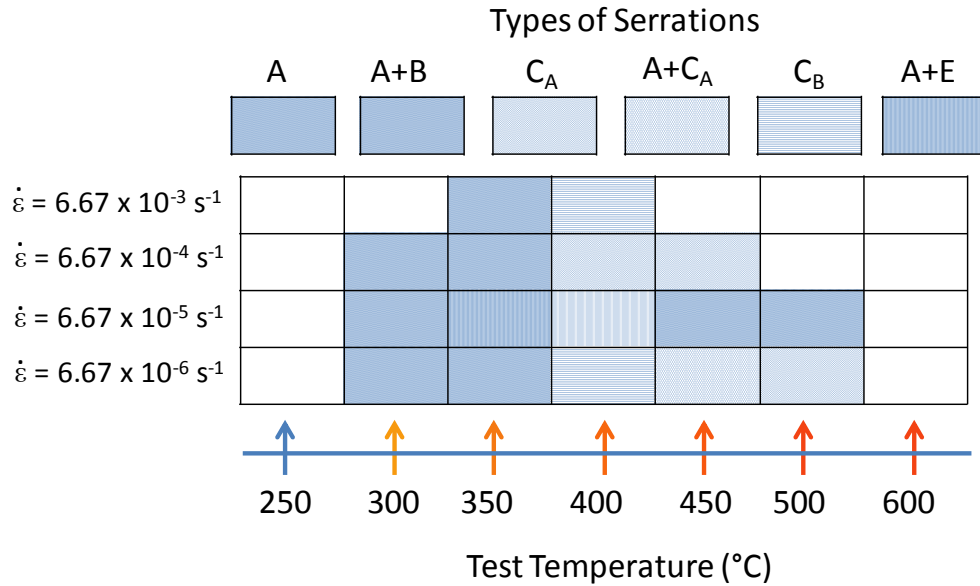


Fig. 4.9 Serration map of alloy 834 without Si showing the classification of serrations as a function of temperature and strain rate.

4.3.2 Tensile Properties

Variation of 0.2% yield strength (0.2% YS) and ultimate tensile strength (UTS) at a strain rate of 10^{-5} s^{-1} of Timetal 834 within the temperature regime studied is shown in Fig. 4.10a together with error bars. While both 0.2% YS and UTS decreased gradually till about 400°C, they remained unaffected by temperature till about 500°C, beyond which they again decreased gradually to 600°C. The tensile ductility, expressed as % total elongation was also found to be the nearly same up to 375°C (Fig. 4.10b). Beyond 375°C, it decreases to a minimum value of 8.0% at 450 °C and thereafter it again increases with increasing test temperature.

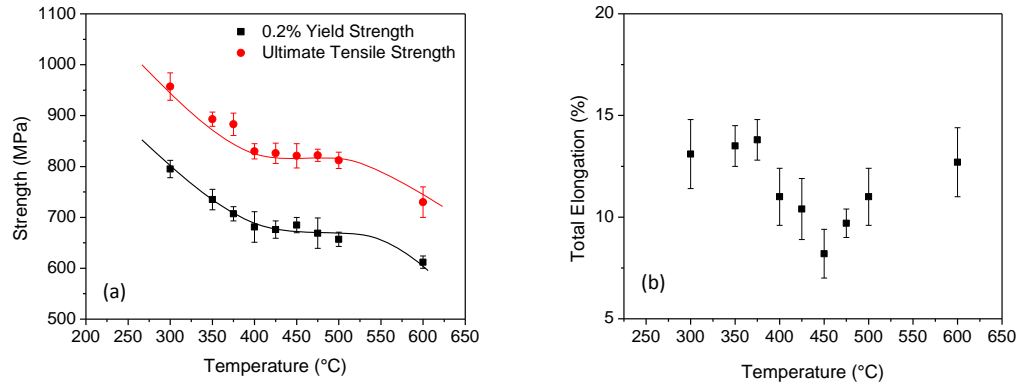


Fig. 4.10 (a) Variation of 0.2% yield strength and ultimate tensile strength and (b) ductility in terms of total elongation as a function of temperature of Timetal 834.

In order to understand the strain hardening of the alloy at various test conditions, the flow was evaluated using Ludwik equation [Markandeya 2006] which was fitted to the plastic true stress – strain flow behavior. It was found that Ludwik equation given below gave the best fit:

$$\sigma = \sigma_0 + K\varepsilon^n \quad (4.1)$$

where, σ_0 is the value of stress at 0% plastic strain, K is strength coefficient and n is the strain hardening exponent. The K and n values obtained at different strain rates are also given in Table 4.1. A representative plot showing the above fit for lowest strain rate at 450°C in Timetal 834 alloy is shown in Fig. 4.11a. The variation of n with test temperature at the strain rate 10^{-5} s^{-1} is shown in Fig. 4.11b.

Table 4.1: Monotonic strain hardening exponent (n) and coefficient (K) at various temperatures

Temperature (°C)	n	K
300	0.048	1408
350	0.036	1488
375	0.047	1416
400	0.078	1296
425	0.091	1201
450	0.110	1292
475	0.088	1294
500	0.074	1306
600	0.047	1410

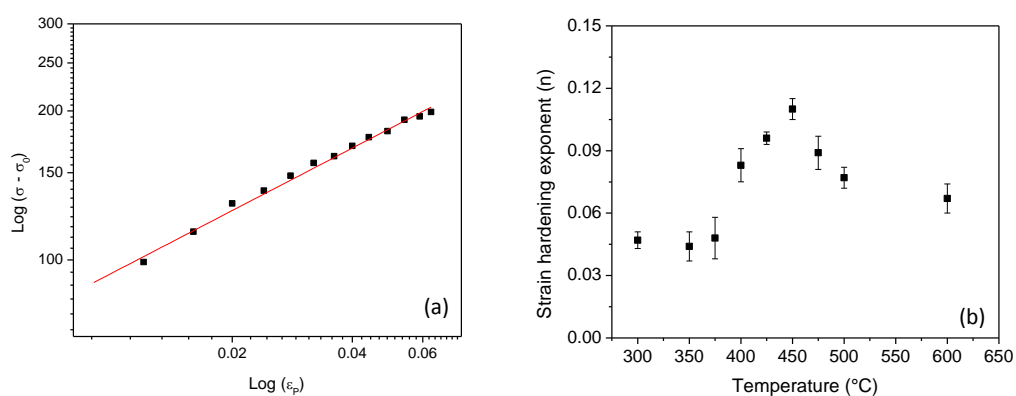


Fig. 4.11 (a) Result of fit flow relationship of log true stress-strain at 10^{-5} s^{-1} (b) variation of strain hardening exponent as a function of temperature of Timetal 834.

It is evident from Fig. 4.11b that n remain nearly same up to 375°C, thereafter which it increases rapidly with increase in temperature up to 450°C. Beyond 450°C, it decreases with increase in temperature. The variation of tensile properties (0.2% YS, UTS, % total elongation and n) of alloy 834 without Si with temperature at the strain rate of 10^{-5} s^{-1} are shown in Fig. 4.12a-c. It is clear from these figures that the trend in the variation of 0.2%YS, UTS, % total elongation and n with temperature is observed to be same as that of Timetal 834. However, the temperature range for occurrence of plateau in the variation of strength (0.2%YS and UTS) with temperature is observed to be wider i.e., 300°C to 500°C as compared to Timetal 834. Moreover, the minimum ductility and maximum strain hardening exponent is observed at 350°C.

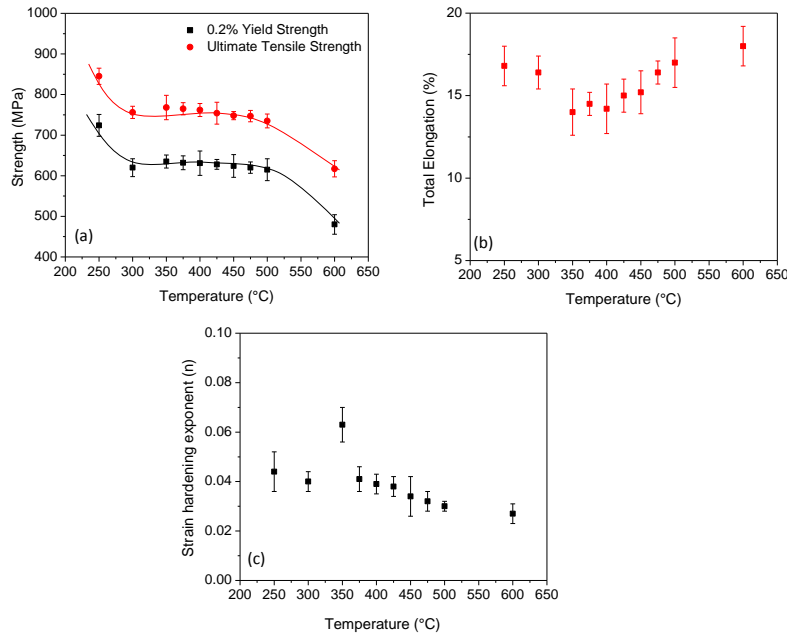


Fig. 4.12 Variation of (a) 0.2% yield strength and ultimate tensile strength (b) total elongation and (c) strain hardening exponent as a function of temperature at 10^{-5} s^{-1} .

Strain rate jump (SRJ) tests were conducted to analyze the strain rate sensitivity of the both the alloys [Dieter 1988]. These tests were conducted at the beginning of plastic deformation i.e. at a small plastic strain of $\varepsilon_p = 0.02$. The representative stress-strain curves obtained during SRJ tests corresponding to the temperature range of occurrence of serrated (450°C) and non-serrated flow (300°C) of Timetal 834 are shown in Fig. 4.13a and b, respectively. It is evident from Figs. 4.13a and b that a sudden decrease in strain rate leads to increase in stress at 450°C, whereas, a sudden increase in strain rate leads to increase in stress at 300°C.

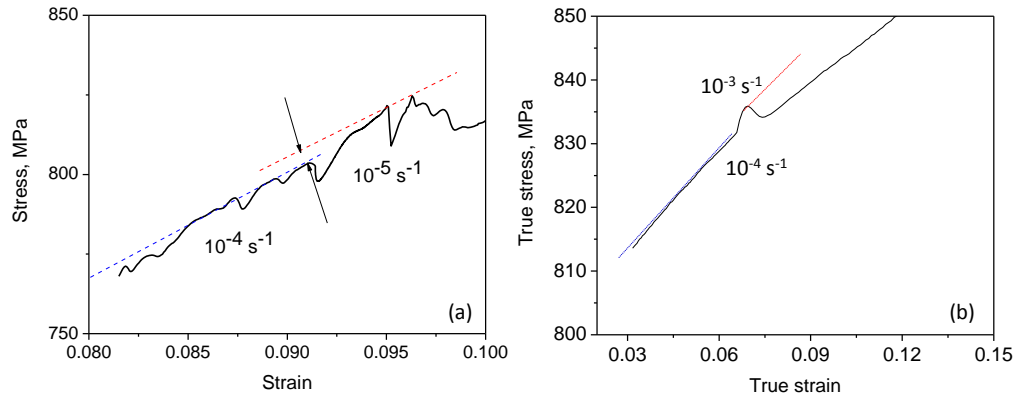


Fig. 4.13 Nature of transients during strain rate jump tests at (a) 450°C, serrated region and (b) 300°C, non-serrated region of Timetal 834.

The stress increment ($\Delta\sigma$) which occurs directly after SRJ has been estimated by means of extrapolation as indicated in these figures. The strain rate sensitivity (SRS) is evaluated through the relation [Dieter 1988]:

$$SRS = \frac{d\sigma}{d \ln \dot{\varepsilon}} \cong \frac{\Delta\sigma}{\Delta \ln \dot{\varepsilon}} \quad (4.2)$$

The variation of SRS with temperature for both the alloys is shown in Fig. 4.14. While SRS values are positive at 300, 350, 500 and 600°C where the flow curves are smooth, it is negative at 375, 400, 425, 450 and 475°C where serrated flow is observed for Timetal 834 alloy. In case of alloy 834 without Si, SRS values are negative at 300, 350, 400, 450, and 500°C, whereas, it is positive at 250, 550 and 600°C.

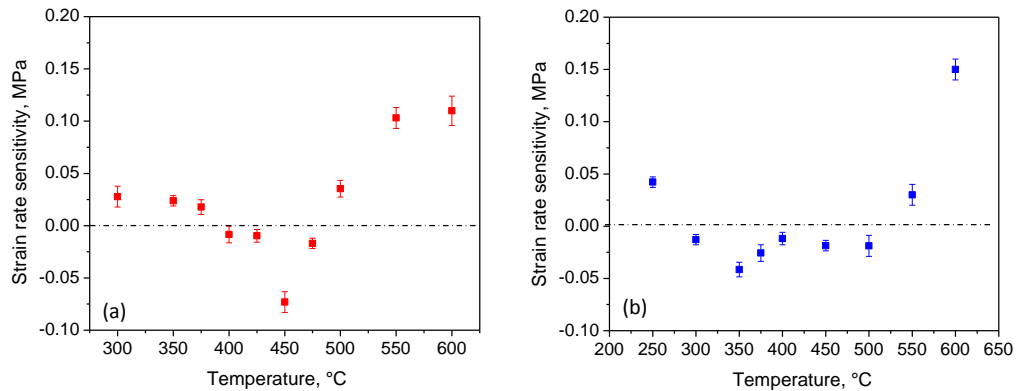


Fig. 4.14 Variation of strain rate sensitivity as a function of temperature of (a) Timetal 834 and (b) alloy 834 without Si.

4.3.3 Dislocation behavior in tensile deformation

A detailed study of the dislocation substructure at 0.2% plastic strain was carried out at room temperature (non-serrated region) and at 450°C (serrated region) in the alloy 834 without Si as well as Timetal 834 to find out the effect of

DSA on dislocation sub-structure. Detailed investigation is carried out using TEM images captured under two beam conditions. The burger vector (b) of dislocations was determined using classical visibility/invisibility (out-of-contrast) conditions $g \cdot b = 0$, where g is the diffraction vector [Bill and Carter 2004]. However, this analysis is done carefully and in a controlled way by identifying a common location in each micrograph of various g vectors as the shape and position of dislocations change significantly while tilting the sample to reach the required diffraction conditions. The dislocations which are analysed and identified unambiguously are labeled in the TEM micrographs. In addition, TEM images are taken in multi-beam conditions to understand the general deformation at room temperature as well as at 450°C.

4.3.3.1 Dislocation Behavior at Room Temperature (Non-Serrated Region)

Figs. 4.15-4.17 show the TEM micrographs of the alloy 834 without Si at different zone axis. While Figs. 4.15a-d corresponds to the $[2\bar{1}\bar{1}0]$ zone axis, Figs. 4.16 and Figs. 4.17 were taken along $[1\bar{1}01]$ and $[4\bar{2}\bar{2}3]$ zone axis, respectively. The g vectors used in the analysis along with the visibility/invisibility conditions of the dislocations (Figs. 4.15 to 4.17) are shown in Table 4.2. Visibility-invisibility analysis (Table 4.2) indicates that the curved dislocations as shown schematically in Fig. 4.15c are ‘a₃’ dislocations with burger vector, b ($1/3[11\bar{2}0]$) and shorter segments of straight dislocations are ‘c’ dislocations and b $[0002]$. Fig. 4.15a is imaged with $g = 0002$ such that the ‘a’ dislocations are invisible.

Complete invisibility of a_3 dislocations can be seen in Fig. 4.15a, 4.16a, and 4.17c. A schematic of the visibility-invisibility of these dislocations are shown in Fig. 4.14. Trace analysis suggests that these dislocations lie on $(1\bar{1}0\bar{1})$ pyramidal plane. All reflections are indicated in stereographic projection of Fig. 4.18.

TEM micrographs of Timetal 834 taken along four different zone axes are shown in Figs. 4.19 to 4.22.

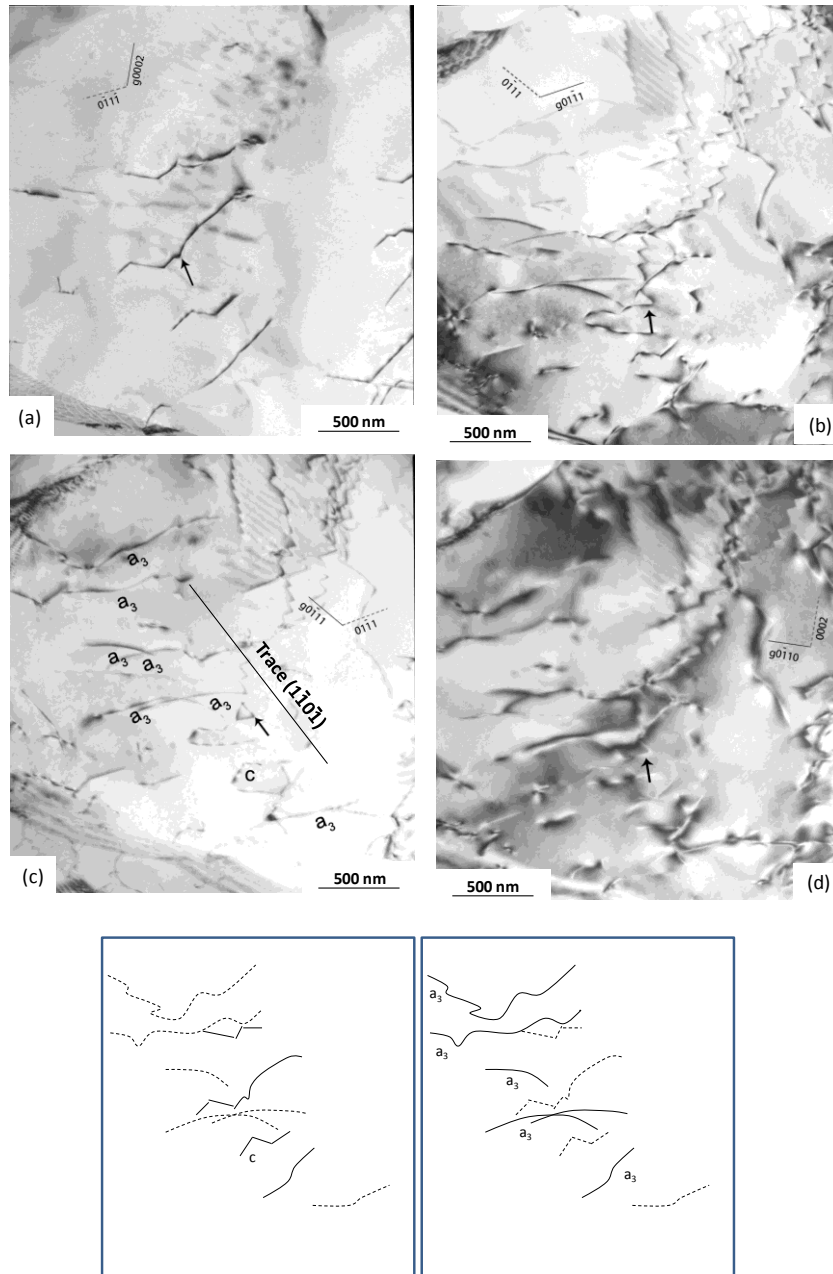


Fig. 4.15 Bright field TEM micrographs of alloy 834 without Si deformed at room temperature. These images are taken along $[2\bar{1}\bar{1}0]$ zone axis showing a slip band of ' a_3 ' dislocations with burger vector, $b=1/3[11\bar{2}0]$ in the $(1\bar{1}0\bar{1})$ pyramidal plane. Common locations marked by arrow in all micrographs. Schematic

illustration of visibility/invisibility of relatively straight and curved dislocations is shown in this figure.

- (a) $g = 0002$, showing complete visibility of relatively straight dislocation segments
- (b) $g = 01\bar{1}1$, showing visibility of straight and curved dislocation segments
- (c) $g = 0\bar{1}11$, showing complete visibility of curved dislocation segments
- (d) $g = 0\bar{1}10$, showing a fringe contrast running along the band

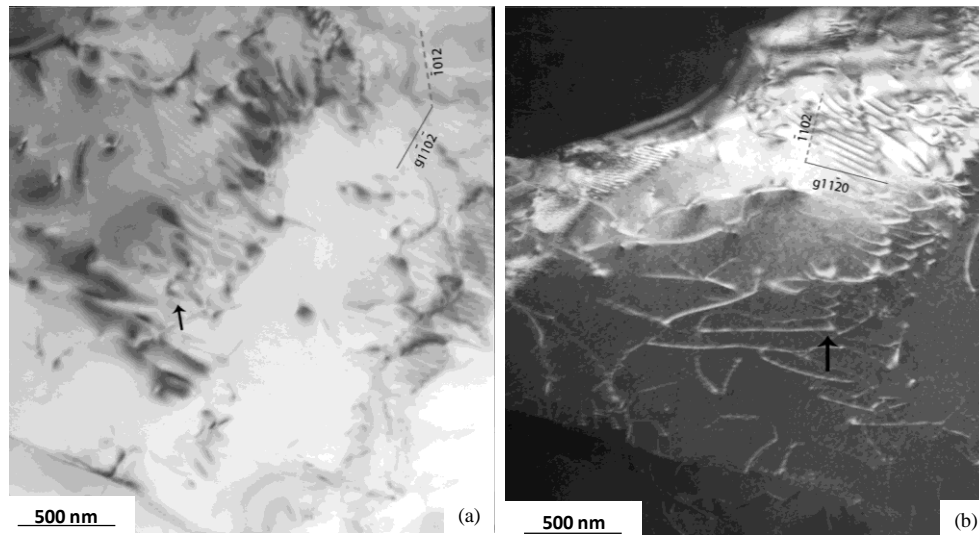


Fig. 4.16 TEM micrographs of alloy 834 without Si deformed at room temperature taken along $[1\bar{1}01]$ zone axis. Common locations marked by arrow in all micrographs.

- (a) $g = 1\bar{1}0\bar{2}$, showing complete invisibility.
- (b) $g = 11\bar{2}0$, showing complete visibility.

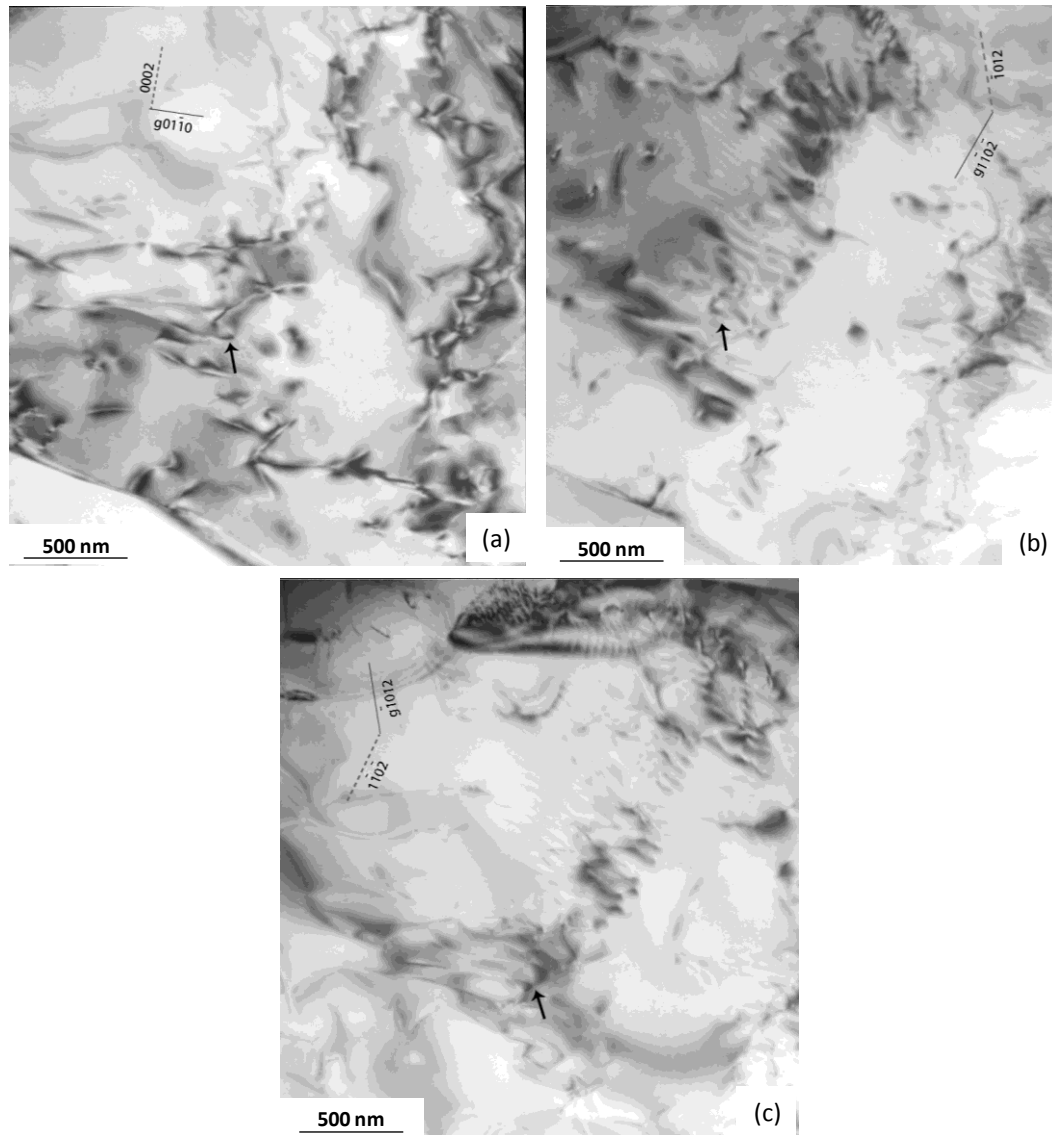


Fig. 4.17 Bright field TEM micrographs of alloy 834 without Si deformed at room temperature taken along $[4\bar{2}\bar{2}3]$ zone axis. Common locations marked by arrow in all micrographs.

(a) $g = 01\bar{1}0$, showing residual visibility

(b) $g = 1\bar{1}0\bar{2}$, showing complete invisibility

(c) $g = \bar{1}012$, showing complete invisibility

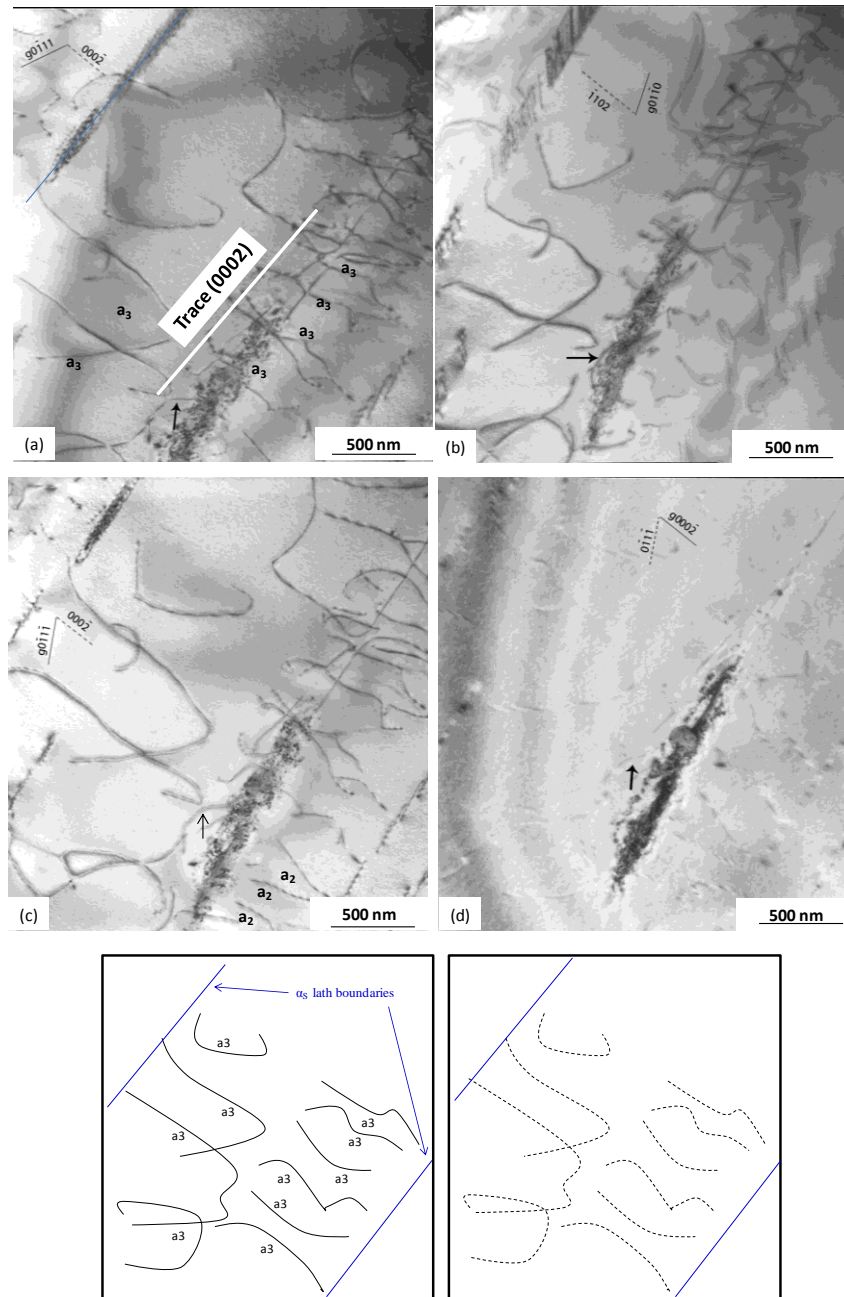


Fig. 4.19 Bright field TEM micrographs of deformed specimen of Timetal 834 at room temperature taken along $[2\bar{1}\bar{1}0]$ zone axis showing a dislocation pile up of ‘ a_3 ’ dislocations ($b=1/3[11\bar{2}0]$) slip band in the (0002) basal plane. Common

locations marked by arrow in all micrographs. Visibility/invisibility of curved dislocations is schematically illustrated.

- (a) $g = 0\bar{1}11$, showing complete visibility
- (b) $g = 01\bar{1}0$, showing complete visibility
- (c) $g = 0\bar{1}1\bar{1}$, showing residual visibility
- (d) $g = 000\bar{2}$, showing complete invisibility

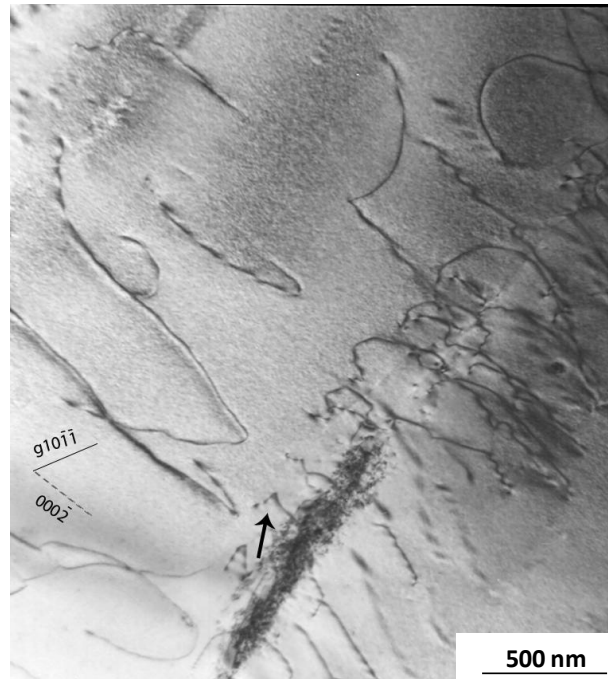


Fig. 4.20 Bright field TEM micrographs of tensile interrupted specimen of Timetal 834 at ambient temperature taken along $[1\bar{2}10]$ zone axis showing complete visibility of dislocations at $g = 10\bar{1}\bar{1}$.

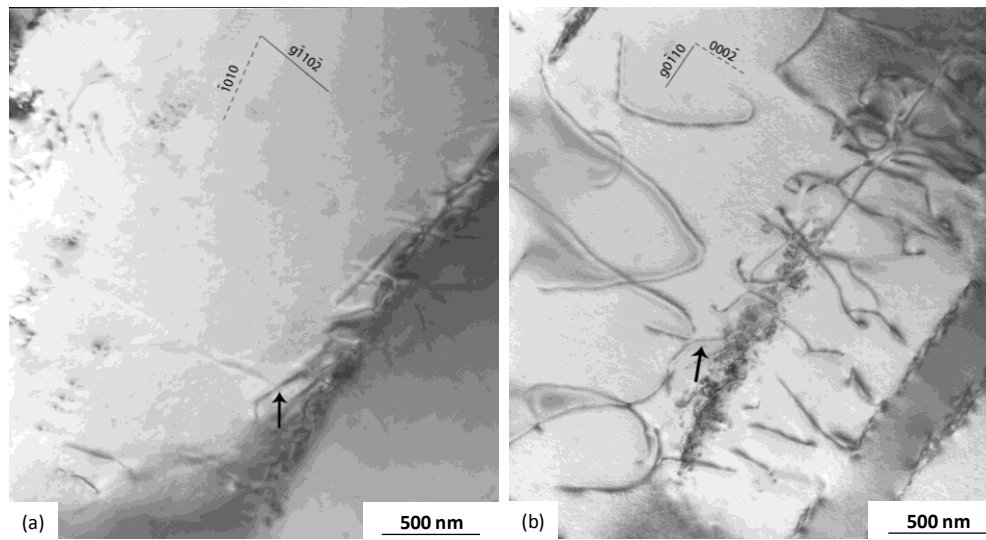


Fig. 4.21 Bright field TEM micrographs of tensile interrupted specimen of Timetal 834 at room temperature taken along $[4\bar{2}\bar{2}3]$ zone axis showing (a) complete invisibility, $g = 101\bar{2}$ and (b) complete visibility, $g = 0110$.

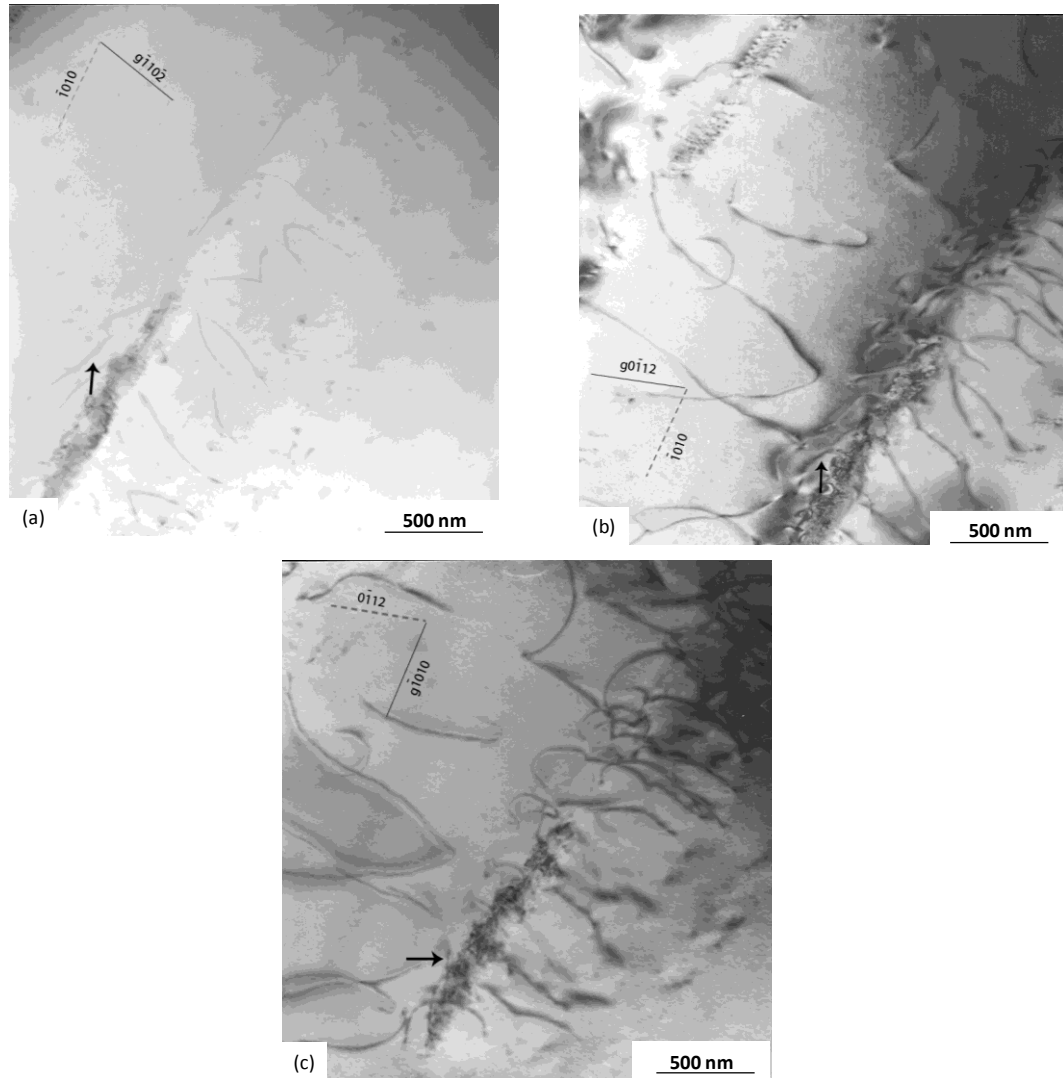


Fig. 4.22 Bright field TEM micrographs of deformed specimen of Timetal 834 at ambient temperature. These images are taken along $[2\bar{4}2\bar{3}]$ zone axis.

- (a) $g = \bar{1}10\bar{2}$, showing complete invisibility
- (b) $g = 0\bar{1}1\bar{2}$, showing complete visibility
- (c) $g = \bar{1}010$, showing residual visibility

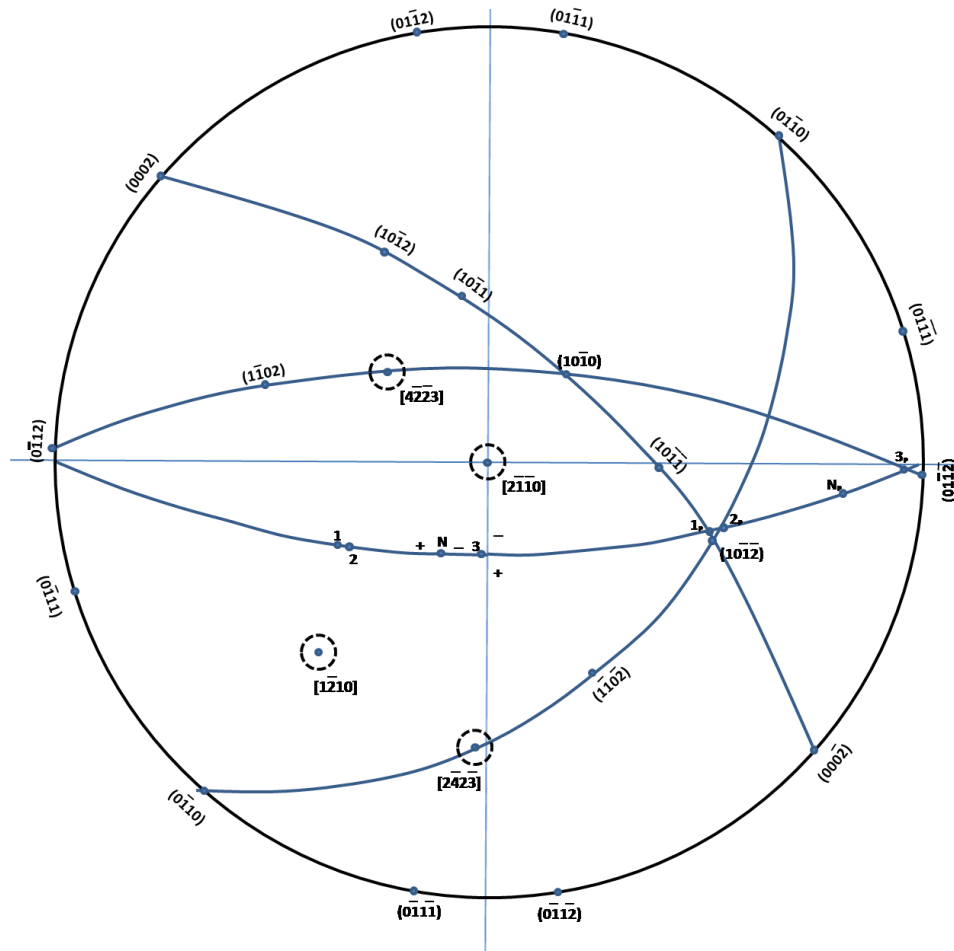


Fig. 4.23 Stereographic projection showing the orientations and trace analysis of Figs. 4.19-4.22.

Table 4.2 g vectors and zone axis for the tensile tested specimen of alloy 834 without Si at ambient temperature.

Zone axis	g vector	a ₁	a ₂	a ₃	c
[2 $\bar{1}\bar{1}$ 0]	0002	-	-	-	√
	0 $\bar{1}$ 11	-	-	√	√
	0 $\bar{1}$ 1 $\bar{1}$	-	-	√	√
	0 $\bar{1}$ 10	-	-	√	-
[1101]	1 $\bar{1}$ 0 $\bar{2}$	-	-	-	√
	11 $\bar{2}$ 0	-	-	√	-
[4223]	0 $\bar{1}$ 10	-	-	√	√
	1 $\bar{1}$ 0 $\bar{2}$	-	-	-	√
	$\bar{1}$ 01 $\bar{2}$	-	-	√	√

The curved dislocation as observed in these images and also shown schematically in Figs. 4.19 are invisible with $g = 0002$ (Fig. 4.19d) taken along [2 $\bar{1}\bar{1}$ 0] zone axis, $g = 1\bar{1}0\bar{2}$ (Fig. 4.21a) taken along [4 $\bar{2}\bar{2}$ 3] zone axis, and $g = 1\bar{1}02$ (Fig. 4.22a) taken along [2 $\bar{4}\bar{2}\bar{3}$] zone axis. The g vectors used in the analysis along with the visibility/invisibility conditions of the dislocations (Figs. 4.19 to 4.22) are shown in Table 4.3. These dislocations are visible in other g vectors in these figures indicating that the burger vector is $(1/3[11\bar{2}0])$. Visibility-invisibility analysis (Table 3) also indicates few 'a₂' dislocations (Fig. 4.19c). Trace analysis suggests that these dislocations lie on to the (0002) basal plane. All reflections are indicated in stereographic projection of Fig. 4.23.

Table 4.3 g vectors and zone axis for the tensile tested specimen at ambient temperature for Timetal 834.

Zone axis	g vector	a ₁	a ₂	a ₃	c
[2 $\bar{1}$ 10]	0 $\bar{1}$ 11	-	√	√	-
	0 $\bar{1}$ 10	-	√	√	-
	0 $\bar{1}$ 1 $\bar{1}$	-	√	√	-
	0002	-	-	-	-
[1 $\bar{2}$ 10]	10 $\bar{1}$ $\bar{1}$	-	-	√	-
[4 $\bar{2}$ 23]	1 $\bar{1}$ 0 $\bar{2}$	-	√	-	-
	0 $\bar{1}$ 10	-	√	√	-
[2 $\bar{4}$ 23]	1 $\bar{1}$ 02	-	√	-	-
	01 $\bar{1}$ 2	-	√	√	-
	10 $\bar{1}$ 0	-	-	√	-

4.3.3.2 Dislocation Behavior at 450°C (Serrated Region).

TEM micrographs of alloy 834 without Si taken along three zone axes are shown in Figs. 4.24 – 4.26. Figs. 4.24a-b are taken along [0001] zone axes, Figs. 4.25a-c are taken along [11 $\bar{2}$ 3] zone axes and Figs. 4.26a-b are taken along [1 $\bar{2}$ 13] zone axes. The g vectors used in the analysis along with the visibility/invisibility conditions of the dislocations (Figs. 4.24 – 4.26) are shown in Table 4.4. Based on invisibility/invisibility conditions, the relatively straight dislocation segments are identified as ‘a₃’ dislocations (Fig. 4.24a), whereas, the curved dislocations as shown schematically in the same figure are identified as ‘a₁’ dislocations (Fig. 4.24a). These curved dislocations are completely invisible in Figs. 4.24b, 4.25a and 4.26b. However, the straight dislocations are invisible in Figs. 4.25c (g = 1 $\bar{1}$ 00) and Fig. 4.26a (g = 1 $\bar{1}$ 0 $\bar{1}$). It has been confirmed by trace analysis that ‘a₃’

dislocations lie on (0001) basal plane and ‘a₁’ dislocations lie on (01 $\bar{1}$ 1) pyramidal plane. The burger vectors as deduced from the invisibility conditions for ‘a₃’ dislocations is (1/3[11 $\bar{2}$ 0]), whereas, it is (1/3[$\bar{2}$ 110]) for ‘a₁’ type dislocations. The stereographic projection used for the detailed analysis is shown in Fig. 4.27.

The bright field images for Timetal 834 alloy taken along three different zone axes are shown in Figs. 4.28 – 4.30. The image taken with $g = 0\bar{1}11$ along [$\bar{1}2\bar{1}3$] zone axes show dislocation pile – ups in two slip bands (Fig. 4.28a). The same is shown schematically in Fig. 4.28. The g vectors used in the analysis along with the visibility/invisibility conditions of the dislocations (Figs. 4.28 – 4.30) are shown in Table 4.5. Both the pile – ups are completely invisible with $g = 1\bar{1}01$ (Fig. 4.28b), $g = 0\bar{1}12$ and $g = 1\bar{1}02$ in Figs. 4.29a-b and $g = 0\bar{1}10$ (Fig. 4.30a). The visibility/invisibility condition indicates that both the pile – ups are composed of ‘a₃’ dislocations with b (1/3[11 $\bar{2}$ 0]). One of the pile – up which appears to cross from one lath to other lie on (0001) basal plan as found out from the trace analysis. However, the dislocation pile-up which traverses along the α lath lie on (1 $\bar{1}$ 01) pyramidal plane. The stereographic projection of these images is shown in Fig. 4.31.

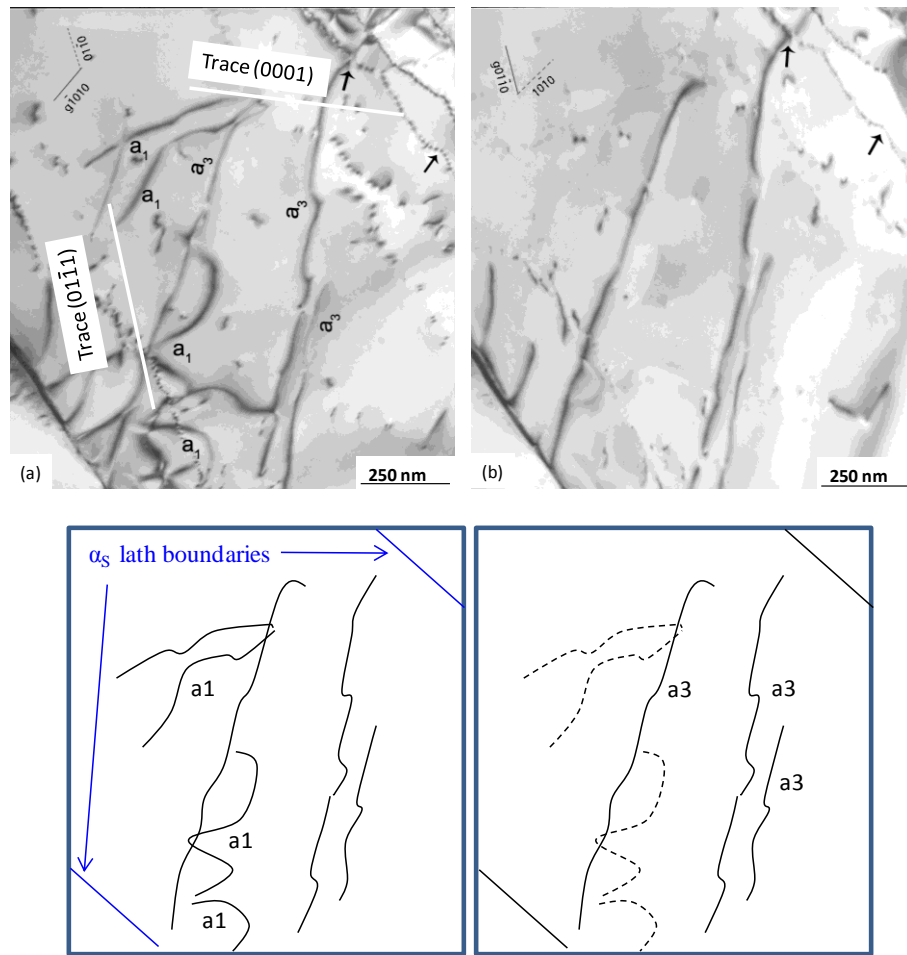


Fig. 4.24 Bright field TEM micrographs of deformed specimen of Alloy 834 without Si at 450°C taken along [0001] zone axis showing two dislocation pile ups of ‘ a_1 ’ dislocations ($b=1/3[2\bar{1}\bar{1}0]$) in pyramidal $(01\bar{1}1)$ plane and ‘ a_3 ’ dislocations ($b=1/3[11\bar{2}0]$) in basal plane. Common locations marked by arrow in all micrographs. Visibility/invisibility of a_1 and a_3 dislocations is schematically illustrated.

(a) $g = \bar{1}010$, showing complete visibility

(b) $g = 01\bar{1}0$, showing complete visibility for a_3 dislocations.

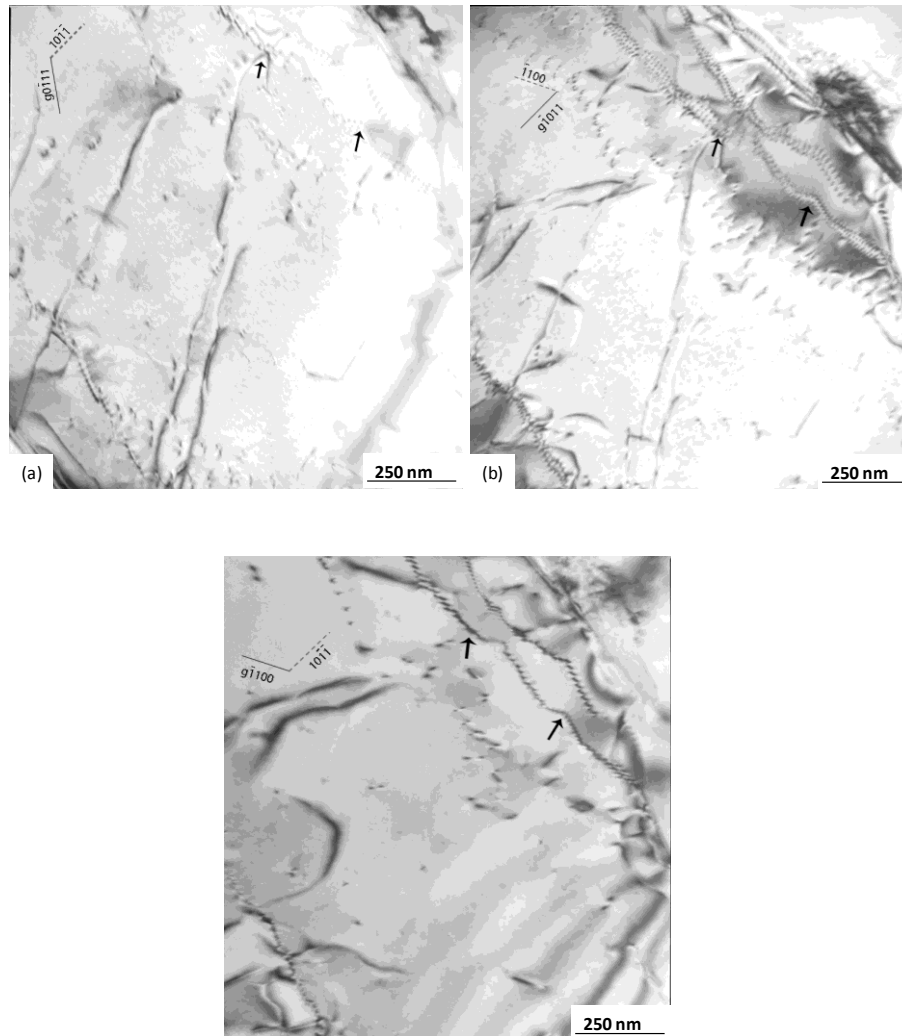


Fig. 4.25 Bright field TEM micrographs of tensile interrupted specimen of alloy 834 without Si at 450°C taken along $[11\bar{2}3]$ zone axis. Common locations marked by arrow in all micrographs.

- (a) $g = 0\bar{1}11$, showing complete visibility of a_3 dislocations
- (b) $g = \bar{1}011$, showing residual visibility
- (c) $g = \bar{1}100$, showing complete invisibility

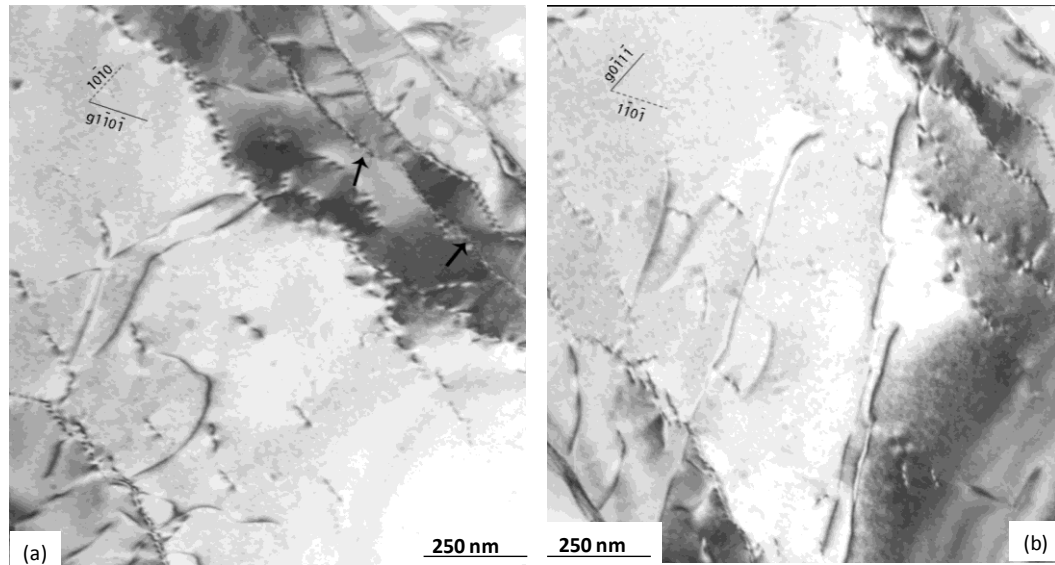


Fig. 4.26 Bright field TEM micrographs of tensile interrupted specimen of Alloy 834 without Si at 450°C taken along $[1\bar{2}13]$ zone axis. Common locations marked by arrow in all micrographs.

- (a) $g = 1\bar{1}0\bar{1}$, showing residual visibility of a_1 dislocations and complete invisibility of a_3 type of dislocations
- (b) $g = 0\bar{1}1\bar{1}$, showing complete invisibility of a_1 dislocations and residual visibility of a_3 type of dislocations

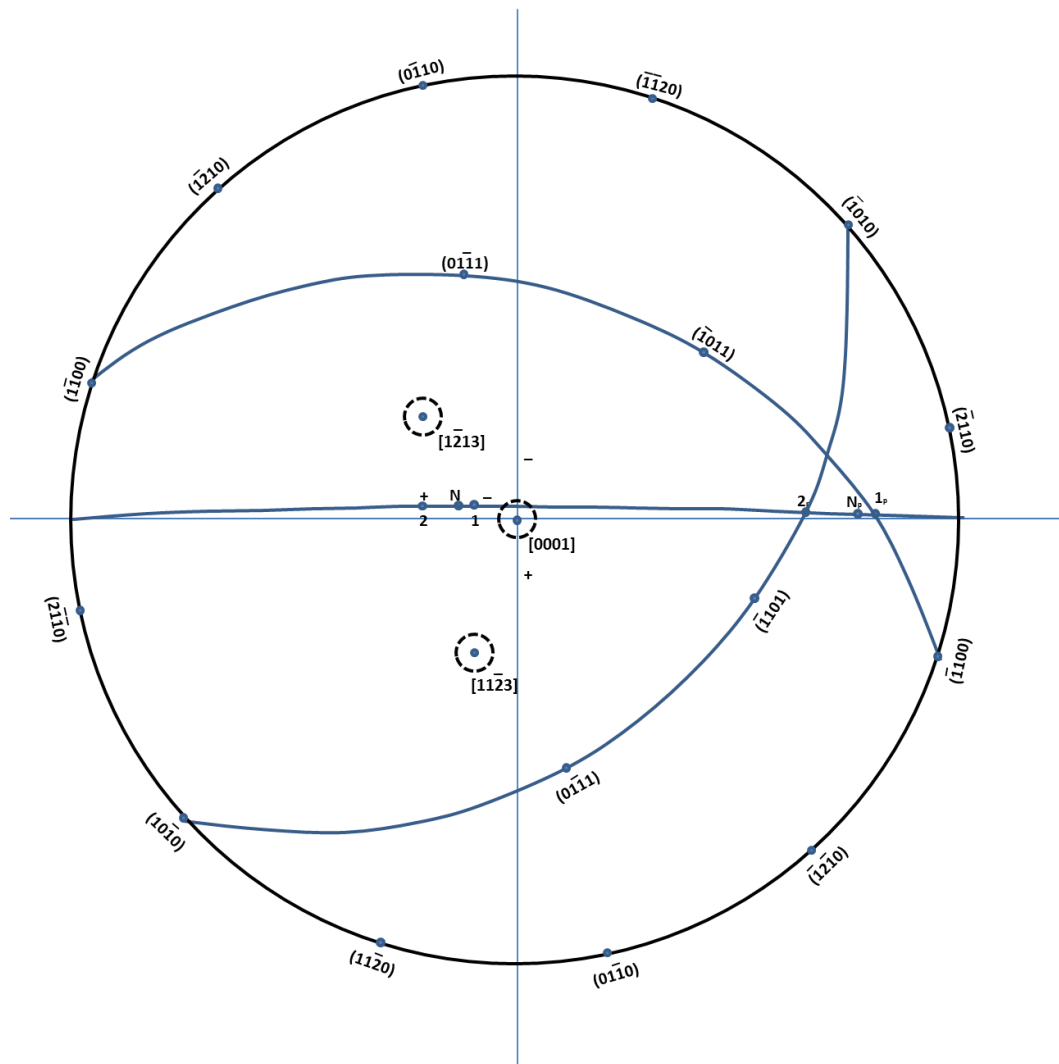


Fig. 4.27 Stereographic projection showing the orientations and trace analysis of Figs. 4.24-4.26.

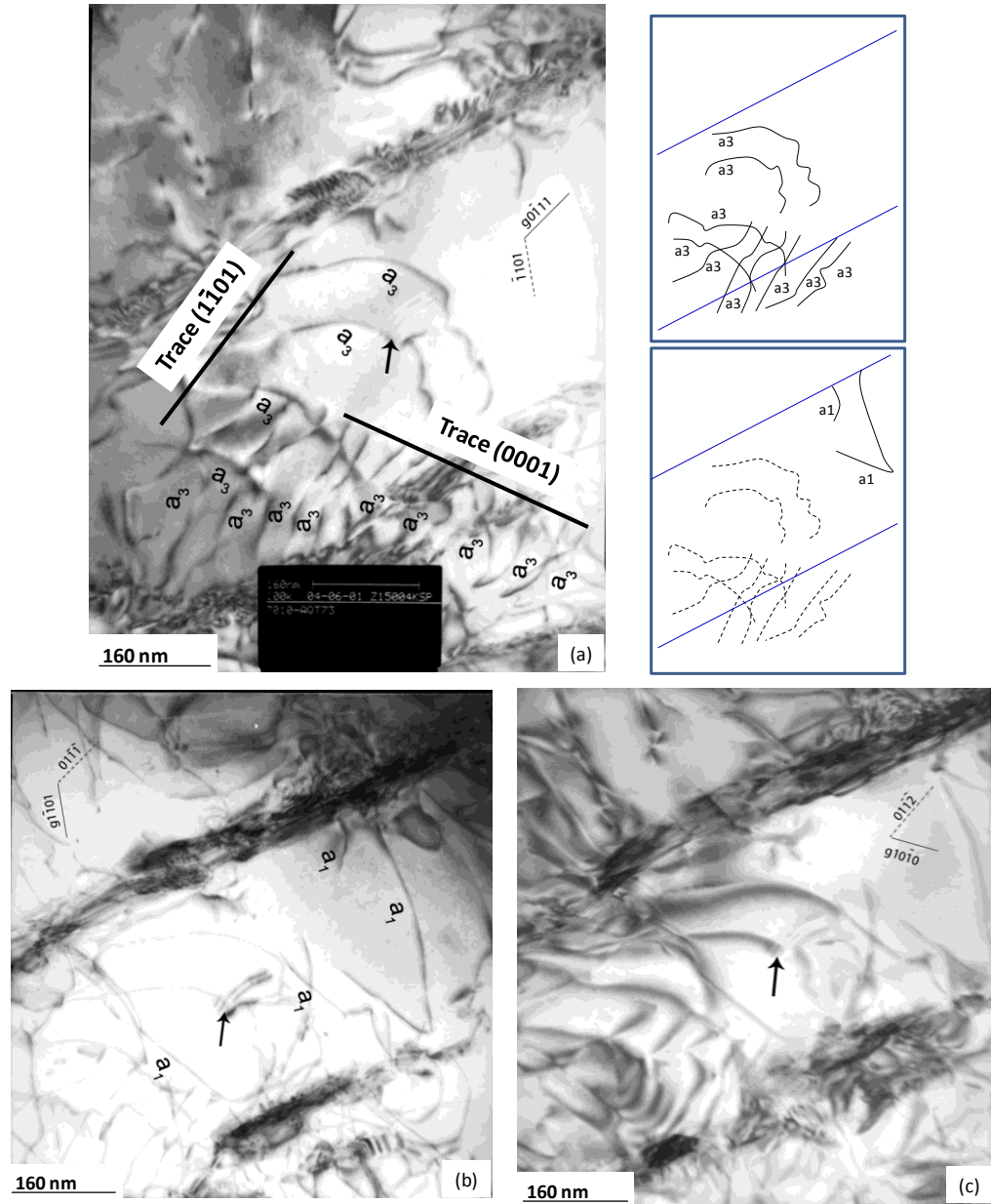


Fig. 4.28 Bright field TEM micrographs of tensile interrupted specimen of Timetal 834 at 450°C taken along $[\bar{1}2\bar{1}3]$ zone axis showing two dislocation pile ups (also shown schematically) of ' a_3 ' dislocations ($b=1/3[11\bar{2}0]$) in the $(1\bar{1}01)$ pyramidal and (0001) basal plane. Common locations marked by arrow in all micrographs.

(a) $g = 0\bar{1}11$, showing complete visibility

(b) $g = 1\bar{1}01$, showing complete invisibility

(c) $g = 10\bar{1}0$, showing residual visibility

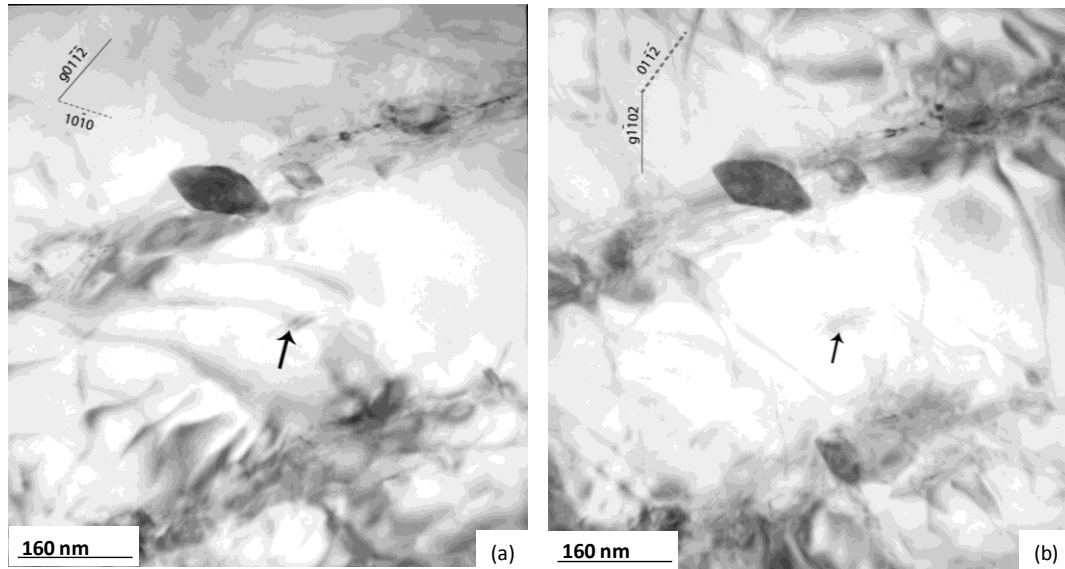


Fig. 4.29 Bright field TEM micrographs of tensile interrupted specimen of Timetal 834 at 450°C taken along $[\bar{2}4\bar{2}3]$ zone axis. Common locations marked by arrow in all micrographs.

(a) $g = 01\bar{1}\bar{2}$, showing complete invisibility

(b) $g = 1\bar{1}02$, showing complete invisibility

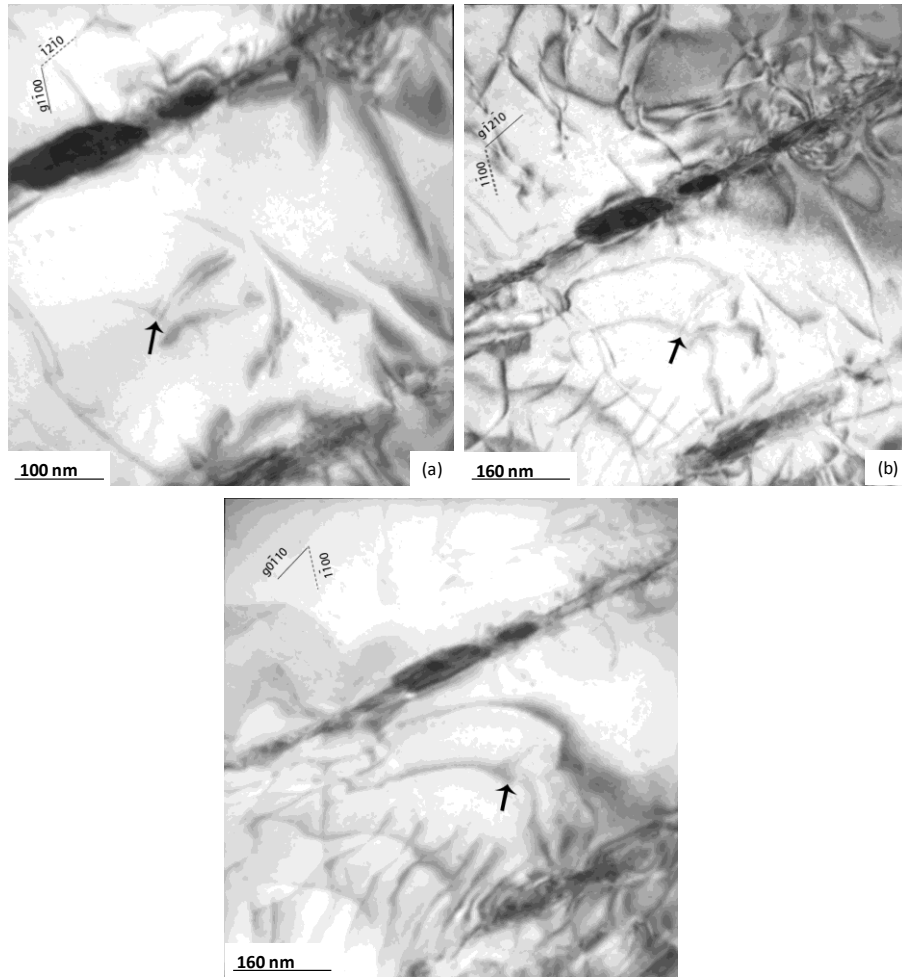


Fig. 4.30 Bright field TEM micrographs of tensile interrupted specimen of Timetal 834 at 450°C taken along [0001] zone axis. Common locations marked by arrow in all micrographs.

- (a) $g = 1\bar{1}00$, showing complete invisibility
- (b) $g = \bar{1}2\bar{1}0$, showing residual visibility
- (c) $g = 0\bar{1}10$, showing residual visibility

Table 4.4: g vectors and zone axis for the tensile tested specimen at 450°C for alloy 834 without Si.

Zone axis	g vector	a ₁	a ₂	a ₃	c
[0001]	0 $\bar{1}$ 10	-	-	$\sqrt{}$	-
	10 $\bar{1}$ 0	$\sqrt{}$	-	$\sqrt{}$	-
[1 $\bar{2}$ 13]	1 $\bar{1}$ 0 $\bar{1}$	$\sqrt{}$	-	-	-
	0 $\bar{1}$ 1 $\bar{1}$	-	-	$\sqrt{}$	-
[11 $\bar{2}$ 3]	0 $\bar{1}$ 11	-	-	$\sqrt{}$	-
	$\bar{1}$ 011	$\sqrt{}$	-	$\sqrt{}$	-
	1 $\bar{1}$ 00	$\sqrt{}$	-	-	-

Table 4.5: g vectors and zone axis for the tensile tested specimen at 450°C for Timetal 834.

Zone axis	g vector	a ₁	a ₂	a ₃	c
[1 $\bar{2}$ 13]	10 $\bar{1}$ 0	$\sqrt{}$	-	$\sqrt{}$	-
	1 $\bar{1}$ 01	$\sqrt{}$	-	-	-
	0 $\bar{1}$ 11	-	-	$\sqrt{}$	-
[0001]	0 $\bar{1}$ 10	-	-	$\sqrt{}$	-
	1 $\bar{2}$ 10	$\sqrt{}$	-	$\sqrt{}$	-
	1 $\bar{1}$ 00	$\sqrt{}$		-	
[24 $\bar{2}$ 3]	0 $\bar{1}$ 12	-	-	$\sqrt{}$	-
	1 $\bar{1}$ 02	$\sqrt{}$	-	$\sqrt{}$	-

4.3.3.3 Deformation Substructures at Room Temperature and at 450°C

The deformed substructure of Timetal 834 at room temperature is shown in Figs. 4.32-4.34. Examination of TEM images as shown in a form of montage in Fig. 4.32 revealed dislocation pile ups as indicated by A and B, very straight dislocation segments as indicated by C and D, cusped or pinned dislocations as indicated by E and F. Dislocation pile ups and random tangles of dislocations (Figs. 4.33a and b) is also observed in other locations. At 450°C, distinct and intense slip bands are observed within a single alpha lath (Fig. 4.34a-c). These slip bands as shown schematically in Fig. 4.34b are termed as type I and type II. Type I dislocation pile up traverses from one end of α lath boundary to the other end as indicated by A₁, A₂, A₃, and A₄ in Fig. 4.34a. High magnification image of selected region of this type of pile up is shown in top corner of the Fig. 4.34a. These dislocations appear cusped or pinned. However, dislocation pile up of type II traverses along the alpha lath as indicated by B in Fig. 4.34a. High magnification image of the selected area of type II pile up as shown in bottom corner of the Fig. 4.34a and the montage of dislocation pile ups of this type of dislocations as shown in Fig. 4.34c reveal that these dislocations are composed of shorter segments of dislocations. Dislocations decorated along type I and type II pile ups can be seen more legibly in Fig. 4.34c. Numerous pinned dislocation segments (Fig. 4.35a) and random dislocation tangles (Fig. 4.35b) can be seen in other regions.

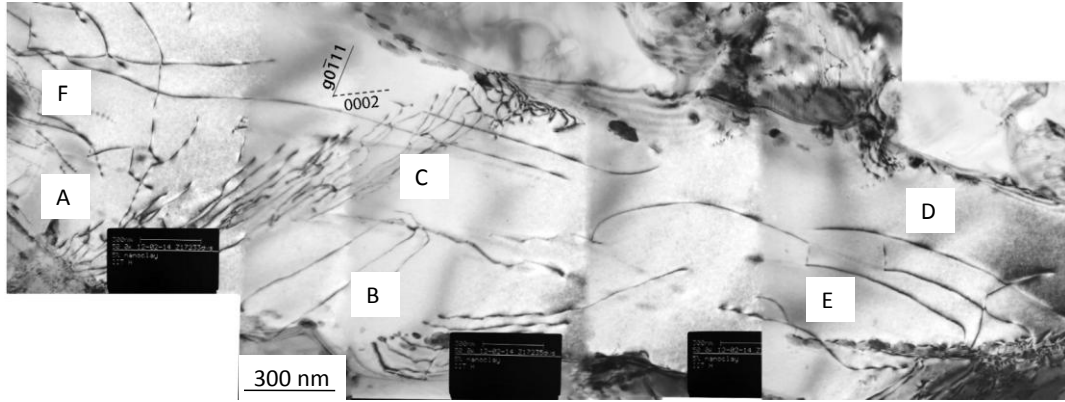


Fig. 4.32 Dislocation substructure taken with $g = 0\bar{1}11$ in two beam orientation in Timetal 834 tensile tested at room temperature.

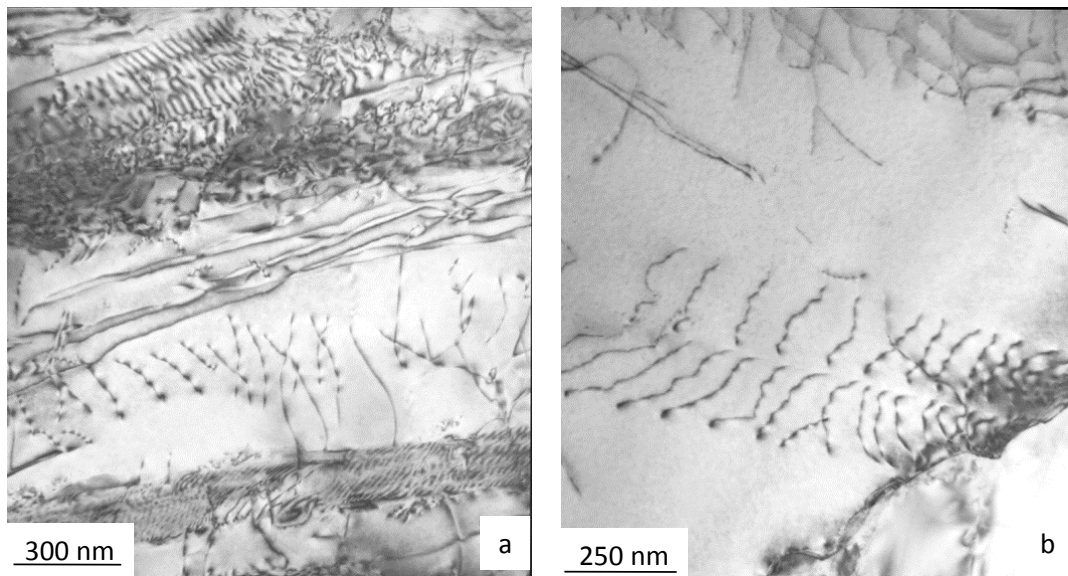


Fig. 4.33 Dislocation substructure taken with multi beam orientation showing dislocation pile-ups in Timetal 834 tensile tested at room temperature.

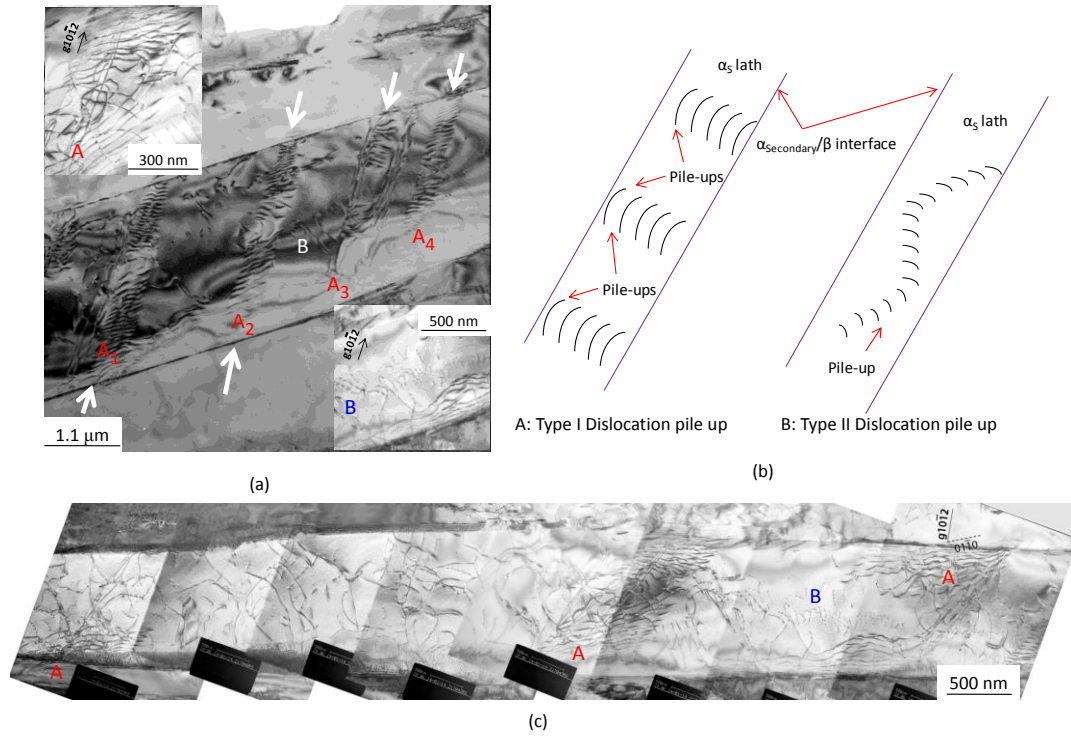


Fig. 4.34 (a) Dislocation substructure in Timetal 834 tensile tested at 450°C showing two types of dislocation pile-ups (Type I is indicated by A and type II is indicated by B) as shown in insets. Two types of dislocation pile ups are shown schematically in (b) and with high magnification micrographs in (c).

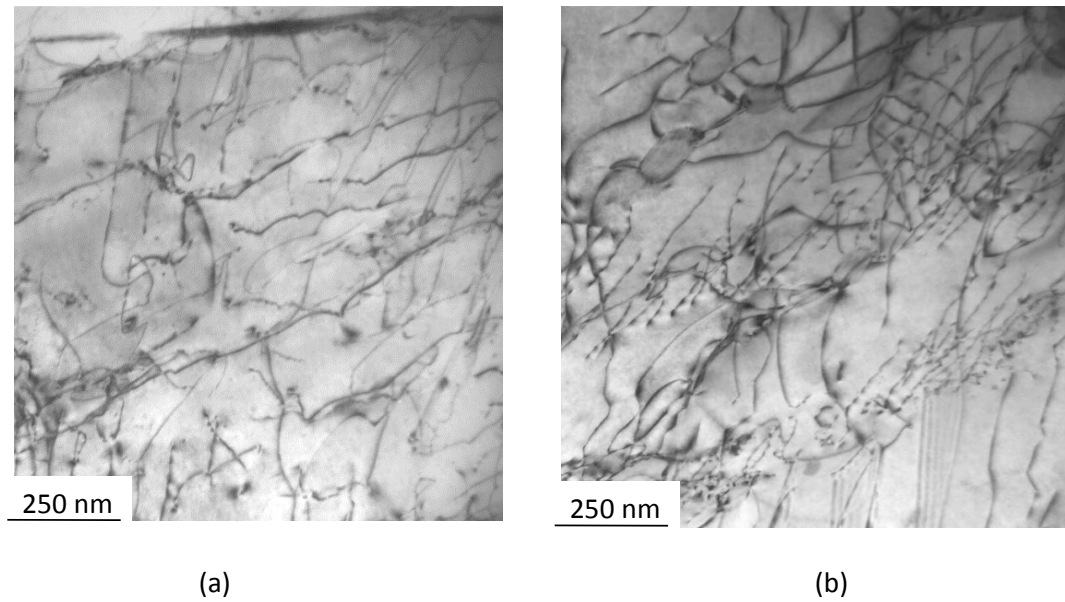


Fig. 4.35 (a) Dislocation substructure in Timetal 834 tensile tested up to 0.2% plastic strain at 450°C showing (a) pinned dislocation segments and (b) random tangles of dislocations.

The deformation substructures of alloy 834 without Si at room temperature are shown in Figs. 4.36a-d. Dislocation pile ups within α laths (Fig. 4.36a-b), dislocation tangles (Fig. 4.36c) and cusped dislocations (Fig. 4.36d) can be seen in these images. The deformation substructures of alloy 834 without Si at 450°C are shown in Figs. 4.37 and 4.38. Dislocation tangles (Fig. 4.37a), sub-boundaries (Fig. 4.37b-c), isolated dislocations (Fig. 4.37b) and long curved dislocation segments (Fig. 4.37d) could be seen in these figures. Fig. 4.38 shows the dislocation substructure taken near the α lath boundary. Since the micrograph as shown in Fig. 4.38a is taken with imaging reflection of (0002), these dislocations could be either 'c' type or 'c+a' type dislocations. When the foil is tilted to $g = 01\bar{1}1$, curved dislocations in other direction appears on top of the 'c' character dislocations (Fig. 4.38b). The curved dislocations are invisible in $g=0002$ reflection as shown schematically in Fig. 4.38c and hence could be of 'a' type dislocations.

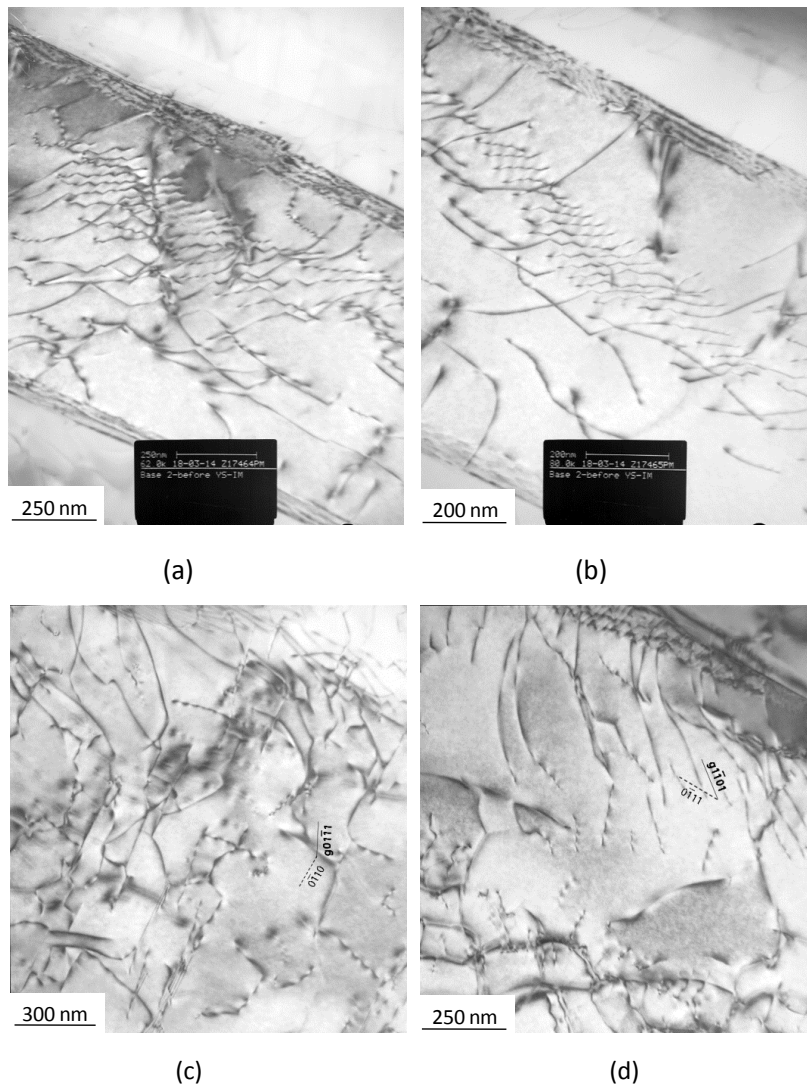


Fig. 4.36 Dislocation substructure in alloy 834 without Si tensile tested up to 0.2% plastic strain at room temperature showing (a-b) dislocation pile – ups (c) dislocation tangles and (d) cusped dislocations.

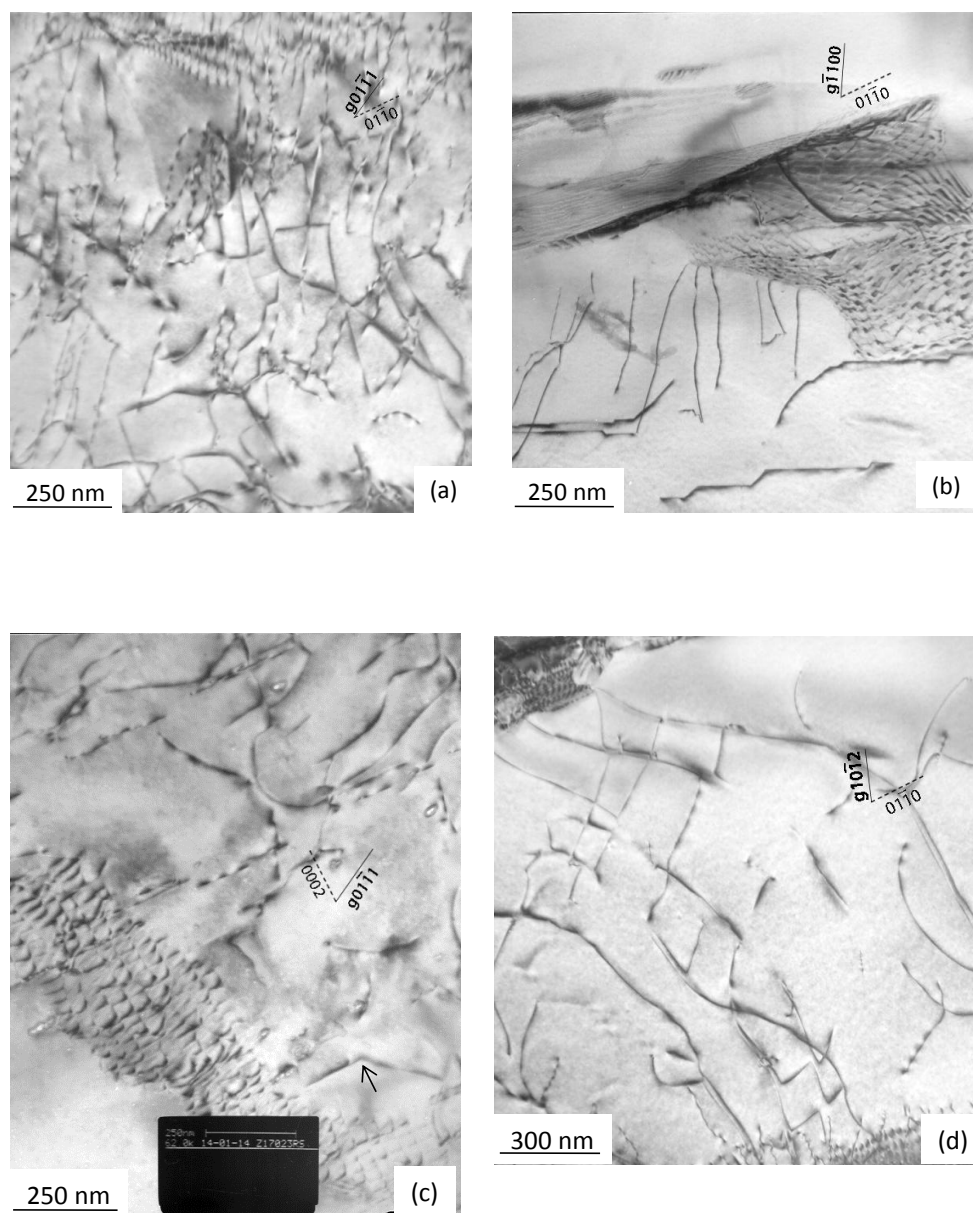


Fig. 4.37 Dislocation substructure in alloy 834 without Si tensile tested up to 0.2% plastic strain at 450°C showing (a) dislocation tangles (b-c) sub-boundaries and isolated dislocations and (d) long curved dislocations.

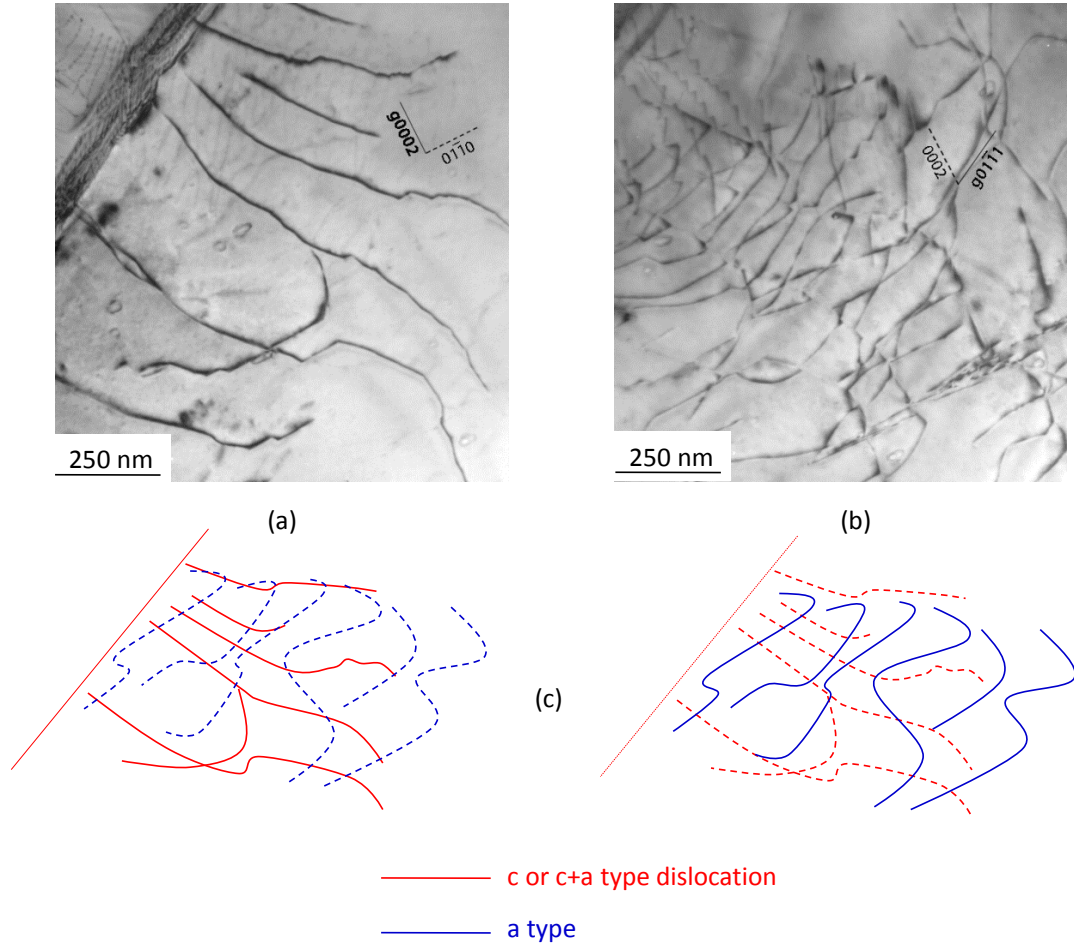


Fig. 4.38 Dislocation substructure in alloy 834 without Si tensile tested up to 0.2% plastic strain at 450°C showing (a) relatively straight dislocations with $g = 0002$ and (b) curved dislocations with $g = 01\bar{1}1$. Visibility/invisibility of these dislocations is shown schematically in (c).

4.3.4 Tensile Fracture Behavior

The SEM fractographs of the fracture surfaces at 300, 400, 450 and 500°C at 10^{-5} s⁻¹ and at the lowest and highest strain rates of both Timetal 834 and alloy 834 without Si are shown in Figs. 4.39-48. The macrograph of the fractured surface at a low magnification of 20X and the high magnification image of the central region are shown in these figures.

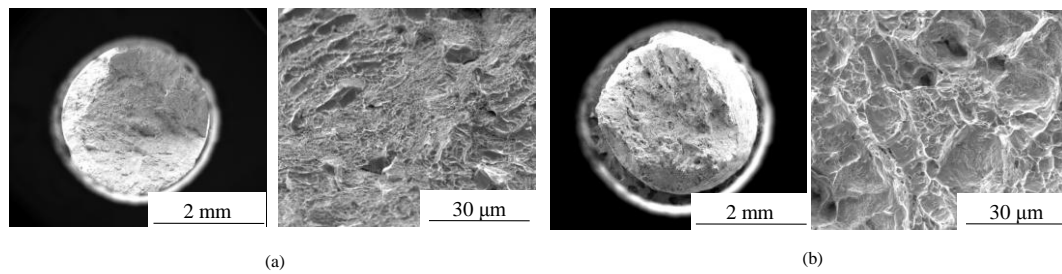


Fig. 4.39 Low and high magnification SEM fractographs of (a) Timetal 834 and (b) alloy 834 without Si at 300°C at 10^{-5} s⁻¹.

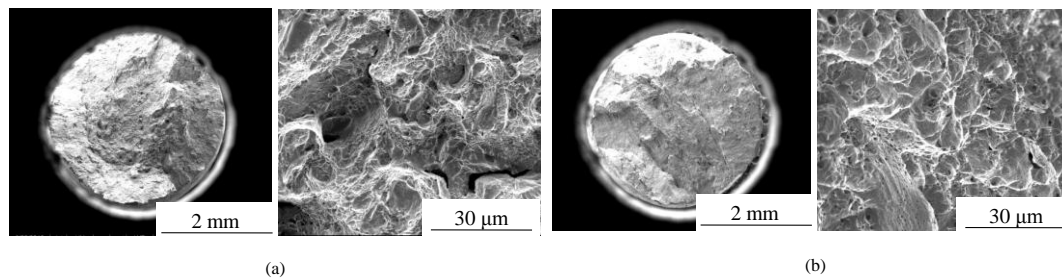


Fig. 4.40 Low and high magnification SEM fractographs of (a) Timetal 834 and (b) alloy 834 without Si at 400°C at 10^{-5} s⁻¹.

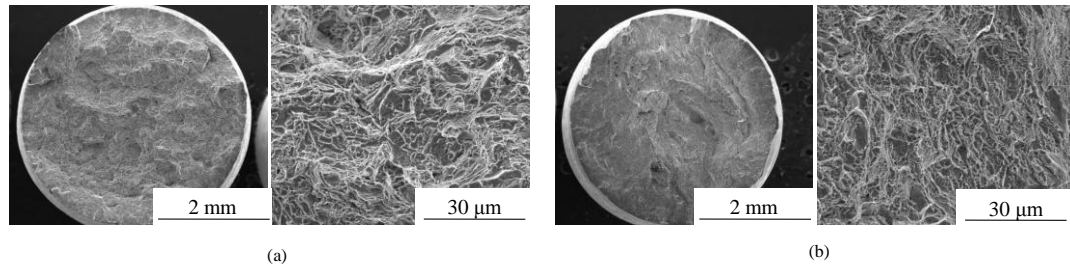


Fig. 4.41 Low and high magnification SEM fractographs of (a) Timetal 834 and (b) alloy 834 without Si at 450°C at 10^{-5} s^{-1} .

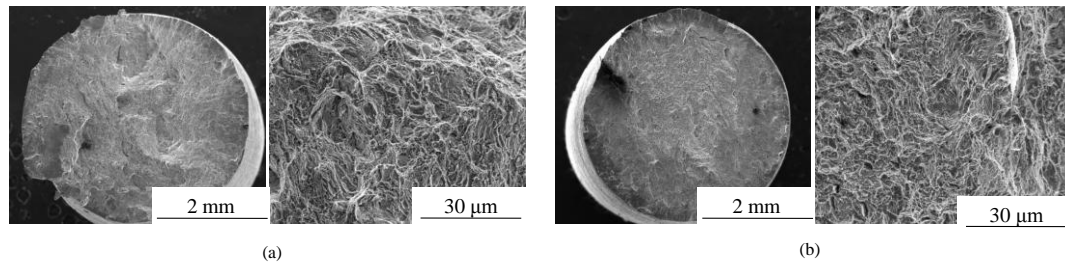


Fig. 4.42 Low and high magnification SEM fractographs of (a) Timetal 834 and (b) alloy 834 without Si at 500°C at 10^{-5} s^{-1} .

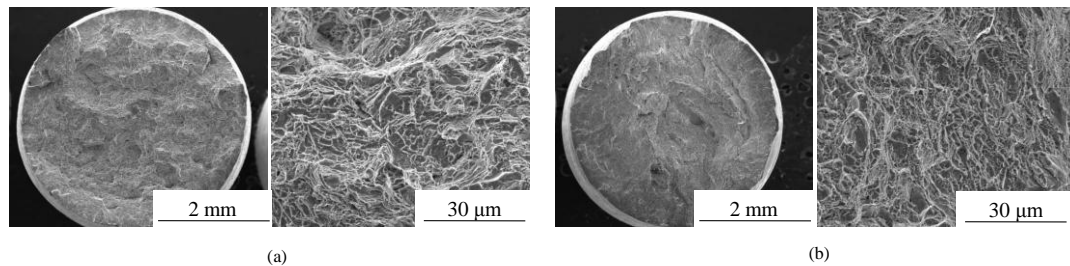


Fig. 4.43 Low and high magnification SEM fractographs of Timetal 834 at (a) lowest and (b) highest strain rates at 300°C.

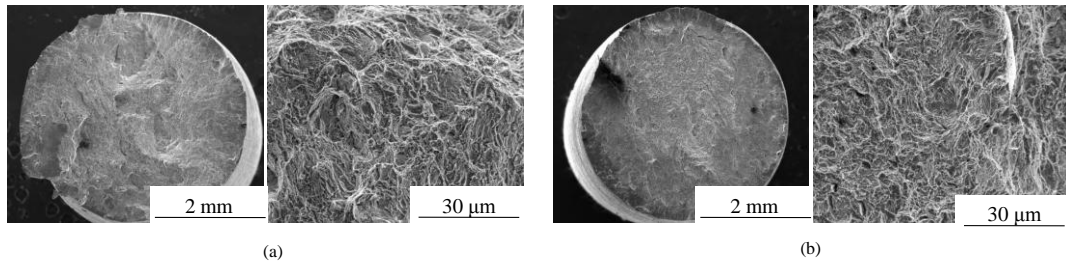


Fig. 4.44 Low and high magnification SEM fractographs of alloy 834 without Si at (a) lowest and (b) highest strain rates at 300°C.

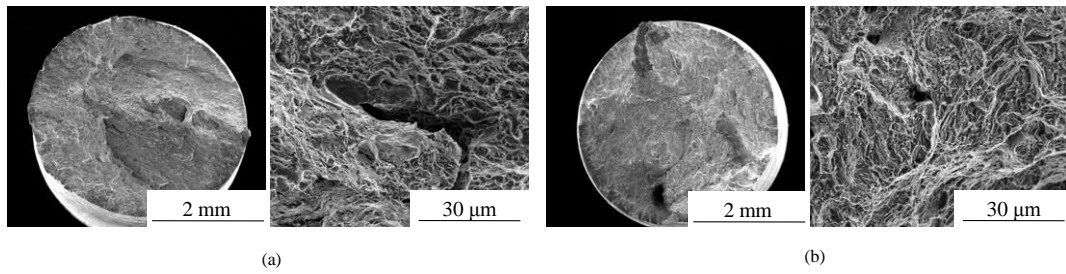


Fig. 4.45 Low and high magnification SEM fractographs of Timetal 834 at (a) lowest and (b) highest strain rates at 350°C.

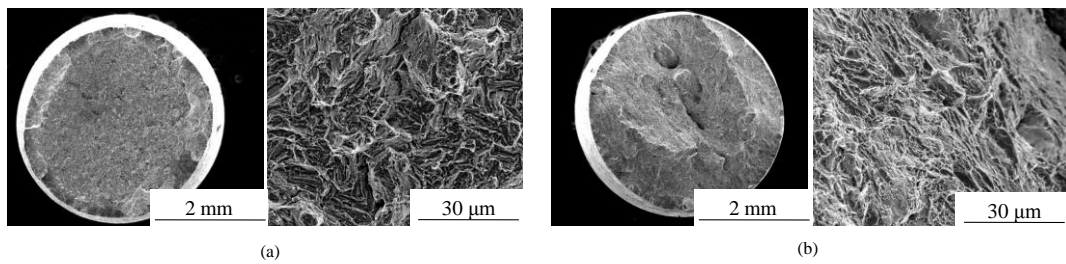


Fig. 4.46 Low and high magnification SEM fractographs of alloy 834 without Si at (a) lowest and (b) highest strain rates at 350°C.

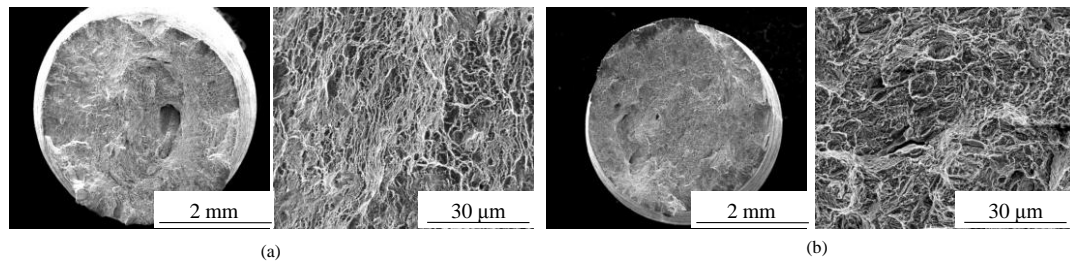


Fig. 4.47 Low and high magnification SEM fractographs of Timetal 834 at (a) lowest and (b) highest strain rates at 450°C.

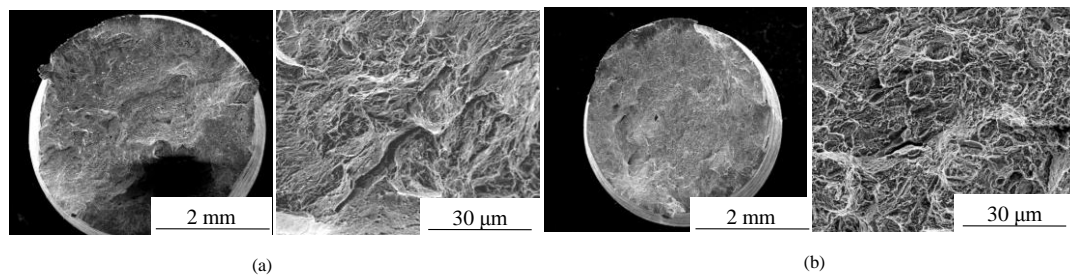


Fig. 4.48 Low and high magnification SEM fractographs of alloy 834 without Si at (a) lowest and (b) highest strain rates at 450°C.

It is evident from these figures that fracture surface in these alloy consists of quasi-cleavage facets as well as dimples. The quasi-cleavage facets are comparable in size to primary α grains. There is also no significant difference in the fracture features for the specimens with the highest and lowest strain rates (Figs. 4.43 – 4.49). The SEM fractographs of the fracture surfaces at 600°C at the highest strain rate for both the alloys are shown in Fig. 4.49. While quasi-cleavage facets could not be observed in these surfaces, it consists of only dimples. It can be inferred,

qualitatively, that the size of dimples are finer in alloy 834 without Si as compared to Timetal 834.

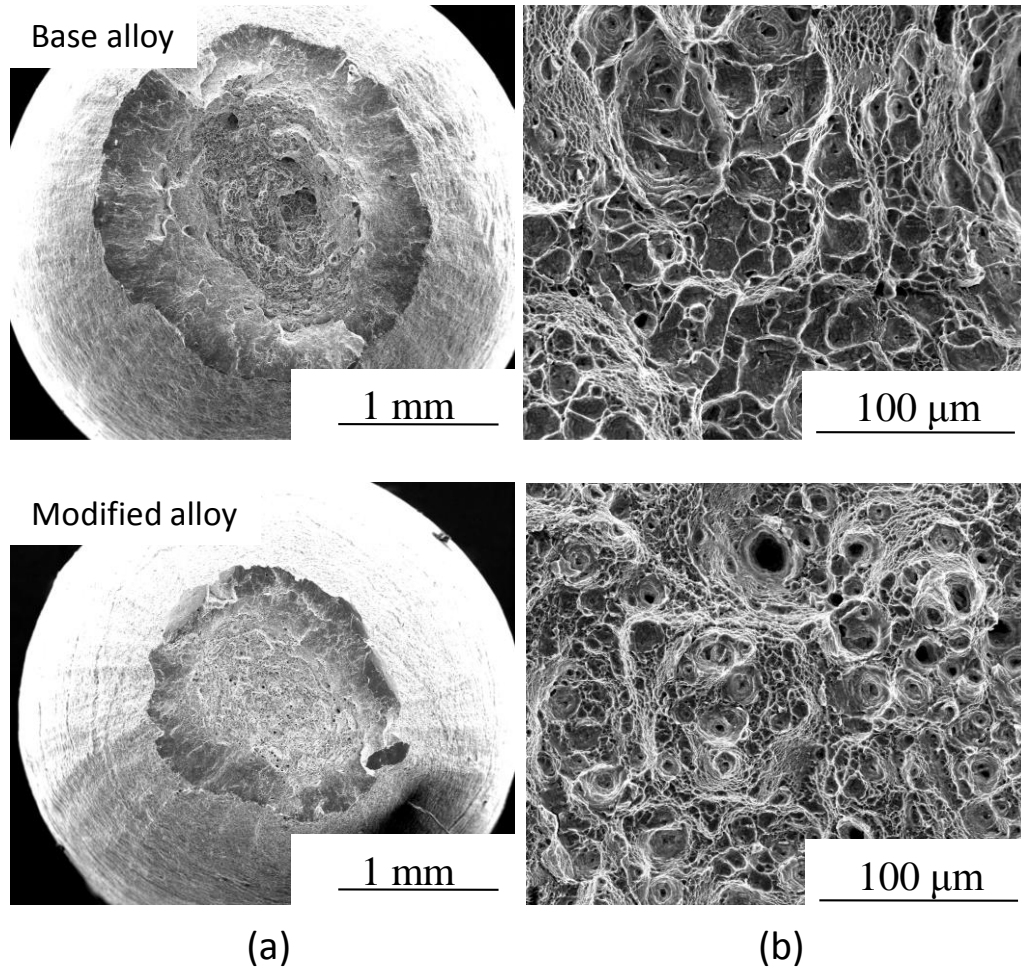


Fig. 4.49 SEM fractographs showing (a) entire fracture surface (20 X) and (b) central region (500 x) of base and modified alloy at 600 °C at strain rate of 10^{-3} s^{-1} .

4.4 Discussion

It is clear in this study that the tensile test parameters viz., temperature and strain rate strongly influences the tensile properties viz., 0.2% YS, UTS, % total elongation and strain hardening exponent. The manifestation of serrations in the flow curve (Figs. 4.4 and 4.5), a plateau in the variation of strength values (0.2% YS and UTS, Fig. 4.10a and Fig. 4.12a), a local minimum and maximum in the variation of ductility (Fig. 4.10b and Fig. 4.12b) and n (Fig. 4.11b and Fig. 4.12c), respectively, and negative strain rate sensitivity (4.14) confirms the occurrence of dynamic strain aging in both the alloys [Rodriguez 1984, Robinson and Shaw 1994].

While DSA is a phenomenon which involves the interaction of mobile dislocation segments and diffusing solute elements in a specific combination of strain rate and temperature [Reed-Hill and Abbaschian 2003], it is quite a challenging task to identify the solute element (s) interacting with the mobile dislocation segments. In the present study, attempt has been made to identify the solute element (s) using an indirect method i.e. calculation of apparent activation energy from tensile stress-strain data and a direct method viz., elemental mapping of a lightly deformed tensile sample in atomistic scale around the dislocations. These approaches are discussed below. Furthermore, a mechanism of DSA in this alloy has been suggested in light of the serrated flow.

4.4.1 Determination of Activation Energy for the Occurrence of DSA

Researchers have reported various methods to determine the activation energy in order to understand the underlying mechanisms for the tensile stress – strain data [McCormick 1972, Pink and Grinberg 1982, Valson Rodriguez 2001]. As discussed in section 2.2.1.4 of chapter II (literature survey), activation energy can be determined using three methods i.e. *McCormick*, *Intercept* and *Stress-Drop* methods. The first two methods rests on the determination of critical true plastic strain (ϵ_c) from the true stress – true plastic strain plots, whereas, the last method needs the input of magnitude of serrations from the flow curve. In the present study, the strain corresponding to the peak of first serration (depending on the type of serrations) is considered as the ϵ_c .

The variation of ϵ_c with strain rates at various temperatures for both the alloys is shown in Figs. 4.50a-b. Negative slope at 450°C (Fig. 4.50a) shows that the Timetal 834 alloy exhibits inverse PLC effect between strain rates of 10^{-2} and 10^{-4} s^{-1} .

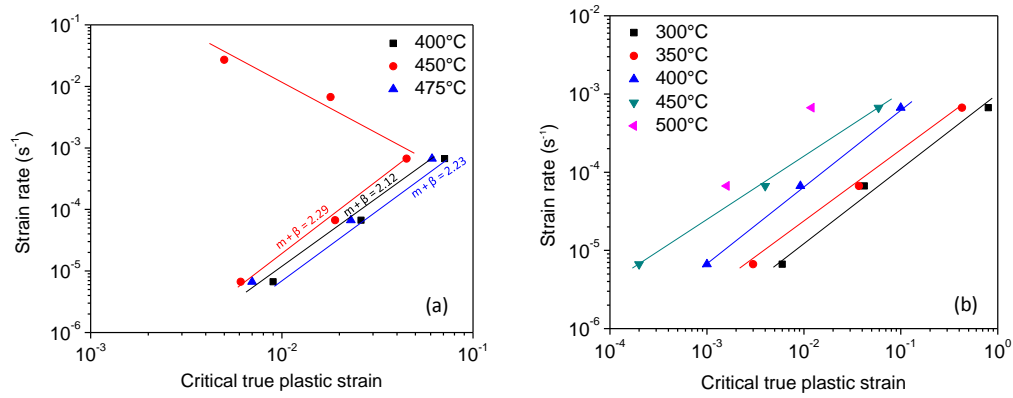


Fig. 4.50 Variation of critical true plastic strain with strain rate for the onset of serrations in (a) Timetal 834 and (b) alloy 834 without Si.

In this plot, in order to have three data points to confirm the negative slope, an additional tensile test has been carried out at the strain rate of 10^{-2} s $^{-1}$ at 450°C. It is clear in this figure that Timetal 834 alloy exhibits inverse as well as normal PLC effect [Brechet and Estrin 1995] within the regime of temperature and strain rate studied. However, the alloy 834 without Si exhibits normal PLC effect (Fig. 4.50b) within the regime of temperature and strain rate studied. While the exponent $m + \beta$ as determined from the positive slopes of Figs. 4.50a-b was found to be in the range of 2.12-2.29 for Timetal 834 alloy, it ranges from 0.86-0.94 for alloy 834 without Si. This further indicates that most likely substitutional solute/solutes might be responsible for DSA in Timetal 834 alloy and interstitial solute/solutes in alloy 834 without Si.

Strain rate vs. critical true plastic strain and critical true plastic strain vs. $1/T$ plots for the determination of activation energy as per *McCormick model* [McCormick 1972] for Timetal 834 alloy are shown in Figs. 4.51a and 4.51b, respectively.

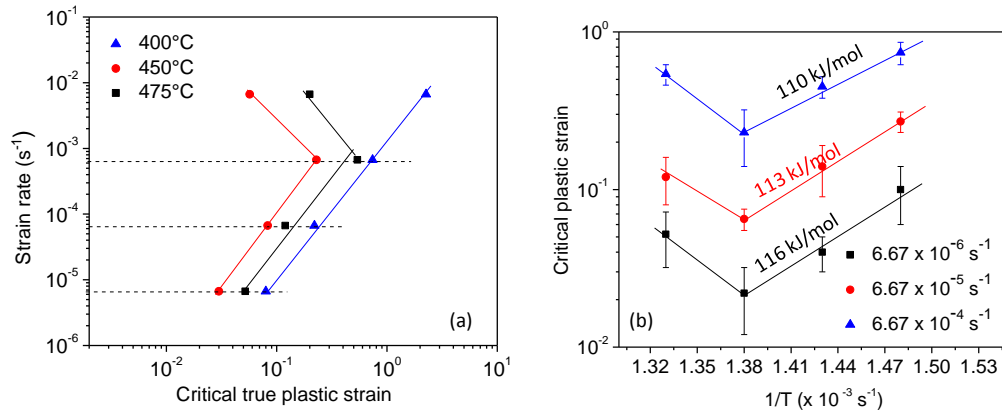


Fig. 4.51 Variation of critical true plastic strain with (a) strain rate and (b) temperature for the determination of activation energy by McCormick's method for Timetal 834.

The activation energies were determined by applying these values to the plots of $\ln \varepsilon_c$ vs. $1/T$ i.e., $Q = \text{slope of } \ln \varepsilon_c \text{ vs. } 1/RT \times (m + \beta)$. This method yields activation energies in the range 110 to 116 kJ/mole. Similarly, the plots of strain rate vs. critical true plastic strain and strain rate vs. $1/T$ as per the *intercept method* for Timetal 834 alloy are shown in Figs. 4.52a and b, respectively. Activation energy thus calculated from this method ranges from 101 to 111 kJ/mole. As per *stress drop method*, the plots of magnitude of serrations ($\Delta\sigma$) vs. strain rate and

strain rate vs. $1/T$ are shown in Figs. 4.53a and b, respectively. This method yields activation energy for serrated flow in the range 77 to 90 kJ/mol. While the activation energy determined using *McCormick and Intercept methods* are in close agreement, the *stress drop method* results in lower value of activation energy.

The activation energy for diffusion of all the solute elements in α -Titanium is listed in Table 4.6 [Doner and Conrad 1973, Conrad 1981]. The experimentally determined activation energy (101 – 116 kJ/mol) matched with the activation energy of Si (105.1kJ/mol). This further indicates that most likely Silicon is responsible for DSA effects in Timetal 834. As $m + \beta$ values (Fig. 4.50a) suggest that substitutional element is element is responsible for DSA effects, it is likely that Si, 21% smaller in size as compared to Titanium [Brandes and Brook 1998], forms the locking atmosphere for the occurrence of serrations. While Si remains in solid solution till about 450°C [Neal and Fox 1993], the occurrence of inverse PLC effect at 450°C could be due to the precipitation of silicides beyond this temperature. This aspect needs a separate detailed study to establish its validity.

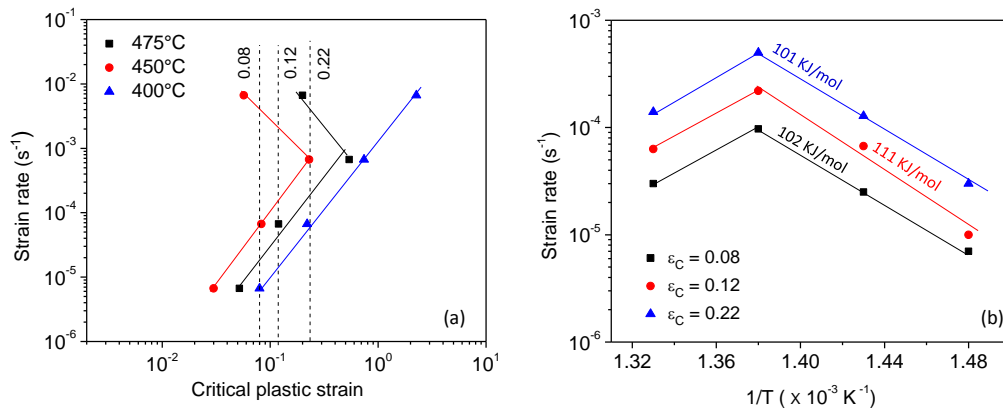


Fig. 4.52 Variation of critical true plastic strain with (a) strain rate and (b) temperature for the determination of activation energy by intercept method for Timetal 834.

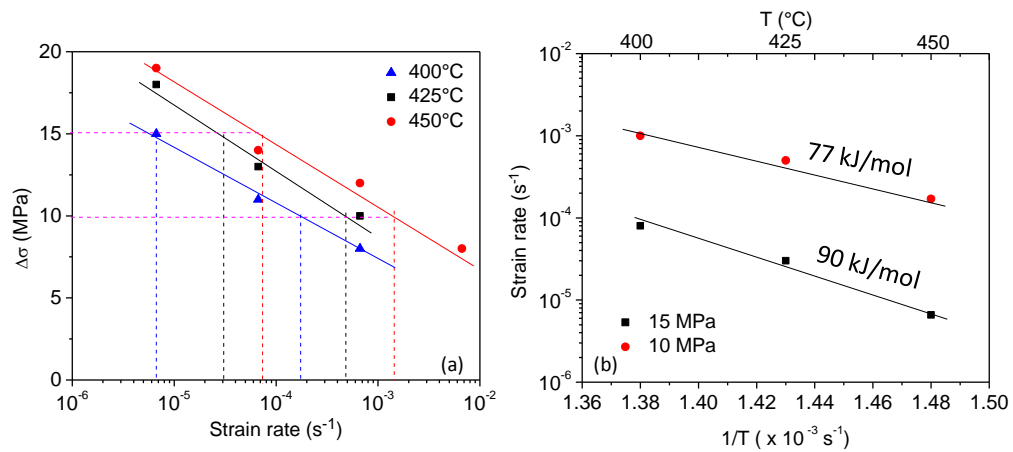


Fig. 4.53 Variation of (a) stress increments with strain rate and (b) strain rate with temperature using intercepts from (a) at various stress increments for Timetal 834.

Table 4.6: Activation energy of various elements in α -Titanium [Doner and Conrad 1973, Conrad 1981].

Elements	Activation Energy (kJ/mol)
<i>Substitutional</i>	
Al	156.4
Mo	180.0
Si	105.1
Nb	164.5
Zr	148.2
Sn	132.1
Self-diffusion (Ti)	192.1
<i>Interstitial</i>	
C	182.1
N	228.4
O	200.0

Similar to that of Timetal 834 alloy, the plots for the determination of activation energy for alloy 834 without Si using *McCormick and stress drop method* are shown in Figs. 4.54 and 4.55, respectively. Activation energy thus determined from *McCormick and stress drop methods* are found to be 188 kJ/mol and 132 kJ/mol, respectively. While the activation energy 188 kJ/mol matches with the diffusion of Carbon (C), the value 132 kJ/mol matches with the diffusion of Tin (Sn). As the $m + \beta$ values (Fig. 4.50b) suggest that an interstitial element is responsible for DSA effects in alloy 834 without Si, it is likely that C which is an interstitial element is causing DSA effects in this alloy.

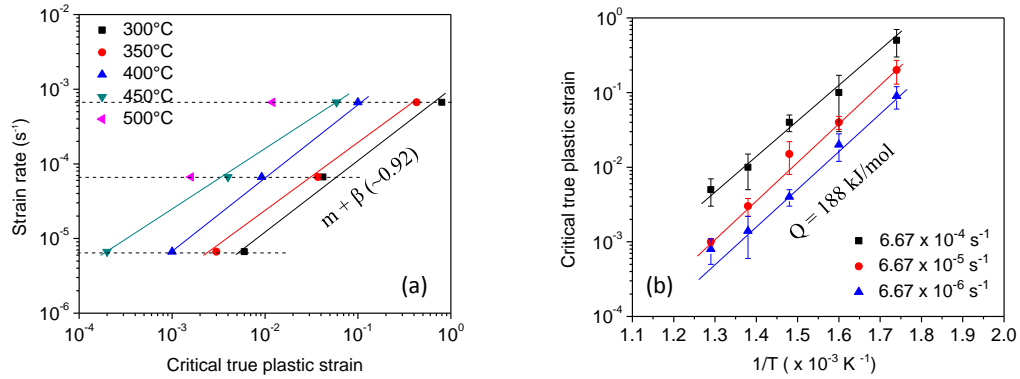


Fig. 4.54 Plots of (a) log (strain rate) vs log (critical plastic strain) and (b) log (critical plastic strain) vs. reciprocal temperature for the determination of activation energy for alloy 834 without Si.

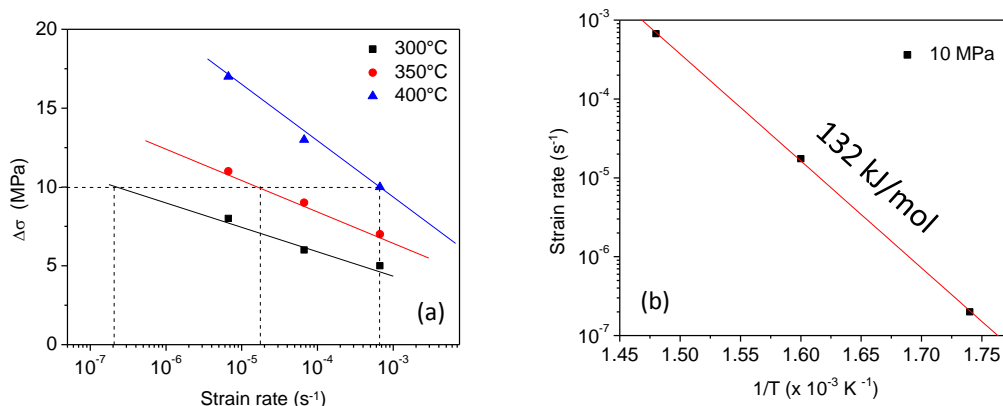


Fig. 4.55 Variation of (a) stress increments with strain rate and (b) strain rate with temperature using intercepts from (a) at various stress increments for alloy 834 without Si.

Though the above mentioned approaches as an indirect method were used to identify the most likely solute/solutes for causing DSA effects, it needs to be viewed in light of the TEM observations made in this study which is discussed below. In order to understand the role of interstitial solute/solutes, this analysis was restricted to only alloy 834 without Si.

4.4.2 Identification of Solute Atmosphere around Dislocations in Alloy 834 without Si

In order to identify the possible element segregating to dislocations, samples prepared from tensile tested specimens deformed to 0.2% plastic strain at 300°C and 450°C were examined in electron filtered transmission electron

microscopy (EFTEM). EFTEM elemental mapping has been attempted in the α laths of transformed β grains and not inside α_P grains for the following reasons: (1) A large number of TEM observations in earlier reports have confirmed that under tensile [Lütjering and Williams 2007], compression [Wang et al. 2006] and fatigue [Baxter et al. 1996, Prasad et al. 2008] deformation, dislocation activity inside α_P grains is primarily favoured by the greater ordering of Ti_3Al particles. Hence it is expected that the influence of interstitial solutes on dislocation is negligible that it can be ignored. (2) Since this alloy does not have Si, the mechanism of pinning of dislocations by silicides which mainly forms along the α lath boundaries can be ruled out. In other words, the dislocation dynamics in transformed β regions are controlled by segregation of solutes to dislocations. The transformed β region constitute more than 85 % volume fraction of the material. Attempts were made to observe the segregation of interstitial solute elements near the anchored dislocations or pile ups which are the typical representative regions for the occurrence of DSA [Bhanu Sanakara Rao et al. 1996, Shankar et al. 2004].

Figs. 4.56 and 4.57 shows the EFTEM elemental mapping in specimens tensile tested to 0.2% plastic strain at 300°C and 450°C, respectively. It can be clearly noticed from these figures that enrichment of C and N only has occurred at dislocations and lath boundaries while no enrichment of oxygen to dislocations or lath boundaries could be seen. In fact, regions enriched with C and N is depleted of oxygen. In specimen tested at 300°C (Fig. 4.56b and e) only carbon enrichment is

seen along the dislocation pile-up (as marked by arrows in Fig. 4.56e) while lath boundaries show enrichment of both C and N.

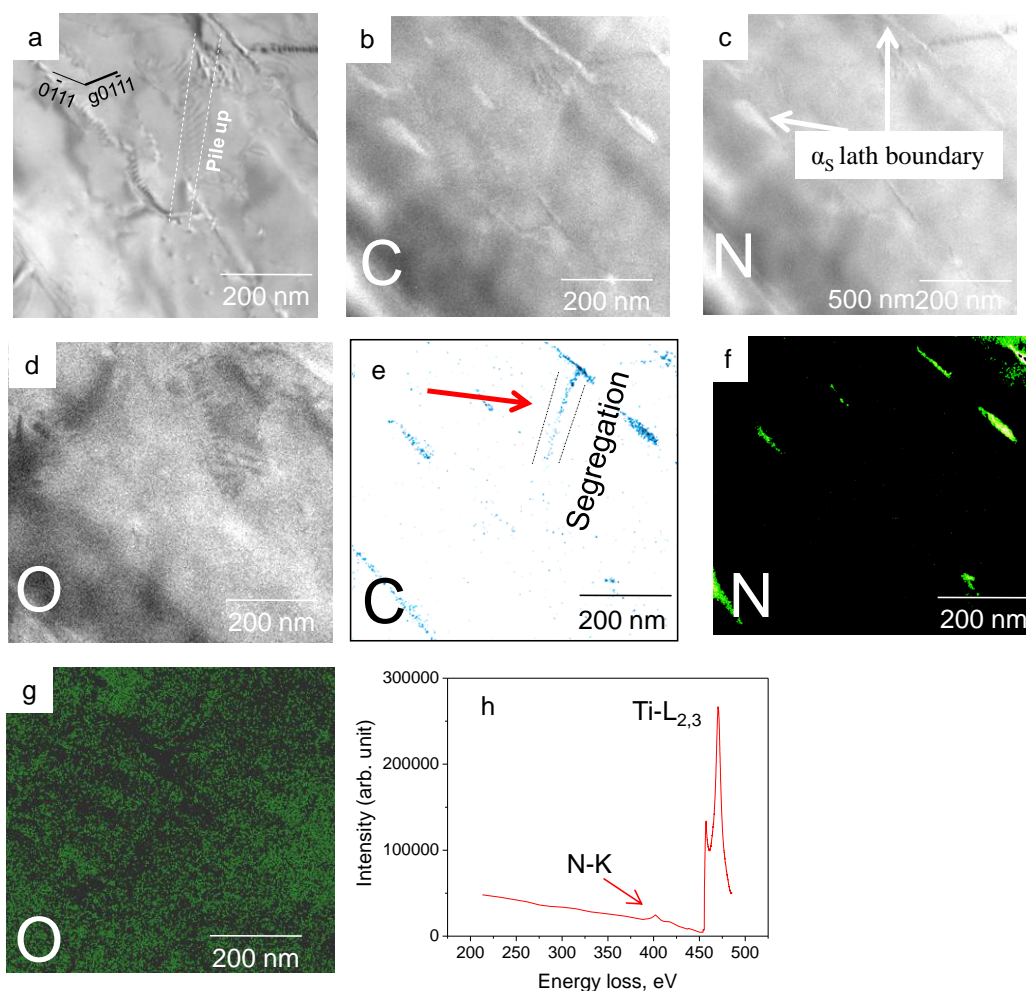


Fig. 4.56 (a) Zero loss image, (b and e) Carbon, (c and f) Nitrogen and (d and g) Oxygen elemental maps taken along $[2\bar{1}\bar{1}0]$ zone axis of 300°C tensile interrupted sample using EFTEM. Electron energy loss spectrum (EELS) of Fig. 4.56e is shown in Fig. 4.56h showing N and Ti edges.

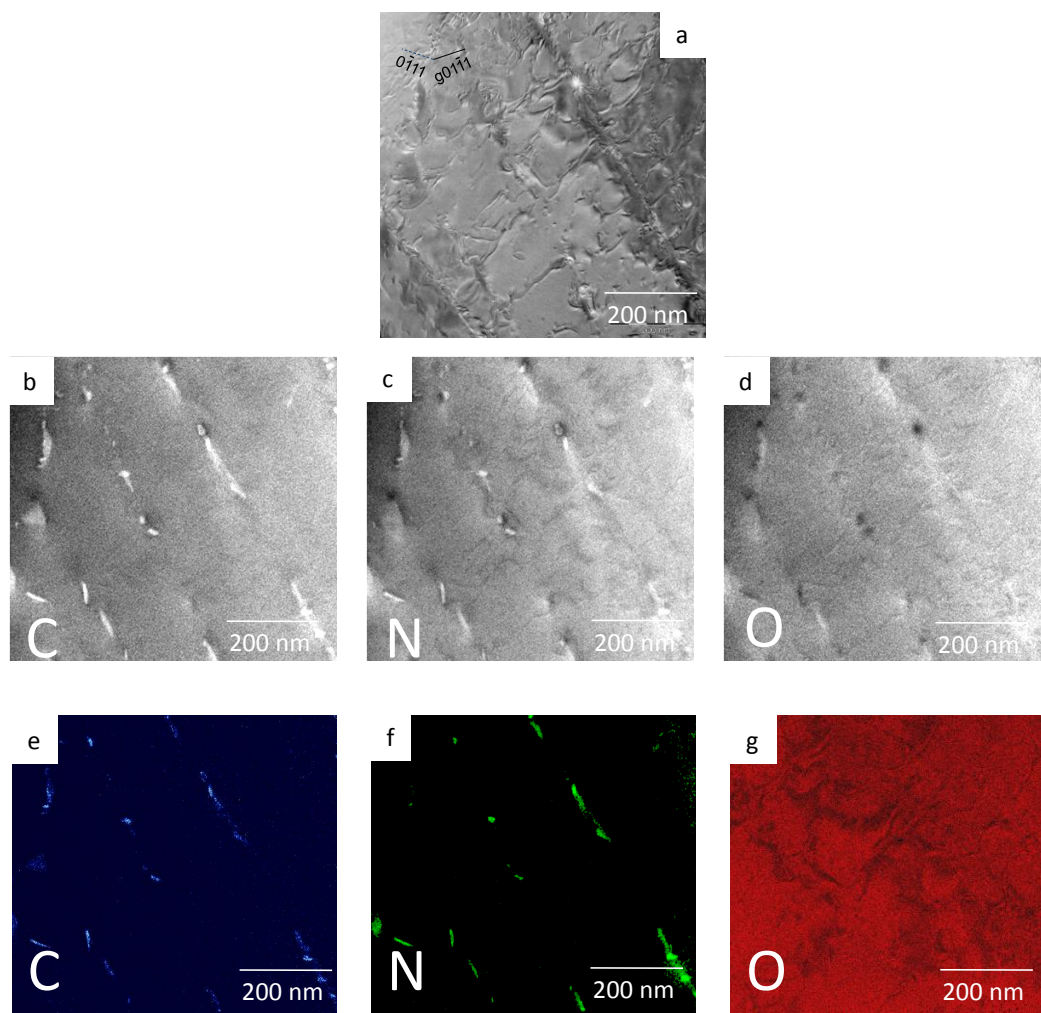


Fig. 4.57 (a) Zero loss image (b and e) Carbon (c and f) Nitrogen and (d and g) Oxygen elemental maps taken along $[2\bar{1}\bar{1}0]$ zone axis of 450°C tensile interrupted sample using EFTEM of alloy 834 without Si.

Since the N content is very low (0.006 at.%) as compared to C (0.27 at.%) and O (0.30 at.%), the electron energy loss spectrum showing a weak N peak is shown in Fig. 4.56h. This figure is shown to confirm the fact that this technique is suitable for mapping even low concentration of interstitial solutes. In 450°C tested sample whichever region shows carbon enrichment, the same region reveals high nitrogen enrichment as well (Fig. 4.57). In order to find out whether the observed segregation is due to static strain ageing effect, EFTEM elemental mapping of room temperature tensile sample deformed to 0.2% plastic strain was carried out at different regions. Representative micrographs are shown in Fig. 4.58. These images clearly reveal that no segregation of interstitial elements like C, N and O to dislocations or lath boundaries has occurred. This observation is also supported by the fact that no upper and lower yield point corresponding to static strain ageing was noticed in the tensile stress strain plot. In fact, upper and lower yield points in commercial Ti alloys tested at different temperatures have already been reported [Turner and Roberts 1968]. They have attributed it to rather very weak DSA (or in other words, strong SSA). Hence it could be concluded that the observed segregation of carbon and nitrogen to lath boundary consisting of dislocation networks and dislocation arrays within the lath is due to dynamic strain ageing effect and not due to static strain ageing. In this context, a recently proposed mechanism [Soare and Curtin 2008] is based on the fact that the solute atmosphere around mobile dislocation develops by pipe diffusion from the forest dislocations pinning it.

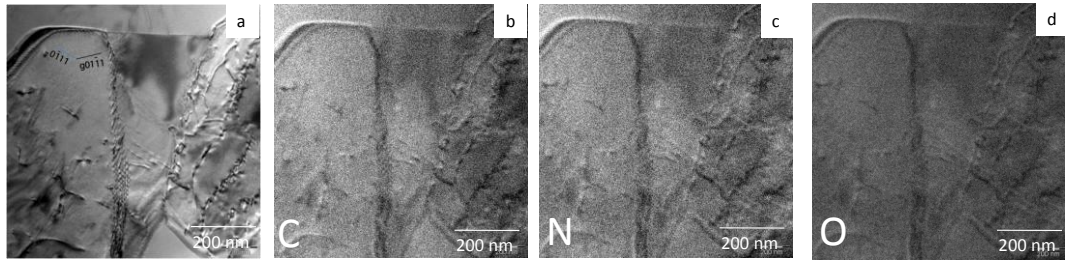


Fig. 4.58 (a) Zero loss image taken in $[2-1-10]$ zone axis orientation from a specimen tensile tested (interrupted test) carried out at ambient temperature: (b) Carbon, (c) Nitrogen and (d) Oxygen elemental maps of alloy 834 without Si. Symbol of elements are indicated in the respective micrographs.

According to their model, the solute atmosphere around forest dislocations occurs till they are saturated by lattice diffusion of the solutes. This process is occurring continuously. The serrations appear because of the competition between the applied stress to break this atmosphere and the increase in strength due to increase in solute atmosphere concentration. The immobile dislocation network at the lath boundaries enriched with interstitial solute atmosphere of carbon and nitrogen is doing the job of forest dislocations saturated with solutes.

4.4.3 Mechanism of Solute Segregation at Different Test Temperatures

It has been mentioned earlier that from the activation energy value determined from $\ln \varepsilon_C$ vs. $1/T$ plot (Fig. 4.54), the element responsible for DSA effect during testing in this alloy could be diffusion of carbon, nitrogen or oxygen simultaneously or independently to dislocations. The activation energy values for A type serrations matches with the activation energy of carbon in α -Ti. It should also be pointed out here that the activation energy for diffusion of substitutional elements used as alloying elements in this alloy (Table 4.6) is lower than the activation energy determined from $\ln \varepsilon_C$ vs. $1/T$ plot except in the case of Mo. The value of diffusivity for interstitial solutes in Ti at 300°C and 450°C are given in Table 4.7.

Table 4.7: Diffusivity of interstitial solute elements in α -Titanium.

Elements	Diffusivity* (m^2s^{-1})	
	300°C	450°C
Carbon	1.31×10^{-22}	3.61×10^{-19}
Nitrogen	4.78×10^{-26}	9.75×10^{-22}
Oxygen	2.63×10^{-25}	1.61×10^{-21}

* $D=D_0e^{(-Q/RT)}$, where D is diffusivity, D_0 is diffusion coefficient, Q is activation energy, R is gas constant ($8.314 \text{ J mol}^{-1} \text{ K}^{-1}$) and T is temperature in Kelvin. D_0 of C, N, and O is $5.10 \times 10^{-4} \text{ m}^2 \text{ s}^{-1}$, $2.9 \times 10^{-5} \text{ m}^2 \text{ s}^{-1}$ and $4.5 \times 10^{-5} \text{ m}^2 \text{ s}^{-1}$ [Conrad 1981].

From this table it is clear that C has higher diffusivity at 300°C compared to nitrogen and hence carbon can segregate to defects faster than nitrogen. Moreover, this value of diffusivity might be sufficient for carbon atoms to diffuse to mobile dislocations at 300°C than nitrogen at the strain rate employed. Hence it is not surprising that the measured activation energy value for A type serrations (seen generally at lower temperatures) matched with activation energy for carbon diffusion in α -Ti. This is also incidentally reflected in the observation of carbon and not nitrogen enrichment on the pile up where dislocations are mobile (and the time for solute atmosphere build up is short) than on lath boundaries where dislocations are immobile. Sufficient time appears to be available for carbon and nitrogen to segregate to this immobile structure (lath boundary) in sufficient quantity for them to be imaged clearly (Figs. 4.56b and e). The enrichment of both carbon and nitrogen to lath boundaries as well as all mobile dislocations at 450°C test temperatures (Fig. 4.57) is due to higher diffusivity of both carbon and nitrogen which is sufficient for them to segregate to the immobile and mobile dislocations at the strain rate employed in the present work.

The EFTEM observations could also be rationalized on the basis of strain introduced in the hcp lattice by these interstitial solutes. It is pertinent to point out here that the interstitial elements C, N and O have high affinity for titanium. It has been reported that among all interstitial solutes [Conrad 1981], carbon produces the largest strain along c (ϵ_c) as well as in a (ϵ_a) direction of the close packed hexagonal phase. The listed values of ϵ_c and ϵ_a for carbon is 0.136 and 0.049, for

nitrogen is 0.072 and 0.008 and for oxygen is 0.111 and 0.000, respectively [Conrad 1981]. Though the solubility of carbon in α -Ti is only 2% it causes significant volume expansion (0.49 \AA^3 per at.%) as compared to nitrogen (0.18 \AA^3 per at.%) and oxygen (0.13 \AA^3 per at.%). From these values, it is clear that segregation of carbon and nitrogen to dislocations will bring about more reduction in strain energy of lattice compared to oxygen segregation to dislocations. This could possibly be aiding the segregation / diffusion of nitrogen and carbon to dislocations even though the concentration of nitrogen is very small compared to oxygen in the alloy.

4.4.4 Nature of Serrations

In this study, A type serration at lower temperatures, A and C type at intermediate temperatures and C type at higher temperatures were observed in the stress strain plot (Fig. 4.9a). In the literature, A-type serrations are considered as locking serrations, characterized by an abrupt rise followed by a drop to below the general level of stress-strain curve. They occur in the low temperature part of the DSA regime. Type C serrations are manifested by yield drop that occur below the general level of the flow curve and are therefore considered to be due to dislocation unlocking. They occur at higher temperatures and lower strain rates than in the case of A type serrations [Rodriguez 1984]. The observation of these serrations at different test temperatures is rationalized qualitatively in this section on the basis of the extent of strain introduced in the lattice by different interstitial

solutes, namely, carbon, nitrogen and oxygen and their influence on enhancing the mobility of solutes at lower temperatures. It is well known that strain influences diffusion in the lattice at all temperatures and the manifestation of it would be that the mobility of solutes is enhanced to lower temperatures than what is observed when only the concentration gradient is considered [Shewmon 1963]. This is true for both interstitial as well as substitutional diffusion. Of the three elements, C is reported to generate maximum strain in the lattice, nitrogen next and O least in this order [Conrad 1981]. On the basis of this knowledge, one should expect the carbon atoms to become mobile at lower temperatures compared to nitrogen and oxygen. However, oxygen should become mobile only at relatively higher temperature when the thermal activation energies are nearly the same. On this basis, one could expect carbon atmosphere at lower temperatures while at intermediate temperatures in addition to carbon, nitrogen should also form atmosphere depending on their mobility. At higher temperatures where all the three interstitial solutes should in principle form atmosphere around dislocation core and the experimental observation is governed by what all elements actually are able to diffuse to dislocations depending on their relative mobility and also on the sensitivity of the technique used to detect them. The present experimental observation of carbon at lower temperatures (300°C and 350°C) and carbon as well as nitrogen at elevated temperatures (400°C to 500°C) conforms to this expectation.

The nature of serrations (A or C type) depend upon the relative competition between the stress necessary to unpin the dislocations from the atmosphere forming around them and the rate at which applied stress is increasing to overcome this pinning stress and make the dislocation mobile again. It is well known that as the deformation progresses, dislocation-dislocation interaction leads to generation of vacancies. At very low temperatures, these vacancies are immobile and the stress response depends only on the competition between the stress necessary to unpin the dislocation (which in turn depends on the rate of formation of solute atmosphere) and the rate at which the applied stress increases. In this scenario, the stress response will show a strong rise up to the point where the dislocation remains unpinned and it drops to a low value after unpinning since the stress necessary now to move the unpinned dislocation is relatively small. This will result in A type of serration in the stress strain plot and our experimental observation at low temperature (300°C and 350°C) matches with this expectation in terms of stress response as well as the type of solute (carbon) forming atmosphere around dislocations. It has been reported earlier in many deformation experiments as well as in radiation damage studies that vacancies generated due to dislocation-dislocation interaction enhances the mobility of solutes to temperatures much lower than $0.5 T_m$ where T_m is the melting temperature of the alloy. Hence it is not unreasonable to assume that at slightly elevated temperatures (400°C to 500°C), the deformation generated vacancies become mobile and they can segregate to compressive side [Dieter 1988] of dislocations and could lead to overall reduction in the stress necessary to unpin the dislocations. The solutes

forming atmosphere around the dislocations are still interstitials which have become mobile (carbon and nitrogen at these temperatures in this alloy). Under such conditions, considerable stress rise is not expected before the dislocations free themselves from the atmosphere and the stress necessary for the freed dislocation to move is small resulting in a large stress drop. This is what is reflected as the C type serrations at slightly elevated temperatures. It is clear from the above discussion that the serrations in this alloy, in spite of their nature (A or C type), are generated by interstitial solute diffusion only. The transition from one type to the other is not expected to be sharp and only a gradual variation is expected as a function of test temperatures. Hence, both A type and C type serrations could appear at transition temperature (400°C to 450°C). The local variation in the dislocation density and hence the non-uniformity of the spatial distribution of dislocation network could be responsible for bringing about some variation in vacancy concentration in the sample spatially and possibly this is responsible for the appearance of both A and C type of serration at some intermediate test temperature (450°C) and only C-type serrations at 400°C. These aspects need a separate detailed consideration to establish their validity and are beyond the scope of this investigation.

4.4.5 Tensile Deformation

In the limited number of TEM micrographs analysed for identifying the types of dislocation and operational slip systems, only basal (Figs. 4.19a, 4.24a,

and 4.28a) and pyramidal slip (Figs. 4.15c, 4.24a and 4.28a) systems observed to be operational in both the alloys. It is noteworthy to mention that activation of these slip systems requires stress level which are considerably higher than that of prismatic plane [Lütjering and Williams 2007], yet prismatic slip plane was not observed in the present study. In this study, it is not clear that what causes the generation of sufficiently high stress level at the α/β interfaces for the activation of basal or pyramidal slip systems. Moreover, the influence of elastic incompatibility stresses at the α/β interfaces due to the different elastic constants of α and β phases is expected to be less in this class of alloy due to the relatively small volume fraction of β phase. In the deformed microstructures, a_1 and a_2 dislocations were occasionally observed near the α/β interfaces, which however they comprise primarily of a_3 dislocations. Because the emission of an a_3 dislocation with $b = 1/3[11\bar{2}0]$ from the α/β interface is equivalent to simultaneous emission of two dislocations with a_1 ($b = 1/3[\bar{2}110]$) and a_2 ($b = 1/3[1\bar{2}10]$) [Lütjering and Williams 2007], emitting a single dislocation of a_3 type rather than two equivalent dislocations by the α/β interface is preferred.

The deformed microstructure of Timetal 834 has been observed primarily for a_3 basal slip (Figs. 4.19a, 4.24a, and 4.28a). As shown in Fig. 4.34, dislocation pile ups of larger length scales are observed near the α/β interface. The curved dislocations (Fig. 4.38b) are bowed in the direction away from the α/β interface, which indicates that they are emitted by the α/β interface. While the relatively close alignment between $a[010]$ direction of β phase and burger vector of a_3

dislocations promotes occasional slip transmission (Fig. 4.27a) [Lütjering and Williams 2007], a_3 direction due to its no closely matched $(a/2) \langle 111 \rangle$ slip direction within the β phase expected to offer difficult slip transmission as seen in Fig. 4.34. Although the type of dislocations as shown in Figs. 4.34 could not be identified, based on their shape and morphology, it is reasonable to consider that these could also be of ' a_3 ' type and α/β interface offers a large barrier to slip transmission. The high value of strain hardening exponent in both the alloys (Fig. 4.11b and Fig. 4.12c) could be attributed to dominance of a_3 slip in Timetal 834 alloy.

The deformed microstructures at room temperature is observed to be consisting of only one slip system i.e. a_3 basal slip in Timetal 834 and a_3 pyramidal slip in alloy 834 without Si. However, activation of additional slip systems is observed at 450°C in both the alloys. This could be attributed to the temperature assisted activation of slip system [Lütjering and Williams 2007]. However, this observation is in contrast with the fact that the ductility decreases with increase in temperature in the serrated flow range. Based on the observations of local clustering of solute atoms and intense dislocation pile-ups, one can speculate that the clusters of solute atoms/solute atmosphere which produces local distortions and hence stress fields which in turn, locally make it difficult for the dislocations to glide in the slip planes. The observation of relatively more segments of dislocations which are cusped or pinned at 450°C supports this hypothesis.

Nevertheless, examination of operational slip systems as shown in Figs. 4.19a, 4.24a, and 4.28a show that Si addition in Timetal 834 favours basal slip.

4.4.6 Activation Volume

In the present investigation, the operational activation volume is determined from the strain rate jump tests using the following equation [Kocks et al. 1975]:

$$\frac{V}{b^3} = MkT \ln \left(\frac{\dot{\epsilon}_2}{\dot{\epsilon}_1} \right) / \Delta\sigma \quad (4.3)$$

Where M is the Taylor factor, k is the Boltzmann's constant, T is the temperature in Kelvin (K), $\Delta\sigma$ is the magnitude of stress increment or decrement during the strain rate jump, and b is the Burgers vector. The magnitude of the Burger vectors as determined from the detailed analysis discussed in section 4.3.3.1 is used in Eqn. (4.3).

The activation volume as determined from Eqn. (4.3) as a function of temperature for both the alloys is shown in Fig. 4.59. While the values of Timetal 834 are observed to be higher than that of alloy 834 without Si, both the alloys shows the same trend in variation of activation volume with temperature. In case of both the alloys, the activation volume initially increases up to a temperature and thereafter it decreases with increase in temperature. While the activation volume

shows a local peak at 450°C in case of Timetal 834, the local maxima was observed at 350°C for the alloy 834 without Si.

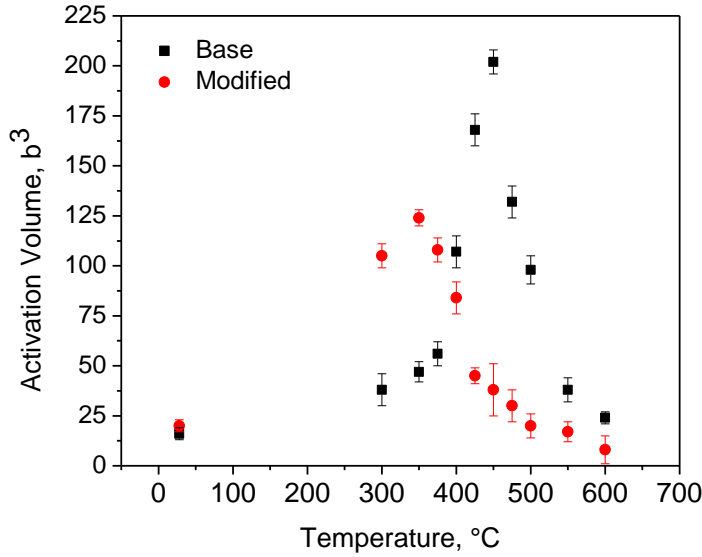


Fig. 4.59 Variation of activation volume as a function of temperature in alloy 834 without Si and Timetal 834.

The activation volume lies in the range of $10^0 b^3$ to $10^4 b^3$ depending on the different types of mechanisms of dislocation interactions during glide process [Conrad 1981]. While the value $\sim 10^0 b^3$ corresponds to climb mechanisms, $10^1 - 10^2 b^3$ corresponds to Peierls-Nabarro mechanism and cross slip mechanisms. Moreover, $10^2 - 10^4 b^3$ corresponds for intersection mechanisms and the non-conservative motion of jogs [Conrad 1981]. The magnitude of activation volume, given in Fig. 4.59 with error bar, suggests that the rate controlling processes for Timetal 834 till about 400°C and beyond 500°C are the Peierls-Nabarro and cross

slip mechanisms. The similar mechanisms appear to be operative in alloy 834 without Si at 300°C and beyond 375°C. It can also be inferred from Fig. 4.59 that intersection mechanisms and the non-conservative motion of jogs are most likely operative mechanisms between 400°C – 475°C for Timetal 834 and at 350°C for alloy 834 without Si. The sharp increase in activation volume beyond 375°C as well as higher magnitude of activation volume in Timetal 834 indicates that the effectiveness of the rate controlling processes operating in Timetal 834 is higher as compared to alloy 834 without Si.

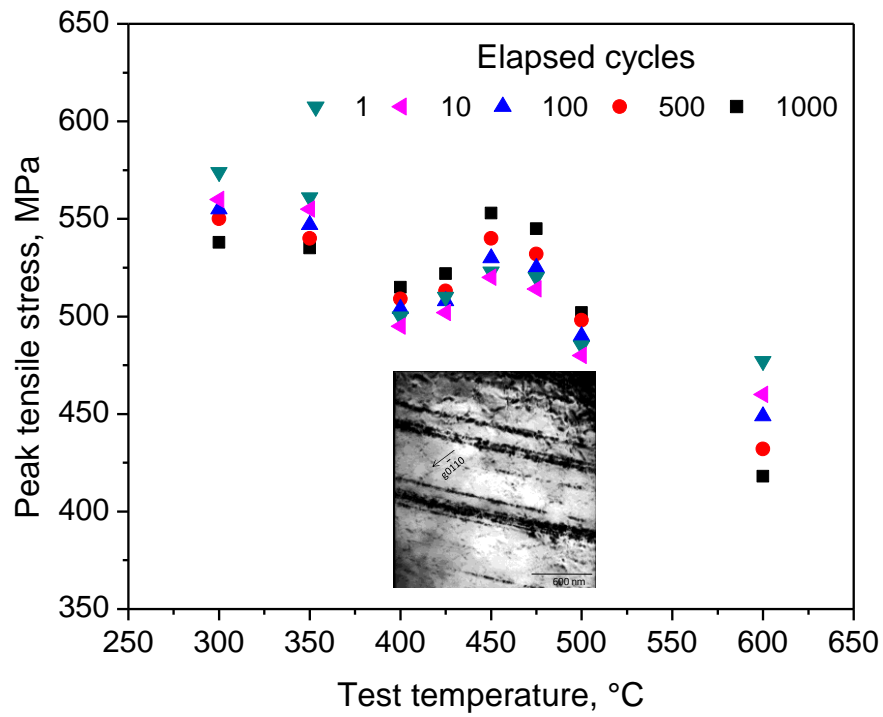
The large activation volumes ($>10^2 b^3$) observed in Timetal 834 matches with the temperature range of occurrence of serrated flow (Fig. 4.6). On the basis of EFTEM observations (Fig. 4.56), it is clear that carbon and nitrogen form atmosphere around dislocations. Hence it is not unreasonable to assume that this segregation is responsible for the repeated locking and unlocking of mobile dislocation segments resulting in serrated flow. It is expected that while the locked dislocation segments is pulled out of the impurity atmosphere at high applied stresses, it also sweeps out a larger activation area under this high applied stress until it is locked again by the impurity atmosphere. Therefore, it is reasonable to conclude that the large activation volume is due to the large activation area as a consequence of pinning-unpinning events. While the indication of strength of impurity atmosphere can be rationalized qualitatively from the magnitude of serrations i.e. large stress drop/serration height is an indicative of dominant impurity atmosphere, it is worthwhile to consider that this is expected to be

significant in Timetal 834 as compared to alloy 834 without Si. Hence, large values of activation volume ($> 10^2 b^3$) in Timetal 834 are due to dominant atmosphere of solute atoms around dislocations. This is also supported by the observation of intense planar slip in form of various types of dislocation pile ups at the same test temperature (Fig. 4.34) in Timetal 834 as compared to alloy 834 without Si.

4.5 Summary

Tensile properties, deformation and fracture of Timetal 834 alloy have been studied in the temperature range of 300°C to 600°C. The serrated flow in the plastic region of stress – strain curves, temperature insensitivity of strength parameters (0.2% yield strength and ultimate tensile strength), decrease in ductility with increase in temperature in the temperature range of occurrence of serrated flow, increase in strain hardening exponent, negative strain rate sensitivity and increase in activation volume with increase in temperature in the temperature range of occurrence of serrated flow has confirmed the occurrence of dynamic strain aging (DSA) in Timetal 834. The influence of strain rate between 10^{-6} to 10^{-3} s⁻¹ was studied to characterize the serrations map and to determine the activation energy of solute element/elements for causing DSA. Silicon is held responsible for causing DSA in Timetal 834. However, in order to understand the role of interstitial solute elements to DSA, alloy 834 without Si which is similar in microstructure as well as in chemistry to that of Timetal 834 was studied under the

same test conditions. This alloy also exhibited the manifestations of DSA, however, the temperature range of occurrence of DSA was observed to be wider than that of Timetal 834. The activation energy values and the characterization of deformed substructure using electron filtered transmission electron microscopy (EFTEM) revealed that DSA effects in this alloy are due to the Carbon and Nitrogen. Microstructural investigations using transmission electron microscopy (TEM) indicate that the dislocation pile ups are more intense in Timetal 834 as compared to alloy 834 without Si. However, deformation occurs through heterogeneous planar slip in both the alloys. The strains are accommodated primarily by basal slip in both the alloys. Both the alloys exhibited mixed quasi-cleavage type of fracture at all the temperature and strain rate studied except at 600°C where ductile fracture was observed.



Chapter V

Low Cycle Fatigue Behavior

5.1 Introduction

As brought out in section 2.1 of chapter II (literature survey), titanium alloys possess excellent strength to weight ratio as compared to other metallic materials [Lützerling and Williams 2007, Polmear 2008]. However, in gas turbine applications, as a cold section component of the front module of the engine, while the fatigue ratio (ratio of endurance limit to yield strength) of titanium alloys is excellent as compared to other metallic materials, the performance of titanium alloys is often limited by the dwell fatigue considerations [Lützerling and Williams 2007]. Likewise, formation of brittle α case and poor burn resistance limits the use of titanium alloys as a “hot section” aeroengine component [Lützerling and Williams 2007]. In addition, creep also significantly contributes in deciding the upper service temperature of titanium alloys. As discussed in section 2.1.3 of chapter II, Timetal 834 belongs to this category of advanced titanium alloys which has been specifically developed as a ‘high pressure compressor module’ with optimized fatigue and creep properties [Neal 1988].

Aeroengine discs are a geometrically large component; the temperature difference between various regions of disc which ranges from maximum at the rim region to minimum at the bore region leads to generation of thermal stresses and hence localised plasticity near the mechanical stress concentration sites such as fir tree or bolt hole regions [Soares 2008, Boyce 2012]. And coupled with the fact that speed changes during operation leads to the development of centrifugal stresses of higher

magnitude near the bore region of the discs, studying LCF properties of disc alloys as a function of temperature holds paramount importance.

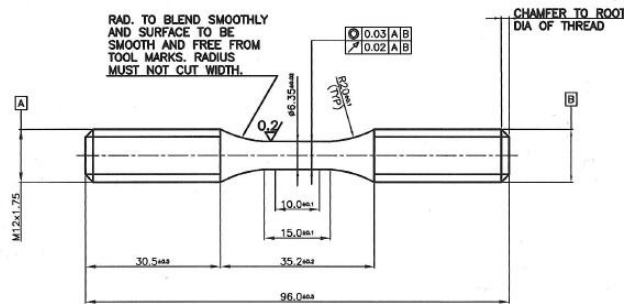
While LCF properties as well as cyclic deformation behavior of Timetal 834 Ti-alloy close to its service temperature ($\sim 600^{\circ}\text{C}$) have been studied to a great extent [Hardt et al. 1999, Kestler et al. 1995, Singh et al. 2007, Pototzky et al. 2008, Pototzky et al. 2009], studies on its LCF behavior in the intermediate temperature range are rather limited in open literature [Kestler et al. 1995, Prasad et al. 2008, Prasad et al. 2010]. Therefore, in this chapter, we examine the LCF behavior as well as LCF properties of Timetal 834 Ti-alloy to bring out the effect of intermediate temperatures (300°C and 450°C) and strain amplitudes (0.4% - 1.2%) on fatigue lives. In order to complement the LCF behavior of these two intermediate temperatures which typically represents the bore/web region of high pressure compressure disc, LCF behavior has also been studied at 600°C which is a representative temperature of rim region of disc. The influence of slip character on evolution of cyclic stresses has been studied at all the test temperatures. The possible role of DSA on LCF behavior of this alloy at 450°C has also been assessed in this chapter.

5.2 Experimental Procedures

5.2.1 Low Cycle Fatigue Testing

Rectangular blanks of size 100 mm x 13 mm x 13 mm (Length x Breadth x Height) were scooped in the T-L orientation of the plate. The heat treated blanks (section 3.2.1 of chapter III) were subsequently machined to cylindrical specimen geometry [ASTM Standard E 606/E606M-12] as shown in Fig. 5.1a.

Circumferential machining marks in the gauge length portion of the specimens were fully removed by polishing parallel to the stress axis to an average surface roughness (R_a) less than 0.2 microns. All LCF tests were conducted on these specimens (Fig. 5.2b).



(a)



(b)

Fig. 5.1 Geometry of cylindrical specimens used for low cycle fatigue (LCF) testing [ASTM Standard E 606/E606M-12] and (b) photograph of LCF specimen.

Tests were carried out at 300°C, 450°C and 650°C in fully reversed mode ($R=-1$, triangular waveform) imposing constant total strain amplitudes, $\Delta\epsilon_T/2$, of 0.4%, 0.6%, 0.8%, 1.0% and 1.2% using extensometers of 12 mm gage length. To study the temperature dependency of cyclic flow stress, additional LCF tests were carried out at 350, 400, 425, 475 and 500°C at only $\Delta\epsilon_T/2$ of 0.6%. Tests at different strain amplitudes were carried out at appropriate frequencies which would result in a strain rate of $1 \times 10^{-3} \text{ s}^{-1}$. Tests were conducted as per ASTM Standard E 606/E606M-12 in a closed loop servo-hydraulic machine (MTS 880, US) of 100-kN load capacity equipped with resistance-heated three-zone split furnace (Fig. 5.2a-b). All tests were started after soaking the specimen for 30 minutes at the test temperature. Temperature during the test was monitored using K-type thermocouples. Minimum 3 tests were conducted at most of the test conditions to confirm reproducibility of results.

5.2.2 Characterization for Cyclic Deformation Behavior

Transmission electron microscopy (TEM) studies of deformation substructures were carried in a FEI Tecnai G² TEM operating at 200 kV. Sample preparation for TEM studies involved sectioning of thin discs at 45°C to the loading axis from the middle portion of gauge length of interrupted LCF tested samples. Subsequently thin discs were mechanically polished to 100 μm in thickness using SiC paper and electro-polished in twin jet electro polisher (FISCHIONE Instruments). Electro-polishing was done using 5% H_2SO_4 and methanol as electrolyte at -50°C and the

voltage was maintained at 20V. The fatigue crack initiation and propagation behavior under different TMF test conditions were examined using scanning electron microscopy (SEM) FEI Quanta 400 equipped with an energy dispersive X-ray spectroscopy (EDS) facility.

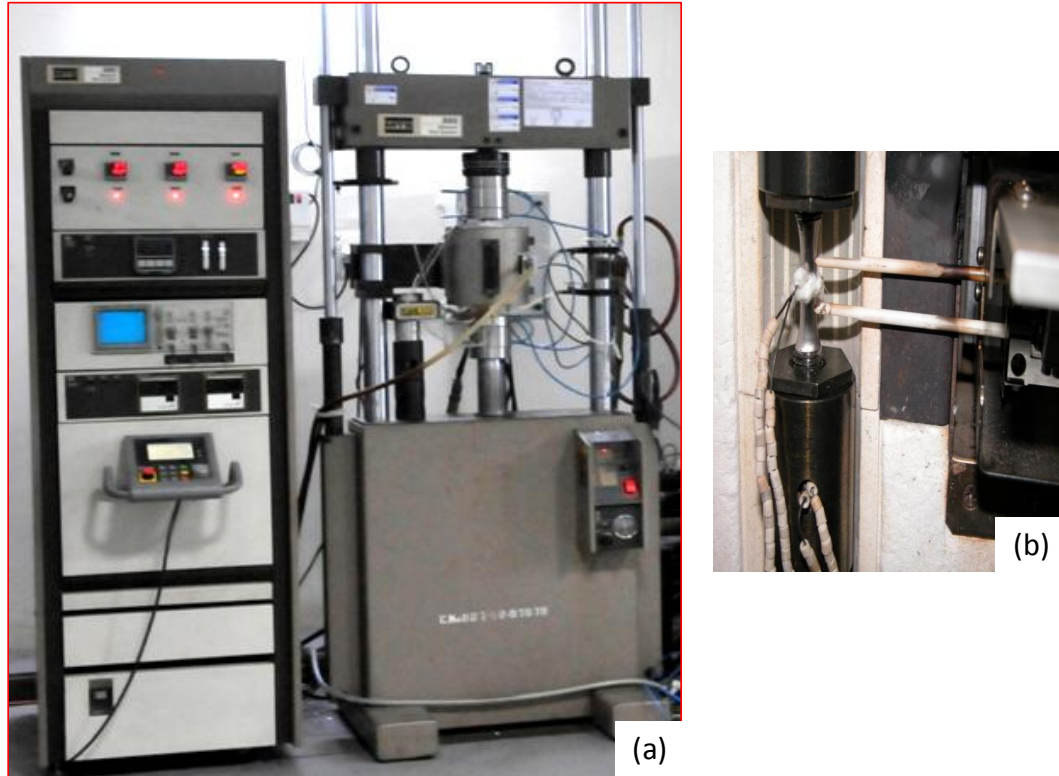


Fig. 5.2 Photographs of (a) MTS servohydraulic test system and (b) mounting arrangement of high temperature extensometer for LCF testing

5.3 Results

5.3.1 Cyclic Stress Response Curves

The cyclic stress response (CSR) curves in terms of variation of stress amplitude (average of tensile and compressive peak stress) with elapsed cycles at 300°C, 450°C and 600°C for $\Delta\epsilon_t/2 \geq 0.4\%$ are shown in Fig. 5.3.

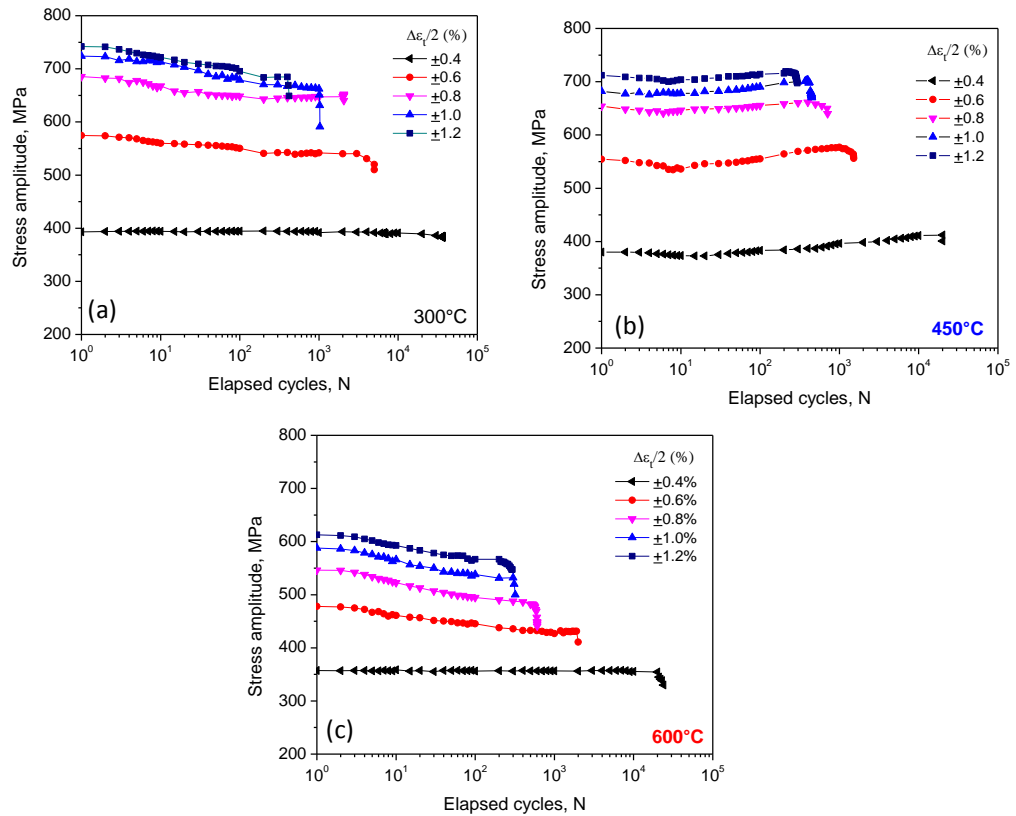


Fig. 5.3 Cyclic stress response curves of Timetal 834 at (a) 300°C (b) 450°C and (c) 600°C

It is evident from Fig. 5.3 that the CSR curve is influenced by both strain amplitude and temperature. At 300°C and 600°C test, CSR of the alloy was observed to be similar (Fig. 5.3a and c). At $\Delta\epsilon_t/2 = 0.4\%$, cyclically stable behavior was observed till failure of the specimen. At $\Delta\epsilon_t/2 > 0.4\%$, the alloy exhibits initial cyclic softening followed by a nearly stable stage, the extent of which decreases with increase in $\Delta\epsilon_t/2$. However, the CSR at 450°C were distinct as compared to 300°C and 600°C. The CSR of 450°C exhibited cyclic hardening after initial cyclic softening for all $\Delta\epsilon_t/2$. The temperature dependence of stress amplitude at $\Delta\epsilon_t/2$ of 0.6% is shown in Fig. 5.4. Between 300°C and 400°C, the stress amplitude decrease continuously. However, increase in stress amplitude was observed in an intermediate temperature range thereby showing local maxima at 450°C with increasing temperature.

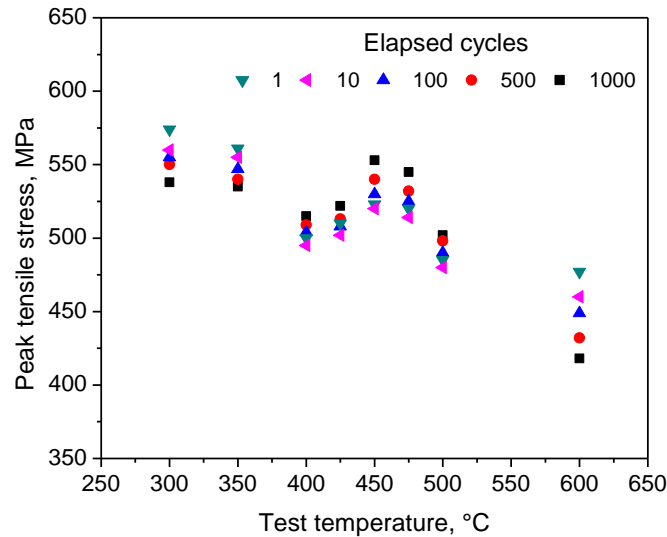


Fig. 5.4 Variation of peak tensile stress vs. test temperature to illustrate the strain aging peak at 450°C.

5.3.2 Cyclic Stress - Strain Response

The cyclic stress-strain (CSS) responses were determined by plotting the stress amplitude ($\Delta\sigma/2$) values recorded at half-life against the imposed $\Delta\epsilon/2$ as per the companion specimen method [Landgraf et al. 1969]. These CSS response curves were compared with the monotonic stress-strain responses, obtained from the first cycle of the specimen subjected to maximum strain amplitude and are shown in Fig. 5.5.

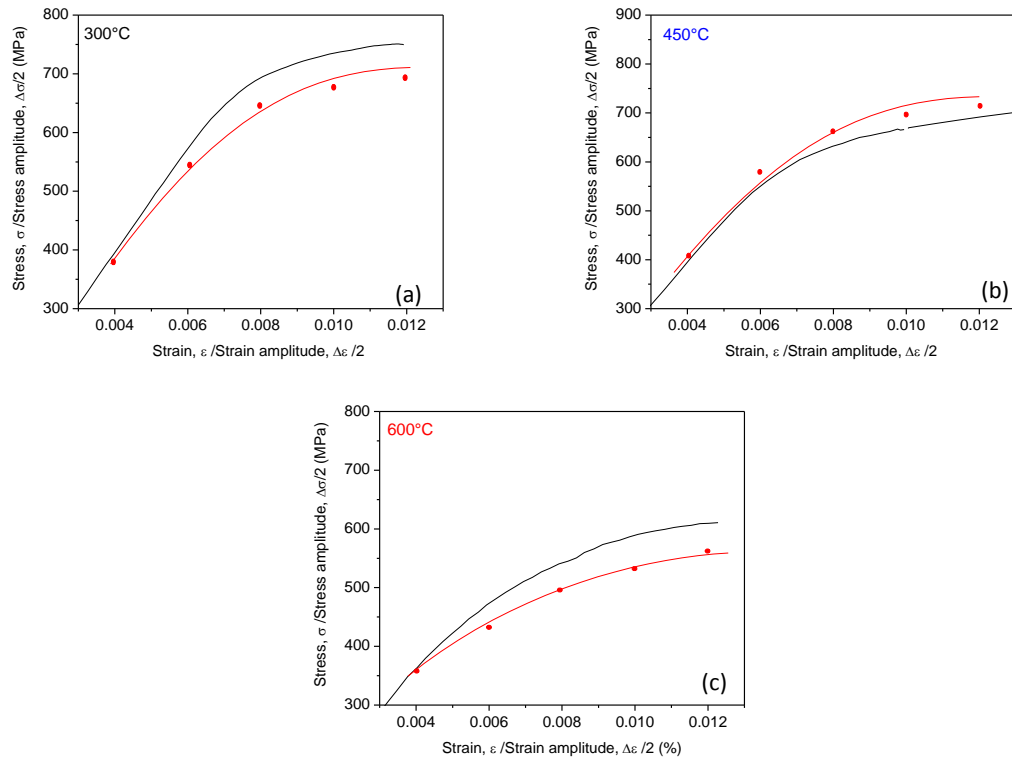


Fig. 5.5 Cyclic stress – strain curves at (a) 300°C (b) 450°C and (c) 600°C

It is evident from Fig. 5.5 that at 300°C and 600°C, CSS curve is below the monotonic curve (i.e., the alloy exhibits cyclic softening) at all strain amplitudes. However, at 450°C, the alloy exhibits ‘cyclic hardening’ i.e., CSS curve is above the monotonic curve at all strain amplitudes.

Monotonic and cyclic stress-strain responses were analysed using the following power law relationships, respectively [Mitchell 1979]:

$$\sigma = K(\varepsilon_p)^n \quad (5.1)$$

$$\Delta\sigma/2 = K' \left(\Delta\varepsilon_p/2 \right)^{n'} \quad (5.2)$$

where n and n' are monotonic and cyclic strain hardening exponents, K and K' are monotonic and cyclic strength coefficients and σ is the true stress, $\Delta\sigma/2$ and $\Delta\varepsilon_p/2$ are stress amplitude and plastic strain amplitude at half life. The values of the constants determined as per Eqns. (5.1) and (5.2) at 300°C, 450°C and 600°C are tabulated in Table 5.1.

Table 5.1: Cyclic and monotonic strain hardening exponent at various temperatures

Temperature (°C)	n	K	n'	K'
300	0.070	1306	0.080	1301
450	0.110	1292	0.114	1272
600	0.047	1410	0.053	1347

5.3.3 Low Cycle Fatigue Lives

Fatigue life, N_f , defined as the total separation of the specimen into two parts obtained as a function of $\Delta\epsilon_t/2$ at the three temperatures studied is plotted in Fig. 5.6a. Best fit curves in Fig. 5.6a show that fatigue lives at 600°C are clearly lower than that of 300°C and at all $\Delta\epsilon_t/2$ and it is lower than that of 450°C at $\Delta\epsilon_t/2 < 1.0\%$. However, fatigue life at 450°C is only marginally lower than that at 600°C for $\Delta\epsilon_t/2 \geq 1\%$. As low cycle fatigue is predominantly plastic strain dependent, LCF lives were analyzed using the Coffin-Manson (C-M) equation [Mitchell 1979]:

$$\Delta\epsilon_p / 2 = \epsilon'_f (2N_f)^c \quad (5.3)$$

where, $\Delta\epsilon_p/2$ is the plastic strain amplitude, ϵ'_f is the fatigue ductility coefficient, c is the fatigue ductility exponent and $2N_f$ is the number of reversals to failure. According to Eqn. (5.3), a plot of $\Delta\epsilon_p/2$ vs. $2N_f$ on log-log axes would result in a straight line with slope c . This has been observed at 300°C, 450°C and 600°C

(Fig. 5.6b). The values of c and ε_f' determined at 300°C, 450°C and 600°C are listed in Table 5.2.

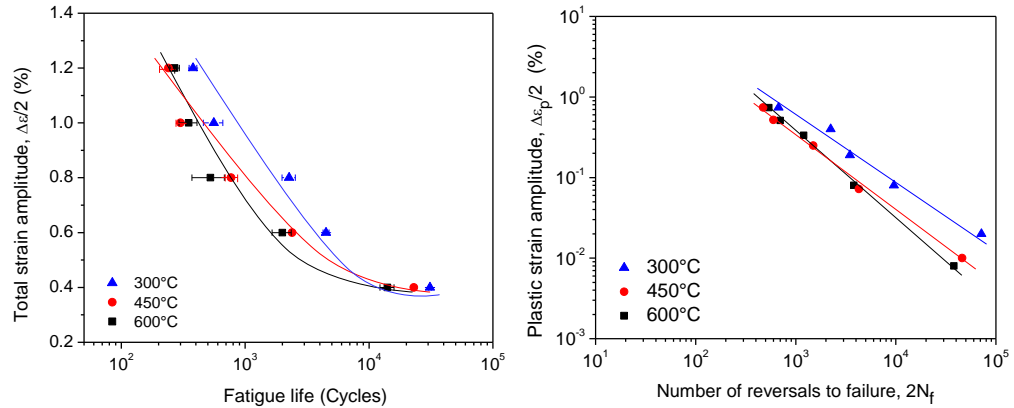


Fig. 5.6 (a) Dependence of fatigue life on imposed total strain amplitude and (b) Coffin-Manson plots of plastic strain amplitude ($\Delta\varepsilon_p/2$) versus number of strain reversals to failure ($2N_f$) at three test temperatures.

Table 5.2: Values of fatigue ductility coefficient and fatigue ductility exponent at three test temperatures.

Temperature (°C)	Fatigue ductility coefficient	Fatigue ductility exponent
300	1.98	-0.80
450	0.74	-0.94
600	1.04	-1.06

5.3.4 Dislocation Substructures

TEM investigations were conducted to assess whether there are any changes in deformation substructures at the three temperatures studied. Since cyclic softening has been observed at 300°C and 600°C for all $\Delta\epsilon_t/2$, LCF tests were interrupted at half life to observe the dislocation substructures. However, due to the distinct behavior of the alloy at 450°C, interrupted LCF tests were carried out at three regimes of cyclic deformation viz. a viz. during initial cyclic softening (N=3), end of cyclic softening (N=10) and cyclic hardening (N=100). All these interrupted tests were carried out at $\Delta\epsilon_t/2 = \pm 1\%$.

In specimens tested at 300°C, the secondary α laths of transformed β grains were relatively free of dislocations (Fig. 5.7c) as compared to primary α grains (Fig. 5.7a). In transformed β grains, occasional secondary α laths with few not fully developed slip bands are observed which traverses across α lath boundaries. Paired dislocations and many dislocation pile-ups were observed inside primary α grains (Fig. 5.7a). Diffraction pattern of the region which consists of paired dislocations (Fig. 5.7a) revealed superlattice diffraction spots which correspond to α_2 (Ti₃Al) reflections (Fig. 5.7b).

Substructures of specimens interrupted at 450°C at three lives namely 3, 10 and 100 cycles are shown in Figs. 5.8-10.

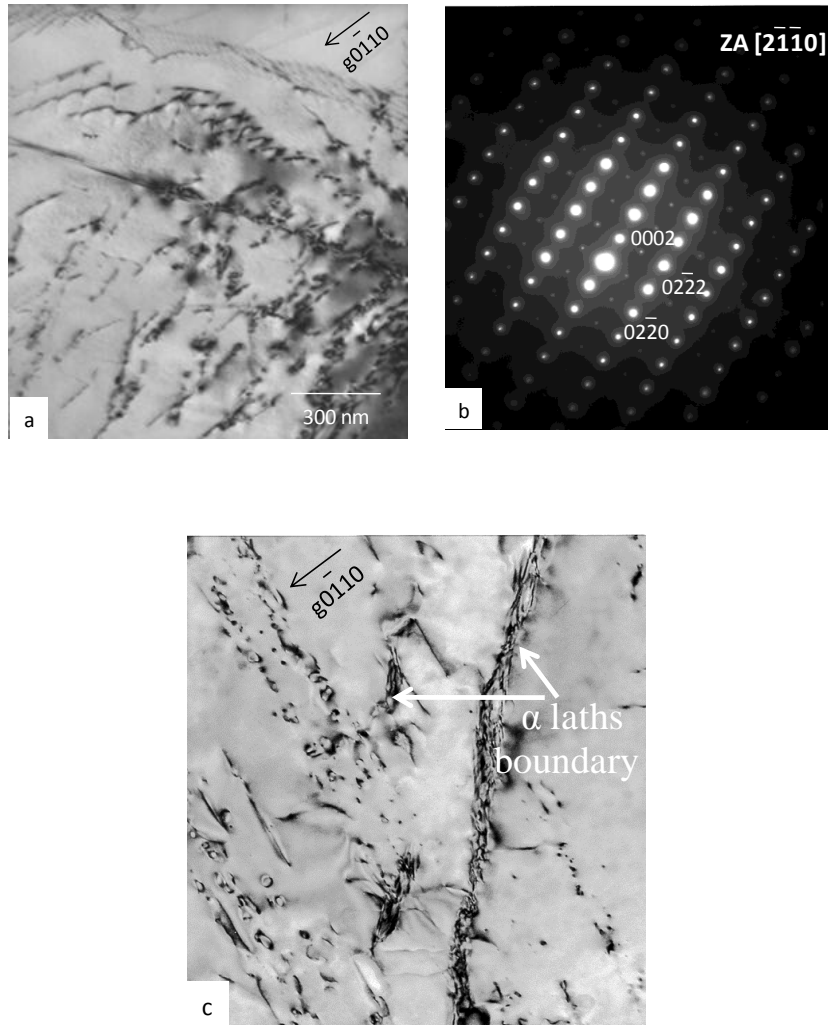


Fig. 5.7 TEM micrographs of deformation substructure in specimens fatigued up to half life at 300°C and $\Delta\epsilon_t/2 = 1.0\%$. General bright-field image of dislocation substructures showing (a) dislocation pile-ups inside primary α grains (b) superlattice diffraction spots and (c) isolated slip bands across α laths of transformed β grains.

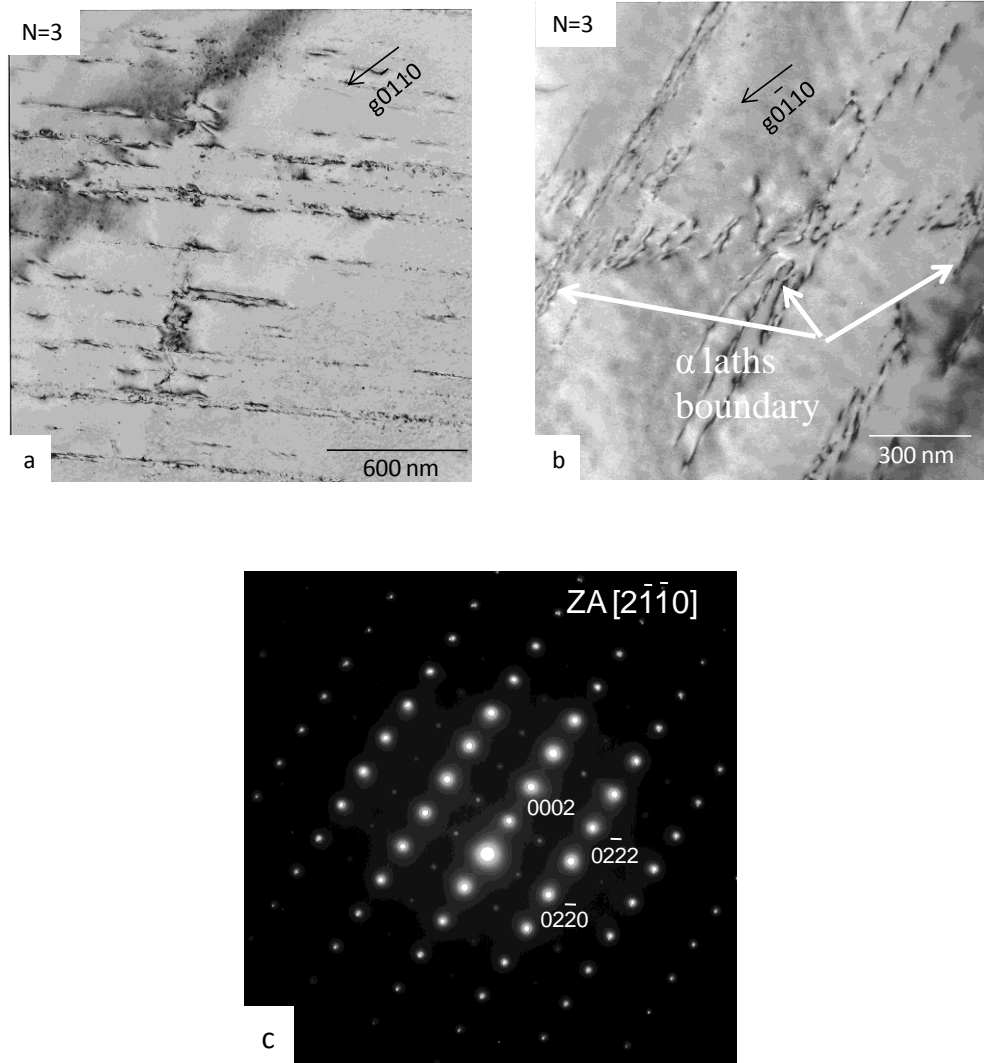


Fig. 5.8 TEM micrographs showing the dislocation substructures during initial cyclic softening (N=3) at 450°C. (a) planar slip bands inside primary α grains (b) paired dislocations inside a pile up in secondary α laths and (c) α_2 superlattice reflections in diffraction pattern corresponding to the region of paired dislocation as shown in (b) can be seen in the micrographs.

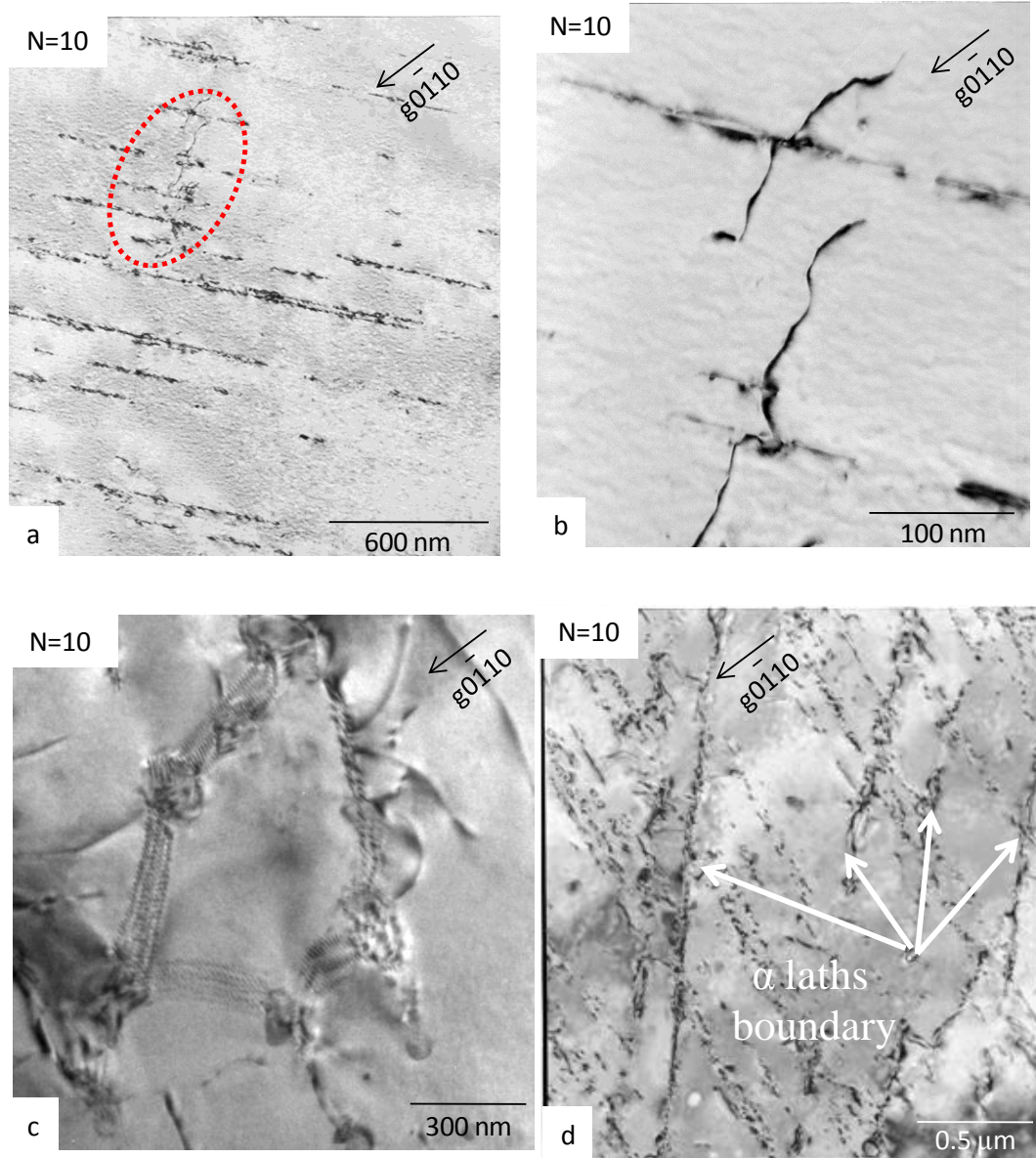


Fig. 5.9 TEM micrographs showing the dislocation substructures at the end of cyclic softening at 450°C. (a) planar slip bands (b) high magnification micrograph of encircled region showing anchored dislocations (c) cellular substructure inside primary α grains and (d) planar slip bands in secondary α laths can be seen in the micrographs.

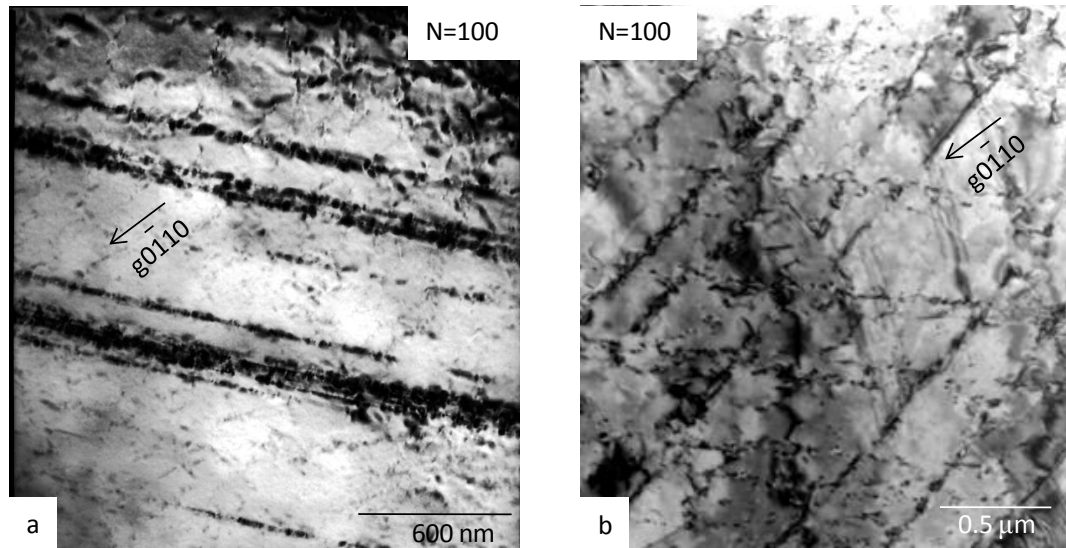


Fig. 5.10 TEM micrographs showing the dislocation substructures during cyclic hardening ($N=100$) at 450°C . Intense planar slip bands can be seen inside (a) primary α grains and (b) secondary α laths.

At $N=3$, dislocation substructure during initial cyclic softening showed well developed slip bands inside primary α grains (Fig. 5.8a). The presence of paired dislocations within a slip band traversing across α lath is also revealed (Fig. 5.8b). Diffraction pattern of this region (Fig. 5.8c) revealed superlattice diffraction spots which correspond to α_2 reflections same as that of Fig. 5.8b. At $N=10$ which is the cycle corresponding to end of cyclic softening, while planar slip bands with relatively less inter slip band spacing (5.9a) as that of Fig. 5.8a were observed inside primary α grains, few anchored dislocations were also observed but rarely across the slip bands as shown in Fig. 5.9b. Cellular substructure could also be observed occasionally within primary α grains (Fig. 5.9c). In secondary α colonies, well developed planar slip bands across several α laths was observed (Fig. 5.9d). During cyclic hardening (100^{th} cycle), intense planar slip bands were observed both inside primary α grains (Fig. 5.10a) as well as secondary α colonies (Fig. 5.10b). However, the degree of intensity was observed to be significantly higher inside primary α grains as compared to secondary α colonies.

Dislocation substructure of specimens tested at 600°C revealed presence of multiple slip bands inside primary α grains (Fig. 5.11a). In addition, bowing out of many dislocation segments are also observed (Figs. 5.11b-c). In secondary α colonies, numerous α laths with bowing out of dislocation segments are observed (Fig. 5.11d).

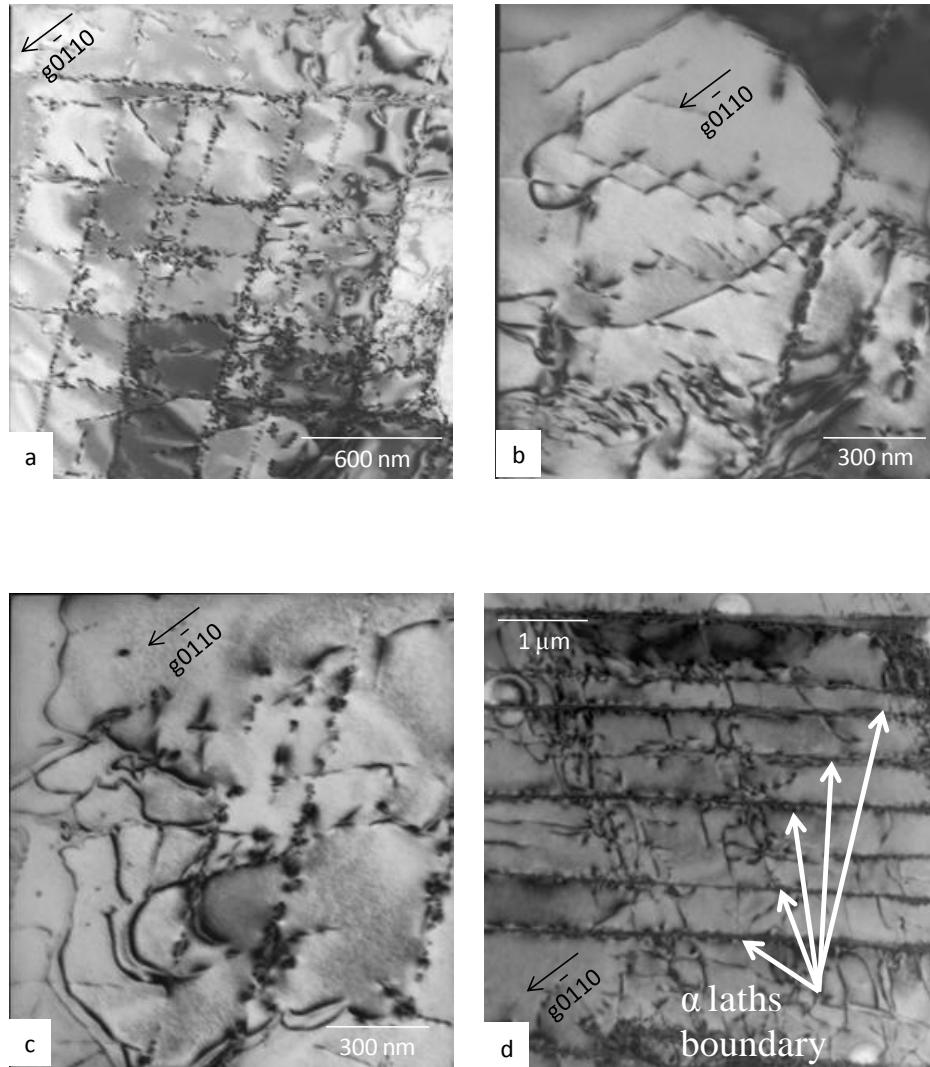


Fig. 5.11 TEM micrographs of deformation substructure in specimens fatigued up to half life at 600°C and $\Delta\epsilon_f/2 = 1.0\%$. General bright-field image of dislocation substructures showing (a) multiple slip bands and (b-c) bowing out of dislocation segments inside primary α grains (d) planar slip bands with threaded dislocations in secondary α laths of transformed β grains.

5.4 Discussion

Materials with low stacking fault energy (SFE) and short range order (SRO) exhibit high degree of planarity in slip, especially at temperature $< 0.4 T_m$, where T_m is the melting point of the material [Suresh 2004]. A high degree of planarity of slip were observed in Timetal 834 alloy up to 600°C in unidirectional tensile deformation as discussed in detail in section 4.4.5 of chapter IV (tensile behavior). It is well established that cyclic and monotonic deformation are synonymous to each other in polycrystalline materials containing shearable precipitates. The results obtained are interpreted in view of deformation substructures observed.

5.4.1 Characteristics of Cyclic Deformation

5.4.1.1 Cyclic Stress Response

It is evident from Fig. 5.3 that cyclic stress response (CSR) is dependent on the test temperature and the magnitude of the imposed total strain amplitude. In all three test temperatures, the cyclically stable behavior observed at low $\Delta\epsilon_t/2 = 0.4\%$ is attributed to minimal dislocation activity observed in primary α as well as secondary α colonies of T_β grains. In LCF, the cyclic deformation at low $\Delta\epsilon_t/2$ is generally considered similar to stage I hardening in unidirectional deformation

[Feltner and Laird 1967]. At low $\Delta\epsilon/2$, the dislocation density and slip length (average travel distances of dislocations) are small, hence only a few complex dislocation interactions occur.

At $\Delta\epsilon/2 \geq 0.6\%$, the alloy exhibited cyclic softening at 300°C and 600°C. In metallic materials, the occurrence of cyclic softening could be attributed to either of the following mechanisms:

- (a) Crack initiation [ASTM Standard E 606/606M-12]
- (b) Rearrangement of high density of dislocations [Feltner and Laird 1967]
- (c) Shearing of ordered and coherent precipitates [Calabrese and Laird 1974, Lützerling and Williams 2007]
- (d) Dissolution of sheared precipitates leading to formation of precipitate free deformation bands [Sundararaman et al. 1989 and 1990, Lützerling and Williams 2007]

It is known that crack initiation can lead to cyclic softening; however, in such a case the peak stress in tension would show a much higher reduction as compared to the peak stress in compression. Nevertheless, in the present investigation, the peak stress in tension and compression were found to reduce equally confirming that cyclic softening is intrinsic to the material and not due to crack initiation.

As discussed in section 3.4 of chapter III (material processing and characterization), the as heat treated bright field TEM microstructures revealed minimal dislocation activity in both primary α as well as secondary α colonies of T_β grains. However, some dislocation activity could be observed near α_{lath} boundaries and α_p/T_β interfaces and is attributed to more strain accommodation so as to maintain the continuity between grains. High angle tilting experiments suggested that the dislocation activity inside α laths or primary α grains is minimal. While the alloy has been solution treated in $(\alpha+\beta)$ field at 1025°C and cooled in oil quenching medium and also it was subsequently subjected to aging treatment at 700°C for 2 hrs and again cooled in air, there is a very less likelihood of presence of high density of dislocations and hence hardening of the material in the heat treated condition. Therefore, the observed cyclic softening could not be attributed solely to rearrangement of high density of dislocations.

In the present investigation, in almost all test conditions, bright field TEM microstructures during cyclic softening revealed superlattice diffraction spots of α_2 (Ti_3Al) type around the regions containing paired dislocations. It is therefore apparent that in Timetal 834 shearing of Ti_3Al particles and work hardening due to dislocation-dislocation interactions occur simultaneously with the more dominating effect dictating the net cyclic stress response. This is illustrated in Fig. 5.12a.

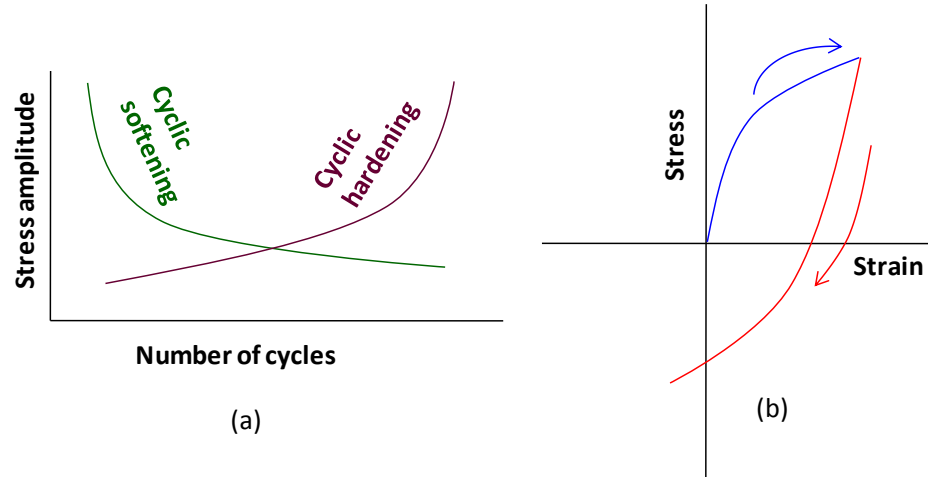


Fig. 5.12 Schematic illustration showing the (a) mutual competition between cyclic softening and cyclic hardening and (b) loading and unloading segments of a hysteresis loop.

Therefore, it is interpreted that the stress levels pertaining to $\Delta\epsilon_f/2 \geq 0.6\%$ values are high enough right from the first cycle leading to early precipitate shearing. The process of shearing dominates the work hardening during the entire life fraction at 300°C and 600°C. It can thus be surmised that the observed cyclic softening is primarily due to shearing of Ti_3Al particles by mobile dislocations. Furthermore, the activation of additional slip systems and easier dislocation climb at 600°C is expected to strengthen the degree of cyclic softening at 600°C as compared to other test temperatures [Singh et al. 2007]. In case of cyclic deformation behavior of Ti-alloys containing smaller size of Ti_3Al particles, the initial cyclic softening is characterized by shearing of these particles by mobile dislocations. The process of shearing of these particles by mobile dislocations occurs during each cycle which in turn reduces their size. This leads to effective reduction in anti-phase boundary

(APB, a region of disorder) area seen in the slip plane by dislocations resulting in stress reduction and thereby localisation of slip to planar bands [Lützerling and Williams 2007]. When the cumulative shearing is high, the precipitates could be completely sheared into two separate halves. At this stage dislocations can move easily in these slip planes to an extent that they offer very little or no resistance to the movement of dislocations. As a result of successive shearing of precipitates, the stress required to shear the smaller particle decreases which eventually lead to cyclic softening. Several studies [Boyed and Hoagland 1973, Williams 2002] have clearly shown the Ti_3Al precipitate sheared by dislocations in titanium alloys. It is thus worthwhile to consider that these precipitates cannot reorder during cyclic deformation. Moreover, it has already been explained that once these precipitates are cut inside the deformation bands, they get disordered and dissolved [Gleiter 1968]. It was attributed to high rate of diffusion processes in the vicinity of the dislocations cutting through the particles [Boyed and Hoagland 1973].

At 450°C, the tendency to cyclically strain harden after initial cyclic softening observed at $\Delta\epsilon_t/2 \geq 0.6\%$ suggests prevalence of an additional strengthening mechanism not operative at 300°C and 600°C. This strengthening mechanism is believed to offset the precipitate shearing mechanism. It is considered that this is a manifestation of dynamic strain aging (DSA) prevailing at this test temperature. As shown in Fig. 5.4, the appearance of hump in the variation of peak tensile stress with temperature is a manifestation of dynamic strain aging. This anomalous temperature dependence of LCF behavior has already been reported in several

materials such as pearlitic eutectoid steel [Tsuzaki et al. 1991], type 304 austenitic stainless steel [Tsuzaki et al. 1983], superalloy [Castelli et al. 1993] and titanium alloy [Feaugas and Clavel 1997] and is attributed to be caused by DSA. The observed cyclic hardening after initial cyclic softening due to Ti_3Al precipitation is ruled out in the present study as kinetics plays an important role for Ti_3Al precipitation during deformation which is more favourable during long term creep or much lesser frequency conducted fatigue tests [Beranger et al. 1993].

It is also evident from Fig. 5.3b that the tendency to harden is observed only after ~ 10 cycles at all $\Delta\epsilon_f/2$. Bright field TEM microstructures revealed the presence of anchored dislocations and polygon like cellular substructure at this cycle. As discussed already in an earlier report by the authors [Prasad et al. 2008], it has been hypothesized [Tsuzaki et al. 1983, Tsuzaki et al. 1991] that once cellular substructure forms during cyclic deformation, dislocations quickly glide between the cell walls and pile up against the cell-wall, until dislocations move to the cell wall on the opposite side when the stress direction changes. In this process, dislocations approaching near the cell wall are arrested at the cell wall for the period of half a strain cycle. As a result, the arrest time of dislocations with the cell shuttling motion becomes equivalent to aging time. In conjunction with the cell shuttling mechanism, unloading segments during fatigue cycling (Fig. 5.12b) may reduce the driving force for dislocation mobility and provide additional time for solute atoms to diffuse and lock mobile dislocations more strongly. It is believed that at this point the hardening due to solute-dislocation as well as dislocation-

dislocation interaction offsets the softening mechanism and leads to onset of cyclic hardening.

The onset of plastic instability for the occurrence of DSA is primarily dictated by the mutual competition between two microscopic processes i.e. (a) formation of obstacles (retardation of dislocation motion by obstacles) [Fujita and Tabata 1977] and (b) enhancement of vacancies produced through deformation or thermally assisted diffusion [Johnson and Johnson 1965]. While the condition of formation of obstacles for the onset of DSA was reported during tensile deformation [Fujita and Tabata 1977, Tabata and Fujita 1980], the same mechanism was proposed to be operative during cyclic deformation [Tsuzaki et al. 1983, Tsuzaki et al. 1991]. Using high voltage in-situ electron microscopy on tensile deformation of Al-Mg single crystal, it has been reported that some finite value of strain, although not explained quantitatively, related to ‘formation of obstacles’ is indeed required for the onset of plastic instability. While on cyclic deformation behavior of type 304 austenitic stainless steel [Tsuzaki et al. 1983] and pearlitic eutectoid steel [Tsuzaki et al. 1991], prolonged cyclic hardening was attributed to longer arrest time for aging due to cell shuttling motion of mobile dislocations.

In the present study, the cumulative plastic strain corresponds to onset of cyclic hardening at all $\Delta\epsilon_t/2$ was calculated and tabulated in Table 5.3.

Table 5.3: Values of cumulative plastic strain at various strain amplitudes at 450°C.

Total strain amplitude ($\Delta\epsilon_t/2, \%$)	Cumulative plastic strain
0.4	0.071
0.6	0.078
0.8	0.089
1.0	0.914
1.2	0.107

The variation of peak tensile stress versus cumulative plastic strain at $\Delta\epsilon_t/2$ of 0.8% and 1.2% are also shown in Fig. 5.13. It is clear from Table 5.3 and Fig. 5.14 that irrespective of employed strain amplitude, the cumulative plastic strain remains nearly same (~ 0.1) for the onset of cyclic hardening. In a very recent study, it has been explained that onset of secondary hardening due to DSA is related to attainment of finite cumulative plastic strain [Huang et al. 2014]. It is proposed that at this cumulative plastic strain, the cell shuttling time for mobile dislocations equals the aging time. It eventually transpires based on these studies that a critical cumulative plastic strain similar to critical strain widely reported in

monotonic deformation is required for plastic instability to set during cyclic deformation for the onset of DSA.

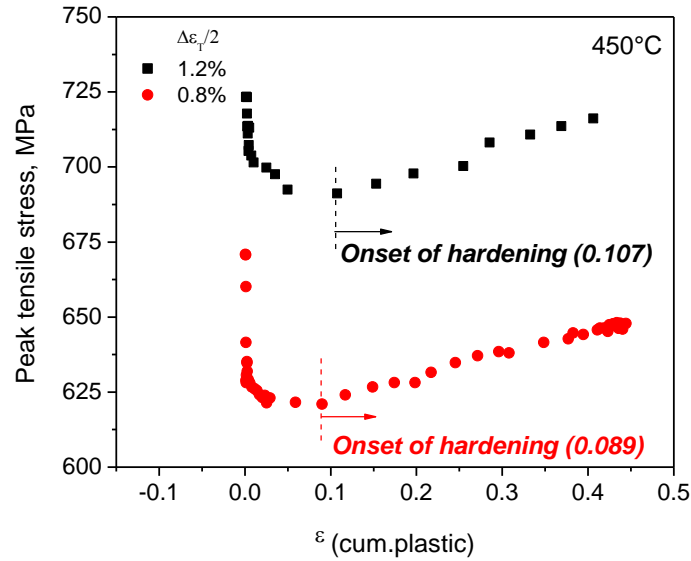


Fig. 5.13 Variation of peak stress with cumulative plastic strain at 450°C showing the onset of cyclic hardening at cumulative plastic strain ~ 0.1 .

Additional fatigue tests have been carried out to further emphasize the existence of DSA during cyclic hardening. Negative strain rate sensitivity is one of the manifestations of DSA [Rodriguez 1984]. In the present study, one LCF test has been initially started with a strain rate of order of 10^{-3} s^{-1} and was instantaneously changed to the strain rate of 10^{-4} s^{-1} during the period of cyclic hardening. The strain rate jump kind of test has been carried out three times during cyclic hardening. The resulted cyclic stress response curve is shown in Fig. 5.14.

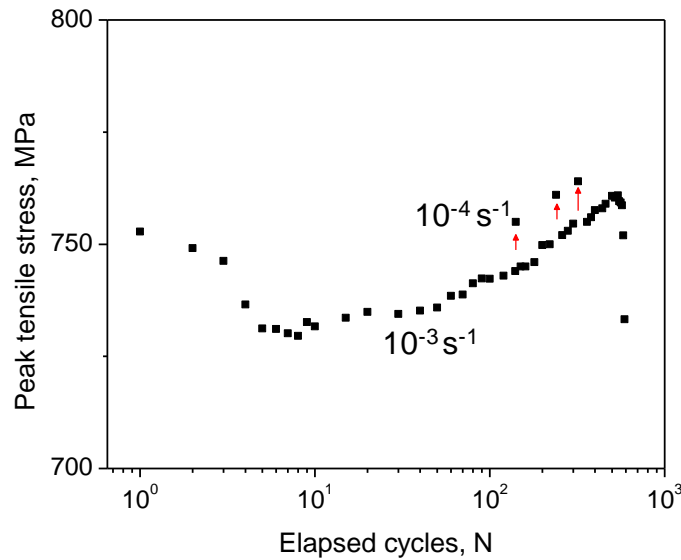


Fig. 5.14 Variation of peak tensile stress vs. elapsed cycles at $\Delta\epsilon/2 = 1.0\%$ at 450°C showing instantaneous increase in stress response at lower strain rate.

Fig. 5.14 shows that upon changing the strain rate from higher to lower, the magnitude of peak tensile stress raised beyond the level of original CSR curve. This eventually shows that the alloy manifests itself in the form of negative strain rate sensitivity during cyclic hardening which is one of the important manifestations of DSA. Similar study was reported by researchers to claim the presence of DSA during cyclic hardening [Miner and Castelli 1992]. Nevertheless, it has been reported [Hähner et al. 1996, Gopinath et al. 2009] that SRS might decrease in DSA regime; it should be aided by other mechanisms like dislocation – dislocation interactions to make SRS negative. However, it is plausible to consider that the onset of cyclic hardening is fundamentally more related to the onset of DSA aided by dislocation-dislocation interaction mechanism inside the slip bands.

5.4.1.2 Monotonic and Cyclic Stress-Strain Behavior

The steady state cyclic deformation response of a metal is generally described by the cyclic stress-strain curve. However, $\Delta\sigma/2$ values at half-life which corresponds to steady state are generally used for plotting the cyclic stress-strain (CSS) curves [Suresh 2004]. In Timetal 834, this concept holds true at 300°C and 600°C since steady state behavior has been observed in cyclic stress response curves (Figs. 5.3a and c). However, due to distinct response of the alloy at 450°C (Fig. 5.3b) thereby showing initial softening followed by hardening, the position of CSS curves can vary depending on the fraction of the life chosen for plotting them. Therefore, as per the general convention, CSS curves at 450°C were plotted using half-life.

For metals which cyclically harden, the cyclic stress-strain curve will be above the monotonic stress-strain curve; for metals which soften, the cyclic stress-strain curves will be below the monotonic curve [Suresh 2004]. In the present study, the alloy softens at 300°C and 600°C in which the CSS curves lies below the monotonic curves and it hardens at 450°C thereby showing CSS curve above than that of monotonic curve. The validity of this approach is substantiated by value of monotonic strain hardening exponent (n). It has been well documented based on extensive database that that metals with n less than 0.1 are observed to soften, however, those having n values greater than 0.1 are either remain cyclically stable or harden [Dieter 1988]. At 300°C and 600°C, the n values are lower than 0.1

(Table 4.1, chapter IV) and it is greater than 0.1 at 450°C. Hence, the observations of softening 300°C and 600°C and hardening at 450°C can be understood based on the trend of variation of n with test temperatures.

5.4.1.3 Fatigue Lives and Deformation Substructures

It is evident from the plot of $\Delta\epsilon_t/2$ vs. N_f (Fig. 5.6a) that both $\Delta\epsilon_t/2$ and temperature influence fatigue lives. Fatigue lives at 600°C are lower than those at 300°C for all $\Delta\epsilon_t/2$ and it is lower than 450°C for $\Delta\epsilon_t/2 < 1.0\%$. If fatigue lives are assessed as a function of $\Delta\epsilon_p/2$, lower $\Delta\epsilon_p/2$ at 450°C (Fig. 5.15) compared to 600°C should have resulted in higher fatigue lives than 600°C. As $\Delta\epsilon_p/2 = \Delta\epsilon_t/2 - [(\Delta\sigma/2)/E]$ where the $\Delta\epsilon_p/2$ developed for any imposed $\Delta\epsilon_t/2$ depends on the flow stress required to attain $\Delta\epsilon_t/2$ and Young's modulus. Young's modulus of the Timetal 834 alloy gradually reduces from 120 GPa at ambient temperature to 100 GPa at 400°C [Brandes and Brrok 1998]. It is noted from chapter IV that uniaxial flow stress remains unaffected or marginally increased by temperature until about 500°C. Therefore as temperature increase between 300°C and 400°C, E decreases and σ remains unaffected and therefore $\Delta\epsilon_p/2$ at 450°C is lower than that at 300°C as shown in Fig. 5.15.

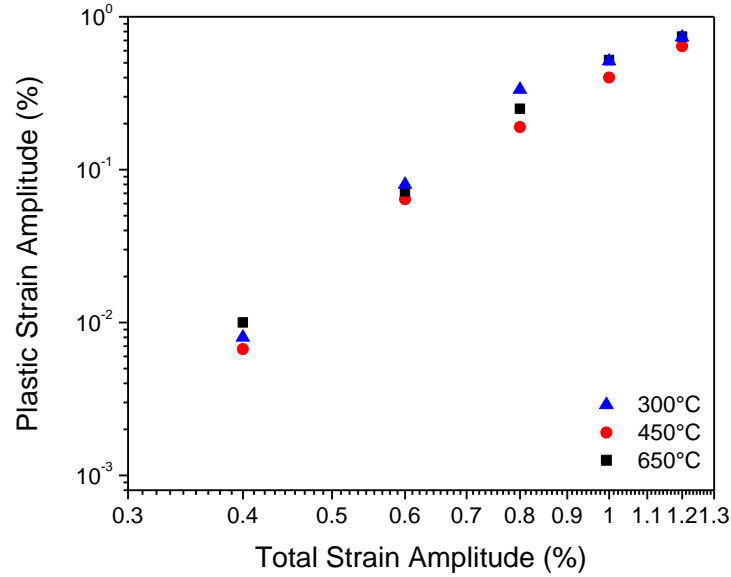


Fig. 5.15 Plastic strain amplitude developed at half-life as a function of imposed total strain amplitude at the three temperature studied.

However, lower fatigue lives at 450°C as compared to 300°C suggest possibility of some other effects that influences the fatigue lives. The increase in temperature from 300°C to 450°C could have introduced more homogeneity of slip, however, more intense planar slip bands (Fig. 5.10) was observed at 450°C. As DSA is known to increase the planarity of slip [Bhanu Sankara Rao et al. 1990], the early crack initiation due to high stress concentration associated with the dislocation pile-ups is expected to decrease the fatigue lives at 450°C. The lower fatigue lives observed at 450°C is hence due to net result of the DSA and dislocation-dislocation interactions rather than a function of $\Delta\epsilon_p/2$ alone.

As confirmed by TEM observations, although the slip planarity prevails up to 600°C, the homogeneity of slip increases at this temperature due to activation of additional slip systems (Fig. 5.11). However, the lower fatigue lives at 600°C despite $\Delta\epsilon_p/2$ levels not being significantly different compared to 450°C for $\Delta\epsilon_t/2 < 1\%$ is attributable to the effect of oxidation in air environment. The presence of striations on severely oxidized fractured surface at 600°C (Fig. 5.16c) as compared to other test temperatures confirms this hypothesis. Adverse effects of air environment on fatigue lives at 600°C have been reported in Timetal 834 [Hardt et al. 1999, Pototzky 1998]. However, for $\Delta\epsilon_t/2 \geq 1.0\%$, the marginally lower fatigue lives at 450°C as compared to 600°C could be attributed to high rate of crack propagation due to more intense planar slip acting at the head of the pile-up.

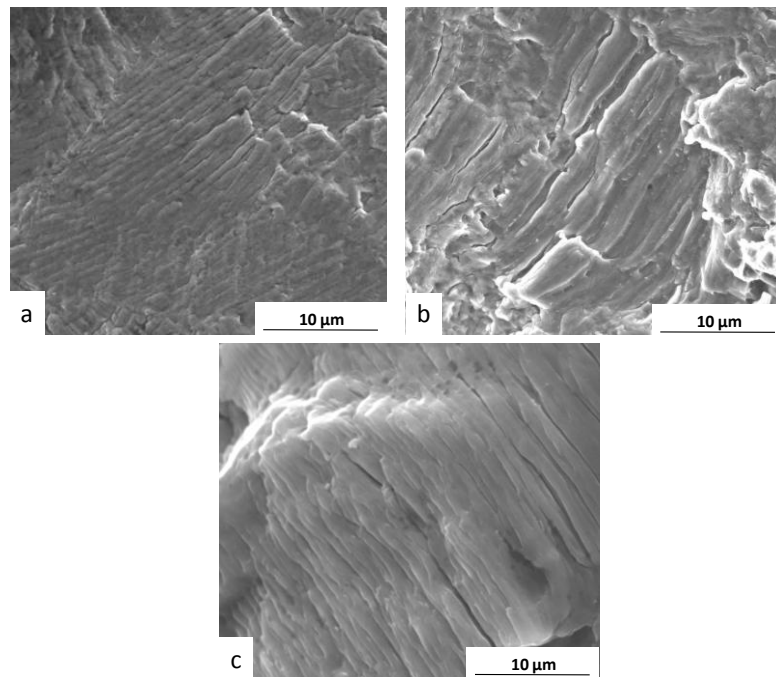
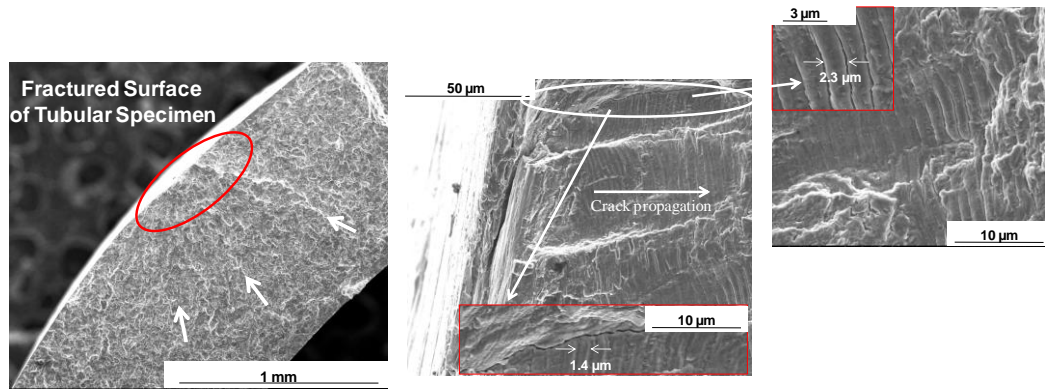


Fig. 5.16 SEM fractographs at strain amplitude of 0.4% for specimens tested at (a) 300°C (b) 450°C (c) 600°C.

5.5 Summary

Low cycle fatigue behavior of Ti-alloy Timetal 834 has been studied at 300°C, 450°C and 600°C under fully reversed constant total strain amplitudes ($\Delta\epsilon_t/2$) ranging from 0.4% to 1.2%. At lower strain amplitudes ($\Delta\epsilon_t/2 = 0.4\%$), the alloy exhibited cyclic stability at 300°C and 600°C. Amongst the temperature studied, the alloy exhibited initial cyclic softening followed by cyclic hardening at 450°C for $\Delta\epsilon_t/2 \geq 0.4\%$. At 300°C and 600°C, cyclic softening followed by cyclic stability, the extent of which decreases with increase in $\Delta\epsilon_t/2$ was observed in the cyclic stress response curves for $\Delta\epsilon_t/2 > 0.4\%$. Precipitate shearing was observed to be the micro-mechanism responsible for cyclic softening. However, dislocation-dislocation and dislocation – solute interaction was observed to be the micro-mechanism responsible for cyclic hardening only at 450°C. TEM observations revealed that planar slip is the major deformation mode under the examined conditions which prevails up to 600°C. However, the severity of planar slip is found to peak at 450°C.



Chapter VI

Thermomechanical Fatigue Behavior

6.1 Introduction

In an aero engine, there are situations depending upon the type of the applications it is being used, large thermal gradients may be generated in high temperature components. Thermal gradient causes thermal stresses which may eventually initiate and propagate fatigue cracks [Spera 1975]. In context to gas turbine aero-engine components, more realistically, internally air cooled high pressure blades and vanes made of superalloys experiences thermal fatigue in which thermal stresses are self-equilibrating in nature due to large thermal gradients across the cooling channels [Reed 2006]. However, in case of rear stage high pressure compressor module made of high temperature titanium alloys, thermal gradients do exist around stress concentration sites such as bolt holes and fir-tree regions of disc and tip of blades due to start-up and shut-down and large variation in throttle handling of the aircraft [Boyce 2012]. It may thus be concluded that although thermal fatigue, as a damaging process per se, is more realistically occurring for internally air cooled high pressure turbine blades and vanes, its prevalence in situations with relatively lesser degree of external constraint around stress concentration sites in high pressure titanium compressor module which can see temperature $\sim 600^{\circ}\text{C}$ during service cannot be ruled out. In order to understand the material Behavior under thermal fatigue, researchers carry out thermomechanical fatigue (TMF) testing as a laboratory testing practice in which external forces

applied on a test specimen are used to simulate the internal thermal stresses in an actual component [Spera 1975, Sehitoglu 1985, Hahner et al. 2006].

The near α titanium alloy Timetal 834 which has been developed as a high temperature titanium alloy with an intended application upto 600°C [Neal 1988], has met with success in use as a high pressure compressor module [Lütjering and Williams 2007]. Apart from environmental interactions and burn resistance [Lütjering and Williams 2007], performance of this alloy which possess improved low cycle fatigue life and creep resistance upto temperature $\sim 600^\circ\text{C}$ gets affected by metallurgical instabilities notable of which are overaging, precipitation and dynamic strain aging (DSA) [Prasad et al. 2008, Singh et al. 2007, Sounim 2001]. Microstructural response of this alloy which contains Si during high temperature cyclic deformation has been rationalized by considering multiple factors such as depletion of Si from the solid solution, coarsening of silicides, deterioration of lath boundaries, heterogeneous distribution of strain in α_P (primary α) and β_T (transformed beta) grains, shearing of Ti_3Al precipitates (α_2 phase) and formation of α -case (oxygen enriched layer). Considering these factors the cyclic deformation Behavior of Timetal 834 have been addressed at the service temperature $\geq 550^\circ\text{C}$ [Hardt et al. 1999, Singh et al. 2007, Kestler et al. 1995, Pototzky et al. 2008, Pototzky et al. 2009] but limited information is available on DSA encompassing intermediate temperature cyclic deformation Behavior [Prasad et al. 2008, Prasad et al. 2011]. It is reported that this alloy exhibits DSA in the intermediate temperature range, the maximum effect of which varies with strain

rate [Prasad et al. 2011]. DSA has also been noted to affect the tensile [Singh et al. 2008, Prasad et al. 2008,] as well as LCF [Prasad et al. 2008] properties. Since the manifestations of DSA in Timetal 834 are observed at service temperatures of most commonly used (300°C-450°C), it would be better to examine the hardening response of this alloy under TMF loading. In TMF conditions, the microstructural changes occurring in two temperature intervals (400°C↔600°C and 400°C↔650°C) evidenced by transmission electron microscopy (TEM) observations has already been reported [Christ and co-workers 1997, 1998, 1999, and 2007]. They have interpreted the results in terms of change in slip character, coarsening of silicides and disintegration of lamellae boundaries occurring at temperature above and below 600°C. However, the role of DSA could not be brought out. The aim of the present investigation is to understand the thermomechanical fatigue response of Timetal 834 with special emphasis on assessing the cyclic hardening Behavior. Furthermore, few unconventional LCF as well as TMF tests have been carried out to emphasize the occurrence of DSA during cyclic deformation. The possible microstructural mechanisms viz. a viz. DSA and precipitation hardening related to cyclic hardening will be discussed in detail.

6.2 Experimental Procedures

6.2.1 Thermomechanical Fatigue Test Procedure

Test coupons for thermomechanical fatigue testing were scooped in the same orientation as discussed in section 5.2.1 of chapter V (low cycle fatigue Behavior). These coupons were subsequently subjected to standard heat treatment cycle as mentioned in section 3.2.1 of chapter III (material processing and characterization). TMF tests were carried out using tubular specimen of gauge section thickness 1 mm and gauge length of 15 mm. The specimen geometry [ASTM Standard E 2368-10] and the photograph of the tubular specimen is shown in Fig. 6.1a and b, respectively.

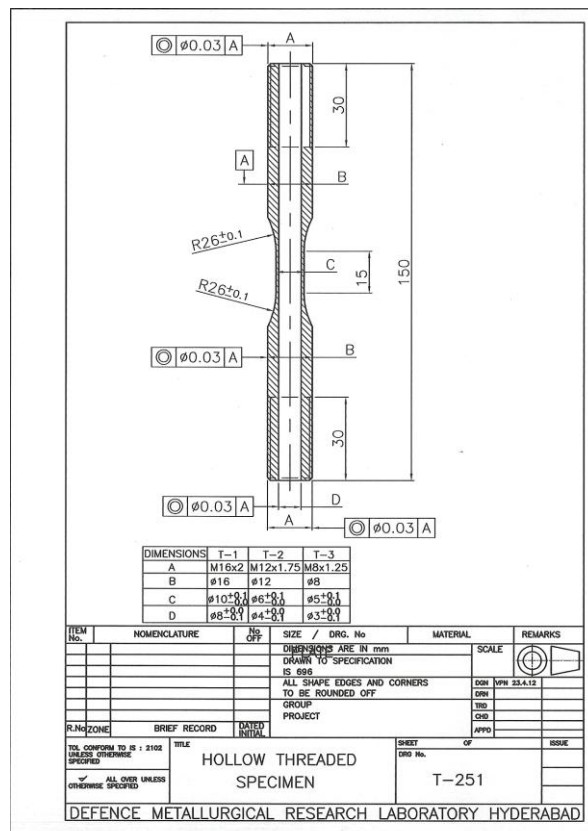


Fig. 6.1 (a) Tubular specimen geometry (all dimensions are in mm) and (b) photograph of tubular specimen used for TMF testing.

Two type of TMF tests namely ‘in-phase’ (IP-TMF) and ‘out-of-phase’ (OP-TMF) were conducted at two temperature intervals of $300^{\circ}\text{C} \leftrightarrow 450^{\circ}\text{C}$ and $450^{\circ}\text{C} \leftrightarrow 600^{\circ}\text{C}$ in fully reversed mode at mechanical strain amplitudes of 0.6, 0.8, 1.0 and 1.2% using an air cooled high temperature extensometer of gauge length 12.5 mm. Since the alloy shows maximum effect of DSA at 450°C under isothermal test conditions (Fig. 5.4 of chapter V) and its upper service temperature as an aeroengine component is $\sim 600^{\circ}\text{C}$ [Neal 1988], the temperature interval for TMF cycling was chosen as $450^{\circ}\text{C} \leftrightarrow 600^{\circ}\text{C}$ as well as $300^{\circ}\text{C} \leftrightarrow 450^{\circ}\text{C}$ so that ascending & descending part of DSA are considered for TMF. In TMF tests, phase is defined by the relationship between mechanical strain waveform and temperature waveform [ASTM Standard E 2368-10]. When the peak of ϵ_m & T (temperature) waveform coincide then the phase angle is defined as 0° and it is called In-Phase TMF and when the peak tensile stress coincides to the T_{\min} then the phase angle is 180° and it is called as out-of-phase TMF. The employed heating and cooling rate during TMF tests was 5°C/s . These tests were conducted as per ASTM Standard E 2368-10 in a 100 kN capacity closed loop servohydraulic test system (Instron 8802) equipped with a 10 kW capacity induction heating system. This test system facilitates to conduct TMF test using four stage TMF test procedure. These stages are related to attainment of dynamic equilibrium in temperature, measurement of thermal strain at zero load, verification of thermal strain compensation at zero load followed by main TMF test. In this test procedure, user has an option to select the number of cycles corresponding to various stages. In the present study, TMF tests were carried out using mechanical strain as the control

parameter which was obtained as per the following relation [ASTM Standard E 2368-10]:

$$\varepsilon_{mech} = \varepsilon_{total} - \varepsilon_{thermal} \quad (6.1)$$

where ε_{mech} is the mechanical strain, ε_{total} is the total strain and $\varepsilon_{thermal}$ is thermal strain. All TMF tests were started at the mean temperature for each temperature interval after soaking the gauge section of specimen for 30 minutes at T_{min} temperature. After suitable positioning of heating coils and optimization of compressed air flow, thermal gradients were maintained below 3°C in both the temperature intervals. The phase shift (difference in phase angle) between two independently controlled waveforms was maintained below 2° during the tests. Depending on the thermal conductivity of the material and T_{min} of the temperature interval, one has to optimize the cooling required to attain T_{min} . Forced cooling was used in both the temperature intervals to meet this objective. The test facility and the specimen mounting arrangement is shown in Fig. 6.2. Representative waveforms showing the variation of temperature and mechanical strain in the temperature interval of 450°C↔600°C IP and OP-TMF tests are shown in Fig. 6.3. It can be inferred from these figures that not only T_{min} was attained during temperature cycling; linearity could also be maintained upto T_{min} during the cooling cycle.

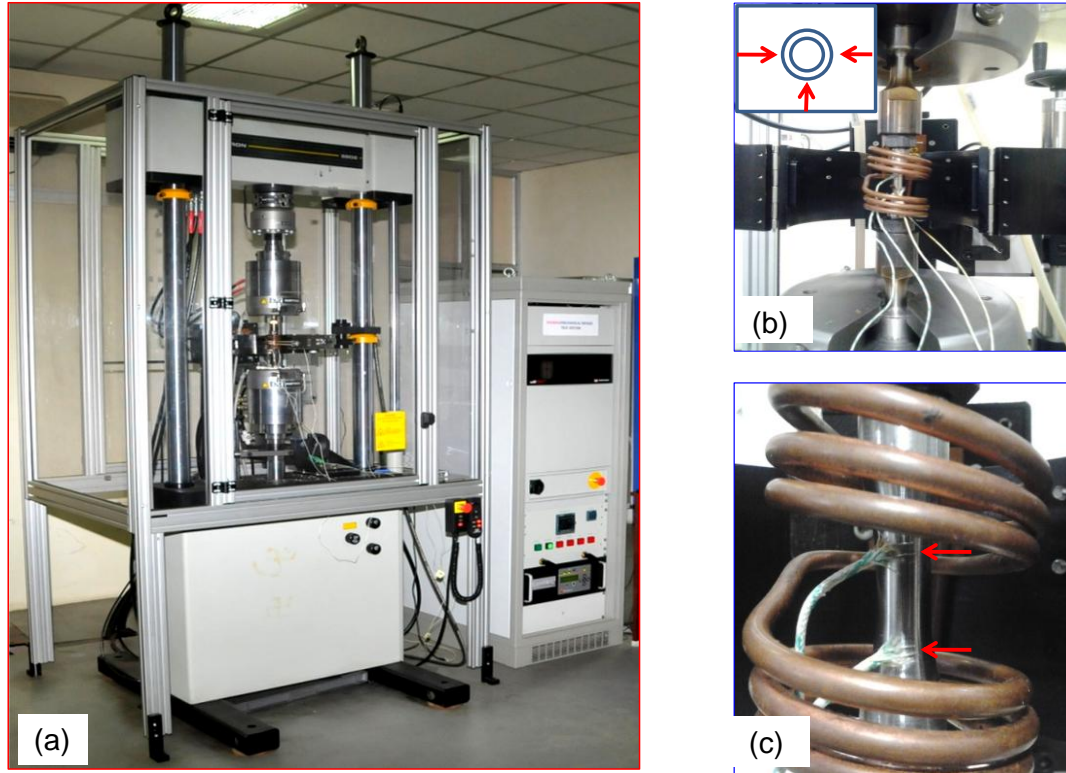


Fig. 6.2 (a) Induction heating based thermomechanical fatigue test system and (b-c) showing specimen mounting arrangement and fixing of thermocouples.

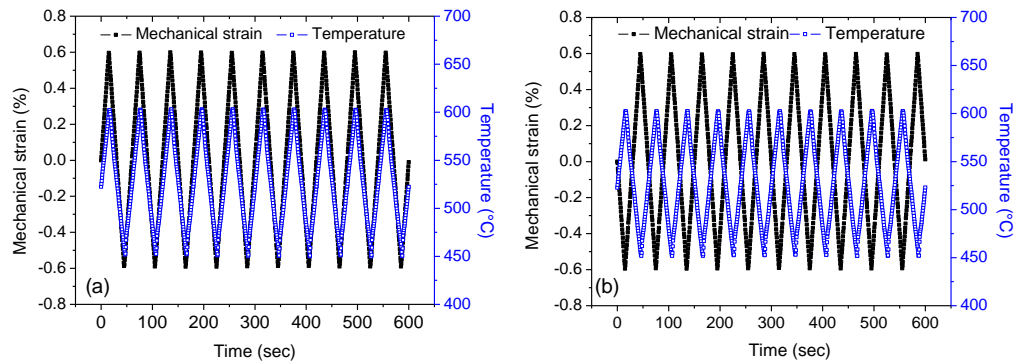


Fig. 6.3 Waveform showing variation of temperature and mechanical strain vs. time during (a) IP-TMF and (b) OP-TMF test conditions in the temperature interval of $450^{\circ}\text{C} \leftrightarrow 600^{\circ}\text{C}$.

6.2.2 Characterization of Deformation and Fracture Behavior

Transmission electron microscopy (TEM) studies of deformation substructures were carried in a FEI Tecnai G² TEM operating at 200 kV. Sample preparation for TEM studies involved sectioning of thin discs perpendicular to the loading axis from the middle portion of gauge length of interrupted TMF tested samples. Subsequently thin discs were mechanically polished to 100 μm in thickness using SiC paper and electro-polished in twin jet electro polisher (FISCHIONE Instruments). Electro-polishing was done using 5% H_2SO_4 and methanol as electrolyte at -50°C and the voltage was maintained at 20V. The fatigue crack initiation and propagation Behavior under different TMF test conditions were examined using scanning electron microscopy (SEM) FEI Quanta 400 equipped with an energy dispersive X-ray spectroscopy (EDS) facility.

6.3 Results

6.3.1 Cyclic Stress Response Curves

The variation in peak tensile and compressive stress with elapsed cycles, at $\Delta\epsilon_m/2 \geq 0.6\%$, at two temperature intervals $300^\circ\text{C} \leftrightarrow 450^\circ\text{C}$ and $450^\circ\text{C} \leftrightarrow 600^\circ\text{C}$ is shown in Fig. 6.4. In both the temperature intervals as well as IP and OP mode of TMF loading, the alloy showed cyclic softening at 300°C and 600°C . Similar to that of isothermal test conditions, at 450°C , initial cyclic softening followed by

cyclic hardening was observed in the temperature interval of $300^{\circ}\text{C} \leftrightarrow 450^{\circ}\text{C}$. However, in the temperature interval of $450^{\circ}\text{C} \leftrightarrow 600^{\circ}\text{C}$, the alloy did not show initial cyclic softening at any $\Delta\epsilon_m/2$ at 450°C (Figs. 6.4c-d). Cyclic hardening till failure both at IP and OP-TMF loading was observed in this temperature interval.

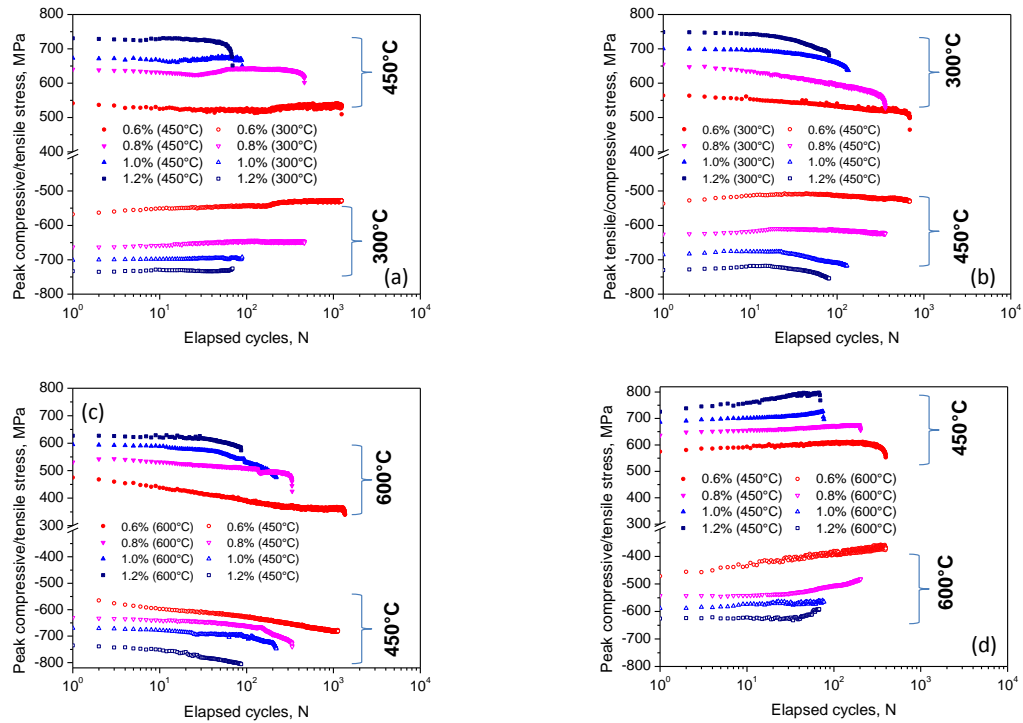


Fig. 6.4 Cyclic stress response curves in the temperature interval of (a) $300^{\circ}\text{C} \leftrightarrow 450^{\circ}\text{C}$ IP-TMF (b) $300^{\circ}\text{C} \leftrightarrow 450^{\circ}\text{C}$ OP-TMF (c) $450^{\circ}\text{C} \leftrightarrow 600^{\circ}\text{C}$ IP-TMF and (d) $450^{\circ}\text{C} \leftrightarrow 600^{\circ}\text{C}$ OP-TMF loading.

6.3.2 Development of Mean Stress during TMF Testing

In the present study, the IP-TMF and OP-TMF hysteresis loops have been observed to be shifted towards the compressive and tensile stress range, respectively, as shown in Fig. 6.5.

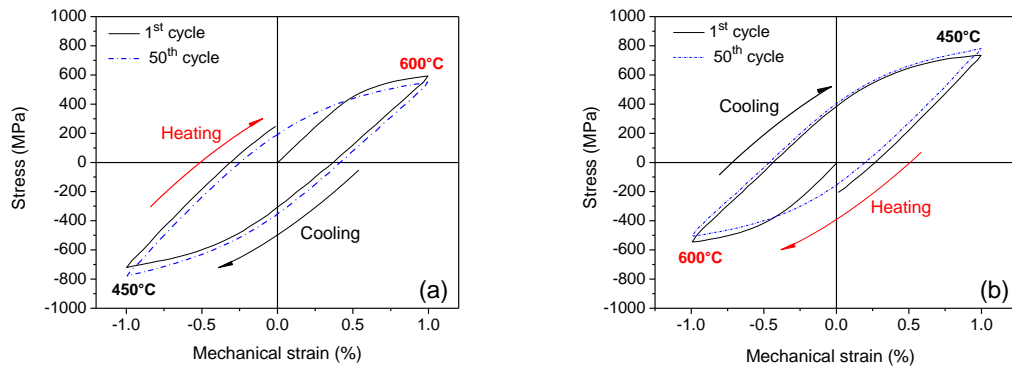


Fig. 6.5 Hysteresis loops (stress vs. mechanical strain) recorded at (a) IP-TMF and (b) OP-TMF test conditions in the temperature interval of $450^{\circ}\text{C} \leftrightarrow 600^{\circ}\text{C}$.

This clearly shows the development of compressive and tensile mean stresses during IP-TMF and OP-TMF loading, respectively, as shown in Fig. 6.6. However, the trend in the variation of mean stress vs. cycles was observed to be same as that of cyclic stress response at 450° in both the temperature intervals. It is to be noted that the maximum tensile mean stress was observed to be ~ 130 MPa and ~ 240 MPa for the temperature interval of $300^{\circ}\text{C} \leftrightarrow 450^{\circ}\text{C}$ (Fig. 6.6b) and $450^{\circ}\text{C} \leftrightarrow 600^{\circ}\text{C}$ (Fig. 6.6d), respectively, for OP-TMF loading. However, the maximum compressive mean stress was observed to be ~ 110 MPa and ~ 380 MPa

for the temperature interval of $300^{\circ}\text{C} \leftrightarrow 450^{\circ}\text{C}$ (Fig. 6.6a) and $450^{\circ}\text{C} \leftrightarrow 600^{\circ}\text{C}$ (Fig. 6.6c), respectively, for IP-TMF loading.

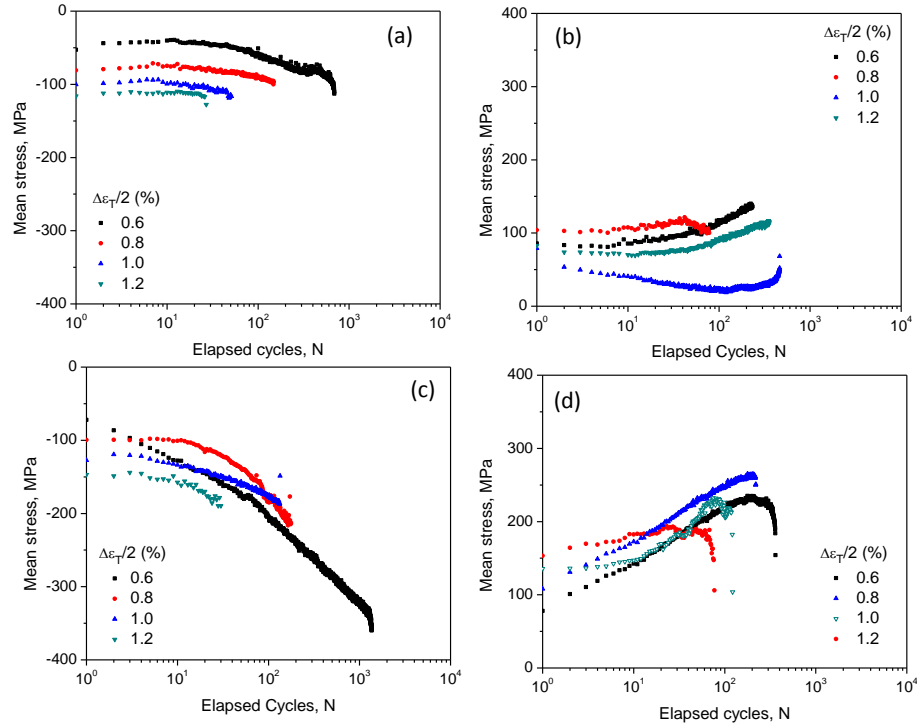


Fig. 6.6 Variation of mean stress with elapsed cycles in the temperature interval of (a) $300^{\circ}\text{C} \leftrightarrow 450^{\circ}\text{C}$ IP-TMF (b) $300^{\circ}\text{C} \leftrightarrow 450^{\circ}\text{C}$ OP-TMF (c) $450^{\circ}\text{C} \leftrightarrow 600^{\circ}\text{C}$ IP-TMF and (d) $450^{\circ}\text{C} \leftrightarrow 600^{\circ}\text{C}$ OP-TMF loading.

6.3.3 Thermomechanical Fatigue Lives

Fatigue life, N_f , defined as the total separation of the specimen into two parts obtained as a function of $\Delta\epsilon_t/2$ at the three temperatures studied is plotted in Fig. 6.7. Best fit curves in Fig. 6.7 show that fatigue lives under OP-TMF loading is

lower than that of IP-TMF loading. It is also evident from Fig. 6.7 that the alloy exhibits lowest fatigue life in 450°C↔600°C OP-TMF loading as compared to other test conditions.

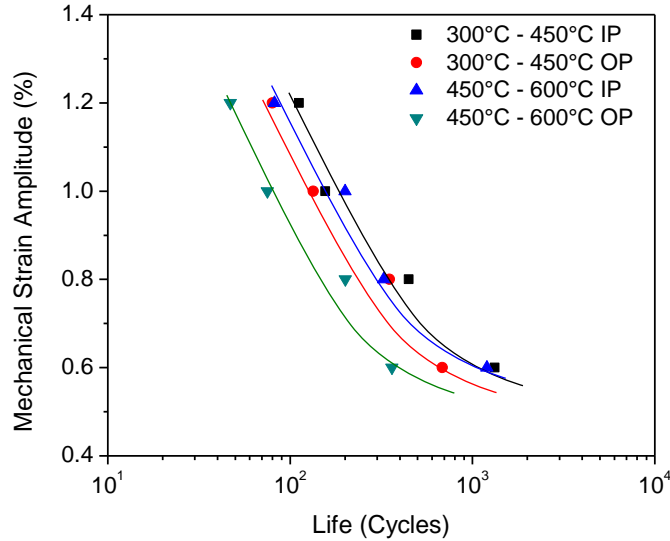


Fig. 6.7 Variation of mechanical strain amplitude with thermomechanical fatigue lives at two temperature intervals and phase relationships.

6.3.4 Dislocation Substructures

In order to assess whether there are any changes in deformation substructures at the two temperature intervals, TEM studies were carried out on the specimens which are interrupted at the half-life at $\Delta\epsilon_m/2 = \pm 1\%$. Bright field TEM micrographs of the samples which are representative of 300°C↔450°C as well as 450°C↔600°C IP and OP-TMF loading are shown in Figs. 6.8-6.10.

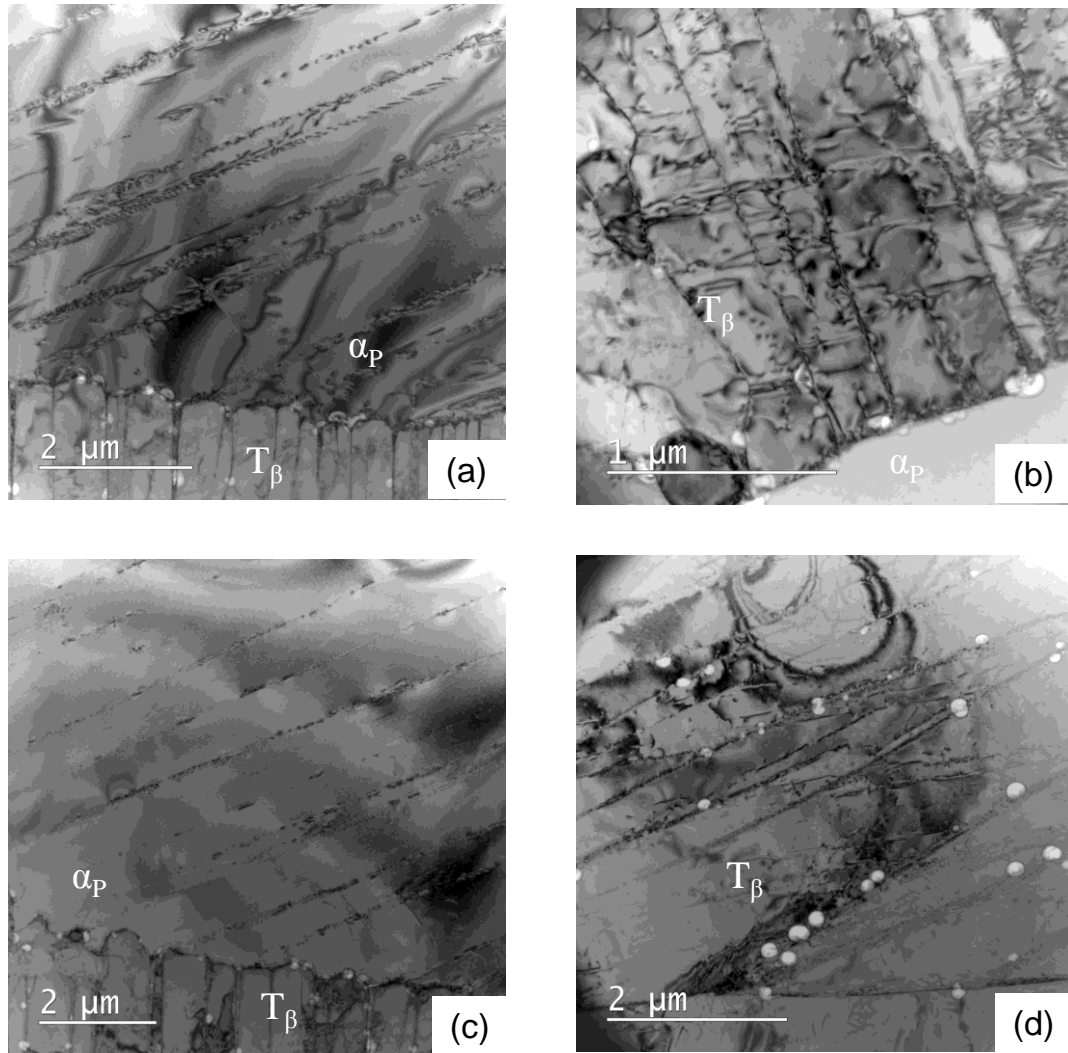


Fig. 6.8 Bright field TEM micrographs of $300^\circ\text{C} \leftrightarrow 450^\circ\text{C}$ TMF loading showing planar slip bands under (a-b) IP-TMF and (c-d) OP-TMF test conditions.

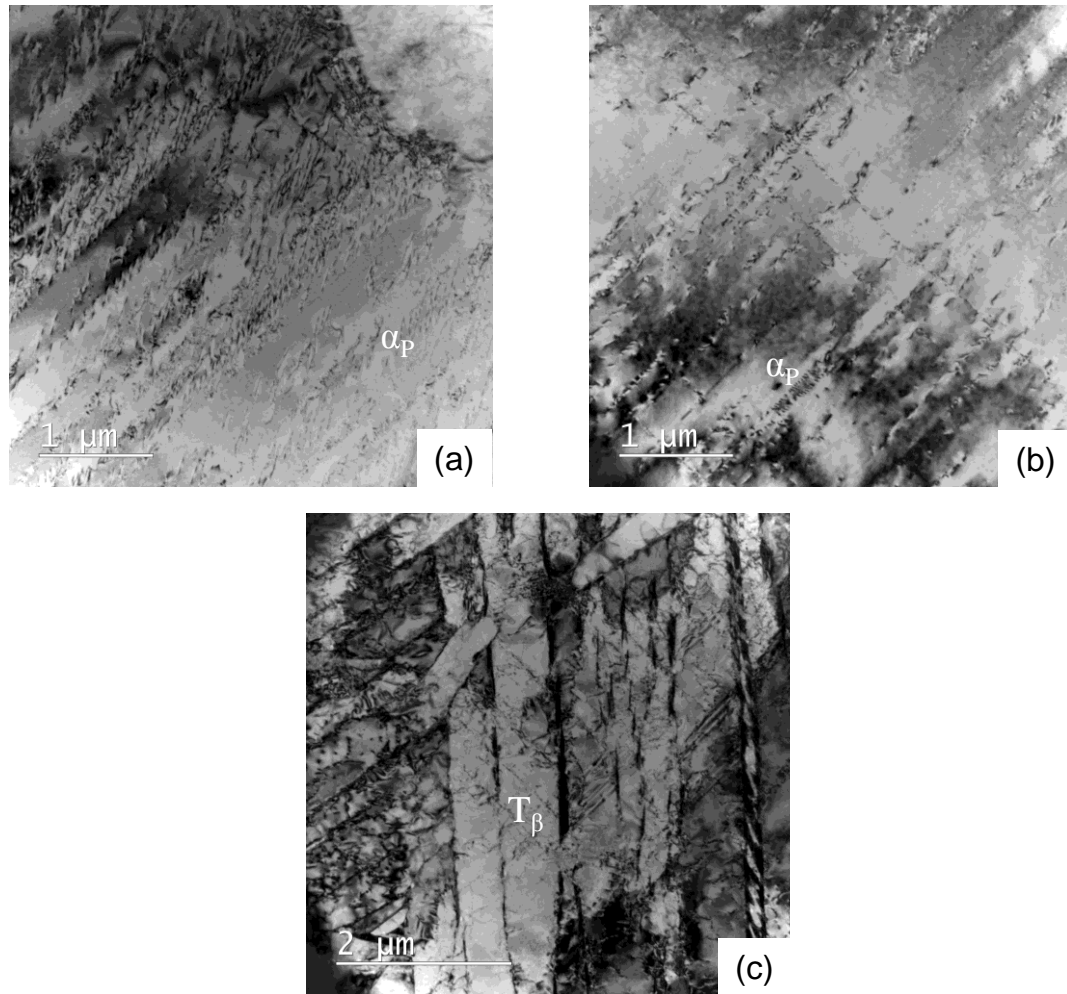


Fig. 6.9 Bright field TEM micrographs of 450°C↔600°C IP-TMF loading showing (a) planar slip bands (b) additional slip systems inside α_p grains and (c) stacking fault fringes in secondary alpha colonies of T_β grains.

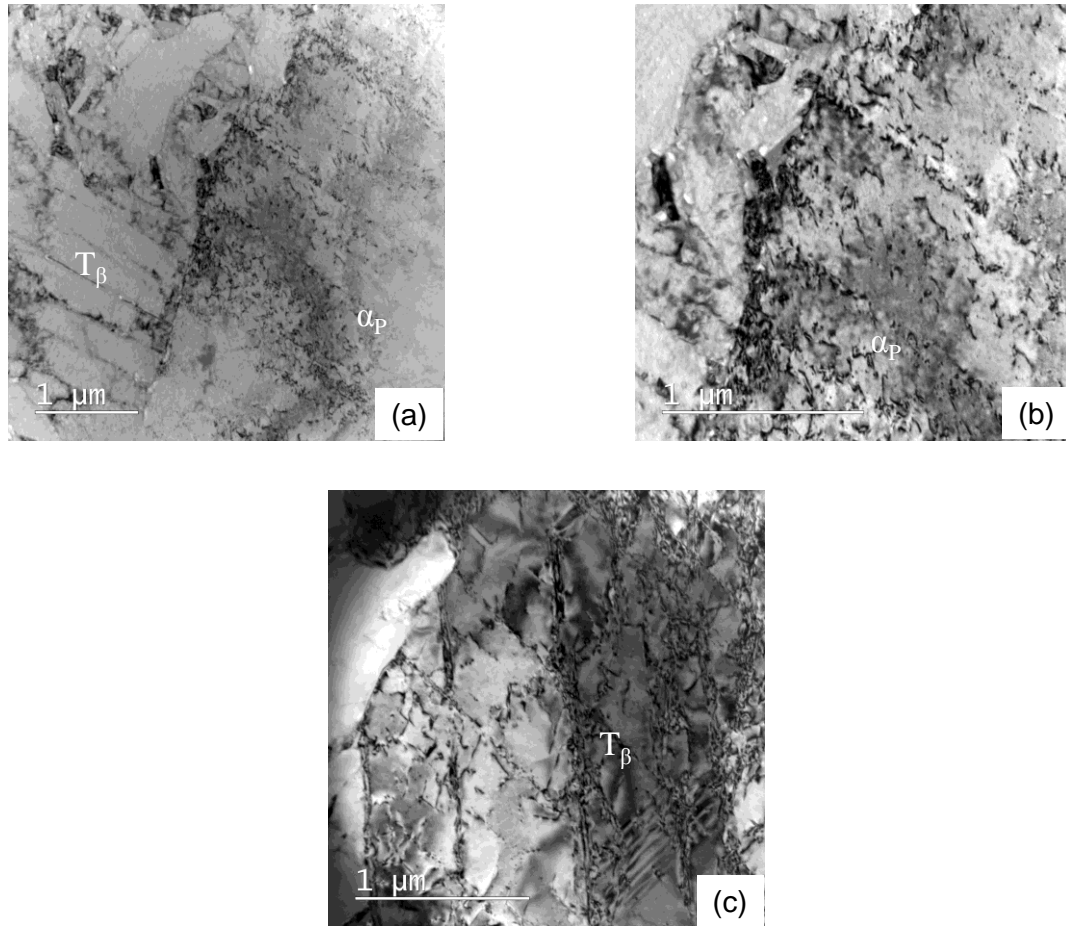


Fig. 6.10 Bright field TEM micrographs of 450°C↔600°C OP-TMF loading showing (a) planar slip bands (b) intense slip bands inside α_P grains and (c) stacking fault fringes in secondary alpha colonies of T_β grains.

It is evident from these micrographs that the primary mode of deformation is planar slip in both the temperature intervals. However, the planar slip is observed to be coarser in 300°C↔450°C (Fig. 6.8a and c) as compared to 450°C↔600°C (Fig. 6.9a and 6.10a) temperature interval. In 450°C↔600°C IP-TMF loading, slip systems in addition to primary slip system is observed inside α_p grains (Fig. 6.9b). The severity of planarity is observed to be more in 450°C↔600°C OP-TMF loading (Fig. 6.10a-b).

6.3.5 Fracture Behavior under TMF Loading

In failed TMF specimens, crack initiation region has been identified by tracking the radial pattern to its origin as shown in a representative SEM fractograph in Fig. 6.11a. Fig. 6.11b shows high magnification SEM fractographs of crack growth region depicting increase in striation spacing with increase in crack length. Considering this observation, efforts were made to measure the striation spacing at the same distance from the crack origin in all fractured TMF specimens. These images at the lowest and highest $\Delta\epsilon_m/2$ (0.6% and 1.2%) under IP and OP-TMF loading, respectively, in both the temperature intervals are presented in Figs. 6.12-15. Striation spacing thus measured from Figs. 6.12-15 is tabulated in Table 6.1.

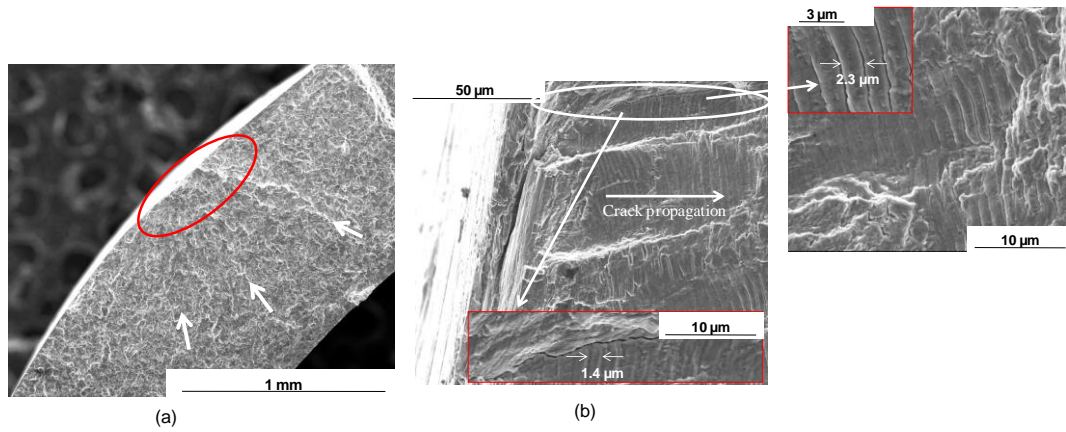


Fig. 6.11 (a) SEM fractograph of a failed TMF tested tubular sample. Crack initiation region identified by tracking the radial pattern to its origin is encircled.
(b-c) Increase in striation spacing can be seen with increase in crack length.

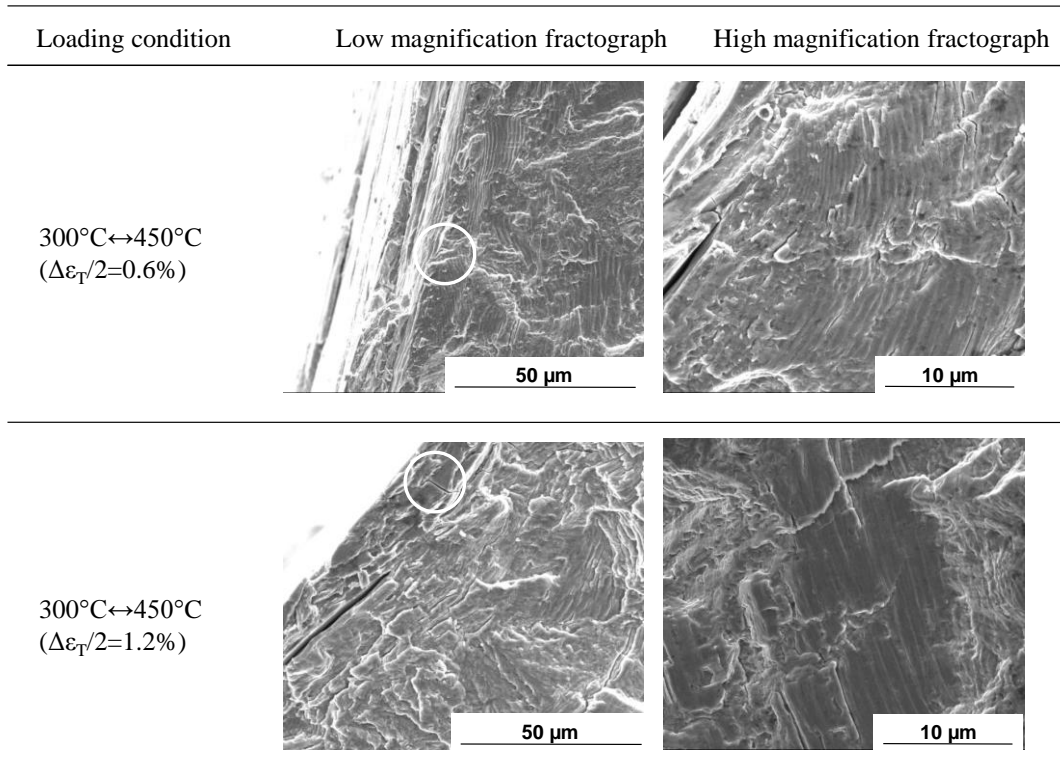


Fig. 6.12 SEM fractographs at relatively low and high strain amplitudes for specimens tested at $300^{\circ}\text{C} \leftrightarrow 450^{\circ}\text{C}$ IP-TMF loading.

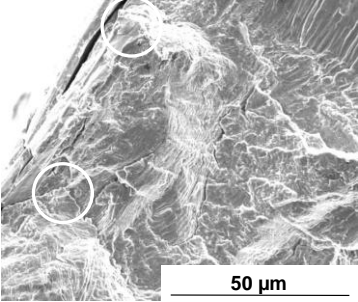
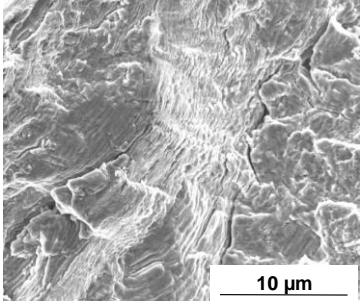
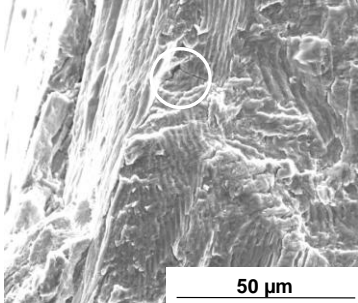
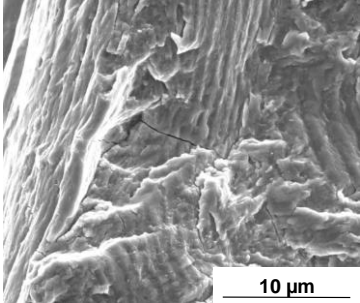
Loading condition	Low magnification fractograph	High magnification fractograph
$300^{\circ}\text{C} \leftrightarrow 450^{\circ}\text{C}$ $(\Delta\epsilon_T/2=0.6\%)$		
$300^{\circ}\text{C} \leftrightarrow 450^{\circ}\text{C}$ $(\Delta\epsilon_T/2=1.2\%)$		

Fig. 6.13 SEM fractographs at relatively low and high strain amplitudes for specimens tested at $300^{\circ}\text{C} \leftrightarrow 450^{\circ}\text{C}$ OP-TMF loading.

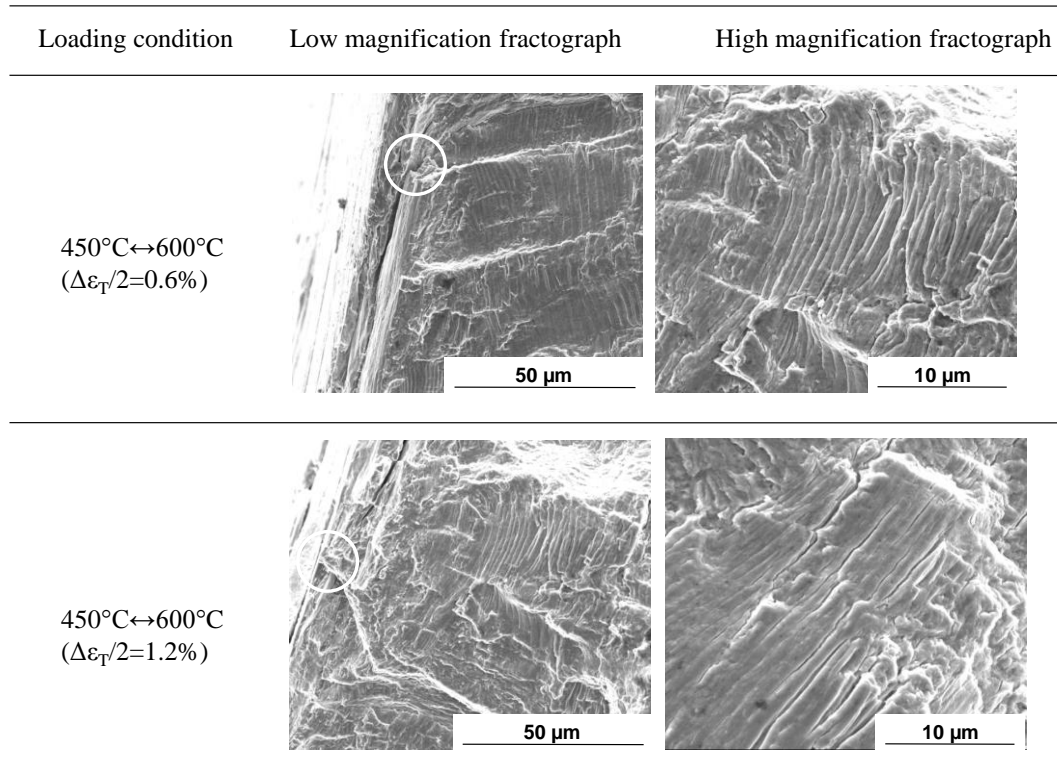


Fig. 6.14 SEM fractographs at relatively low and high strain amplitudes for specimens tested at $450^{\circ}\text{C} \leftrightarrow 600^{\circ}\text{C}$ IP-TMF loading.

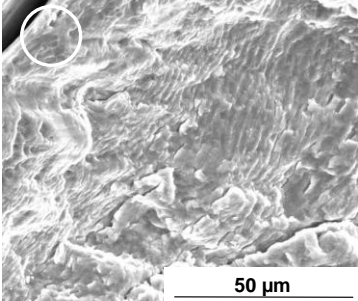
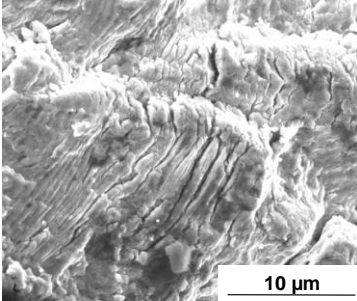
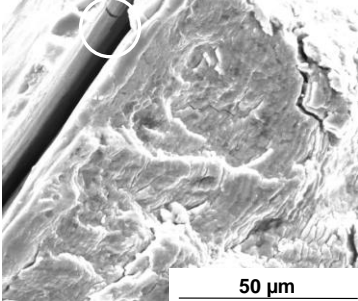
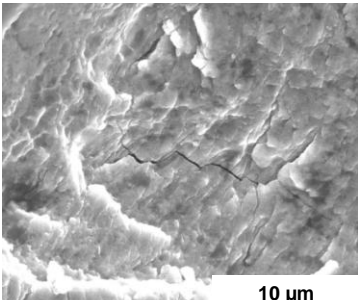
Loading condition	Low magnification fractograph	High magnification fractograph
$450^{\circ}\text{C} \leftrightarrow 600^{\circ}\text{C}$ $(\Delta\epsilon_T/2=0.6\%)$		
$450^{\circ}\text{C} \leftrightarrow 600^{\circ}\text{C}$ $(\Delta\epsilon_T/2=1.2\%)$		

Fig. 6.15 SEM fractographs at relatively low and high strain amplitudes for specimens tested at $450^{\circ}\text{C} \leftrightarrow 600^{\circ}\text{C}$ OP-TMF loading.

Table 6.1 Average striation spacing at a distance of 25 μm (approximately) from the crack initiation region at various TMF loading conditions.

Temperature interval ($^{\circ}\text{C}$)	Phasing	Strain amplitude (%)	Striation spacing (μm)
300↔450	IP	0.6	0.16
		1.2	0.72
	OP	0.6	0.46
		1.2	0.98
450↔600	IP	0.6	1.02
		1.2	1.32
	OP	0.6	1.16
		1.2	2.16

It is clear from Table 6.1 that at the same $\Delta\epsilon_m/2$, the striation spacing at $450^\circ\text{C} \leftrightarrow 600^\circ\text{C}$ TMF loading is higher than that of $300^\circ\text{C} \leftrightarrow 450^\circ\text{C}$ TMF loading. However, in an identical temperature interval, striation spacing was observed to be higher under OP-TMF loading as compared to IP-TMF loading. It is also evident from Fig. 6.15 that the fractured surface is heavily oxidized in $450^\circ\text{C} \leftrightarrow 600^\circ\text{C}$ OP-TMF loading as compared to other test conditions. The EDS plot of fractured surface of the $450^\circ\text{C} \leftrightarrow 600^\circ\text{C}$ IP and OP-TMF loading is shown in Fig. 6.16. Fig. 6.16 shows that the concentration of oxygen is much higher in $450^\circ\text{C} \leftrightarrow 600^\circ\text{C}$ OP-TMF loading as compared to IP-TMF loading.

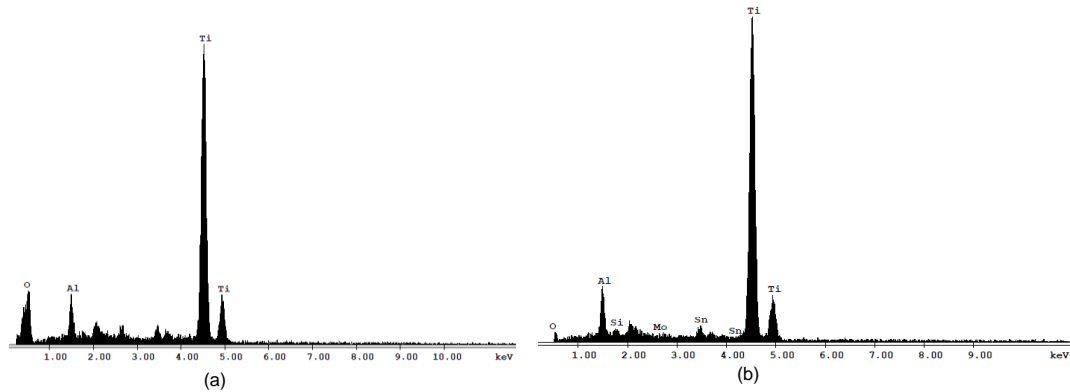


Fig. 6.16 EDAX plots from the striated area showing dominant peak of oxygen at (a) OP-TMF loading as compared to (b) IP-TMF loading in the temperature interval of $450^\circ\text{C} \leftrightarrow 600^\circ\text{C}$.

6.4 Discussion

As discussed in section 4.4.5 of chapter IV (tensile Behavior) and 5.4.1 of chapter V (low cycle fatigue Behavior), the deformation substructure of Timetal 834 alloy is characterized by planar slip up to 600°C under both monotonic as well as LCF loading. This was primarily attributed to the difference in critical resolved shear stress (CRSS) of different slip systems, low stacking fault energy (SFE) and the presence of short range order (SRO) in this alloy [Lütjering and Williams 2007]. The results obtained and deformation substructures observed as a part of this chapter are interpreted in view of these findings and based on some unconventional fatigue tests carried out under TMF loading.

6.4.1 Characteristics of Cyclic Deformation

6.4.1.1 Cyclic Stress Response and Fatigue Lives

It is evident from Figs. 6.4a-d that cyclic stress response (CSR) is dependent on the temperature interval and the magnitude of the imposed mechanical strain amplitude. In contrast to LCF Behavior where the cyclic stress response was observed to be identical in tension as well as compression due to the constant temperature, in TMF loading, the response of the material is different in tension and compression as the temperature is also cycled along with strain

amplitude. In view of this, it is very important to find out the temperature (T_{\min} or T_{\max}) of a temperature interval which governs the evolution of dislocation substructure during TMF loading. For this, one has to examine and compare the dislocation substructures obtained under TMF and LCF loading. It has been observed that identical microstructure was not established in LCF loading at 300°C, 450°C and at 600°C (Figs. 5.7-5.11 of chapter V). While multiple slip systems are activated at 600°C (Fig. 5.11a of chapter V), cyclic slip dispersal is dictated by the primary slip systems at 300°C and 450°C (Figs. 5.7a and 5.8b of chapter V). However, well developed planar slip was observed at 450°C (Fig. 5.8a of chapter V) as compared to 300°C (Fig. 5.7 of chapter V). Comparing the dislocation substructures of samples fatigued isothermally at 300°C and 400°C and thermomechanically at 300°C↔450°C, it appears that 450°C which shows the establishment of well-defined slip bands is the temperature which primarily governs the evolution of dislocation substructure in this temperature interval. Hence, the cyclic deformation mechanism as discussed in section 5.4.1 of chapter V i.e. initial cyclic softening due to precipitate shearing and subsequent cyclic hardening due to dislocation-dislocation and dislocation-solute interaction hold true for thermomechanically fatigued Timetal 834 in the temperature interval of 300°C↔450°C. The cumulative plastic strain for the onset of cyclic hardening in this temperature interval and 450°C isothermal test condition is listed in Table 6.2. Table 6.2 shows that the critical value of cumulative plastic strain for the onset of cyclic hardening is same (~ 0.2) in both IP as well as OP-TMF loading (Fig. 6.17)

which further shows that a similar mechanism operates in both IP and OP-TMF loading.

Table 6.2 Cumulative plastic strain^a amplitude for the onset of secondary cyclic hardening during 300°C↔450°C TMF and 450°C LCF.

Temperature Interval (°C)	Phasing	Mechanical strain amplitude (%)	Cummulative plastic strain
300↔450	IP	0.6	0.198
		0.8	0.184
		1.0	0.194
		1.2	0.186
	OP	0.6	0.188
		0.8	0.194
		1.0	0.206
		1.2	0.198
450°C	Isothermal	0.6*	0.100
		0.8*	0.096
		1.0*	0.094
		1.2*	0.104

*total strain amplitude

^a $\epsilon_{(P,cum)} = 2 N \epsilon_P$, where $\epsilon_{(P,cum)}$ is the cummulative plastic strain, ϵ_P is the plastic strain at zero stress and N is the elapsed cycles [Feaugas and Clavel 1997]

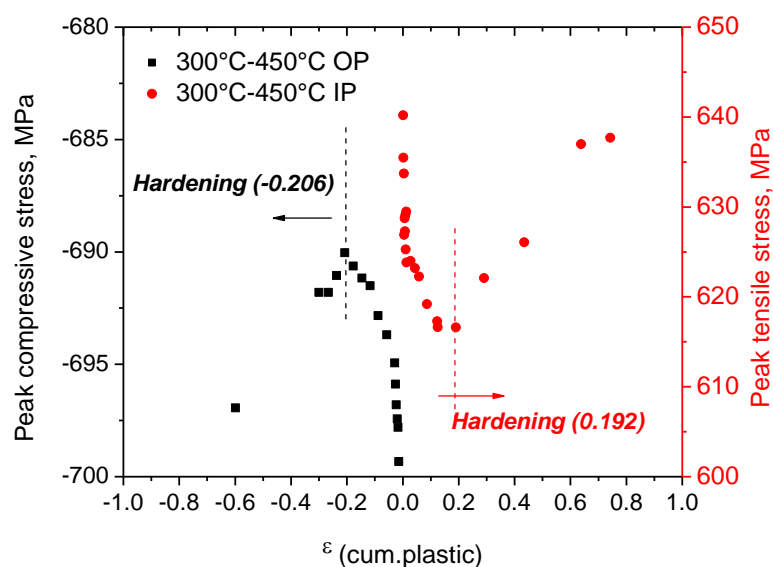


Fig. 6.17 Variation of peak stress with cumulative plastic strain at 450°C during (a) TMF and (b) isothermal loading.

Similarly, considering the dislocation substructures which are fatigued isothermally at 450°C and 600°C and thermomechanically at 450°C↔600°C, the absence of dislocation segments which are representative of wavy slip character (Fig. 5.11b-c of chapter V) and the commonality of deformation getting confined within primary slip systems shows that 450°C as the minimum temperature (T_{\min}) governs the evolution of dislocation substructure in 450°C↔600°C TMF loading. However, activation of additional slip systems (Fig. 5.11a of chapter V and 6.8b) shows that 600°C has marginal role to influence the dislocation substructure during only 450°C↔600°C IP-TMF loading. However, it is interesting to observe that the alloy exhibits cyclic hardening from the first cycle & onwards at 450°C in 450°C↔600°C TMF loading which is different from the isothermally fatigued

response at 450°C. The tendency to cyclically strain harden at 450°C after the 1st cycle at higher temperature interval (450°C↔600°C) suggests prevalence of an additional strengthening mechanism not operative at the lower temperature interval (300°C↔450°C). This strengthening mechanism is believed to offset the precipitate shearing mechanism as discussed in previous chapter and hence it is considered that this is also a manifestation of dynamic strain aging (DSA) prevailing at this temperature interval. This could be attributed to the fact that in the temperature interval of 450°C↔600°C, reversible deformation at 600°C produces significantly more vacancies which in turn aids to more diffusion of substitutional solute atoms (mainly Si, Winstone et al. 1973) for immobilization of dislocations than that at 300°C in temperature interval 300°C↔450°C. In order to support this hypothesis, one unconventional fatigue tests has been carried out. In one of the tests, the alloy was initially cycled isothermally for 50 cycles at 600°C and subsequently cycled at 450°C↔600°C IP-TMF loading. In the other test, before switching to 450°C↔600°C IP-TMF test, the alloy was initially cycled isothermally at 300°C for 50 cycles. The resulted cyclic stress response curves are shown in Fig. 6.18. Fig. 6.18 clearly shows that during TMF cycling, the hardening response of the alloy at 450°C is more in 600°C pre-cyclically deformed condition as compared to 300°C. This undoubtedly supports the hypothesis that temperature assisted deformation induced vacancies influences the degree of cyclic hardening which in turn is related to the ease of diffusion of substitutional solute elements for immobilizing dislocations [Dowsen 1968, Rosenberg 1958, Mecking and Estrin 1980].

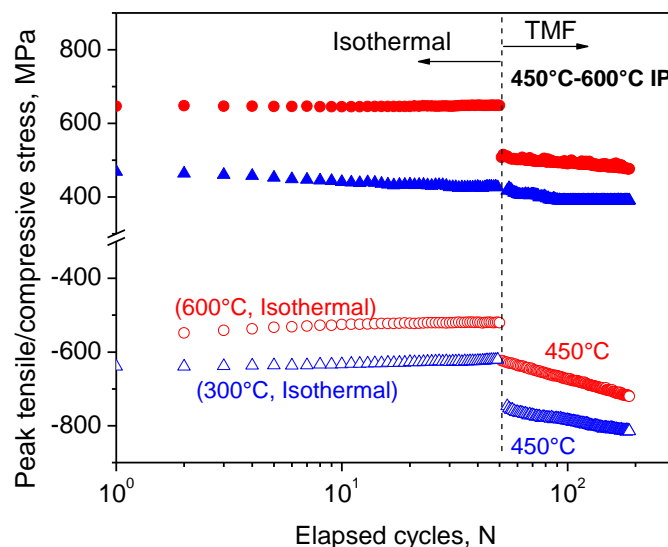


Fig. 6.18 Cyclic stress response curves initially run isothermally at 300°C and 600°C for 50 cycles and subsequently switched to 450°C↔600°C IP-TMF test.

In order to gain more insight into the role of the cyclic hardening to DSA, two additional TMF tests have been conducted in the temperature interval of 450°C↔600°C IP-TMF and the response of the alloy was observed at 450°C. While the first test was conducted with superimposed hold time of 60 seconds at the peak compressive strain at 450°C, the second test was conducted in a solution treated condition without imposing hold time. If DSA is operative in these test conditions, the hardening response of the alloy should be higher in case of solution treated specimen since the presence of Si in solid solution will facilitate effective dislocation – solute interaction. This has indeed been observed in Fig. 6.19. Fig. 6.19b which shows the response of the alloy only at 450°C clearly shows that the hardening response of the alloy is higher in superimposed hold time test which

facilitates extra time during hold time for pinning of dislocations by the diffusing solute atoms as that of without hold time test in as-aged microstructure of the alloy. However, the solution treated specimen exhibits even greater extent of hardening as compared to other two conditions.

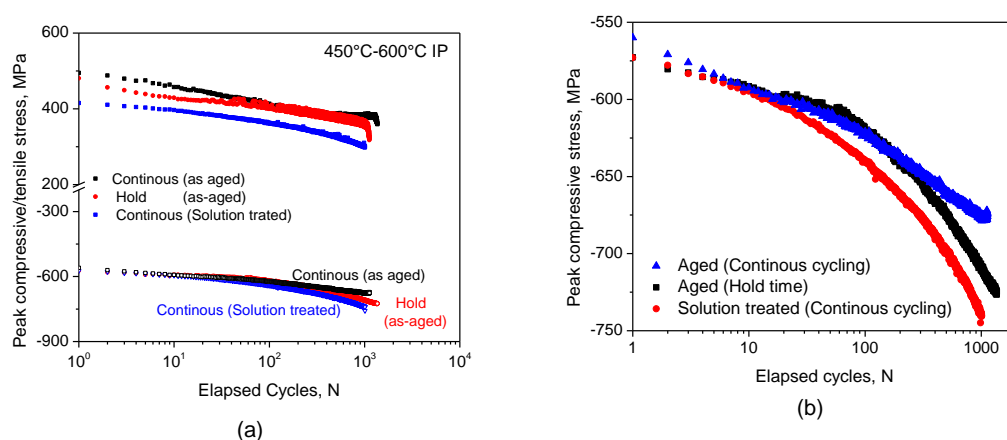


Fig. 6.19 Cyclic stress response curves of Timetal 834 Ti-alloy in (a) aged and solution treated condition during 450°C ↔ 600°C IP-TMF test (b) cyclic stress response of the alloy only at 450°C for aged and solution treated condition of the alloy.

As discussed in section 5.4.1 of chapter V, the onset of plastic instability for the occurrence of DSA is primarily dictated by the mutual competition between formations of obstacles and (b) enhancement of vacancies produced through deformation or thermally assisted diffusion. In the present study, based on the TEM micrographs and the unconventional fatigue tests, it appears that while the condition of formation of obstacles for the onset of DSA is realized in isothermal and 300°C ↔ 450°C TMF loading, deformation or temperature assisted

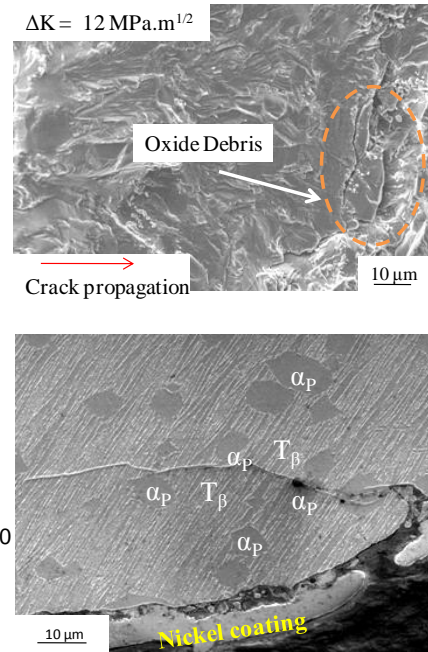
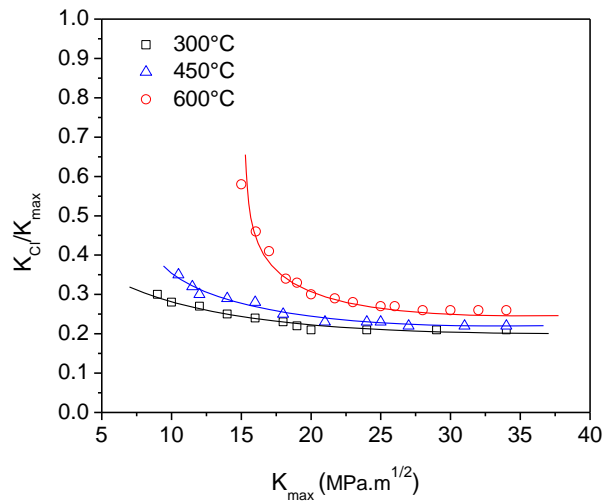
enhancement of vacancies as per vacancy model [Beukal 1983] favors the occurrence of DSA in $450^{\circ}\text{C} \leftrightarrow 600^{\circ}\text{C}$ TMF loading.

Lower fatigue lives at $450^{\circ}\text{C} \leftrightarrow 600^{\circ}\text{C}$ OP-TMF loading is attributable to the combined effect of cyclic hardening which is believed to be due to DSA and oxidation in air environment. The intense slip bands observed in this test condition as compared to other test conditions can lead to early crack initiation. Moreover, the OP-TMF loading is more amenable for oxidation damage as the fresh surface of crack exposed to high temperature and getting oxidized in tension can easily crack during subsequent compressive portion of cycling. The high rate of crack propagation in this test condition as confirmed from the striation spacing (Table 6.1) can further reduce the fatigue life which is evident in Fig. 6.7. Studies on TMF behavior of this alloy [Pototzky et al. 1998, Pototzky et al. 1999] also suggests that it exhibits reduced fatigue lives under OP-TMF loading.

6.5 Summary

Thermomechanical fatigue Behavior of Ti-alloy Timetal 834 has been studied at two temperature intervals viz. $300^{\circ}\text{C} \leftrightarrow 450^{\circ}\text{C}$ and $450^{\circ}\text{C} \leftrightarrow 600^{\circ}\text{C}$ under mechanical strain controlled cycling. Amongst the temperature studied, the alloy exhibited initial cyclic softening followed by cyclic hardening at 450°C in temperature interval of $300^{\circ}\text{C} \leftrightarrow 450^{\circ}\text{C}$. However, gradual hardening was observed at 450°C in $450^{\circ}\text{C} \leftrightarrow 600^{\circ}\text{C}$. At 300°C and 600°C , cyclic softening has been

observed in the cyclic stress response curves in both the temperature intervals. The dislocation substructure was observed to be planar in both the modes of TMF loading, however, slip band spacing was observed to be higher in $300^{\circ}\text{C} \leftrightarrow 450^{\circ}\text{C}$ as compared to $450^{\circ}\text{C} \leftrightarrow 600^{\circ}\text{C}$ TMF loading. Based on TEM microstructures and few unconventional fatigue tests, the observed cyclic hardening is attributed to dynamic strain aging. The lowest fatigue life at $450^{\circ}\text{C} \leftrightarrow 600^{\circ}\text{C}$ OP-TMF loading was attributed to the combined effect of cyclic hardening (leading to early strain localization and crack initiation), oxidation and development of tensile mean stresses. Development of mean stresses and oxidation led to reduced fatigue life under TMF loading as compared to isothermal loading.



Chapter VII

Fatigue Crack Growth Behavior under Isothermal Loading

7.1 Introduction

Studies on fatigue crack growth behavior provide mechanistic information of cracks that invariably initiates in most of the structures during service [Broek 1984]. In order to realize the fullest capability of any larger component in service, such studies as an input for damage tolerant design methodology hold paramount importance [Koul et al. (1) (2) 1990]. Chapters V and VI were predominantly based on the study of ‘crack initiation life’ of Timetal 834 under externally imposed plastic flow. In this chapter, we examine the ‘crack propagation behavior’ of Timetal 834 under isothermal test conditions.

As discussed in section 2.2.3 of chapter II (literature survey), considering the lifing method of compressor discs on fracture mechanics based damage tolerant criteria, studies on fatigue crack growth behavior of Timetal 834 has been widely studied by many researchers [Dowsen et al. 1992, Spence et al. 1997, Lenets and Nicholas 1998, Evans 95, Cope and Hill 1988, Specht 1988, Nagalaxmi et al. 2005]. The effects of several factors viz., temperature [Evans 1995], stress ratio [Dowsen et al. 1992], frequency [Nagalaxmi et al. 2005], microstructure [Cope and Hill 1998, Dowsen et al. 1992], and types of loading [Lenets and Nicholas 1998, Spence and Evans 1997] have been reported. However, influence of intrinsic factor (mainly slip character) and mechanisms of crack closure were not reported in these studies. Therefore, in this chapter, we examine the fatigue crack growth behavior of

Timetal 834 at intermediate temperatures to bring out the effect of temperature on fatigue crack growth rates. These studies were carried out with focus on three temperatures viz. 300°C, 450°C and 600°C of which 300°C and 600°C represent typical web and rim temperature of high pressure compressor discs of a typical military gas turbine aeroengine.

In view of the importance of intrinsic and extrinsic factors in influencing the fatigue crack growth (FCG) behavior, relevant characterization tools have been used to assess their effects. While intrinsic microstructural damage mechanisms acting ahead of the crack tip have been studied using microhardness measurements, the role of crack closure mechanisms acting at the crack wake have also been studied using auger electron spectroscopy (AES) and stylus based profilometer. Moreover, the effect of crack closure on the FCG behavior is thoroughly discussed on the basis of crack closure measurements and detailed observations of fracture surface in this chapter.

7.2 Experimental Procedures

7.2.1 Extraction and Preparation of Specimens

Compact Tension (CT) specimens with nominal thickness $B=6$ mm, and width $W=40$ mm as shown in Fig. 7.1 were fabricated from 18 mm thick heat treated plates.

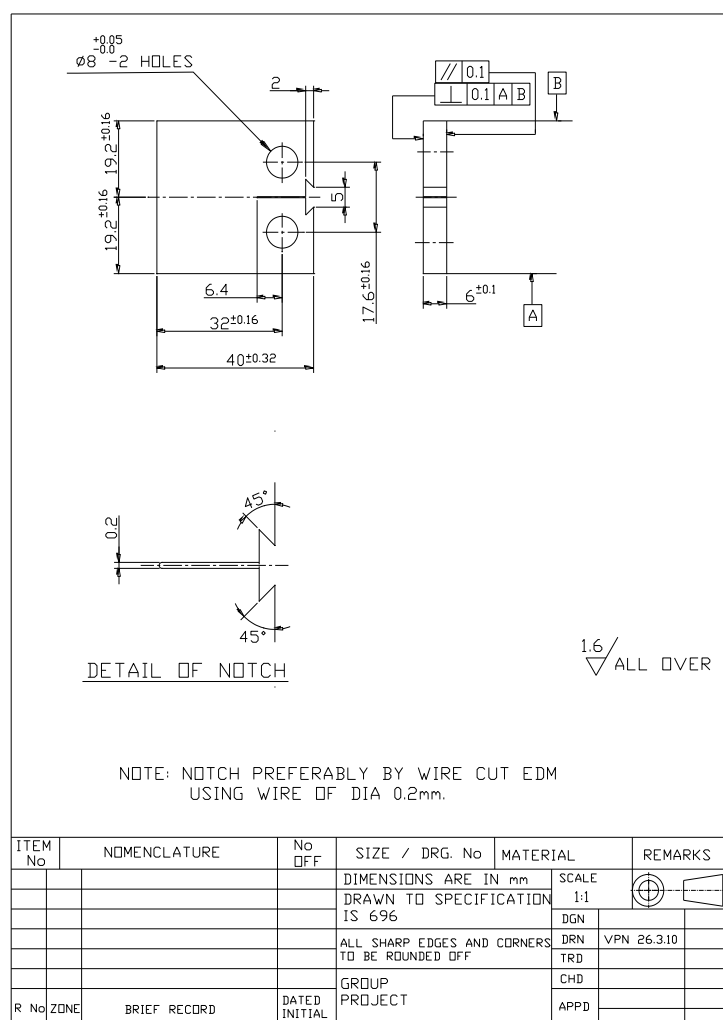


Fig. 7.1 Geometry of CT specimens used for fatigue crack growth testing.

The fracture related properties of a material usually depends on the orientation and direction of propagation of the crack in relation to the anisotropy of the material, which in turn depends on the principal directions of mechanical working or grain flow [Suresh 2004]. In the present study, the plan chosen for cutting out specimen

from the heat treated plates is shown schematically in Fig. 7.2a. Square in-plane section type test coupons were machined to the dimensions of CT specimens as per Fig. 7.1. These specimens were subsequently metallographically polished to facilitate crack length measurement. Further, fatigue starter notch of 2 mm was cut using 0.2 mm diameter wire in an electric discharge machine (EDM, Model No: Electra Supercut 734) in T-L orientation i.e., with the normal to the crack plane in transverse (width) direction, and the crack propagation along longitudinal (rolling) direction. EDM notched specimens were scribed every 0.5 mm in order to measure the crack length, as shown in Fig. 7.2b.

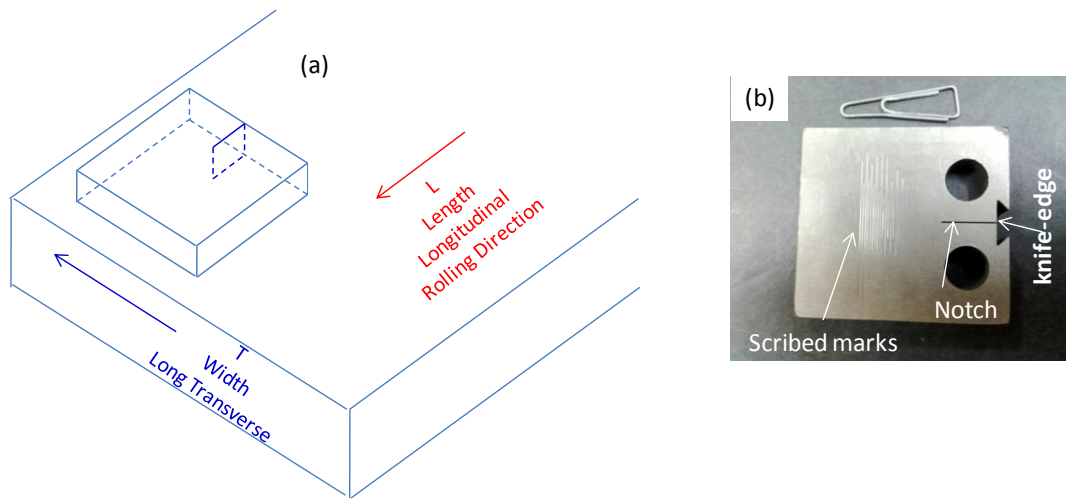


Fig. 7.2 (a) Schematic illustration of orientation of specimen extraction from plates and (b) photograph of CT specimen with knife-edge, fatigue starter notch and scribed marks used for fatigue crack growth testing.

7.2.2 Fatigue Pre-Cracking

A fatigue crack is considered to be the sharpest crack that can be reproduced in the laboratory. In order to meet the assumption of essentially zero notch root radius in the fracture crack growth analysis, the machined notch is extended in fatigue. The fatigue crack should extend at least $0.05W$ ahead of the machined notch to eliminate any effects of the geometry of the machined notch [ASTM Standard E: 647-13]. In the present study, fatigue pre-cracking was carried out at frequency of 10 Hz on Instron 8500 plus computer controlled servohydraulic test system as shown in Fig. 7.3 in laboratory air environment which provided the range of loading conditions necessary for pre-cracking from the machined notch. Tests were conducted under load shedding procedure [ASTM Standard E: 647-13]. For precracking the notched specimens, initial maximum load (P_{\max}) considering $R = 0.1$, was calculated used as per the following equation given in ASTM Standard E 647-13:

$$\Delta P = \Delta K \times B \times \sqrt{W} \times \frac{(1 - \alpha)^{3/2}}{(2 + \alpha) \times (0.886 + 4.64\alpha - 13.32\alpha^2 + 14.72\alpha^3 - 5.6\alpha^4)} \quad (7.1)$$

It is suggested that for the load controlled fatigue pre-cracking; the maximum load should be selected such that the maximum stress intensity factor (K_{\max}) in the initial portion of the fatigue cycle does not exceed 80% of the estimated plane strain fracture toughness (K_{Ic}) of the material [ASTM Standard E 647-13]. While

the K_{Ic} of Timetal 834 varies in the range of 38-44 MPa.m^{1/2} under quasi-static loading at room temperature [Prasad et al. 2009], the considered value of K_{max} (12 MPa.m^{1/2}) for calculating maximum load at $R = 0.1$ as per Eqn. (7.1) is ~ 30% of K_{Ic} which falls in the valid range for fatigue precracking. During crack monitoring, when the crack grew by 1 mm, the P_{max} was reduced to 4 kN from the initially applied maximum load of 5 kN. Subsequently, P_{max} was reduced to 3 kN when the crack length grew by 2 mm. Pre-crack size on the front and back side of the specimen was maintained within 0.025W. The emanation of fatigue pre-crack was observed by applying dye to the tip of the starter notch across the scribed marking. Subsequently, the size of the pre-crack was checked using profile projector (Model No: Delta TM 35) and the standard deviation between visually and optically measured precracked size was found to be ± 0.8 mm.

In general, one has to carry out fatigue pre-cracking at the temperature at which fatigue crack growth testing is aimed to be conducted, else the suggested criteria as per the standard is not met [ASTM Standard E: 647-13]. As per this criteria, when fatigue precracking is conducted at temperature T_1 and testing at different temperature T_2 , $K_{max(T1)}$ shall not exceed as per the equation:

$$K_{max(T1)} < 0.6 \left\{ \sigma_{ys(T1)} / \sigma_{ys(T2)} \right\} K_{Ic} \quad (7.2)$$

where $\sigma_{ys(T1)}$ and $\sigma_{ys(T2)}$ are the yield strengths at the respective temperatures T_1 and T_2 . One can use the conditional value of K_Q instead of K_{Ic} in Eqn. (7.2) if K_Q is

not found to be valid for K_{Ic} . As discussed in section 7.1, three temperatures viz. 300°C, 450°C and 600°C were considered for fatigue crack growth testing. Since K_{Ic} of this alloy in these temperatures is not reported in open literature, it was estimated from the reported elastic-plastic fracture toughness parameter J_{Ic} at 450°C and 600°C [Chandra Rao et al. 2008] using the formulae:

$$K_{Ic} = \sqrt{J_{Ic}E / (1-\nu^2)} \quad (7.3)$$

where, E is the Young's modulus and ν is the Poisson's ratio. The resulted values of K_{Ic} was found to be ~ 64 and 45 MPa.m^{1/2} at 450°C and 600°C, respectively. Considering these values as an input for Eqn. (7.2), the calculated values of K_{max} was found to be 51 and 42 MPa.m^{1/2} at 450°C and 600°C, respectively. Since the K_{max} value used for precracking is less than the required K_{max} as per Eqn. (7.1), fatigue precracking carried out at room temperature is found to be justified. While this estimation could not be attempted at 300°C due to non-availability of fracture toughness parameter in this test temperature, it is expected to fall in the same trend as that of 450°C and 600°C.

7.2.3 Fatigue Crack Growth Experiments

Fatigue crack growth (FCG) tests were carried out at 300°C, 450°C and 600°C as per ASTM Standard E 647-13 on fatigue precracked CT specimens using Instron 8500 plus servohydraulic test system equipped with resistance heated three zone

split furnace. A clevis and pin assembly was used at both top and bottom of the specimen for tension-tension loading, as shown in Fig. 7.3.

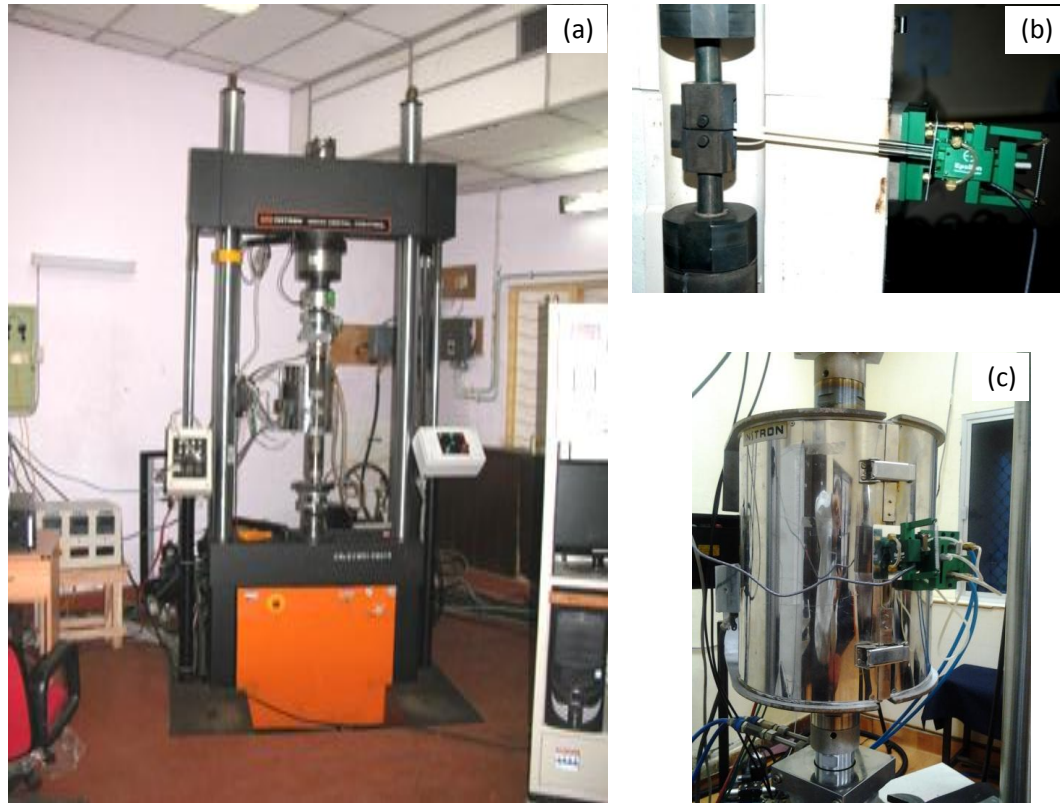


Fig. 7.3 Photographs of (a) Instron 8500 plus servohydraulic test system used for FCG testing and mounting arrangement of high temperature COD gauge (b) before and (b) after closing the resistance furnace.

Satisfactory alignment was obtained by keeping the centre line of the upper and lower loading rods coincident within 0.74 mm during the test and also by centering the specimen with respect to the clevis opening within 0.74 mm. Figs. 7.3a and b show the mounting arrangement of the CT specimen before and after closing the

resistance furnace. All the crack growth experiments were performed at a frequency of 1 Hz using a sinusoidal waveform and with load ratio of 0.1 in the laboratory air environment. All tests were started after soaking the specimen for 30 minutes at the test temperature. Crack lengths were measured by the elastic compliance technique [ASTM Standard E 647-13] using the high temperature crack opening displacement gauge (COD, Model No: Epsilon 3543-COD-005M-040M-ST) mounted on the front face of the CT specimen. In all these tests, to ensure accurate crack length measurement, the tests were interrupted 8 times and crack lengths were measured with an optical microscope (Model No: Leica DFC 295). For the tests carried out at 600°C, oxide layers were removed by polishing with emery papers before examining the interrupted specimen under microscope for crack length measurement. Three tests were conducted in all test conditions to confirm reproducibility of results.

The fatigue crack growth (da/dN) at each ΔK level was computed using the secant method as per ASTM Standard E 647-13:

$$(da/dN) = (a_{n+1} - a_n) / (N_{n+1} - N_n) \quad (7.4)$$

and ΔK was calculated using the formula,

$$\Delta K = \frac{\Delta P}{B\sqrt{W}} \frac{(2 + \alpha)}{(1 - \alpha)^{3/2}} (0.886 + 4.64\alpha - 13.32\alpha^2 + 14.72\alpha^3 - 5.6\alpha^4) \quad (7.5)$$

where $\alpha = a/W$ and a is the average crack length given by $(a_n + a_{n+1})/2$

7.2.4 Fractography and Measurement of Fracture Surface Roughness

In order to show the representative surface appearances of fatigue starter notch, precracked and crack growth, one half of the tested specimens at each test temperature are shown in Fig. 7.4. Fig. 7.4 shows the distinct precracked features with respect to fatigue starter notch and main crack growth.

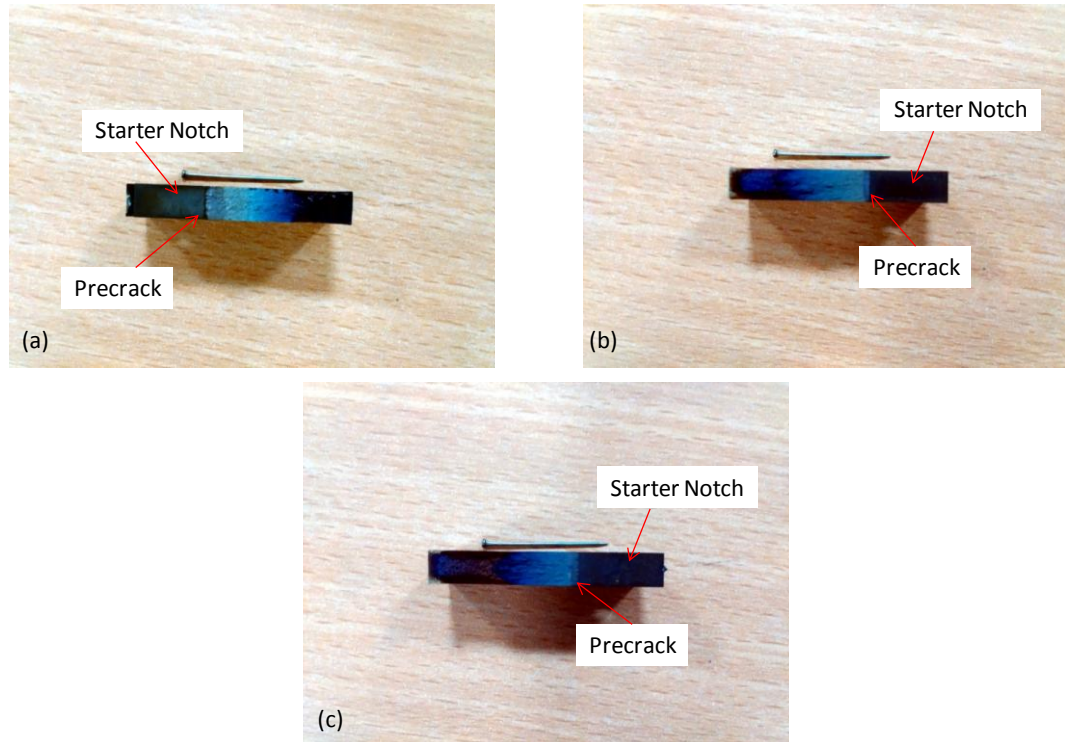


Fig. 7.4 Photographs of fatigue crack growth tested specimen at (a) 300°C (b) 450°C and (c) 600°C

The fracture region corresponding to low and high ΔK levels were cut using an ISOMET low speed saw (Model No: Buehler 11-1280-250). These samples were thoroughly cleaned using an ultrasonic cleaner for 10 minutes and then dried under infrared lamp before examining under SEM (Model No: FEI Quanta 400). The surface roughness profile of the fractured surface along the crack growth direction at low ΔK region was recorded using stylus based profilometer (Model: FORM TALYSURF 50). The average surface roughness (R_a) of this region has been determined using Intra II software of the profilometer.

7.2.5 Measurement of Plastic Zone Size using Microhardness

Plastic zone sizes around the crack tip were estimated from the Vickers microhardness (Model: Matsuzawa MMT X7) measurement as a function of distance from the crack tip at various ΔK levels. These values correspond to the stress intensity factor in the Paris Regime for both the temperature intervals. In microhardness measurement, the applied load was 200 g with a dwell time of 10 sec. Nickel was deposited electrolytically over the specimen along the crack length for the protection of the surface layer during the plastic zone size measurement.

7.2.6 Auger Electron Spectroscopy (AES)

An auger electron spectrometer (Model: OMICRON) with cylindrical mirror analyzer (Model: CMA-100) having an energy resolution of 0.4% was used to

estimate the composition and thickness of the layer formed at the fracture surface during testing. The Auger spectrum was taken with primary beam energy of 3 keV and current of $2 \mu\text{A}$. The Auger spectrum was taken from the fractured surface in the as received condition and also after 30 minutes of sputtering. The beam used for sputtering was 1 keV argon ions.

7.3 Results

7.3.1 Fatigue Crack Growth Rates

One set of representative FCG resistance curves in terms of da/dN versus ΔK corresponding to 300°C, 450°C and 600°C out of three conducted tests are shown in Fig. 7.5.

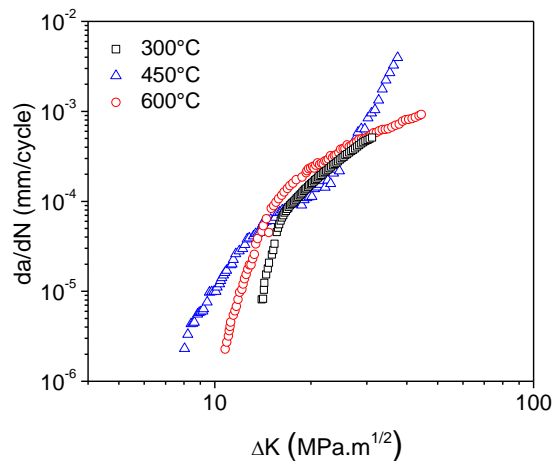


Fig. 7.5 Fatigue crack growth curves of Timetal 834 Ti-alloy at various test temperatures.

The plot clearly shows the well defined near-threshold and Paris regimes. The rate of crack growth in the linear region is known to be related to ΔK by the Paris-Erdogan equation given below [Paris and Erdogan 1963]:

$$da/dN = C(\Delta K)^m \quad (7.6)$$

where m is the slope of the plot in linear region. The value of C is determined by extending the straight line to $\Delta K = 1 \text{ MPa}\cdot\text{m}^{1/2}$. The values of the Paris constants (m and C) as a function of temperature are given in Table 7.1. It is clear from Fig. 7.5 that the alloy shows single slope at 300°C and 600°C as compared to bilinear slope at 450°C in Paris regime. Fig. 7.5 and Table 7.1 also show that the alloy exhibits higher crack growth rate at 450°C as compared to that at 300°C and 600°C.

Table 7.1: Parameters (Paris constants, maximum and cyclic crack tip opening displacement, average surface roughness, thickness of the oxide layer and cyclic plastic zone size) at various test conditions.

Temperature (°C)	δ_{\max} (μm)	δ_{cyclic} (μm)	R_a (μm)	δ_{oxide} (μm)	m	C	m (Closure corrected)	C	Cyclic plastic zone size (μm)
300°C	1.02	0.57	0.56	0.07	2.32	1.07×10^{-7}	2.12	5.17×10^{-7}	110
450°C	0.96	0.51	0.96	0.12	2.27	1.32×10^{-7}	2.22	9.8×10^{-7}	230
					5.96	1.63×10^{-12}	5.90	1.43×10^{-11}	
600°C									

7.3.2 Fracture Behavior

The fracture surfaces of the alloy at low and high ΔK levels for 300°C, 450°C and 600°C are shown in Fig. 7.6 and 7.7, respectively. At all test temperatures, the fracture surface reveals predominantly faceted behavior at low ΔK levels. Microstructural features corresponding to primary α phase as well as α laths within transformed β matrix has been clearly identified as specific facets in Figs. 7.6a-c.

At 600°C, the facets correspond to α phase are not so well defined as in the case of other two temperatures (Fig. 7.6c). However, cracking has been observed near segregated oxide particles (encircled in Fig. 7.6c) at 600°C as confirmed by energy dispersive spectroscopy (EDS) analysis (Fig. 7.6c). This typical appearance of fracture features remains same upto intermediate ΔK levels ($\sim 20 \text{ MPa.m}^{1/2}$). At higher ΔK ($\sim 30 \text{ MPa.m}^{1/2}$), striations were observed at all test temperatures (Fig. 7.7). However, these striations are not seen sharply because of thin oxide scale formation at 600°C (Fig. 7.7c).

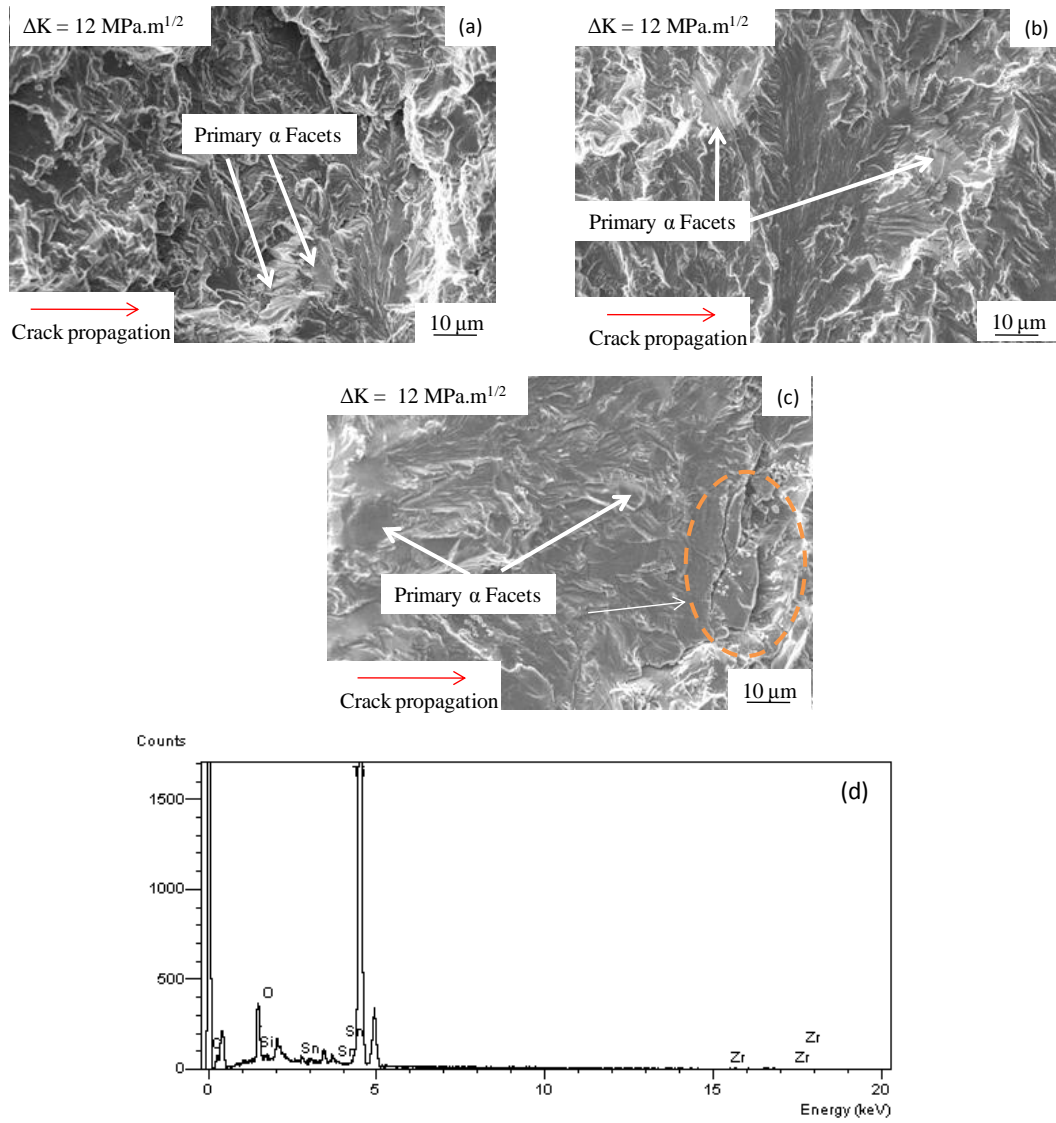


Fig. 7.6 SEM fractographs showing microstructurally sensitive crystallographic mode of stage I crack propagation at near threshold region at (a) 300°C (b) 400°C and (c) 600°C . EDS plot taken from encircled region of figure 7.6c is shown in figure 7.6d.

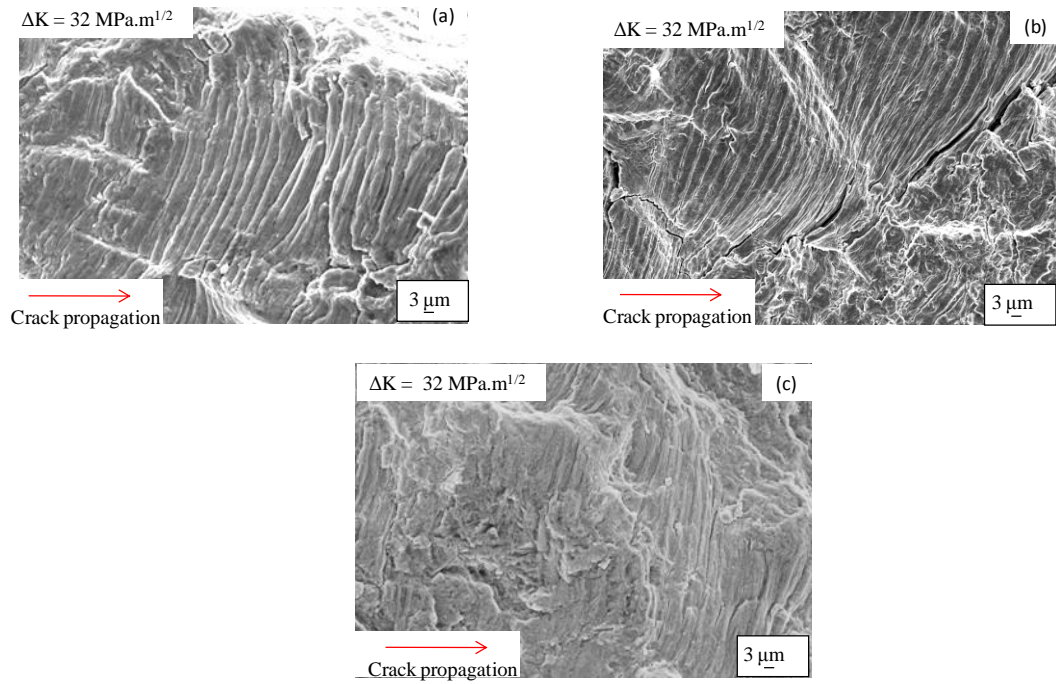


Fig. 7.7 SEM fractographs showing striated mode of crack propagation at (a) 300°C (b) 450°C and (c) 600°C.

7.3.3 Fracture Surface Roughness Profile

The surface roughness profile at low ΔK regime recorded along the crack growth direction at 300°C, 450°C and 600°C are shown in Fig. 7.8.

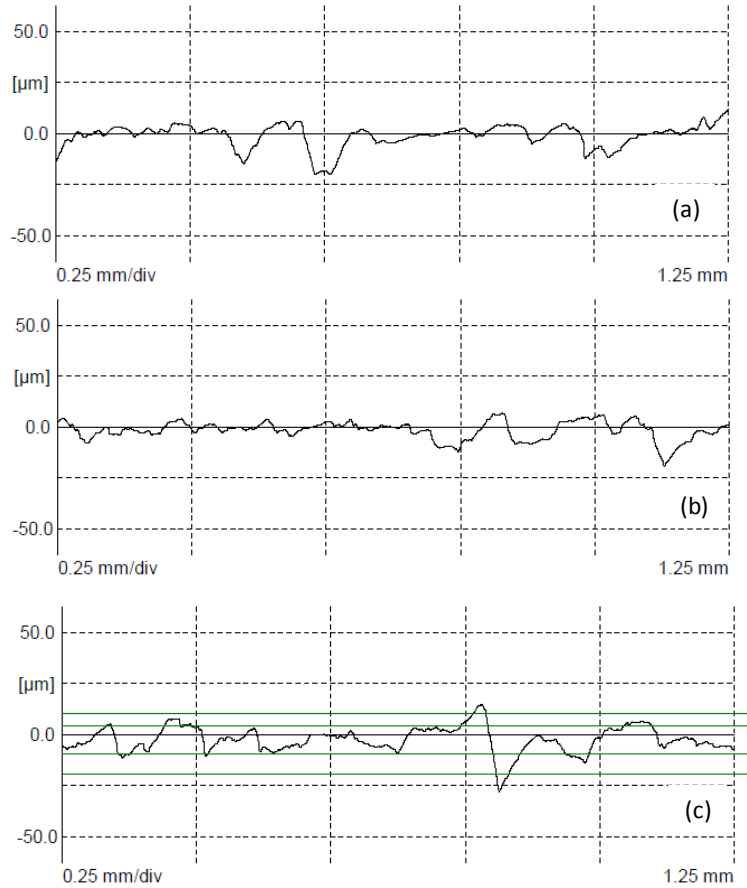


Fig. 7.8 Surface roughness profiles along the crack length direction at low ΔK region at (a) 300°C (b) 450°C (c) 600°C.

The surface roughness features has been observed at two different length scales. The larger length scale corresponds to about 200 μm , while the minimum

perturbations seen at the smaller length scale correspond to about 50 μm . This size is comparable to the prior beta grain size and any information about the influence of lath sizes on the fractured behavior could not be captured using this technique. The surface roughness (R_a) determined at the smaller length scale is included in Table 7.1. The average surface roughness (R_a) is observed to be higher at 600°C as compared to 300°C and 450°C. It is evident from Fig. 7.8 that the frequency of occurrence of perturbations is higher at 600°C as compared to 300°C and 450°C.

7.3.4 Estimation of Plastic Zone Size

The variation of microhardness with distance from the crack tip at all test temperatures is shown in Fig. 7.9. Cyclic and monotonic plastic zone sizes [Bannantine, Comer, Handrock 1990] ahead of the crack tip at all test temperatures have been estimated from the plot shown in Fig. 7.9. At 300°C and 650°C, the microhardness increases initially and levels off up to a certain distance from the crack tip, beyond which it again increases and levels off as a function of increasing distance from the crack tip. However, the microhardness profile at 450°C was observed to be distinct as compared to 300°C and 600°C. At 450°C, the microhardness decreases rapidly and levels off up to a certain distance from the crack tip, beyond which it again decreases and levels off as a function of increasing distance from the crack tip. While the onset of first leveling off represents the cyclic plastic zone size, the second one shows monotonic plastic zone size [Bathias and Pelloux 1973]. Cyclic plastic zone sizes thus measured are

listed in Table 7.1. The cyclic plastic zone increases with increase of test temperature.

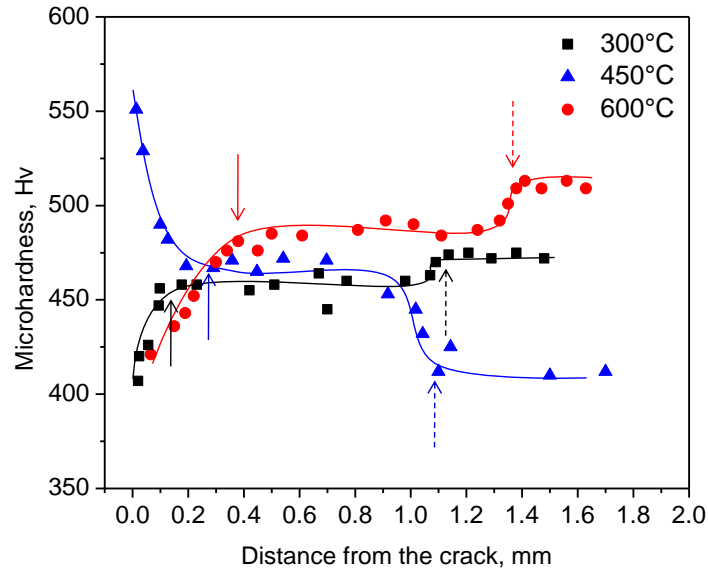


Fig. 7.9 Variation of microhardness as a function of distance from the crack tip at various fatigue crack growth test conditions. Solid and dashed arrows indicate the cyclic and monotonic plastic zone size, respectively.

7.3.5 Auger Electron Spectroscopy

The Auger electron spectra for all test conditions are shown in Figs. 7.10a-c. In general, apart from a peak of Ti, the as received spectrum contains peaks due to three interstitial elements C, N and O. The spectrum obtained after 30 min of sputtering for each sample is shown by dashed lines in Fig. 7.10.

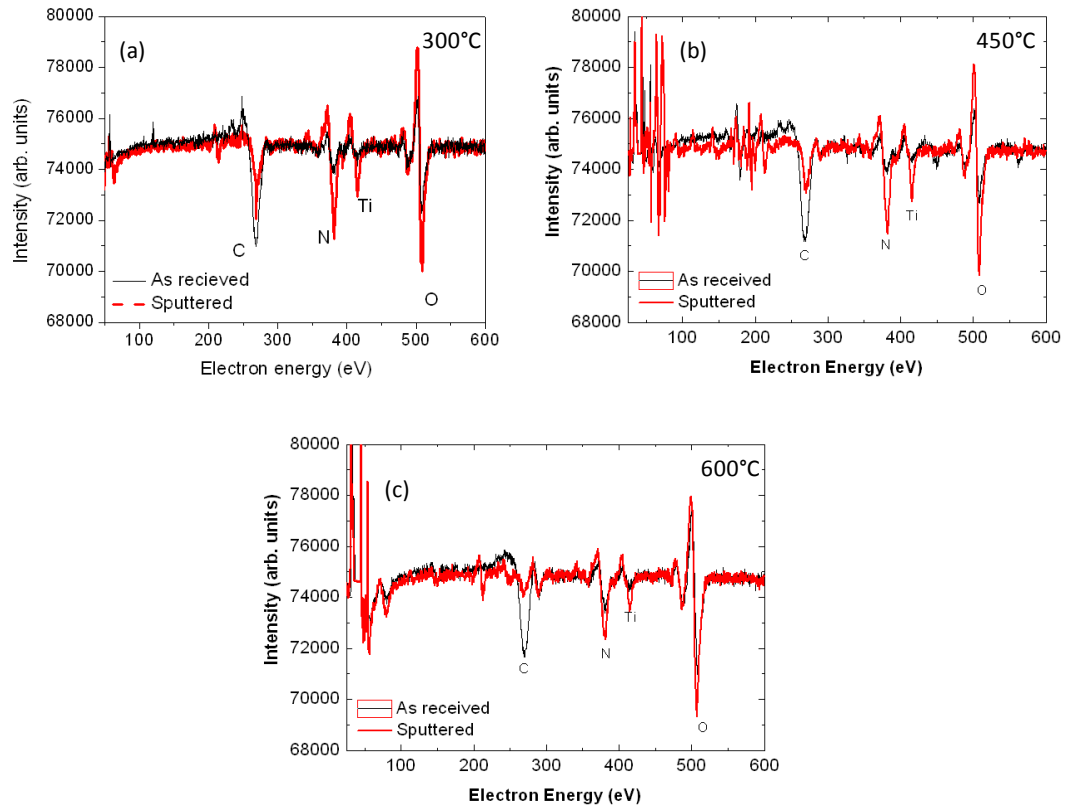


Fig. 7.10 Auger spectrum of tested specimens in near threshold region.

After 30 min of sputtering, all the four elements are present on the sample surface but the concentration of titanium has increased relative to that of interstitial elements. Since titanium nitride forms at temperature above 700°C [Koc and Glatzmaier 1997], it is presumed that in the temperature range over the testing has been done and whatever the nitrogen that is seen in the auger spectrum could be the molecular nitrogen adsorbed on to the sample surface. It is known that the TiC can form at temperature as low as 200°C [Koc and Glatzmaier 1997]. On the basis of this information, it is safe to assume that the layer which has formed at the crack tip is a mixture of TiC and TiO₂. Based on this assumption and EDS results as discussed in section 7.3.2, this layer is henceforth considered as oxide layer. The

sputtered oxide layer thickness determined from the AES analysis is listed in Table 7.1. It is imperative to note that the actual oxide layer thickness formed during the testing may be marginally lower than the determined values as AES is carried out after FCG testing.

7.4 Discussion

In general, fatigue crack growth behavior of metallic materials is influenced by modulus, yield strength, slip character at the crack tip and the kinetics of environmental interactions [Suresh 2004, Schijve 2009]. All these factors strongly depend on temperature. Hence the test temperature has an important role on fatigue crack growth behavior on these materials. In the present discussion, the effects of variation in modulus and the combined effect of modulus and yield strength on fatigue crack growth response through mechanistic viewpoint is discussed in section 7.4.1. As brought out in chapter II (Literature Survey), while stage I crack growth is predominantly influenced by the extrinsic damage micro-mechanisms such as crack closure, intrinsic damage micro-mechanisms predominantly influences the stage II crack growth behavior. Therefore in section 7.4.2, stage I and II crack growth behavior have been addressed using crack closure and microhardness measurements, respectively. In crack closure mechanisms, the possible role of surface roughness induced crack closure (RICC) and oxide induced crack closure (IOCC) at near threshold region will be critically assessed in this section. In addition to microhardness measurements, considering

FCG fundamentally a cyclic deformation process occurring at the crack tip [Saxena and Antolovich 1975, Bathias and Pelloux 1973], the closure corrected FCG curves in relation with the cyclic stress response of the alloy as a part of intrinsic damage micro-mechanism will be discussed in section 7.4.3.

7.4.1 Effects of Yield Strength and Modulus

In order to take into account the effect of temperature dependency of yield stress (σ_y) and modulus (E), the FCG curves as shown in Fig. 7.5 is replotted in terms of $\Delta K/E$ and $\Delta K^2/(\sigma_y E)$ as shown in Figs. 7.11a and b, respectively. Here, the crack driving force ΔK has been normalized with respect to σ_y and E. The values of σ_y and E as obtained from tensile tests at respective test temperatures (chapter IV) are considered for this analysis. While Fig. 7.11a can be considered as a normalization of the crack driving force with modulus, Fig. 7.11b can be viewed as a crack growth response as a function of CTOD ($CTOD \sim \Delta K^2/\sigma_y E$), [Suresh 2004] which inherently takes into account the combined effect of variation in yield strength and modulus with test temperature. It is clear from Fig. 7.11a that the normalization of ΔK with E results in consolidation of FCG curves at 300°C and 600°C. Moreover, Fig. 7.11b shows that although the difference in FCG rates are considerably reduced with respect to normalization with $\sigma_y E$, but a complete collapse into a single curve has not been observed.

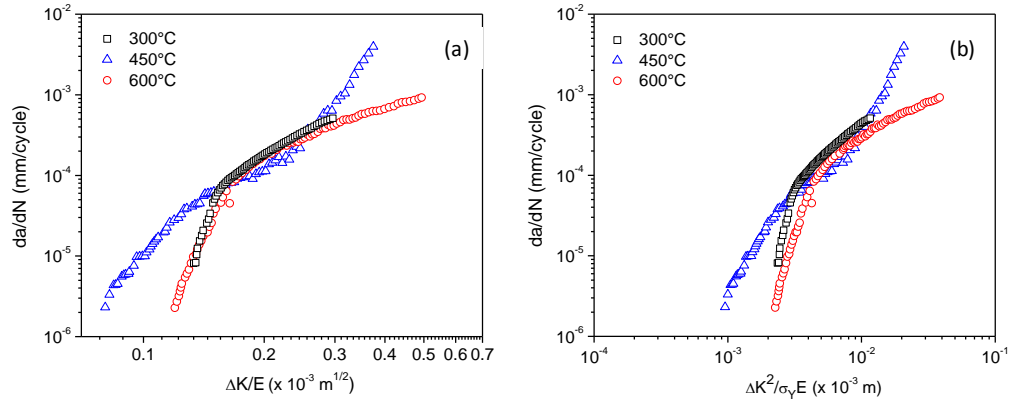


Fig. 7.11 (a) da/dN versus $\Delta K/E$ and (b) da/dN versus $\Delta K^2/\sigma_y E$ at various test conditions

It is apparent from these figures that the variation in yield strength and modulus does not fully account for the change in fatigue crack growth. In order to study the influence of extrinsic damage micromechanisms, the effect of crack closure on fatigue crack growth behavior is studied and discussed in subsequent section.

7.4.2 Characteristics of Crack Closure

In order to quantify the crack closure effects, the effective stress intensity, ΔK_{eff} , values were obtained from the equation [ASTM Standard E647-13]:

$$\Delta K_{eff} = K_{max} - K_{cl} \quad (7.7)$$

where, K_{cl} was determined using the recommended practice for determination of fatigue crack opening load from compliance method mentioned [ASTM Standard E 647-13] details of which has been explained in Appendix A. The FCG resistance curves in terms of da/dN versus ΔK_{eff} are shown in Fig. 7.12.

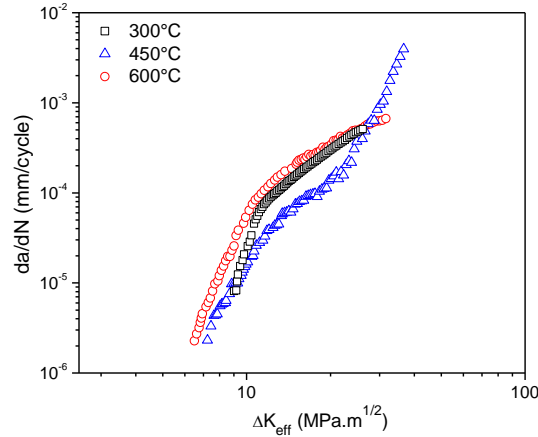


Fig. 7.12 Closure corrected fatigue crack growth curves at various test temperatures.

The slope of the Paris regime determined from Fig. 7.12 is listed in Table 7.1. It can be seen from Table 7.1 that after closure correction, m decreases significantly at 600°C as compared to 300°C and 450°C. This in turn shows that closure has a maximum effect at 600°C, however, its effect is marginal at 300°C and 450°C. It can be also be inferred from Fig. 7.12 that the near threshold region of intrinsic FCG curves were shifted to lower ΔK_{eff} ranges as compared to Fig. 7.5. Similar to the analysis as that of section 7.4.1, these intrinsic FCG curves were replotted as a function of $\Delta K_{eff}/E$ and $\Delta K_{eff}^2/(\sigma_y E)$ and are shown in Figs. 7.13a and b,

respectively. Considering the influence of these parameters on FCG response of the alloy, it is evident from Fig. 7.13a that the near threshold region of all FCG curves is converged to a narrow band for all test temperatures. Collapsing of TMFCG data using $\Delta K^2/(\sigma_y E)$ shows that the crack growth is not only affected by closure but it is also a function of CTOD.

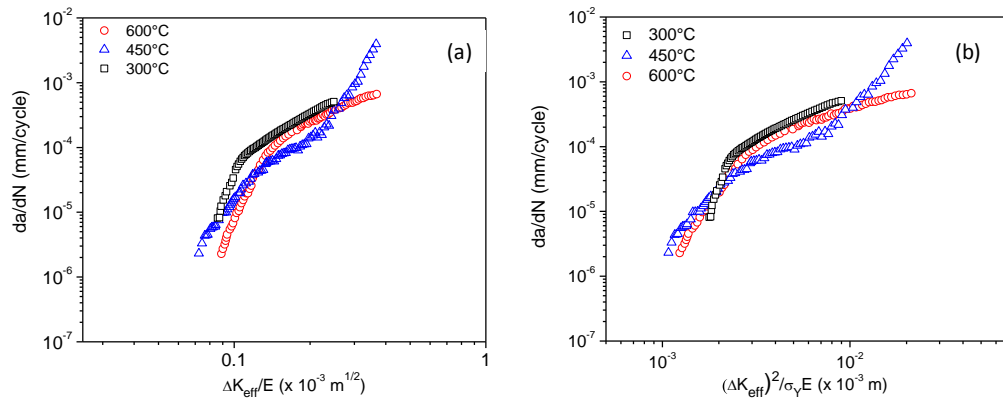


Fig. 7.13 Closure corrected fatigue crack growth curves as a function of (b) modulus and (c) CTOD at various test temperatures

The schematic layout (Fig. 7.14) illustrating the signature of different types of crack closure mechanisms namely plasticity (PICC), surface roughness or asperity (RICC) and oxide debris (OICC) when they are present together is presented in open literature [Allison 1988]. It can be seen from Fig. 7.14 that these interactions can be viewed by investigating the dependence of opening or closing stress intensity factor (K_{op} or K_{cl}) on maximum stress intensity factor (K_{max}). While in case of PICC K_{cl} increases linearly with increase in K_{max} , OICC which is restricted to low values of ΔK because it is there that the CTOD are small and lead to

enhanced fretting assisted oxidation of the fractured surfaces, K_{cl} decreases rapidly with increase in K_{max} . Considering RICC primarily due to mode II crack tip displacements, K_{cl} decreases or at most remain insensitive with increase in K_{max} .

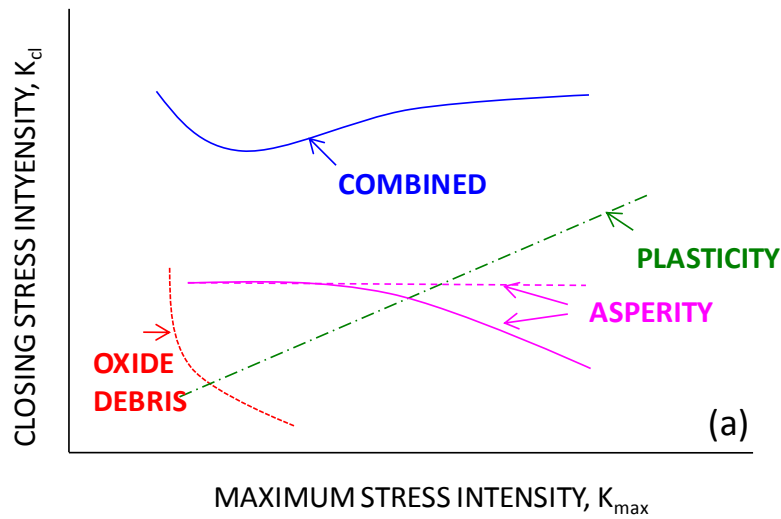


Fig. 7.14 Schematic plot of K_{cl} versus K_{max} illustrating various types of crack closure mechanisms [Allison 1988]

In the present investigation, the dependence of K_{cl} on K_{max} has been investigated in order to identify the most likely operative crack closure mechanism in these test conditions. The variation of K_{cl} versus K_{max} for all FCG test conditions is shown in Fig. 7.15a. At 600°C, K_{cl} is found to be initially decreasing rapidly with increasing K_{max} up to $\sim 20 \text{ MPa.m}^{1/2}$. Beyond this K_{max} , it increases upto $\sim 25 \text{ MPa.m}^{1/2}$ and thereafter levels off as a function of increasing K_{max} . However, at 300°C and 450°C, the variation in K_{cl} does not show the same trend. In these temperatures, K_{cl} decreases gradually with increasing K_{max} up to $\sim 15 \text{ MPa.m}^{1/2}$, beyond which it

increases upto $\sim 20 \text{ MPa.m}^{1/2}$ and levels off. The trend in the variation of K_{Cl} with K_{max} shows that although the combined effects of crack closure mechanisms operate at near threshold region, however, as is clear from Fig. 7.14, the effects of RICC and OICC appears to be predominant. The variation of closure ratio (K_{Cl}/K_{max}) versus K_{max} is shown in Fig. 7.15b. Fig. 7.15b shows that the closure level increases with decreasing K_{max} and most importantly, the alloy exhibits highest level of crack closure at 600°C than that of 300°C and 450°C .

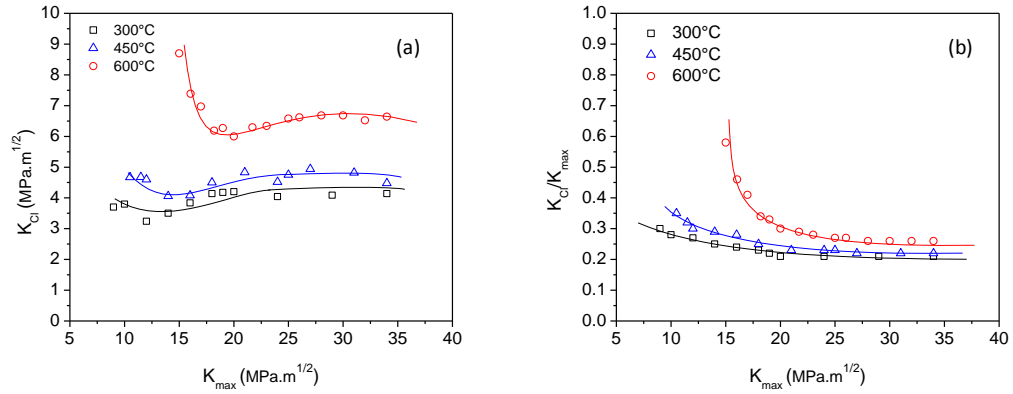


Fig. 7.15 Variation of (b) K_{cl} versus K_{max} and (c) K_{cl}/K_{max} versus K_{max} at various test temperatures.

While each crack closure mechanism is associated with a characteristic value, comparison of this value with that of cyclic crack tip opening displacement (CTOD) provides a reasonable assessment for the confirmation of crack closure mechanism [Suresh 2004]. The characteristic value for RICC and OICC are the average surface roughness (R_a) and thickness of oxide layer (δ_{oxide}), respectively [Suresh 2004]. The values of R_a and δ_{oxide} as determined from the stylus based

profilometer and AES analysis at near threshold region is included in Table 7.1. The CTOD parameters (maximum and cyclic) were computed using the formulae [Suresh 2004]:

$$\delta_{\max} \approx (0.5K_{\max}^2 / \sigma_Y E) \quad (7.8)$$

$$\delta_{\text{cyclic}} \approx (0.5K_{\max}^2 / 2\sigma_{CY} E) \quad (7.9)$$

where, δ_{\max} is the maximum crack tip opening displacement, δ_{cyclic} is the cyclic crack tip opening displacement, K_{\max} is the maximum stress intensity factor, σ_Y is monotonic yield strength, σ_{CY} is the cyclic yield strength and E is the Young's modulus. δ_{\max} and δ_{cyclic} are also enumerated in Table. 7.1. σ_{CY} is determined from the hysteresis loops at half-life at respective test temperatures (chapter V). It is clear from Table 7.1 that the values of R_a are higher than that of corresponding CTOD parameters for all test conditions. While the values of δ_{oxide} are lower than that of the CTOD parameters at 300°C and 450°C, it is comparable at 600°C. Most importantly, R_a appears to be higher in magnitude as compared to δ_{oxide} in all FCG loading.

From a comparison of the characteristic values of crack closure and CTOD parameters, it is apparent that the RICC is a dominant crack closure mechanism at all test conditions. However, the combined effect of RICC and OICC is noticeable at 600°C. The dominance of RICC in titanium alloys can be primarily attributed to the fact that limited ductility of hcp crystal structure due to lower symmetry [Yoo

1981, Kocks and Westlake 1967] generally results in poor accommodation of misfitting opposite fracture surfaces. Faceted crack growth behavior as observed in Fig. 7.6 is attributed to propagation of crack on low index planes highly inclined to the stress axis along slip bands that were developed during prior loading cycles [Yoder et al. 1977, Gray et al. 1983, Pilchak et al. 2009]. This might lead to development of significant mode II displacements at the crack tip which eventually promotes the RICC [Chesnutt et al. 1984, Minakawa and McEvily 1981]. This explanation is further supported by the observation of very large ratio of mode II to mode I crack opening displacements at near threshold region [Vander Velde and Koss 1981]. On the other hand, based on the observation of oxide layer of thickness comparable to that of cyclic crack tip opening displacements at 600°C, it is conceivable that the oxide layer which forms at this temperature could effectively wedge the crack tip and leads to OICC. The transition from crystallographic to striated region at this temperature has been observed at $\Delta K \sim 22 \text{ MPa.m}^{1/2}$. The shifting of this transitional behavior can be rationalized on the basis that the formation of oxide layer of comparable thickness as that of δ_{cyclic} can enhance the RICC with the contribution from mixed mode displacements at 600°C. In order to validate this statement, crack paths have been observed at low and high ΔK regions. In order to observe the crack path profile, nickel coating has been applied on the fracture surface to preserve the crack face before mounting on bakelite block. At all test temperatures, crack branching has been observed at low ΔK regions as shown in Figs. 7.16a-c. However, the propensity of main crack towards crack branching was observed to be higher at 600°C than that at 300°C

and 450°C. At 450°C, the secondary crack path profile shows branching predominantly across α_p grains (Fig. 7.16b). However, at 600°C, unlike 450°C, the secondary crack path clearly shows crack branching along α_p/β interface which further advances to the nearest α_p/β interface (Fig. 7.16c). This qualitative interpretation shows that considerable mixed mode displacements occurring due to the combined effect of OICC and RICC leads to preferential crack branching at 600°C than that at other test temperatures.

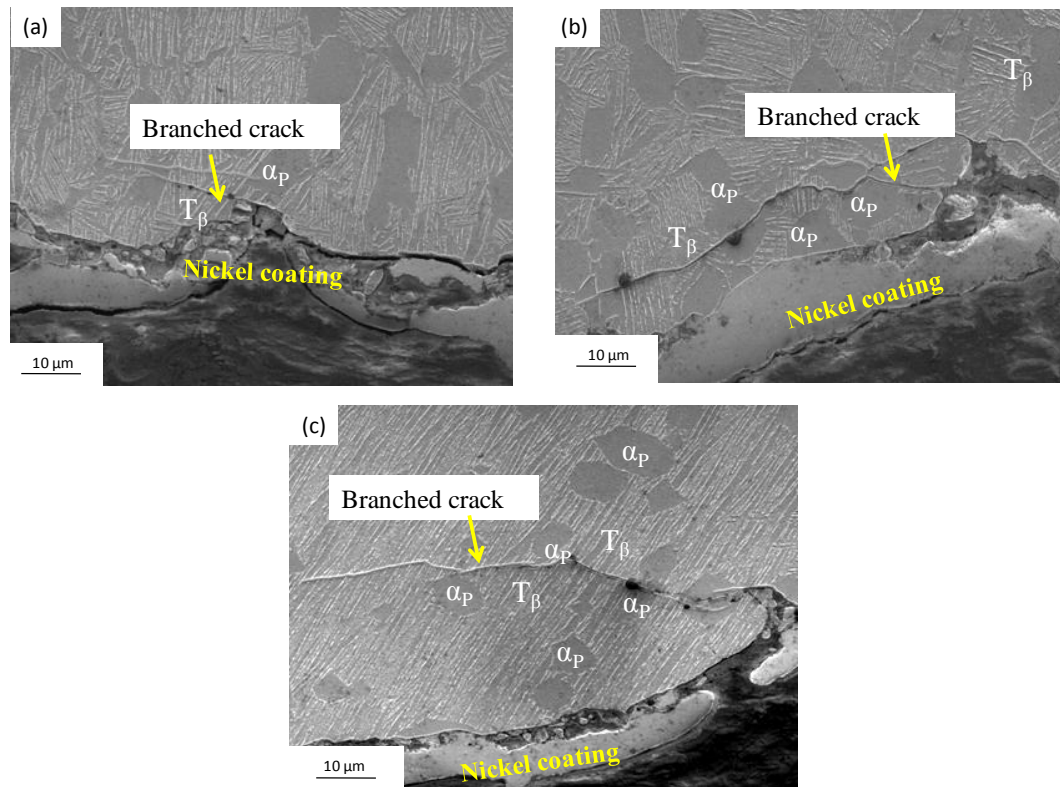


Fig. 7.16 SEM microstructures at low ΔK region showing different extent of crack branching at (a) 300°C (b) 450°C and (c) 600°C.

At higher ΔK regions, relatively straight crack propagation has been observed without any evidence of crack branching at all the temperatures as shown in Fig. 7.17. It is believed that “oxide induced RICC” in addition to “symmetry induced RICC” leads to significant increase in R_a at 600°C which is nearly three times as that of other two test temperatures. This is in line with the observation that the transient response of K_{cl} extends up to higher value of K_{max} at 600°C than that of other two test temperatures (Fig. 7.15b). This further confirms that closure has a significant effect at 600°C where delay in onset of striated mode of crack propagation leads to decrease in fatigue crack growth rate. This analysis is partly in agreement to the study which showed that the closure correction on the da/dN vs. ΔK plot decreases the slope of the curve, particularly in the low ΔK , stage I region [Ghonem and Foerch 1991].

7.4.3 FCG Based on Micro Crack Tip LCF Process

The propagation of a fatigue crack is accompanied by a plastically deformed region at its tip [Wei 2010] and the amount of plastic deformation is restricted by the surrounding elastic material. The size of this plastically deformed region is commonly referred as plastic zone size which influences the state of stress occurring at the crack tip [Broek 1984]. An estimation of its size can be attempted empirically using fracture mechanics [Broek 1984] or more realistically using characterization tools [Bathias and Pelloux 1973, Klesnil and Lukas 1969, Liu and Iino 1969].

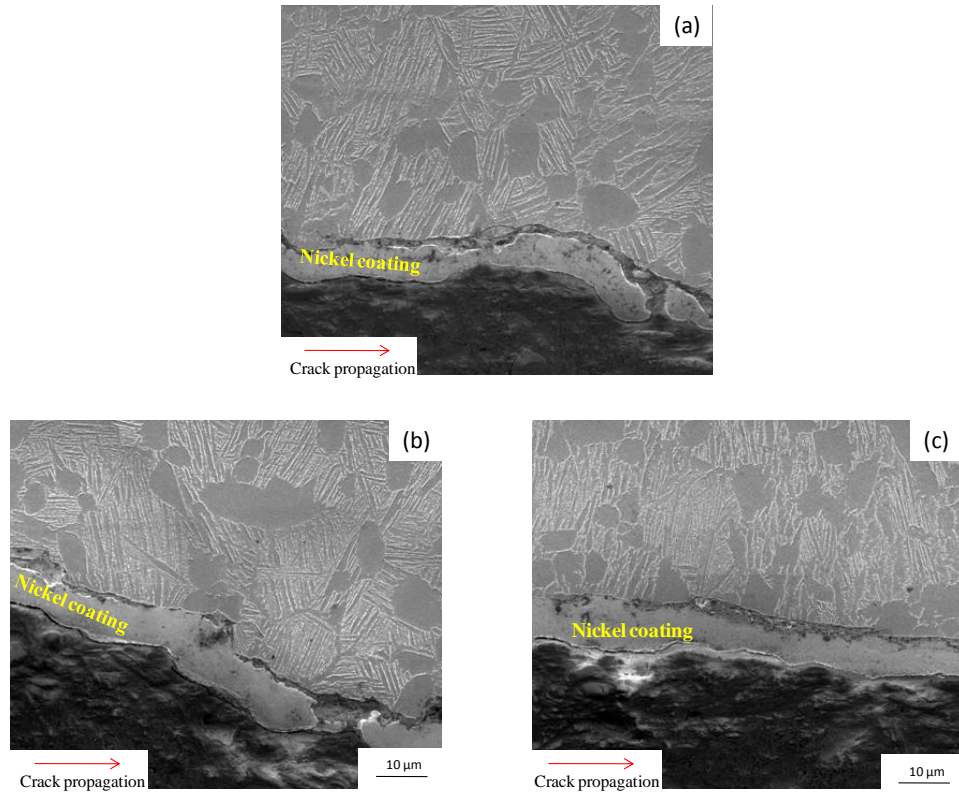


Fig. 7.17 SEM crack path profile at higher ΔK region at (a) 300°C (b) 450°C and (c) 600°C.

While both sizes of plastic zones can be estimated with relative ease using microhardness which can detect local work hardening due to plastic strains as small as 1 pct. [Bathias and Pelloux 1973], the trend in the variation of microhardness versus distance to the crack tip provides invaluable information about cyclic hardening or softening occurring at the crack tip. The characteristics of cyclic hardening and softening in terms of variation of microhardness with distance from the crack tip are shown schematically in Fig. 7.18. While microhardness decreases with increase in distance to the crack tip in case of cyclic

hardening, cyclic softening is characterized by the increase in microhardness with increase in distance from the crack tip. Based on this trend, it can be inferred from Fig. 7.9 that in the present study, the alloy exhibits cyclic hardening at the crack tip at 450°C and cyclic softening at both 300°C and 600°C. The relatively higher crack growth rate observed at 450°C could partly be attributed to cyclic hardening at 450°C (Chapter V). Although the transient LCF response in terms of cyclic hardening/softening of smooth specimens could not be directly correlated with increase or decrease in fatigue crack growth rate because of the development of complex stress/strain fields at the crack tip of fracture mechanics type specimens, it is important to mention that for high strength materials, the driving force for crack propagation is maximum stress which results from the imposed cyclic straining and not the applied strain range or the strain energy density [Marchand et al. 1988].

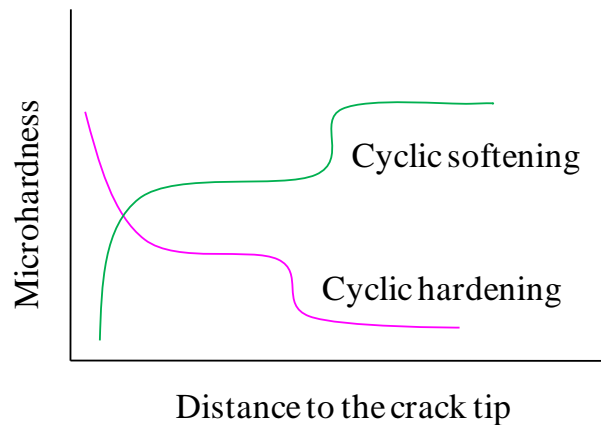
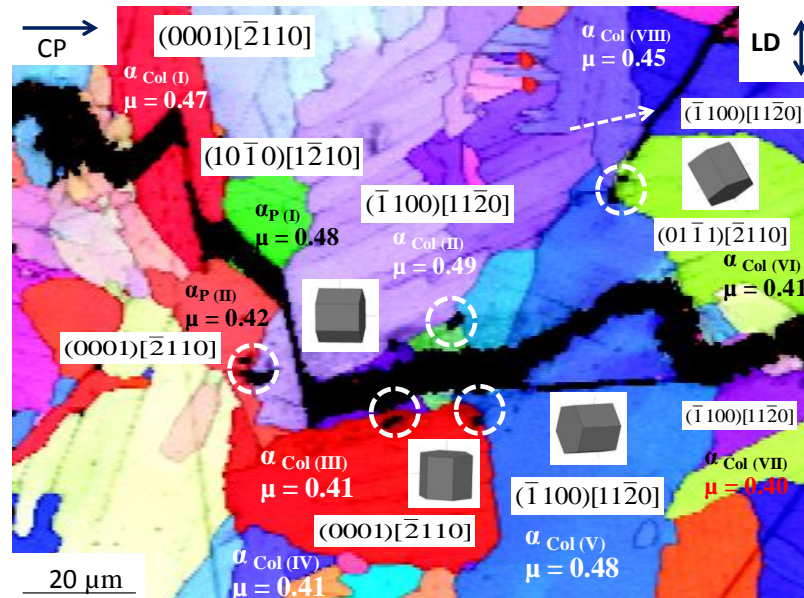


Fig. 7.18 Schematic illustration of cyclic softening and hardening behavior at the crack tip

Considering this vital fact in the present investigation (the peak tensile stress as the maximum stress increases significantly after short period of initial cyclic softening at 450°C (chapter V)), the increase in stress acting at the head of the dislocation pile-up is expected to increase the crack growth rate during cyclic hardening [Antolovich and Armstrong 2014, Embley and Russel 1984]. This is most likely if the fracture criterion is stress based wherein the driving force for cracking is maximum tensile stress (σ_{\max}) [Antolovich and Armstrong 2014] and not strain based. And it has been confirmed that the fracture criteria in this alloy is stress based at ambient as well as at high test temperatures [Prasad and Kamat 2010, Chandra Rao et al. 2008]. While this cyclic hardening is primarily due to dynamic strain aging (DSA) (chapter V), it is concluded that DSA increases the crack growth rate at 450°C. The detailed view on the mechanical environment around the crack tip due to DSA has been reported [Graff et al. 2005]. They have reported the development of intense strain localization bands at the crack tip through FE simulations. It is anticipated that the strain bursts in these bands and heterogeneous movement of bands at the crack tip could lead to increase in crack growth rate. In this alloy, decrease in mode I as well as mixed mode II fracture toughness [Chandra Rao et al. 2008] and reduction in LCF life [Prasad et al. 2008] in the intermediate temperature region 350°C-500°C due to DSA also support this observation. Thus, as discussed in section 7.4.2, since stage II crack growth behavior is influenced by CTOD per cycle in conjunction with crack closure mechanisms, the effect of cyclic hardening at the crack tip cannot be ruled out.

7.5 Summary

Fatigue crack growth behavior of Ti-alloy Timetal 834 has been studied at 300°C, 450°C and 600°C under constant load amplitude cycling. Amongst the temperature studied, the alloy exhibited higher crack growth rate at 450°C as compared to 300°C and 600°C. Cyclic hardening occurring at the crack tip as revealed by microhardness measurements was attributed to increase in the crack growth rate at 450°C. Surface roughness induced crack closure as a predominant crack closure mechanism influences the stage I crack growth rates at all temperatures. However, the effect of oxide induced crack closure as revealed by Auger electron spectroscopy was found to be significant at 600°C as compared to 300°C and 450°C. It is surmised that the oxide induced crack closure leads to increase in average surface roughness which eventually retards the crack growth rate at 600°C.



Chapter VIII

Thermomechanical Fatigue Crack Growth Behavior

8.1 Introduction

In designing critical components of an advanced gas turbine engine, the synergism between thermomechanical fatigue (TMF) and damage-tolerant approach has not attracted the same attention as that of TMF and safe-life approach. This could be largely attributed to the inherent difficulties and uncertainties in carrying out fatigue crack growth (FCG) experiments under TMF loading (TMFCG) using fracture mechanics type SENT or CT specimens and partly due to unavailability of international standard for carrying TMFCG experiments [Marchand et al. 1988]. Limited available information in open literature also makes these experiments extremely challenging. The reliability of damage tolerant based TMF database depends on the understanding of the researcher towards various associated errors and corrections involved during the experiments and analysis of test results. Although initial reports on TMFCG have been published in open literature in late 1970s, details pertaining to TMFCG experiments and analysis of test results have been emphasized by three research groups [Koizumi & co-workers 1983 and 1987, Pelloux & co-workers 1984, 1986, 1988 and Nicholas & co-workers 1988 and 1989]. It is imperative to note that long crack based TMFCG tests can be carried out in fully elastic (small scale yielding) and elastic-plastic (large scale yielding) conditions. Although in load controlled TMFCG experiments, the condition of thermal strain compensation does not arise, one need to ensure the absolute minimum thermal gradients near the in-plane and out-of-plane dimensions adjacent to the crack tip prior to starting the TMFCG tests [Yuan and Kalkhof 1999].

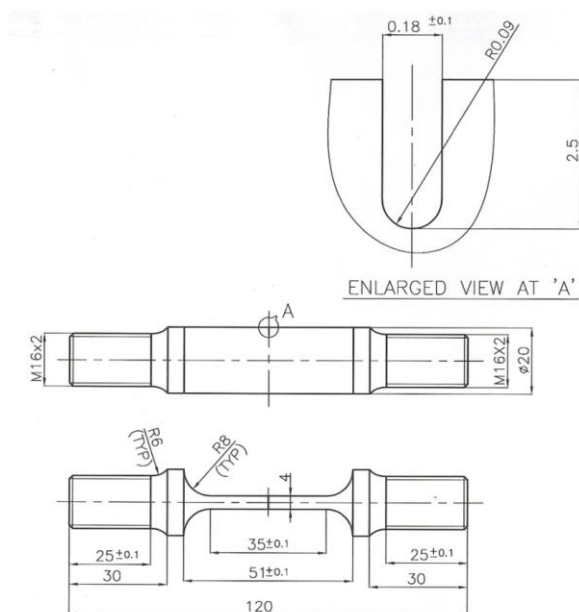
The fatigue crack growth behaviour of Timetal 834 under isothermal test conditions has been discussed in chapter VII. However, as an input to damage tolerant design methodology under non-isothermal (thermomechanical) loading, no report is available in open literature on TMFCG behaviour of high pressure compressor discs made of titanium alloys. Therefore, in this chapter, we examine the fatigue crack growth behaviour of Timetal 834 under thermomechanical loading to bring out the effects of phase angle i.e. in-phase and out-of-phase and temperature intervals ($300^{\circ}\text{C} \leftrightarrow 450^{\circ}\text{C}$ and $450^{\circ}\text{C} \leftrightarrow 600^{\circ}\text{C}$) on fatigue crack growth rates. While TMFCG behaviour in context to intrinsic and extrinsic damage micro-mechanism has been studied using the same characterisation tools as outlined in chapter VII, an additional technique using electron back scattered diffraction has been employed to implicitly understand the effect of local crystallographic orientation on crack growth.

8.2 Experimental Procedures

8.2.1 Extraction and Preparation of Specimens

Single edge notched tension (SENT) type specimens as per ASTM Standard E 647-13 having a width of 20 mm and thickness of 4 mm as shown in Fig. 8.1 were fabricated from 18 mm thick heat treated plates. The schematic illustration of orientation of test coupon extraction is shown in Fig. 8.2. In these specimens, the fatigue starter notch was cut in the same orientation as that of CT specimens (Chapter VII) i.e. in T-L orientation

with the crack propagation along rolling direction of the plate. These specimens were metallographically polished and subsequently scribed with marks to facilitate crack



length measurement.

Fig. 8.1 Single edge notch tensile (SENT) specimen geometry used for TMFCG tests (all dimensions are in mm).

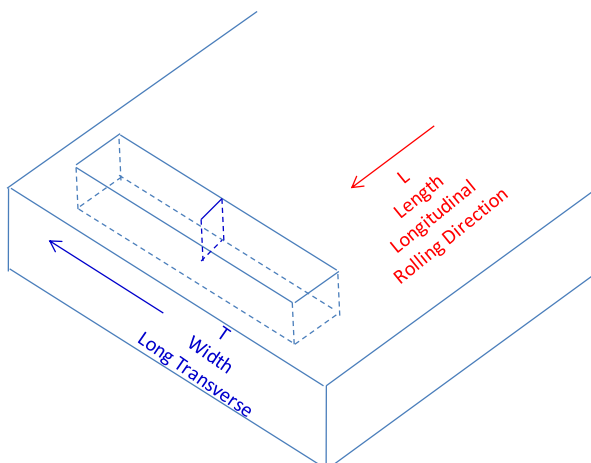


Fig. 8.2 A schematic illustration of orientation of test coupon with respect to rolling direction of plate.

8.2.2 Fatigue Pre-Cracking

A fatigue starter notch of 2 mm was cut using 0.2 mm diameter wire in an electric discharge machine (EDM, Model No: Electra Supercut 734) in the orientation as shown in Fig. 8.2. Fatigue pre-cracking was carried out at frequency of 10 Hz on ± 100 kN capacity computer controlled MTS 880 servohydraulic test system in laboratory air environment. Tests were conducted under load shedding method with load ratio, $R = 0.1$. For precracking the notched specimens, initial maximum load (P_{\max}) corresponding to stress intensity factor of $12 \text{ MPa}^{1/2}$ at $R = 0.1$, was calculated used as per the following equation given in ASTM Standard E 647-13:

$$\Delta P = \Delta K \times B \times \sqrt{W} \times \frac{1}{\alpha^{1/2} [1.4 + \alpha] [1 - \alpha]^{3/2} F(\alpha)} \quad (8.1)$$

$$F(\alpha) = 3.97 - 10.88\alpha + 26.25\alpha^2 - 38.9\alpha^3 + 30.15\alpha^4 - 9.27\alpha^5$$

where α is a/w .

The exercise as explained in detail in section 7.2.2 of chapter VII for ensuring the validity of fatigue precracking at room temperature holds true for SENT specimens also. During fatigue precracking, it was ensured that the maximum stress intensity factor (K_{\max}) in the initial portion of the fatigue cycle does not exceed 60% of the estimated plane strain fracture toughness (K_{Ic}) of the material. In all specimens, crack grew to the extent of 2

mm by load shedding procedure. Pre-crack size on the front and back side of the specimen was maintained within 0.025W. Same methods as explained in chapter 7 were adopted for detecting the onset of crack extension (dye) and checking crack length (profile projector). The standard deviation between visually and optically measured precracked size was found to be ± 0.07 mm.

8.2.3 Measurement of Thermal Gradient and TMFCG Test Procedure

An in-house developed Infrared heating based TMF test facility [Prasad and Kumar 2011] was utilized for carrying out TMFCG experiments. All TMFCG experiments were performed at a frequency of 1 Hz under constant load using a triangular waveform and with load ratio of 0.1 in the laboratory air environment. Fatigue crack growth experiments were carried out employing the same waveforms i.e. ‘in-phase’ (IP-TMF) and ‘out-of-phase’ (OP-TMF) and temperature intervals $300^{\circ}\text{C} \leftrightarrow 450^{\circ}\text{C}$ and $450^{\circ}\text{C} \leftrightarrow 600^{\circ}\text{C}$ as that of TMF experiments on tubular specimens (chapter VI). The employed heating and cooling rates during these experiments were also maintained same as that of tubular specimens (5°C/s). All tests were started after soaking the specimen for 30 minutes at the maximum test temperature of respective temperature intervals. In all these tests, to ensure accurate crack length measurement, crack lengths were also measured optically by interrupting the tests 10 times with an optical microscope (Model No: Leica DFC 295). For the tests carried out at higher temperature intervals viz. $450^{\circ}\text{C} \leftrightarrow 600^{\circ}\text{C}$, oxide layers were removed by polishing with emery papers before examining the interrupted specimen under microscope for crack length measurement.

In TMF testing, it is imperative to note that the specimen geometry, thermal conductivity of the material, heating and cooling rate, positioning and design of the heating medium (Quartz bulbs in case of infrared heating or coils in case of induction heating) plays an very important role as it strongly effects the development of thermal gradient in the test specimen [Hahner et al. 2006]. Standard on TMF testing [ASTM Standard E 2368-10] clearly specifies the acceptable level of axial thermal gradient ($\pm 1\%$ of T_{\max} , where T_{\max} is the maximum cyclic temperature), beyond which it may lead to various inherent uncertainties in carrying out TMF tests. In the present investigation, in order to ensure the absolute minimum temperature gradients which invariably ensure the dominance of larger zone of crack driving force [Yuan and Kalkhof 1999], longitudinal and transverse thermal gradients have been measured. Four K-type thermocouples TC₁, TC₂, TC₃ and TC₄ were spot-welded in the central section of the SENT specimen as shown schematically in Fig. 8.3.

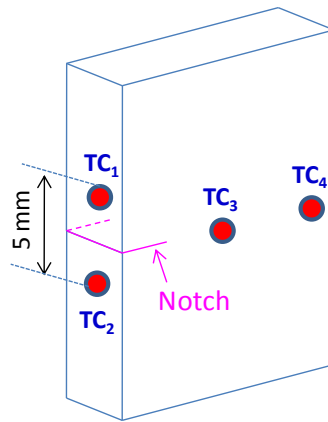


Fig. 8.3 Schematic illustration of positioning of various thermocouples (TC₁, TC₂, TC₃ and TC₄) near fatigue starter notch of central section of SENT specimen for the measurement of temperature gradient.

Temperature was controlled using TC₁ thermocouple and other three were used as measuring thermocouples. Longitudinal temperature difference was calculated by subtracting TC₂ readouts with TC₁. Similarly, transverse temperature difference was calculated by subtracting TC₃ and TC₄ readouts with TC₁. Several exploratory tests have been carried out in these two temperature intervals at zero load by adjusting the pressure rate of compressed air (forced cooling) to ensure the absolute minimum temperature gradients near the central notched section of the SENT specimen. After conducting several exploratory tests, longitudinal as well as transverse thermal gradients were achieved below 3°C which is less than 1% of T_{max} of both the temperature intervals.

8.2.4 Generation of Calibration Curves for the Measurement of Crack Length

The calibration curve for generation of crack length was generated from the correlation plot between crack length measured optically and using an alternating current potential drop (ACPD) system with lock-in amplifier. In the present set up, the COD technique was not employed to measure crack length since the geometry of infra red furnace set up used for fast specimen heating do not permit insertion of clip on gauge. ACPD uses high frequency AC current of constant amplitude passing through the specimen and measuring the potential drop between the potential leads [Wei and Brazil 1981]. In these experiments, one needs to conduct several exploratory tests to identify the magnitude of current and reliable probe material which should be thermally and electrically stable at high temperatures. Platinum wires of 0.5 mm were found to be spot weld compatible with

titanium alloys for both the current as well as potential leads. The current leads were spot welded at two end portions near grip locations and potential leads across the crack mouth in thickness direction at a distance of 2 mm. While Fig. 8.4a shows the TMF test facility in its entirety thereby showing infra-red furnace and ACPD (Model No: MATELECT CGM-7), the close view of mounting arrangement of SENT and infra-red furnace can be seen in Figs. 8.4b and c, respectively. During the test, an alternating current of 2 amps through an AC system was passed through the specimen and voltage drop across the crack mouth was continuously sampled by MTS controller and recorded by a high end computer interfaced with MTS test system.

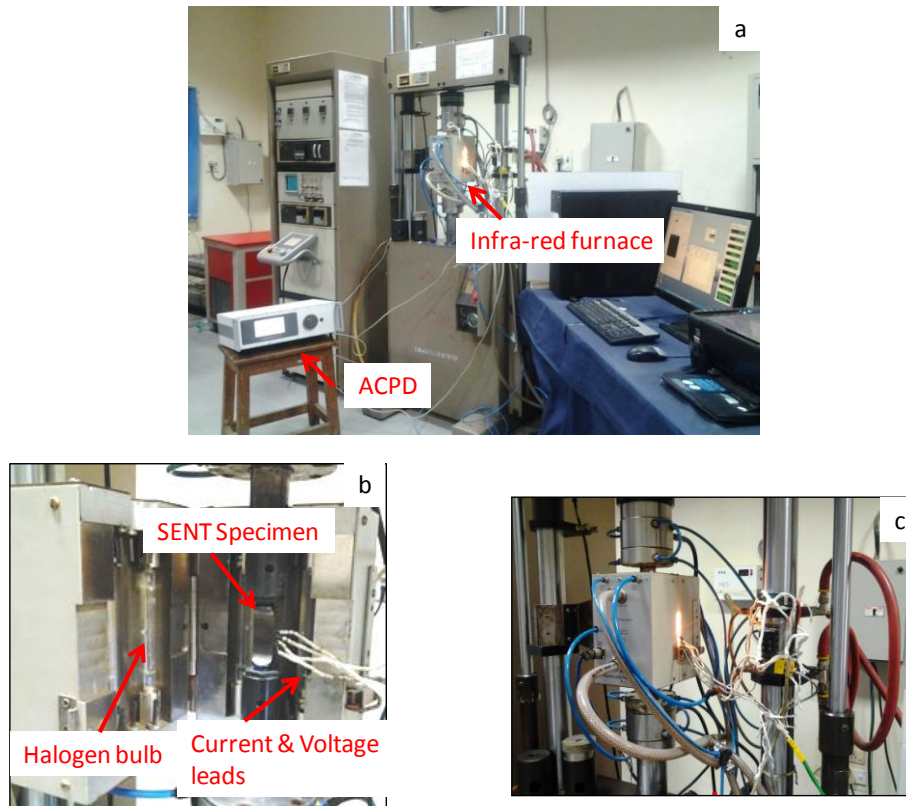


Fig. 8.4 Photographs of (a) TMF test facility for carrying out fatigue crack growth testing under TMF loading (b) mounting arrangement of SENT specimen inside the infra-red furnace and (b) an ongoing test in the temperature interval of $450^{\circ}\text{C} \leftrightarrow 600^{\circ}\text{C}$.

The specimen was initially cycled between the two temperature (T) intervals at zero load (P) to observe the variation of potential (V), if any. The variation of $V(T, P=0)$ versus time for a temperature interval $300^{\circ}\text{C} \leftrightarrow 450^{\circ}\text{C}$ has been shown in Fig. 8.5a. The same trend has been observed in high temperature interval $450^{\circ}\text{C} \leftrightarrow 600^{\circ}\text{C}$. It has been confirmed that the cycling of temperature has little influence on potential (Fig. 8.5a) as the temperature interval is too less to effect the potential. However, the potential curve under load cycling ($V(T, P=P_i)$, where P_i is the instantaneous load)) clearly shows the variation in potential with elapsed cycles as shown in Fig. 8.5b. Since temperature alone has no significant effect on potential at zero load, the effect of applied load on variation in potential is obtained directly from Fig. 8.5b.

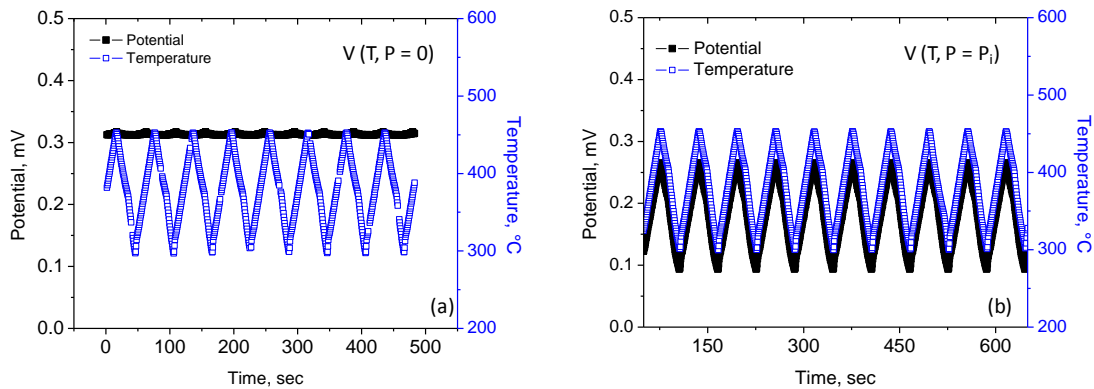


Fig. 8.5 Potential curves with temperature cycling between $300^{\circ}\text{C} \leftrightarrow 450^{\circ}\text{C}$ under (a) zero load and (b) with load cycling.

In general, oxide layers of higher thickness can introduce very large resistance into the excitation and measurement circuits of ACPD system. While this ACPD system is equipped with a lock-in amplifier which has the capability of recovering small signals from strong noise, signals of interest smaller than 1 μV could be captured in the higher temperature interval $450^{\circ}\text{C} \leftrightarrow 600^{\circ}\text{C}$ of cycling in which thicker oxide layer is expected to form. This has helped in measuring K_{cl} values more accurately after cooling the specimen to ambient temperature without removing the oxide layer from the sample.

The precracked SENT specimens were TMFCG tested employing the test parameters as mentioned in section 8.2.3. The voltage drop measured at test temperatures was observed to increase with elapsed fatigue cycles. For calibration purpose, the crack length was measured optically on both sides of specimen at ambient temperature by interrupting the test intermittently. During the interruption of the test, the sample was cooled to ambient temperature at 80% of maximum load. A few cycles (10 nos.) of test at ambient temperature were also done to determine closure load (P_{Cl}) and the tests were then resumed at high temperature. One of the SENT specimens interrupted at $450^{\circ}\text{C} \leftrightarrow 600^{\circ}\text{C}$ temperature interval for crack length measurement is shown in Fig. 8.6.



Fig. 8.6 Photograph of a SENT specimen interrupted during testing for crack length measurement.

During each test, the ratio of difference between instantaneous sampled voltage and initial voltage to initial voltage $(V_i - V_0)/V_0$ was recorded as a function of elapsed time. It has been reported that the normalized potential depends only on changes in specimen resistance due to crack propagation keeping all other variables constant [Wei and Brazil 1981]. In order to yield da/dN vs ΔK curves, the following four steps were adopted as a kind of data reduction algorithm:

Step I: Generation of calibration equation: A second order polynomial fit between optically measured crack length (a_p) vs. $(V_i - V_0)/V_0$ data pair resulted in fitting constants as A_0 , A_1 and A_2 . The nature of the calibration was found to be:

$$a = A_0 + A_1 \{(V_i - V_0)/V_0\} + A_2 \{(V_i - V_0)/V_0\}^2 \quad (8.2)$$

Step II: Using calibration equation 1, crack length vs. time data was generated from $(V_i - V_0)/V_0$ vs. time data pairs.

Step III: The crack length vs. time data pair were further processed to yield crack length vs. elapsed cycles data pairs (elapsed cycles = frequency x time).

Step IV: da/dN is calculated by secant method [ASTM Standard E 647-13] as follows:

$$da/dN = (a_{i+1} - a_i)/(N_{i+1} - N_i) \quad (8.3)$$

where a_i is the instantaneous crack length and N_i the corresponding elapsed cycles. ΔK is calculated by using the following equation:

$$\Delta K = (\Delta P / B.W^{1/2}) / \sqrt{a} [1.4 + \alpha] F(\alpha) \quad (8.4)$$

$$F(\alpha) = 3.97 - 10.88\alpha + 26.25\alpha^2 - 38.9\alpha^3 + 30.15\alpha^4 - 9.27\alpha^5$$

where a is the crack length, W is the width, B is the thickness, α is the ratio of a -to- W and ΔP is the applied load range ($\Delta P = P_{\max} - P_{\min}$).

The typical representative plots from step I to step III for IP and OP-TMFCG loading in one temperature interval are shown in Fig. 8.7.

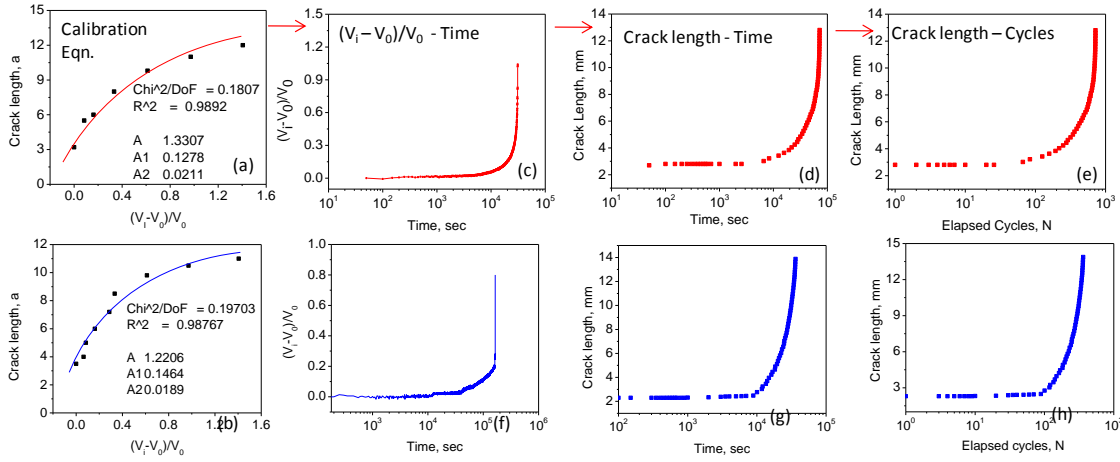


Fig. 8.7 Variation of optically measured crack length vs. $(V_I - V_0)/V_0$ for determination of coefficients A_0 , A_1 and A_2 under (a) IP-TMFCG loading and (b) OP-TMFCG loading at $300^\circ\text{C} \leftrightarrow 450^\circ\text{C}$ temperature interval. $(V_I - V_0)/V_0$ vs. time, crack length vs. time and crack length vs. elapsed cycles under (c-e) IP-TMFCG loading and (f-h) OP-TMFCG loading at the same temperature interval.

8.2.5 Fractography and Measurement of Fracture Surface Roughness

In order to show the representative surface appearance of fatigue starter notch, precracked and main crack growth, one of the tested specimen corresponding to the temperature interval of $300^\circ\text{C} \leftrightarrow 450^\circ\text{C}$ IP-TMFCG loading is shown in Fig. 8.8. Fig. 8.8 shows the distinct precracked features with respect to fatigue starter notch and main crack growth.

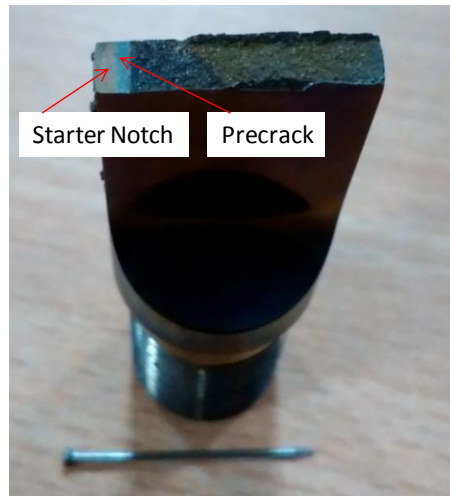


Fig. 8.8 Fracture surface of the tested specimen in the temperature interval of 300°C↔450°C temperature interval.

Fracture surfaces of tested specimens were analyzed in the same manner as that of isothermal test conditions as outlined in section 7.2.4 of chapter VII. The fracture region corresponding to low and high ΔK levels were cut, cleaned, dried and examined under the microscope (Model No: FEI Quanta 400). Furthermore, the surface roughness profile of the fractured surface along the crack growth direction at low ΔK region was recorded using stylus based profilometer (Model: FORM TALYSURF 50). The average surface roughness (R_a) of this region has been determined using Intra II software of the profilometer.

8.2.6 Measurement of Plastic Zone Size using Microhardness

The plastic zone sizes (monotonic and cyclic) [Suresh 2004] were estimated from the Vickers micro-hardness (Model No: Matsuzawa MMT X7) measurement as a function of distance from the crack tip at various ΔK levels which corresponds to stress intensity factor of Paris Regime for both the temperature intervals. In micro-hardness measurement, the applied load was 200 g with a dwell time of 10 sec. As mentioned in section 7.2.5 of chapter VII, Nickel was deposited electrolytically over the specimen along the crack length for the protection of the surface layer during the plastic zone size measurement.

8.2.7 Electron Back Scattered Diffraction

In order to observe the crack path profile, region of interest along the crack path which corresponds to the stress intensity factor range of $\Delta K = 30.0 \text{ MPa.m}^{1/2}$ for all the tested specimens have been captured using field emission gun - scanning electron microscope (FEG-SEM). Small size rectangular cross section samples of the heated treated alloy were machined, hot mounted and mechanically polished using emery papers with grit sizes ranging from 220, 600, 800 and 1200, respectively. The samples were subsequently polished on velvet cloth using diamond paste with particle size of 9 μm down to less than 1 μm . Final polishing using colloidal silica was performed over the polished samples, as it is known to give exceptional results and the level of finish required to perform EBSD. EBSD analysis were carried out on a Zeiss Supra 55 FEG-SEM equipped with an orientation imaging microscopy (OIM) system developed by HKL. EBSD patterns were recorded on an Oxford Instruments Nordlys camera. EBSD measurements were

performed with a scanning step size of 0.5 μm , an accelerating voltage of 20 keV and a beam current of 20 nA. All the EBSD maps obtained were post-processed using CHANNEL5's project suite.

8.3 Results

8.3.1 Thermomechanical Fatigue Crack Growth Rates

The TMFCG curves obtained for the two temperature intervals and phase relationships in terms of da/dN versus ΔK for Timetal 834 alloy are shown in Fig. 8.9 and it was found to be sigmoidal in shape. In the temperature interval of $300^\circ\text{C} \leftrightarrow 450^\circ\text{C}$, the TMFCG rate is higher at OP as compared to IP test conditions for ΔK above 20 $\text{MPa.m}^{1/2}$. Similar behaviour has been observed in the temperature interval of $450^\circ\text{C} \leftrightarrow 600^\circ\text{C}$ for ΔK above 25 $\text{MPa.m}^{1/2}$. The rate of crack growth in the ΔK range beyond 20 and 25 $\text{MPa.m}^{1/2}$ for the temperature interval of $300^\circ\text{C} \leftrightarrow 450^\circ\text{C}$ and $450^\circ\text{C} \leftrightarrow 600^\circ\text{C}$, respectively, is determined using Paris-Erdogan equation [Paris and Erdogan 1963]:

$$da/dN = C(\Delta K)^m \quad (8.5)$$

where m is the slope of the plot in linear region. The value of C is determined by extending the straight line to $\Delta K = 1 \text{ MPa.m}^{1/2}$. The values of the Paris constants (m and C) are listed in Table 8.1. The value of slope given in Table 8.1 clearly indicates that the

alloy exhibits higher crack growth rate at OP-TMCG loading as compared to IP-TMCF loading in both the temperature intervals.

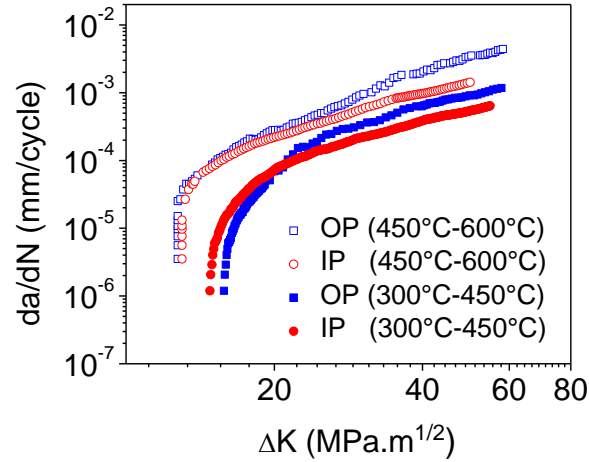


Fig. 8.9 Fatigue crack growth resistance curves (da/dN vs. ΔK) of Timetal 834 under TMF loading.

Table 8.1: Parameters (Paris constants, maximum and cyclic crack tip opening displacement, average surface roughness, thickness of the oxide layer and cyclic plastic zone size) at various test conditions.

Temperature Interval (°C)	Mode of loading	δ_{max} (μm)	δ_{cyclic} (μm)	R_a (μm)	δ_{oxide} (μm)	m	C	m (Closure corrected)	C (Closure corrected)	Cyclic plastic zone size (μm)
300°C↔450°C	IP	1.02	0.57	0.56	0.06	2.32	1.07×10^{-7}	2.12	5.17×10^{-7}	140
300°C↔450°C	OP	1.16	0.63	1.76	0.10	2.50	2.67×10^{-7}	1.98	9.8×10^{-7}	50
450°C↔600°C	IP	0.92	0.18	2.16	0.15	2.35	3.12×10^{-7}	2.08	7.87×10^{-7}	250
450°C↔600°C	OP	0.98	0.20	2.97	0.18	3.2	1.27×10^{-8}	2.57	2.82×10^{-7}	80

8.3.2 Fracture Behaviour

The fracture surface of the specimens tested at low ($\Delta K \sim 15 \text{ MPa.m}^{1/2}$) and high ($\Delta K \sim 30 \text{ MPa.m}^{1/2}$) ΔK region, are depicted in Figs. 8.10 and 8.11, respectively. At low ΔK levels, faceted behaviour was observed in the fractured surfaces (Fig. 8.10). EDS analysis was carried out to determine the composition of different features of the fractures surface. The region encircled in the Fig. 8.11d showed relatively more concentration of oxygen as shown in Fig. 8.12a than nitrogen and carbon compared to other regions (Fig. 8.12b). On this basis, it was concluded that these encircled regions contain predominantly oxides of titanium. This feature is evident only at $450^\circ\text{C} \leftrightarrow 600^\circ\text{C}$ OP-TMFCG loading.

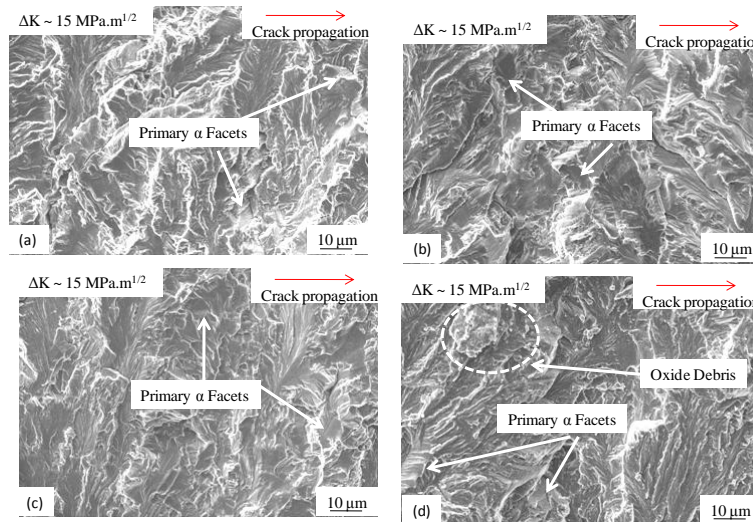


Fig. 8.10 SEM fractographs showing microstructurally sensitive crystallographic mode of stage I crack propagation at near threshold region at $300^\circ\text{C} \leftrightarrow 450^\circ\text{C}$ IP (b) $300^\circ\text{C} \leftrightarrow 450^\circ\text{C}$ OP (c) $450^\circ\text{C} \leftrightarrow 600^\circ\text{C}$ IP and (d) $450^\circ\text{C} \leftrightarrow 600^\circ\text{C}$ OP –TMFCG test conditions.

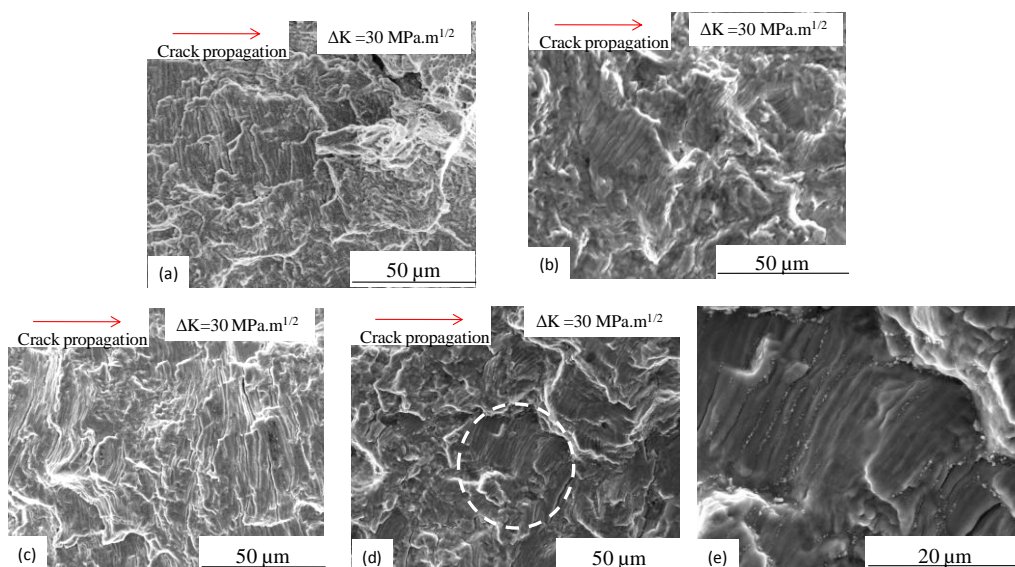


Fig. 8.11 SEM fractographs showing striated mode of stage II crack propagation at (a) 300°C ↔ 450°C IP (b) 300°C ↔ 450°C OP (c) 450°C ↔ 600°C IP and (d) 450°C ↔ 600°C OP –TMFCG test conditions. Fig. 8.11e is the high magnification micrograph of encircled region of Fig. 8.11d.

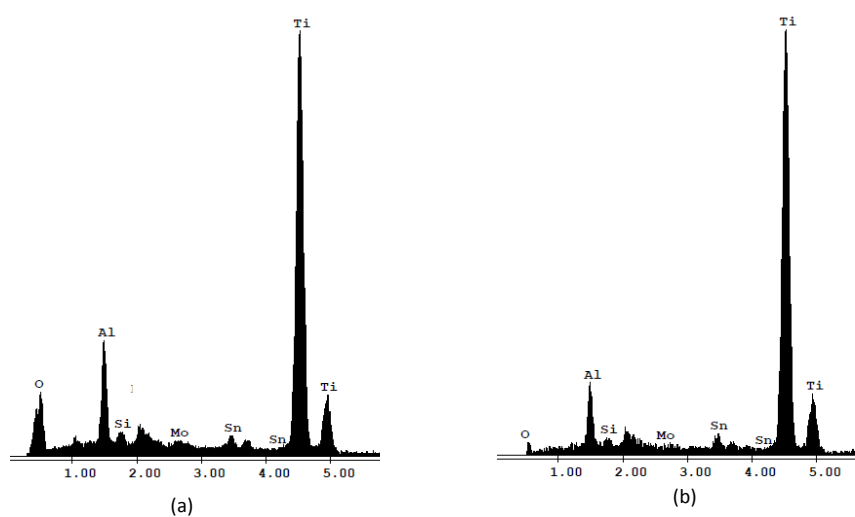


Fig. 8.12 EDS plots taken from Fig. 8.11d showing (a) dominant peak of oxygen in the encircled region and (c) weak oxygen peak from the matrix.

At higher ΔK levels, striations were seen throughout the fractured surface (Fig. 8.11). In general, the width of the striations was noticed to be larger in out-of-phase than in-phase testing for both the temperature intervals. At higher magnifications, oxide debris was found to decorate the prior β grain and interlamellar boundaries (Fig. 8.11e).

8.3.3 Fracture Surface Roughness Profile

The surface roughness profile at low ΔK regime recorded along the crack growth direction in all test conditions are shown in Fig. 8.13.

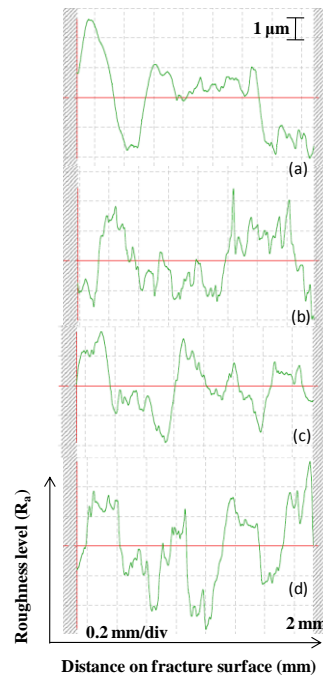


Fig.8.13 Fracture surface roughness profiles along the direction of crack propagation at near threshold region at (a) 300°C↔450°C IP (b) 300°C↔450°C OP (c) 450°C↔600°C IP and (d) 450°C↔600°C OP –TMFCG test conditions.

The surface roughness (R_a) determined at the smaller length scale is given in Table 8.1. It could be noticed that this value increases from 0.56 μm to 2.97 μm with an increase in temperature interval. It is evident from Fig. 8.13 that the frequency of occurrence of perturbations is higher at OP-TMFCG test conditions as compared to IP-TMFCG test conditions. At identical temperature interval, the values of R_a are observed to be higher at OP-TMFCG test conditions as compared to IP-TMFCG test conditions. Furthermore, the highest value of R_a is observed at 450°C↔600°C OP-TMFCG loading. At a larger length scale, all the specimens show the same surface roughness of about 5 μm .

8.3.4 Auger Electron Spectroscopy

The auger electron spectra for the four TMFCG test conditions in as received and after 30 minutes of sputtering are shown in Figs. 8.14a-d. As observed under isothermal test conditions (chapter VII), apart from a peak of Ti, the as received spectrum contains peaks due to three interstitial elements C, N and O. It can be seen from Fig. 8.14 that the concentration of titanium has increased relative to that of interstitial elements. The sputtered oxide layer thickness determined from the AES analysis is listed in Table 8.1. This alloy contains more carbon (0.27% C at.%) than nitrogen and oxygen (0.30% O and 0.006% N, all in at.%). Moreover, carbon is reported to generate maximum strain in the HCP lattice than nitrogen and oxygen [Conrad 1981].

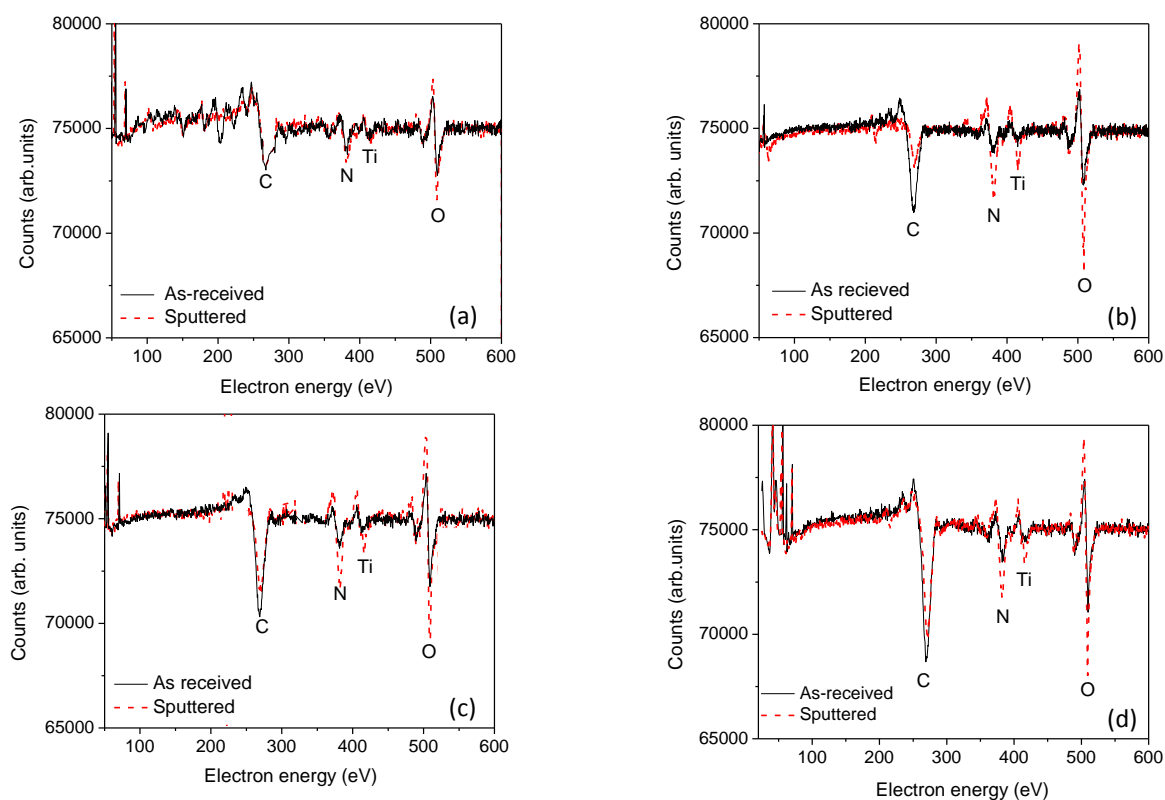


Fig. 8.14 Auger spectrums of tested specimens in near threshold region at (a) $300^{\circ}\text{C} \leftrightarrow 450^{\circ}\text{C}$ IP (b) $300^{\circ}\text{C} \leftrightarrow 450^{\circ}\text{C}$ OP (c) $450^{\circ}\text{C} \leftrightarrow 600^{\circ}\text{C}$ IP and (d) $450^{\circ}\text{C} \leftrightarrow 600^{\circ}\text{C}$ OP – TMFCG test conditions.

It is also known that strain enhances the diffusion coefficient and hence it is reasonable to expect C to diffuse fast to region having high strain which in this particular case turns out to be near the vicinity of the crack tip. Considering diffusivity values (Table 4.7 of chapter IV) and activation energy (Table 4.6 of chapter IV) [Conrad 1981, Doner and Conrad 1973] of interstitial elements as well, one can expect carbon atoms to become more mobile at lower temperatures as compared to other interstitial elements in this alloy. It is also known that the TiC can form at temperature as low as 473K (200°C) [Koc and Glatzmaier 1995]. Hence it is not unreasonable to conclude that carbon diffusing from the bulk of the sample to crack tip as well as the one getting adsorbed at the crack tip from atmosphere result in the formation of TiC there. Since Ti has got a high affinity for all these interstitial elements, in addition to carbon, nitrogen and oxygen would also get adsorbed on the freshly exposed crack surface. From the diffusivity values given in table 4.7 of chapter IV and the concentration of N in the bulk of the bulk of the sample, one could surmise that the concentration of nitrogen seen on the cracked surface could have come only from molecular nitrogen adsorbed on the sample surface from the atmosphere and the possibility of this nitrogen forming TiN compound could be ruled out since titanium nitride forms at temperature above 973K (700°C) [Koc and Glatzmaier 1995]. On the basis of above discussion, it is safe to assume that the layer which has formed at the crack tip is a mixture of TiC and TiO₂. Based on this assumption and EDS results discussed in section 8.3.2, this layer is henceforth considered as oxide layer. The sputtered oxide layer thickness determined from the AES analysis is listed in Table 8.1.

8.3.5 Estimation of Plastic Zone Size

Plastic zone sizes (monotonic and cyclic) have been estimated from the plots shown in Figs. 8.15a and b for both the temperature intervals. It is evident from these figures that the microhardness decreases rapidly and levels off up to a certain distance from the crack tip, beyond which it again decreases and levels off as a function of increasing distance from the crack tip. Cyclic plastic zone sizes thus measured are listed in Table 8.1. The alloy shows larger plastic zone size at IP-TMFCG loading as compared to OP-TMFCG loading (Table 8.1). In general, it has been found that plastic zone size at IP-TMFCG loading is nearly three times higher than that of OP-TMFCG loading in both the temperature intervals.

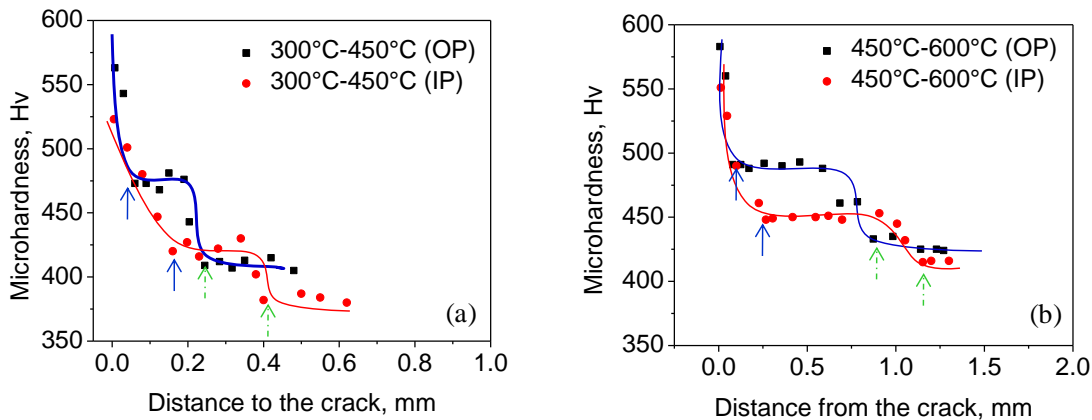


Fig. 8.15 Variation of microhardness as a function of distance from the crack tip under (a) 300°C↔450°C and (b) 450°C↔600°C TMFCG loading. Solid and dashed arrows indicate the cyclic and monotonic plastic zone size, respectively.

8.3.6 Microstructural characterization using EBSD

The inverse pole figures (IPF), pole figures (PF) and EBSD maps of IP and OP-TMFCG tested samples are shown in Figs. 8.16 and 8.17, respectively. Among the various microstructural units as discussed in section 2.1.2 of chapter II (literature survey), in the present investigation, an attempt has been made to understand the effect of only primary α grains and secondary α colonies on the TMFCG behaviour of this alloy. The average crystallographic orientation of equiaxed primary α and secondary α colonies of four different EBSD maps as shown in Figs. 8.16 and 8.17 are deduced from the respective Euler angles ϕ_1 , ϕ , ϕ_2 that corresponds to a rotation of about the Z-X-Z axes in the Bunge system [Dingley and Randle 1992].

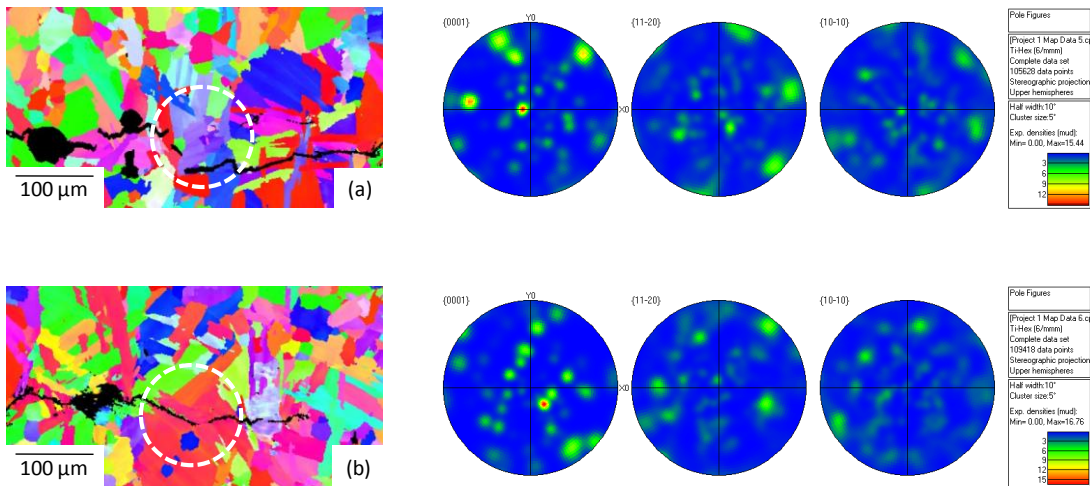


Fig. 8.16 Local hcp pole figures around crack wake of (a) 300°C ↔ 450°C (b) 450°C ↔ 600°C OP-TMFCG loading interrupted sample at 30 MPa.m^{1/2}

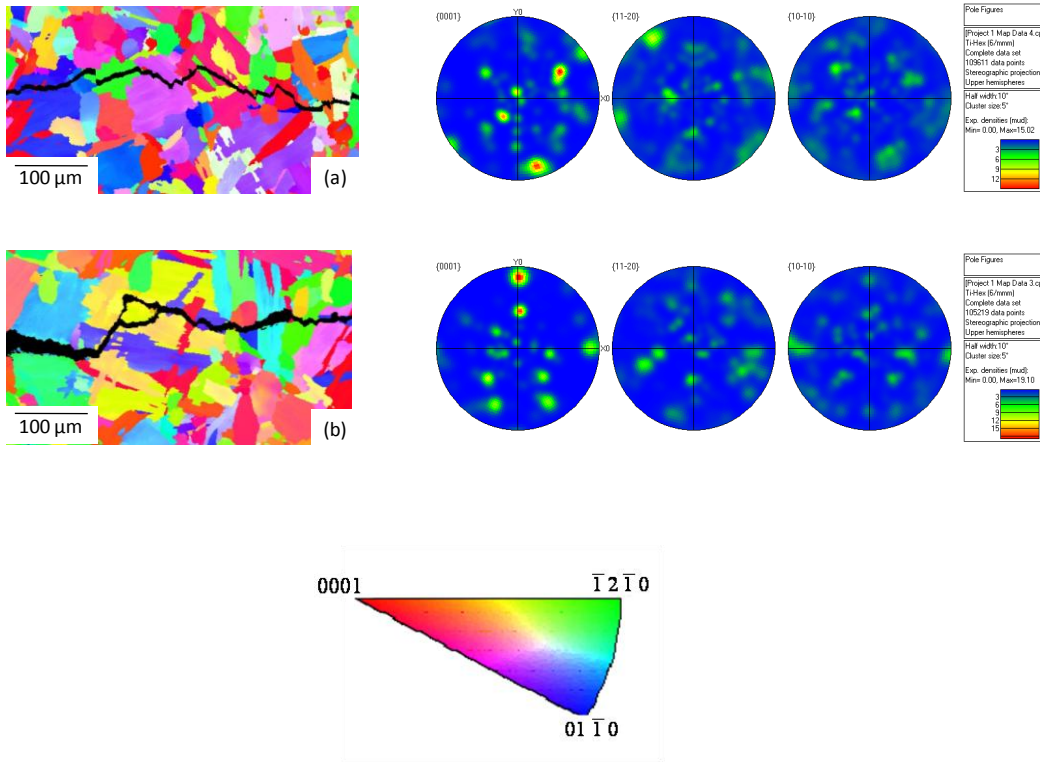


Fig. 8.17 Local hcp pole figures around crack wake of (a) 300°C ↔ 450°C (b) 450°C ↔ 600°C OP-TMFCG loading interrupted sample at 30 MPa.m^{1/2}.

The orientation $\{hkil\}\langle uvw \rangle$ of respective microstructural unit were evaluated as per the following relationship with $g\{\phi_1, \phi, \phi_2\}$ in the Bunge system [Li 2008]:

$$\begin{bmatrix} h \\ k \\ i \\ l \end{bmatrix} = \begin{bmatrix} \frac{\sqrt{3}}{2} & \frac{-1}{2} & 0 \\ 0 & 1 & 0 \\ -\frac{\sqrt{3}}{2} & \frac{-1}{2} & 0 \\ 0 & 0 & c/a \end{bmatrix} \begin{bmatrix} \sin\phi_2 \sin\phi \\ \cos\phi_2 \sin\phi \\ \cos\phi \end{bmatrix} \quad (8.6)$$

$$\begin{bmatrix} u \\ v \\ t \\ w \end{bmatrix} = \begin{bmatrix} \frac{2}{3} & \frac{-1}{3} & 0 \\ 0 & \frac{2}{3} & 0 \\ \frac{-2}{3} & \frac{-1}{3} & 0 \\ 0 & 0 & c/a \end{bmatrix} \begin{bmatrix} \cos\phi_1 \cos\phi_2 - \sin\phi_1 \sin\phi_2 \cos\phi \\ -\cos\phi_1 \sin\phi_2 - \sin\phi_1 \cos\phi_2 \cos\phi \\ \sin\phi \sin\phi_1 \end{bmatrix} \quad (8.7)$$

The indexing is done in the rolling direction.

The specific Schmid factor range of the respective microstructural constituents (α_p and α -colonies) for potential slip systems namely prismatic, basal and pyramidal system have been shown in the form of bar graphs in Figs. 8.18 and 8.19 for the temperature interval of $300^\circ\text{C} \leftrightarrow 450^\circ\text{C}$.

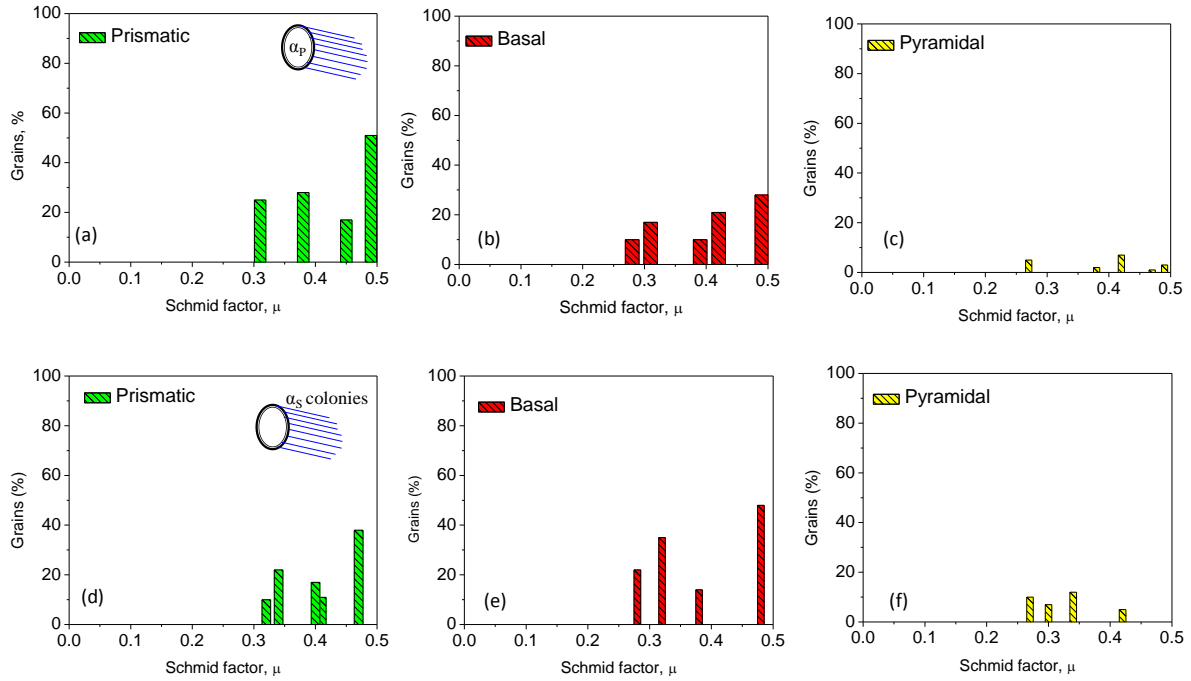


Fig. 8.18 Distribution maps showing the percentage of (a-c) α_p grains and (d-f) secondary α_s colonies deformed under prismatic, basal and pyramidal slip from the observation of $0.5 \times 0.3 \text{ mm}^2$ under $300^\circ\text{C} \leftrightarrow 450^\circ\text{C}$ IP-TMFCG loading, respectively.

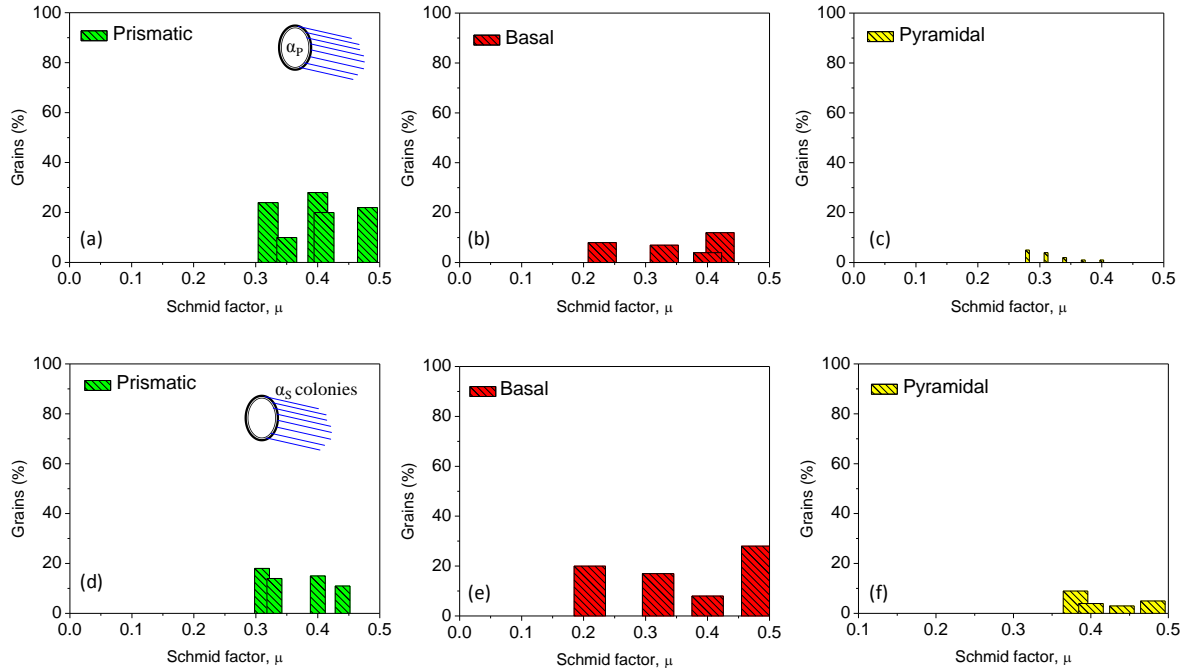


Fig. 8.19 Distribution maps showing the percentage of (a-c) α_p grains and (d-f) secondary α colonies deformed under prismatic, basal and pyramidal slip from the observation of $0.5 \times 0.3 \text{ mm}^2$ under $300^\circ\text{C} \leftrightarrow 450^\circ\text{C}$ OP-TMFCG loading, respectively

Same plots for 450°C↔600°C temperature interval for IP and OP-TMFCG loading have been shown in Figs. 8.20 and 8.21, respectively. It is to be noted that one bar represents the percentage of grains deformed under operative slip system (around 0.5 x 0.3 mm² (length x breadth) area of crack wake) associated with certain range of Schmid factor. In the present study, since the trend in the activation of potential slip systems for α_P grains and α_S colonies has been observed to be the same for two temperature intervals, activated slip systems at 450°C↔600°C temperature interval is being explained. It is evident from Fig. 8.20 that 18-60% of α_P grains are oriented with prismatic Schmid factor 0.30-0.5 and 17-30% α_S -colonies are oriented with prismatic Schmid factor range 0.36-0.5 at IP-TMFCG loading condition for the temperature interval 450°C↔600°C. 05-20% of α_P grains are oriented with basal Schmid factor in the range 0.38-0.49, however, 35-76% of α_S -colonies are oriented with basal Schmid factor in the range 0.28-0.48. Grains oriented for pyramidal slip are restricted to less than 15% which corresponds to 0.36-0.50 and 0.38-0.47 for α_P grains and α_S -colonies, respectively.

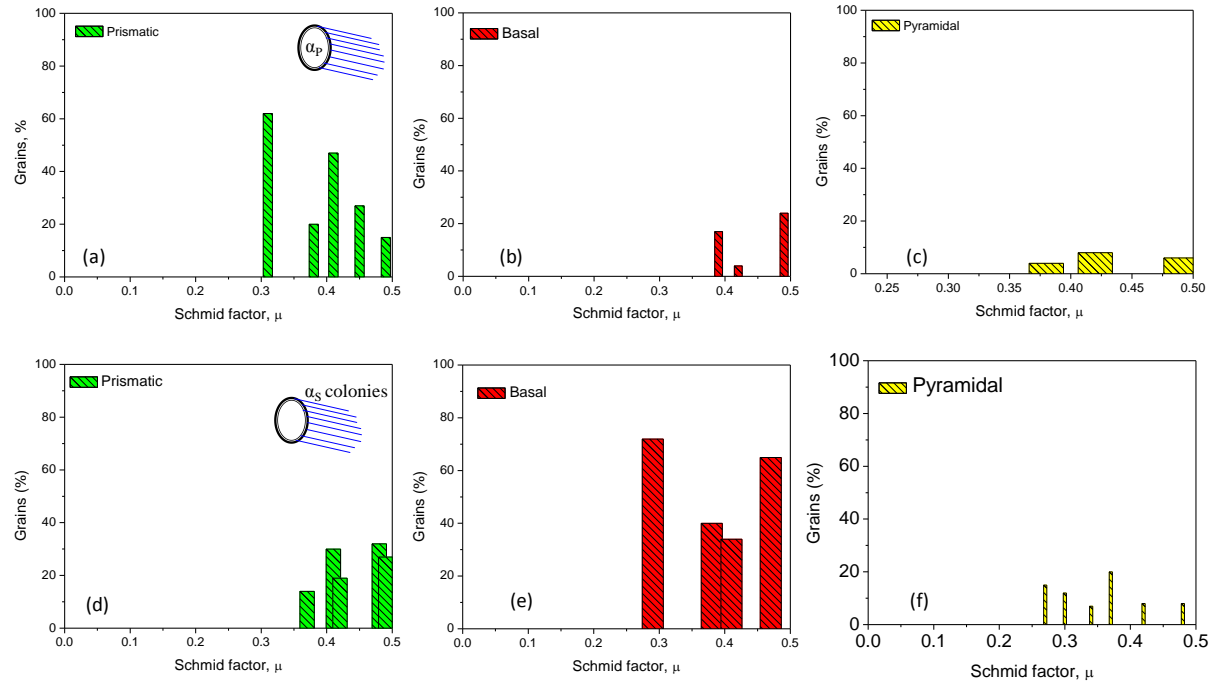


Fig. 8.20 Distribution maps showing the percentage of (a-c) α_P grains and (d-f) α – colonies deformed under prismatic, basal and pyramidal slip from the observation of $0.5 \times 0.3 \text{ mm}^2$ under $450^\circ\text{C} \leftrightarrow 600^\circ\text{C}$ IP-TMF loading, respectively

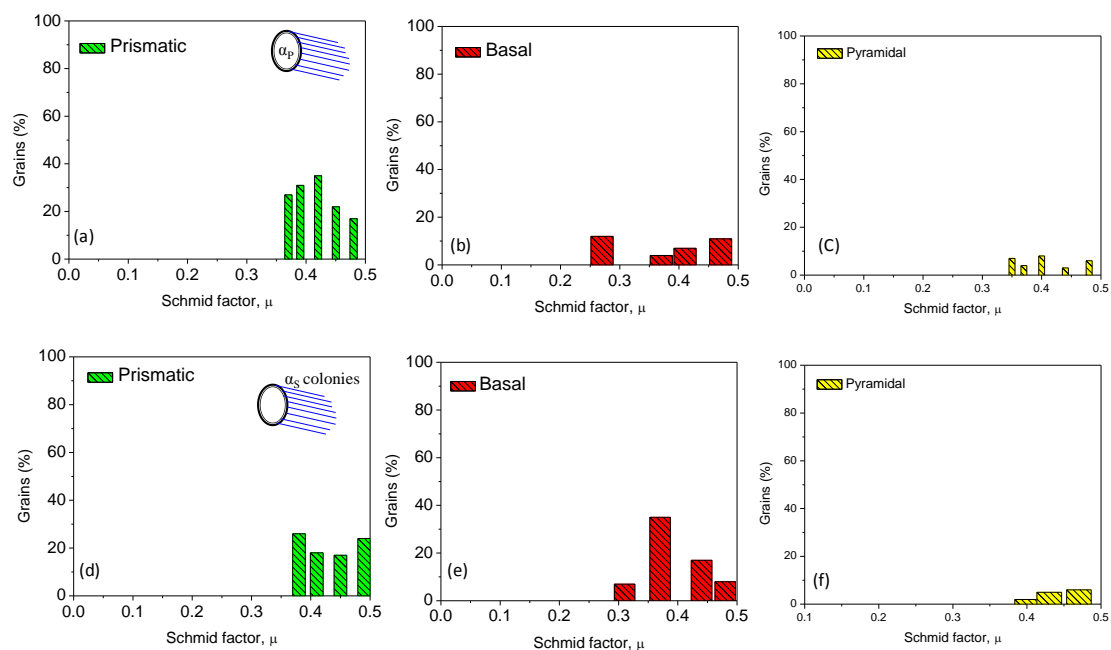


Fig. 8.21 Distribution maps showing the percentage of (a-c) α_p grains and (d-f) α – colonies deformed under prismatic, basal and pyramidal slip from the observation of $0.5 \times 0.3 \text{ mm}^2$ under $450^\circ\text{C} \leftrightarrow 600^\circ\text{C}$ OP-TMFCG loading, respectively

In case of OP-TMFCG loading (Fig. 8.21), 20-38% of α_P grains are oriented for prismatic slip in the Schmid factor range of 0.36-0.47. 17-28% of α_S -colonies are oriented for prismatic slip in the Schmid factor range of 0.37-0.5. Further, 08-33% α_S -colonies are oriented for basal slip in the Schmid factor range 0.28-0.47, whereas, 05-17% α_P grains are oriented for basal slip in the Schmid factor range of 0.25-0.47. α_P grains oriented for pyramidal slip are restricted to less than 10% which corresponds to Schmid factor range 0.36-0.46, however, 07-20% α_S -colonies are oriented to pyramidal slip which corresponds to Schmid factor range 0.27-0.48.

In order to understand the local interaction of propagating crack with the microstructural units like equiaxed α_P and α_S colonies, high resolution EBSD maps of selected regions of Figs 8.16 and 8.17 have been captured with a step size of 0.1 micron. These EBSD maps, SEM images and misorientation of adjacent grains for IP and OP-TMFCG tested samples are shown in Figs. 8.22 to 8.27, respectively. Misorientation of adjacent grains is measured using line scan analysis [Clair et al. 2011]. As clear from the comparison of Figs. 8.16 and 8.17, unlike EBSD maps of OP-TMFCG condition (Fig. 8.17) where one has a choice to select the area for capturing high resolution images, these images could be captured legibly only from the region as shown encircled at IP-TMFCG condition (Fig. 8.16). As a result, in the present study, images have been captured comprising of interaction of crack with (a) only α_S colonies and (b) α_S colonies as well as α_P grains under OP-TMFCG condition in both the temperature intervals. On the other hand, under IP-TMFCG condition, due to limited available area for examination, images showing

interaction of crack with (a) α_S colonies as well as α_P grains at $300^{\circ}\text{C} \leftrightarrow 450^{\circ}\text{C}$ and (b) α_S colonies at $450^{\circ}\text{C} \leftrightarrow 600^{\circ}\text{C}$ only could be captured. Maximum Schmid factor among potential slip systems (basal, prismatic and pyramidal) is also shown on various grains of high resolution maps. The influence of local crystallographic orientation on crack propagation in various temperature intervals is explained in detail in subsequent sections.

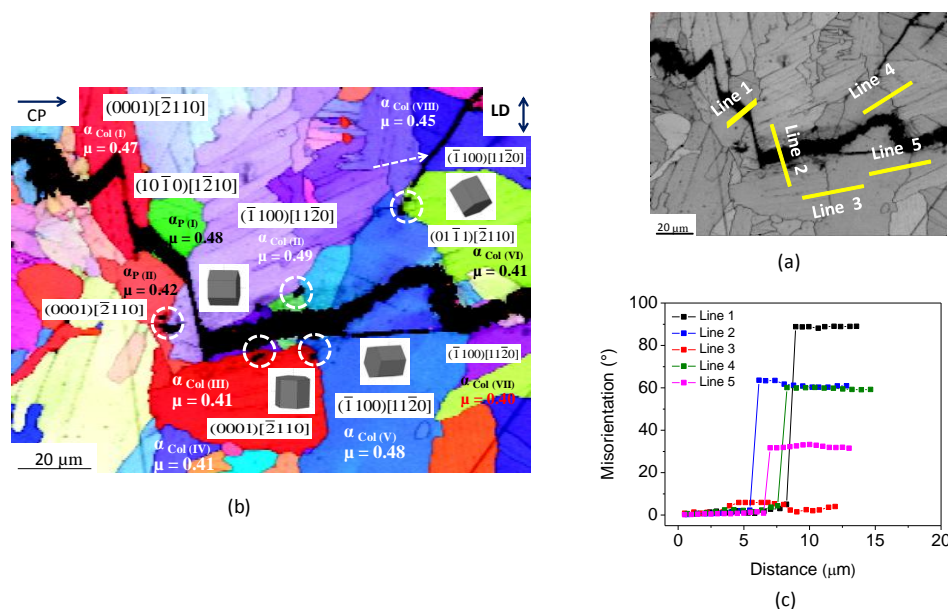


Fig. 8.22 (a) High resolution FEG-SEM images and corresponding (b) EBSD map and (c) misorientation between grains. SEM images and EBSD maps shows the local interaction of growing crack with primary α grains and secondary α – colonies. CP and LD represent direction of crack propagation and loading, respectively. These images are representative of 300°C↔450C IP-TMFCG test condition.

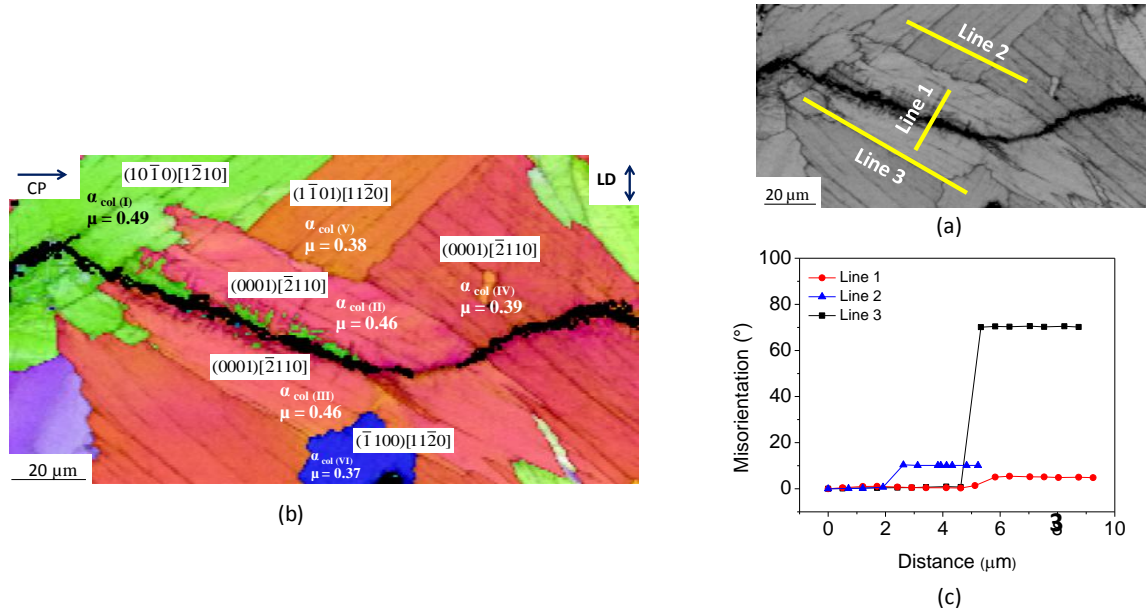


Fig. 8.23 (a) High resolution FEG-SEM images and corresponding (b) EBSD map and (c) misorientation between grains. SEM images and EBSD maps shows the local interaction of growing crack with two secondary α – colonies. CP and LD represent direction of crack propagation and loading, respectively. These images are representative of 450°C↔600°C IP-TMFCG test condition.

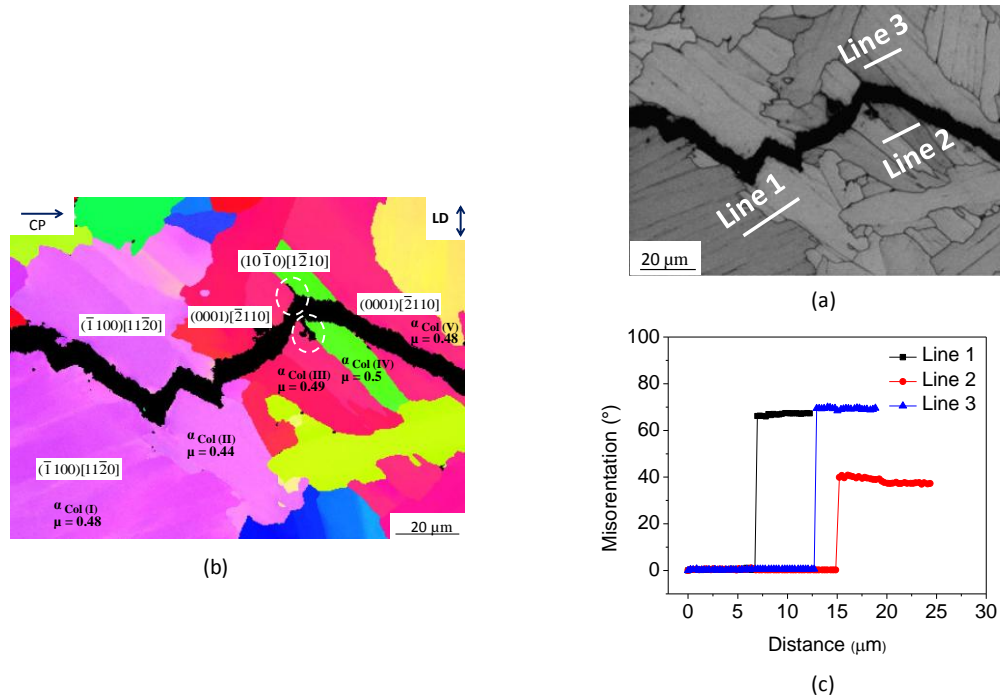


Fig. 8.24 (a) High resolution FEG-SEM images and corresponding (b) EBSD maps and (c) misorientation between adjacent secondary α colonies. SEM images and EBSD maps show the local interaction of growing crack with secondary α colonies. CP and LD represents direction of crack propagation and loading, respectively. These images are representative of 300°C↔450°C OP-TMFCG test condition.

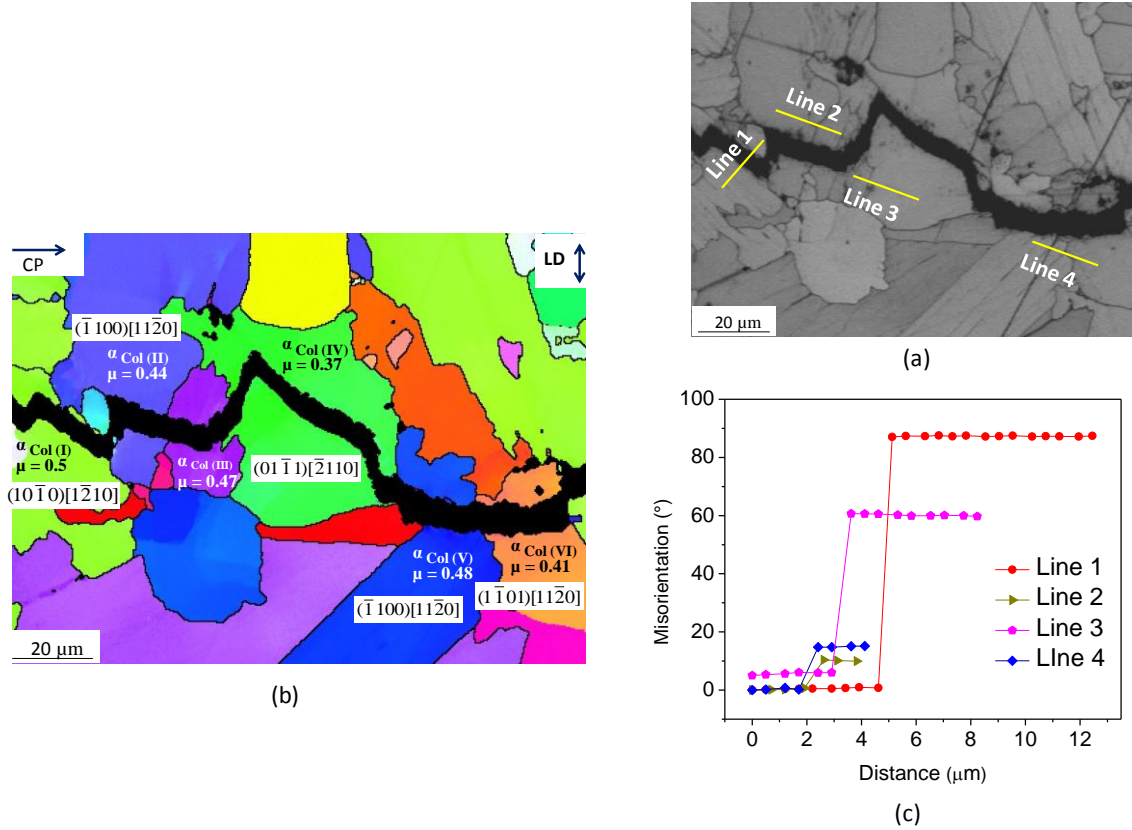


Fig. 8.25 (a) High resolution FEG-SEM image and corresponding (b) EBSD map and (c) misorientation between adjacent grains. SEM image and EBSD map shows the local interaction of growing crack with primary α grains and secondary α colonies. CP and LD represent direction of crack propagation and loading, respectively. These images are representative of 300°C↔450°C OP-TMFCG test condition.

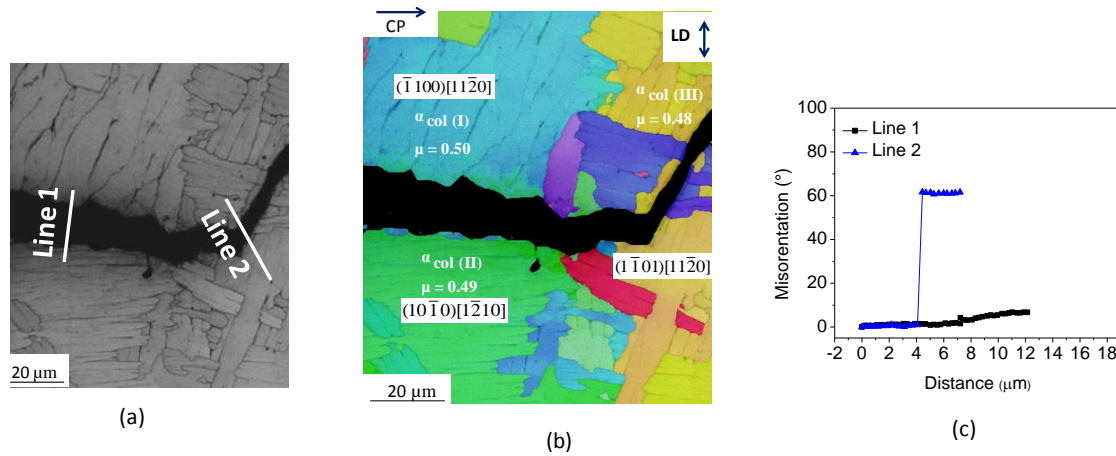


Fig. 8.26 (a) High resolution FEG-SEM images and corresponding (b) EBSD map and (c) misorientation between adjacent secondary α colonies. SEM images and EBSD maps show the local interaction of growing crack with secondary α colonies. CP and LD represent direction of crack propagation and loading, respectively. These images are representative of $450^\circ\text{C} \leftrightarrow 600^\circ\text{C}$ OP-TMFCG test condition.

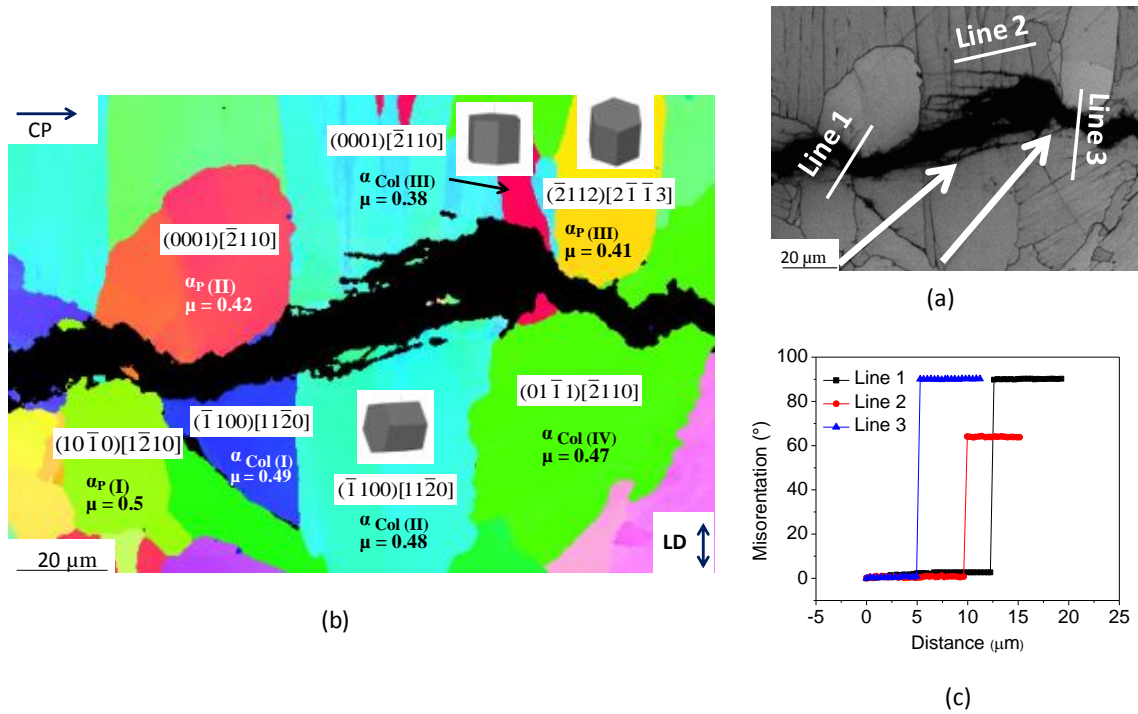


Fig. 8.27 (a) High resolution FEG-SEM image and corresponding (b) EBSD map and (c) misorientation between adjacent grains. SEM image and EBSD map shows the local interaction of growing crack with primary α grains and secondary α colonies. CP and LD represent direction of crack propagation and loading, respectively. These images are representative of 450°C↔600°C OP-TMFCG test condition.

8.3.6.1 IP-TMFCG loading ($300^{\circ}\text{C} \leftrightarrow 450^{\circ}\text{C}$)

Firstly, let us consider EBSD maps which depict the local interaction of crack with α_s colonies as well as α_p grains (Figs. 8.22a-c). In micrograph 8.22a and EBSD map 8.22b, crack propagates interlamellarly in $\alpha \text{ col.}_{(I)}$ which is favourably oriented to basal slip. It then propagates along the interface of two primary α grains. These two primary α grains namely $\alpha_{P(I)}$ and $\alpha_{P(II)}$ are favourably oriented for prismatic and basal slip, respectively. The misorientation angle between $\alpha \text{ col.}_{(I)}$ and $\alpha_{P(I)}$ is 58° and between two primary α grains is 89° . Further, the crack propagates along $\alpha \text{ col.}_{(II)}$ which is favourably oriented for prismatic slip and subsequently gets stopped near $\alpha \text{ col.}_{(III)}$ unfavorably oriented for basal slip. The misorientation angle between $\alpha \text{ col.}_{(II)}$ and $\alpha \text{ col.}_{(III)}$ is 62° . Crack then propagates to the boundary of $\alpha \text{ col.}_{(VI)}$ thereby encompassing $\alpha \text{ col.}_{(IV)}$, two primary α grains (could not be labeled as the space inside map was insufficient for labeling) and a relatively coarser $\alpha \text{ col.}_{(V)}$. The misorientation angle between two relatively finer primary α grains namely $\alpha_{P(III)}$ and $\alpha_{P(IV)}$ (not shown in the map) is only 5° and both are favourably oriented to external loading direction (ELD). It is also clear from Fig. 8.22b that the crack not only changes the direction of propagation but also forms branches once it encounters a $\alpha \text{ col.}_{(VI)}$ which is favorably oriented to pyramidal slip. The branched crack thus propagated along $\alpha \text{ col.}_{(VIII)}$ and the primary crack gets diverted to a $\alpha \text{ col.}_{(VII)}$. Both the α colonies ($\alpha \text{ col.}_{(VII)}$ and $\alpha \text{ col.}_{(VIII)}$) are favorably oriented to prismatic slip. The angle of misorientation between $\alpha \text{ col.}_{(V)}$ and $\alpha \text{ col.}_{(VI)}$ is 60° and $\alpha \text{ col.}_{(V)}$ and $\alpha \text{ col.}_{(VII)}$ is 70° .

Colonies like α col._(VII) and α col._(VIII) are more favorably oriented to ELD as compared to α col._(VI).

8.3.6.2 IP-TMFCG loading ($450^{\circ}\text{C} \leftrightarrow 600^{\circ}\text{C}$)

Fig. 8.23b reveals that crack initially propagates within a α col._(I) favorably oriented for prismatic slip. Examination of Fig. 8.23b and misorientation profile of line 1 as shown in Fig. 8.23c of α col._(II) and α col._(III) confirms the fact that these are indeed an one α_s colony. In addition, Fig. 8.23a shows that the variant along which α_s laths are aligned in both the colonies are indeed the same. It thus appears that the crack has propagated within α col._(I) only and it enters directly to α col._(IV) which is favourably oriented for basal slip. The misorientation angle between α col._(I) and α col._(IV) is observed to be 13° (Fig. 8.23c) and α col._(I) appears to be relatively more favourably oriented to ELD as compared to α col._(IV).

8.3.6.3 OP-TMFCG loading ($300^{\circ}\text{C} \leftrightarrow 450^{\circ}\text{C}$)

Figs 8.24 and 8.25 represent the interaction of crack with α_s colonies and α_s colonies - α_p grains, respectively, in the temperature interval of $300^{\circ}\text{C} \leftrightarrow 450^{\circ}\text{C}$. As clear from Fig. 8.24b, crack initially propagates along the boundary between two adjacent α_s colonies which are both favorably oriented for prismatic slip. Deformation in α col._(II) appears to be more heterogeneous as compared to α col._(I) and the misorientation angle between these two colonies is 68° . The crack then tends to propagate translamellarly across three

adjacent small α colonies. It appears that α col._(III) and α col._(IV) doesn't offer any hindrance to the movement of crack. However, branching of primary crack has been observed when it enters into a grain which is favorably oriented for prismatic slip. This α col._(IV) is ideally oriented to ELD. Subsequently, crack diverts the direction when it encounters α col._(V) which is unfavorably oriented for basal slip. In case of interaction of crack with both α_S colonies and α_P grains, as shown in Figs. 8.25a-c, crack interacts with $\alpha_{P(I)}$ along the interface of α col._(I) - $\alpha_{P(I)}$ and α col._(II) - $\alpha_{P(I)}$ and then propagates to α col._(III). The misorientation angle between α col._(I) and $\alpha_{P(I)}$ is 87° , whereas, it is 10° between α col._(II) and α col._(III). These α_S colonies as well as $\alpha_{P(I)}$ are favourably oriented for prismatic slip. $\alpha_{P(I)}$ is relatively more favourably oriented to ELD as compared to α_S colonies. Frequent crack path diversion can be seen in α col._(IV) which is unfavourably oriented for pyramidal slip. The angle of misorientation between α col._(III) and α col._(IV) is 60° . It appears that crack subsequently propagates without any hindrance to α col._(IV) encompassing α col._(V) both of which are favourably oriented for prismatic slip. The angle of misorientation between α col._(V) and α col._(VI) is 14° .

8.3.6.4 OP-TMFCG loading ($450^\circ\text{C} \leftrightarrow 600^\circ\text{C}$)

Figs. 8.26 and 8.27 represent the interaction of crack with α_S colonies and α_S colonies - α_P grains, respectively. Fig. 8.26b shows the propagation of crack along the boundary of two adjacent α_S colonies both of which are favourably oriented to prismatic slip. These grains are highly unfavourably oriented to basal slip. The misorientation angle of these two α colonies is less than 5° as clear from Fig. 8.26c. It is also clear from Fig. 8.26c that

deformation in α col._(I) appears to be more homogeneous as compared to α col._(II). Furthermore, α col._(I) appears to be oriented relatively more close to ELD as compared to α col._(II). The crack then tends to change the direction when it encounters a grain which is unfavourably oriented to pyramidal slip. Basal slip system is the secondary potential slip system for this α colony. Deformation in α col._(I) appears to be more homogeneous as compared to α col._(III) as clear from Fig. 8.26c. The misorientation angle between α col._(II) and α col._(III) is 60° .

In Figs. 8.27a-c, initial propagation of crack along the boundary between two primary α grains can be seen in which $\alpha_{P(I)}$ grain is favorably oriented for basal slip and $\alpha_{P(II)}$ grain is favorably oriented for prismatic slip. The misorientation angle between these two primary α grains is found to be 88° . However, distribution of deformation appears to be same in both these grains. Subsequently, crack moves translamellarly across two α colonies both of which are favorably oriented for prismatic slip. However, it forms branches in a direction opposite to the direction of propagation once it encounters a relatively finer α colony which is favorably oriented to basal slip. The misorientation angle between α col._(II) and α col._(III) is 63° . Crack then diverts along α col._(IV) which is more favorably oriented to pyramidal slip. In all these α colonies, distribution of deformation appears to be homogeneous.

8.4 Discussion

In this section, the results are analyzed and discussed in same way as that of under isothermal test conditions. In section 8.4.1, TMFCG behaviour is assessed taking into account the effect of variation in yield stress and temperature. The role of intrinsic damage micro-mechanism is addressed using EBSD observations in section 8.4.2. TMFCG behaviour is characterized in terms of crack closure mechanisms in section 8.4.3.

8.4.1 *Effects of Yield Strength and Modulus*

In order to understand the influence of modulus on TMFCG response of the alloy, Fig. 8.9 which depicts the variation of da/dN versus ΔK is replotted as a function of $\Delta K/E$ and $\Delta K^2/(\sigma_y E)$ in Figs. 8.28a and b, respectively. Since the modulus changes continuously while heating and cooling in a TMF cycle, the modulus and cyclic yield strength corresponding to the average test temperature for both the temperature intervals has been considered in the present investigation. This analysis is consistent with the earlier reports on crack propagation studies at TMF test conditions [Marchand et al. 1988]. While Fig. 8.28a can be considered as a normalization of the crack driving force with modulus, Fig. 8.28b can be viewed as a crack growth response as a function of CTOD ($CTOD \sim \Delta K^2/\sigma_y E$), which inherently takes into account the combined effect of variation in yield strength and modulus with test temperature.

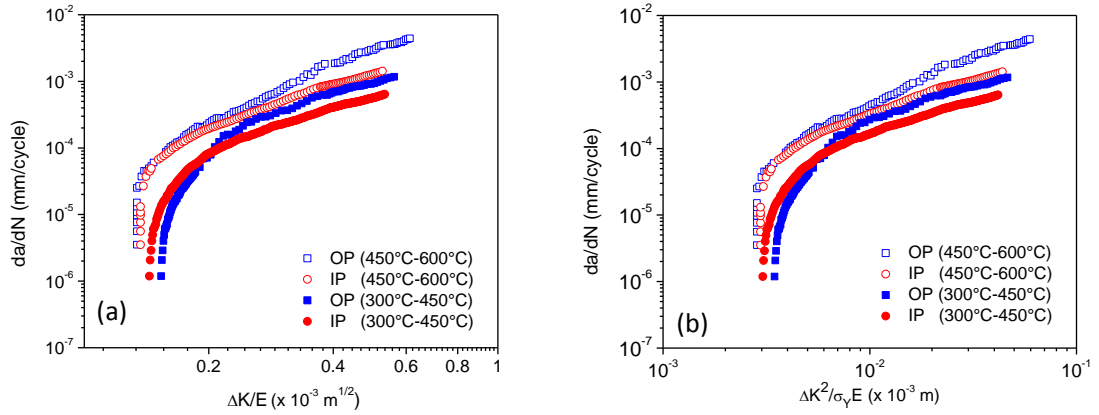


Fig. 8.28 (a) da/dN versus $\Delta K/E$ and (b) da/dN versus $\Delta K^2/\sigma_y E$ at various TMFCG test conditions

Fig. 8.28 shows that while near threshold region of TMFCG curves for the two temperature intervals appears closer to each other as compared to Fig. 8.9, a complete convergence to a single curve could not be observed. It is apparent from these figures that the variation in yield strength and modulus does not fully account for the change in TMFCG behaviour for both the temperature intervals.

8.4.2 Role of Local Crystallographic Orientation on TMFCG Behaviour

It is clear from the high resolution EBSD maps that the orientations of α_P grains and the surrounding secondary α colonies shares common orientation. As observed from Fig. 8.22b, $\alpha_{P(I)}$ shares the prismatic orientation with $\alpha \text{ col.}_{(II)}$ and $\alpha_{P(II)}$ shares the basal

orientation with α col._(I). Fig. 8.25b shows that $\alpha_{P(I)}$ and surrounding α col._(I) shares the prismatic orientation. It can also be seen in Fig. 8.27b that $\alpha_{P(I)}$ and α col._(I) shares the common prismatic orientation, whereas, $\alpha_{P(III)}$ and α col._(IV) shares the pyramidal orientation. This observation is in line with the study [Germain *et al.* 2005] that upon phase transformation from β to α during cooling, to the possible extent α colonies preferentially selects to share the same orientation of the surrounding α_P grain.

If one compares the activation of slip systems at IP and OP-TMFCG loading based on EBSD analysis, not only the fact that large percentage of potential slip systems of α_P grains (50% as compared to 30% under $300^\circ \leftrightarrow 450^\circ\text{C}$ and 60% as compared to 38% under $450^\circ\text{C} \leftrightarrow 600^\circ\text{C}$) and α_S colonies (45% as compared to 25% under $300^\circ \leftrightarrow 450^\circ\text{C}$ and 76% as compared to 33% under $450^\circ\text{C} \leftrightarrow 600^\circ\text{C}$) gets activated at IP-TMFCG loading, it is also clear based on Schmid factor range that grains around the crack wake at IP-TMFCG loading are indicative of highly deformable grains. It is believed that the maximum load at peak temperature assists in activation of large number of slip systems at IP-TMFCG loading which otherwise is expected to be relatively less under OP-TMFCG loading in which maximum load at minimum temperature may not contribute much for slip system activation. It has also been brought out very clearly that α_S colonies primarily deforms under basal slip due to the contribution from retained β body centered cubic phase. It can also be seen that large percentage of α_S colonies are activated for pyramidal slip under OP-TMFCG loading as compared to IP-TMFCG loading.

The observation of large percentage of deformable grains under IP-TMFCG loading as compared to OP-TMFCG loading is in line with the microhardness measurement which clearly revealed that cyclic plastic zone size under IP-TMFCG loading is nearly three times higher than that of OP-TMFCG loading. However, it can be argued that the cyclic plastic zone size has been measured at the crack tip by interrupting the test, however, EBSD maps have been generated around the crack wake and not at the crack tip using the post tested sample. In order to correlate these observations without any ambiguity, in the present study, an attempt has been made to calculate the local average misorientation (LAM) of the EBSD maps shown in Figs. 8.16 and 8.17. LAM is defined as an average misorientation of a point or pixel with all of its neighbours in a grain. It is known that LAM analysis provides a qualitative as well as quantitative picture of plastic strain accumulation either due to surface defects or defects density. The LAM maps of Figs. 8.16 and 8.17 are shown in Figs. 8.29a-d, respectively. In these figures, green colour represents highly strained areas. Qualitatively, it can be inferred from these LAM maps that plastic strain accumulation is much higher under IP-TMFCG loading as compared to OP-TMFCG loading in both the temperature interval. Most importantly, it can be seen that the strained area as shown in green colour are populated mainly near the crack and it diminishes gradually away from the crack. Qualitatively, it can thus be confirmed that results of microhardness measurements and EBSD are comparable. Fig. 8.29e shows the statistical inference of Figs. 8.29a-d in form of a histogram. The rate of occurrence of damaging events in form of plastically strained grains can easily exceed 2% under IP-TMFCG loading, which however, hardly touches a value of 1.5% under OP-TMFCG

loading. This quantitative interpretation further supports the measurement of cyclic plastic zone using microhardness measurements.

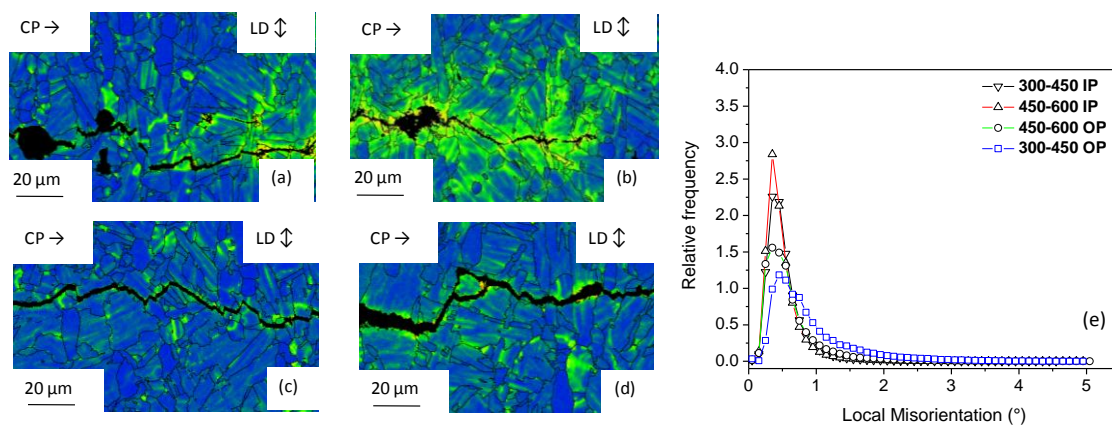


Fig. 8.29 Local misorientation maps of (a) 300°C↔450°C (b) 450°C↔600°C IP-TMF loading interrupted sample, (c) 300°C↔450°C (d) 450°C↔600°C OP-TMF loading interrupted sample, respectively at 30 MPa. $m^{1/2}$ and (e) showing histogram of local average misorientation for the four tested samples.

High resolution EBSD maps showed the evidence of local interaction of growing crack with the surrounding microstructural units. The observations which are found common irrespective of phase relationship (IP or OP) and temperature interval are as follows:

- (I) Crack tends to form branches when it enters a highly deformable secondary α colony favourably oriented for prismatic slip.
- (II) Crack tends to deviate the direction when it encounters a grain which is either (a) favorably oriented to basal slip or pyramidal slip or (b) highly misaligned to each other.
- (III) Crack preferentially propagates along the boundary between two α_p grains when both are oriented at an angle of $\sim 90^\circ$ to each other.
- (IV) Crack propagates along the boundary of two secondary α colonies when both the colonies are oriented for same type of slip systems and are less misaligned to each other.

It may thus be concluded from the present investigation that largely activated (a) pyramidal and basal slip oriented grains acts as an effective barrier and leads to frequent crack path diversion and (b) deformable grains oriented for prismatic slip tends to locally arrest the crack at IP-TMFCG loading. These two processes together contribute to the localised reduction in crack driving force. It can thus be surmised that reduction of crack driving force due to larger cyclic plastic zone size and higher activation of potential slip

systems leads to lower crack growth rate under IP-TMFCG loading as compared to OP-TMFCG loading in both the temperature intervals.

Let us discuss the specific regions of high resolution EBSD maps to understand the frequent occurrence of diversion of crack path when it encounters a favourably oriented basal or pyramidal oriented grain. Figs. 8.22b and 8.27b show the multiple branching of primary crack (as indicated by arrow in these figures) in a direction opposite to the direction of propagation. The crack branching in these specific regions is attributed to the combined effect of grain boundary constraint and crack tip shielding which are explained as follows.

- (a) *Grain boundary constraint:* The highly misoriented boundaries ($\sim 60^\circ$) in these specific regions could lead to the significant development of elastic or elastic-plastic interaction stresses and as a result promotes the crack branching and diversion. In the present study, the authors believe that in polycrystalline titanium alloys, when a grain is unfavourably inclined to ELD (ideally c-axis is parallel to ELD) and also relatively larger misoriented to adjacent grains, the necessity of maintaining ‘elastic or elastic-plastic compatibility’ becomes crucial. In these specific regions, the elastic and plastic deformation in the vicinity of the highly misoriented α_s boundaries are indeed expected to be incompatible due to different elastic constants and operative slip system on either side of the boundaries. This explanation is in agreement with the earlier reports [Anken and Margolin 1980, Hu et al. 2000, Biroasca et al. 2009]. The concept of ‘elastic interaction stresses’

[Ankem and Margolin 1980] and ‘elastic incompatibility stresses’ [Hu et al. 2000] in context to titanium alloys holds the same meaning. The primary objective is to show the compatibility requirement of the interfaces or the grain boundaries. While inclinations of operative slip systems to external loading direction (ELD) is considered for calculating ‘elastic interaction stresses’ [Anken and Margolin 1980], misorientation angle of adjacent grains in addition to inclinations of operative slip systems to external loading direction (ELD) has also been accounted in other study [Hu et al. 2000]. The observation of local diversion of crack due to unfavourably oriented α_s colony for pyramidal slip could be attributed to the fact that the strength of pyramidal slip system is significantly higher than that of the prismatic slip system (nearly 3 times) [Lützerling and Williams 2007].

- (b) *Crack tip shielding by the hard grain*: It is evident from Fig. 8.22a that α col._(V) oriented for prismatic slip and α col._(VI) oriented for pyramidal slip acts as a soft and hard grains, respectively. In these α_s colonies, c-axis of soft and hard grain is normal and parallel to ELD, respectively, as clearly shown in the form of embedded hexagons. Similarly, it is evident from 8.27b that α col._(II) is essentially a soft grain in which the c-axis is normal to the ELD and α col._(III) is a hard grain in which c- axis is parallel to the ELD. Apart from the grain boundary constraint, the observation of manifold crack branching in these regions could also be attributed to shielding mechanism in which crack has to dissipate more energy to propagate through a hard grain. This is attributed to a mechanism where greater

stiffness of c-axis oriented hard grain shields the neighboring grains by reducing the stresses or strains on it [Bantounas et al. 2007, Hasija *et al.* 2003, Rugg et al. 2007, McDowell and Dunne 2010]. It has been explained that hard grain acts as a primary grain and carries higher load as compared to soft grain.

The propagation of ‘edge on’ crack on two α colonies namely α col._(I) and α col._(II) in IP-TMF loading (Fig. 8.22bb) is due to the fact that these are the ideally favourably oriented colonies to ELD in which tensile stress is negligible and the respective plane i.e., basal in α col._(I) and prismatic α col._(II) is vertical [Bache et al. 1996].

In order to study the influence the extrinsic damage micromechanisms, the effect of crack closure on TMFCG behaviour is studied and discussed in subsequent section.

8.4.3 Characteristics of Crack Closure

As mentioned in the experimental section, closure load was determined using ACPD technique since clip on gauge cannot be inserted through the experimental set up used in the present work. The ACPD potential versus load curve at 600°C (T_{\max} level of temperature interval 450°C↔600°C under OP-TMF loading and at ambient temperature is shown in Fig. 8.30. The plot at ambient temperature is generated during intermittent cooling of the specimen to measure crack growth optically as mentioned in experimental section. It is clear from this figure that there is some fluctuation in the lower region of ACPD potential for elevated test temperature measurement and it is attributed to very

large resistance in the excitation and measurement circuits introduced by the oxide scales. The closure load (P_C) is determined from this plot from the intersection of extension of the upper and the lower linear regimes (Fig. 8.30a). It is important to note that if best linear fit is taken for lower regime of high temperature ACPD values, then the P_C value determined from ambient temperature and high temperature measurement plots are almost identical. However, the sensitivity of ACPD signal is high for ambient temperature measurement. Hence ACPD measurement at ambient temperature is used to determine P_{Cl} . It is obvious from this figure that the P_{Cl} value is not affected by the test temperature.

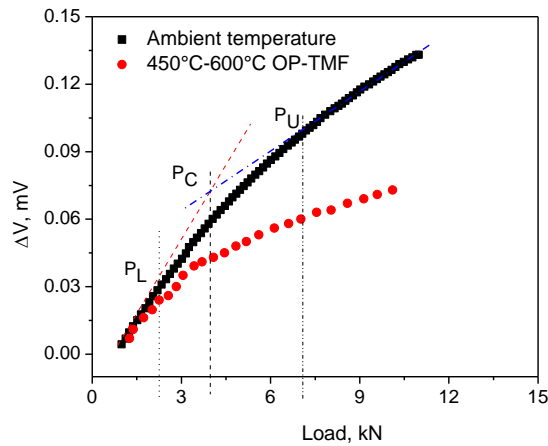


Fig. 8.30 Variation of potential versus applied load in the temperature interval of $450^{\circ}\text{C} \leftrightarrow 600^{\circ}\text{C}$ OP –TMFCG test condition.

In the present study, in order to quantify the crack closure effects, the effective stress intensity, ΔK_{eff} , values were obtained from the equation [ASTM Standard E 647-13]:

$$\Delta K_{\text{eff}} = (\Delta P / B.W) \cdot \sqrt{a} \cdot F(\alpha) \quad (8.8)$$

$$\Delta P = P_{\text{max}} - P_{\text{cl}} \quad (8.9)$$

$F(\alpha)$ is same as that of Eqn. (8.4)

The TMFCG curves as shown in Fig. 8.9 are then replotted as a function of ΔK_{eff} (Fig. 8.31a). Fig. 8.31a illustrates the consolidation of intrinsic crack growth data upto $\sim 20 \text{ MPa.m}^{1/2}$ and $\sim 25 \text{ MPa.m}^{1/2}$ for the temperature interval of $300^\circ\text{C} \leftrightarrow 450^\circ\text{C}$ and $450^\circ\text{C} \leftrightarrow 600^\circ\text{C}$, respectively. It can also be inferred from Fig. 8.31a that the near threshold region of intrinsic TMGCF curves were shifted to lower ΔK_{eff} ranges as compared to Fig. 8.9. Similar to the analysis as that of section 7.4.1 of chapter VII, these intrinsic TMGCF curves were replotted as a function of $\Delta K_{\text{eff}}/E$ and $\Delta K_{\text{eff}}^2/(\sigma_y.E)$ and are shown in Figs. 8.31b and c, respectively.

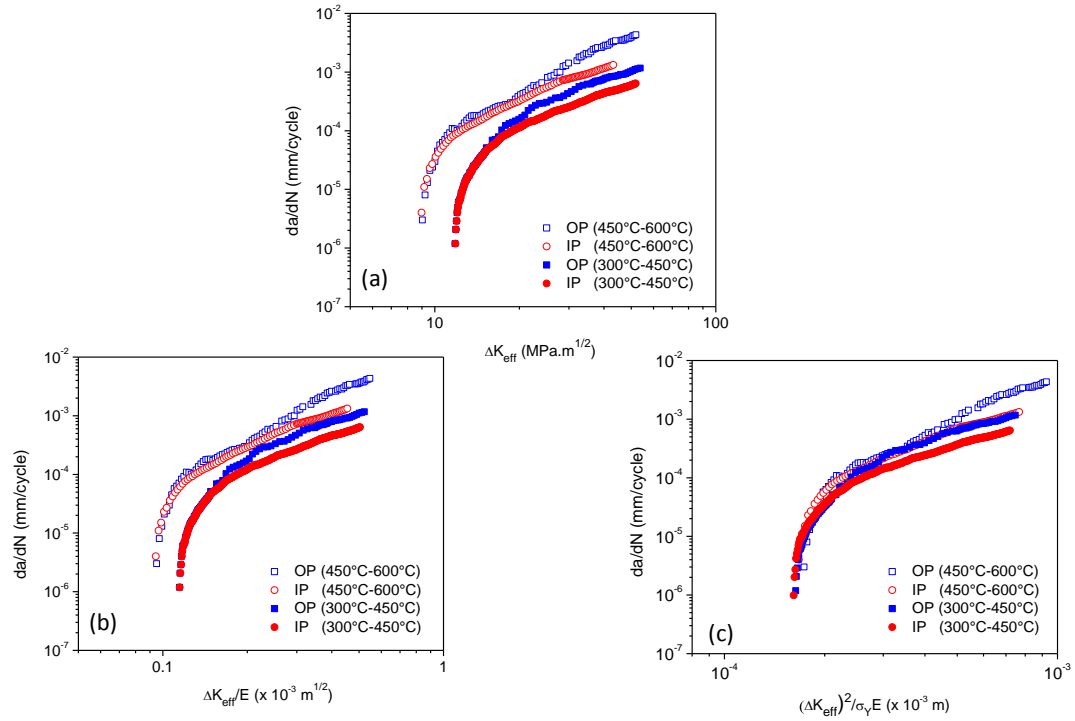


Fig. 8.31 (a) da/dN versus effective ΔK curves. Closure corrected fatigue crack growth curves as a function of (b) modulus and (c) CTOD at various TMFCG test conditions.

While the difference in the crack growth rate at near threshold region for the two temperature intervals is marginally reduced as a function of $\Delta K_{\text{eff}}/E$ (Fig. 8.31b), it is evident from Fig. 8.31c that this region of all TMFCG curves are converged to a narrow band for both the temperature intervals. However, apart from the near threshold region, Paris regime too is converged to a single curve for 300°C↔450°C OP and 450°C↔600°C IP test conditions (Fig. 8.31c). Collapsing of TMFCG data using $\Delta K_{\text{eff}}^2/(\sigma_y E)$ shows that the crack growth is not only affected by closure, however, it is also a function of CTOD.

The dependence of K_{cl} on K_{max} has been investigated in order to identify the most likely operative crack closure mechanism in these test conditions [Allison 1988]. The variation of K_{cl} versus K_{max} for all TMFCG test conditions is shown in Fig. 8.32a. K_{cl} is found to be initially increasing with increasing K_{max} up to $\sim 12 \text{ MPa.m}^{1/2}$. Beyond this K_{max} , it decreases and thereafter again increases and levels off as a function of increasing K_{max} . However, at 300°C↔450°C IP test conditions, the variation in K_{cl} do not show the same trend and remain unchanged with increasing K_{max} up to $\sim 17 \text{ MPa.m}^{1/2}$, beyond which it increases and levels off. It can also be inferred from Fig. 8.32a that the K_{max} value at which K_{cl} levels off was observed to be marginally higher ($\sim 25 \text{ MPa.m}^{1/2}$) for OP as compared to IP ($\sim 20 \text{ MPa.m}^{1/2}$) TMFCG test conditions. The trend in the variation of K_{cl} with K_{max} shows that although the combined effects of crack closure mechanisms operate at near threshold region, however, as clear from Fig. 8.32a, the effects of RICC and OICC appears to be predominant. The variation of closure ratio ($K_{\text{cl}}/K_{\text{max}}$) versus

K_{\max} is shown in Fig. 8.32b. Fig. 8.32b shows that the closure level increases with decreasing K_{\max} and most importantly, the alloy exhibits highest level of crack closure at $450^{\circ}\text{C} \leftrightarrow 600^{\circ}\text{C}$ OP test conditions.

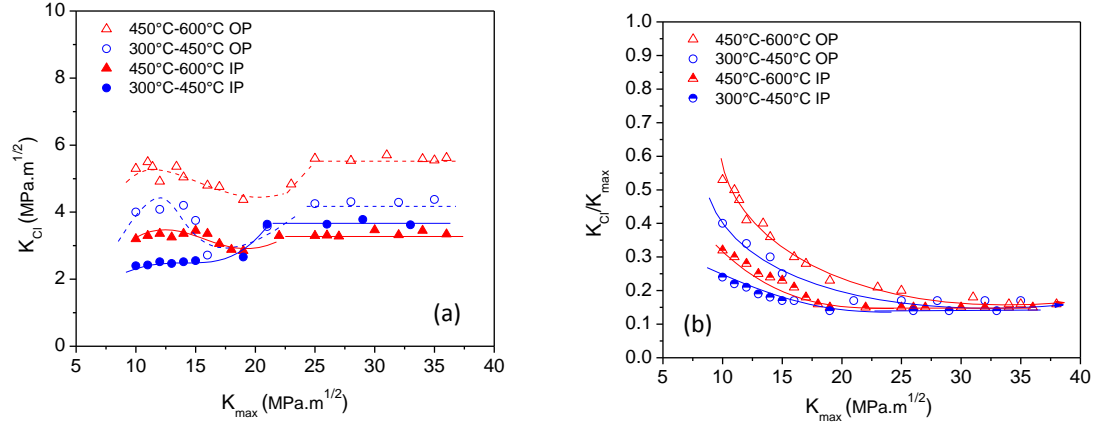


Fig. 8.32 Variation of (a) K_{cl} versus K_{\max} and (b) K_{cl}/K_{\max} versus K_{\max} under various TMFCG test conditions.

The characteristic values of crack closure namely average surface roughness (R_a) for surface roughness induced crack closure and oxide layer thickness (δ_{oxide}) for oxide induced crack closure as determined from the stylus based profilometer and AES analysis at near threshold region is included in Table 8.1. The CTOD parameters as computed from eqns. 7.8 and 7.9 of chapter VII for respective temperature intervals are also included in Table 8.1. It is clear from Table 8.1 that the values of R_a are higher than that of corresponding CTOD parameters at all TMFCG test conditions. While the values of δ_{oxide} is lower than that of the CTOD parameters in $300^{\circ}\text{C} \leftrightarrow 450^{\circ}\text{C}$ TMFCG loading, it is comparable in the temperature interval of $450^{\circ}\text{C} \leftrightarrow 600^{\circ}\text{C}$ TMFCG test conditions. Most

importantly, R_a appears to be higher in magnitude as compared to δ_{oxide} in all TMFCG loading. Considering the comparison between the characteristic values of crack closure and CTOD parameters, it is apparent that the RICC is dominant crack closure mechanism at all TMFCG loading. However, the combined effect of RICC and OICC operates at higher temperature $450^{\circ}\text{C} \leftrightarrow 600^{\circ}\text{C}$ TMFCG loading. Since the fracture behaviour is observed to be the same (faceted) at low ΔK levels under isothermal (Fig. 7.6, chapter VII) and TMF loading (Fig. 8.10), as brought out in section 7.4.2 of chapter VII, same reasons holds true for dominance of RICC in titanium alloys under TMFCG loading. Furthermore, based on the observation of comparable oxide layer as that of cyclic crack tip opening displacements at higher temperature interval, it is conceivable that the oxide layer which forms at $450^{\circ}\text{C} \leftrightarrow 600^{\circ}\text{C}$ TMFCG loading could effectively wedge the crack tip and leads to OICC. It is also evident from Table 8.1 that in this temperature interval, the effect of crack closure is relatively more dominant at OP-TMFCG loading as compared to IP-TMFCG loading. Observation of oxide debris (Fig. 8.11d) also supports this conclusion. This could be attributed to the fact that in case of OP-TMF loading, an oxide layer can form in compression at higher temperature and then rupture during the subsequent low temperature tensile portion of the loading cycle where the oxide layer is more brittle [Sehitoglu 1985]. The oxide layer can thicken to a larger extent in OP-TMF loading as compared to IP-TMF loading due to “fretting mechanism” [Suresh 2004] in which repeated rupturing and reforming leads to increase the oxide layer thickness. Thus, in the near threshold region, RICC is the dominant closure mechanism and OICC contributes as a second order effect only in the temperature interval of $450^{\circ}\text{C} \leftrightarrow 600^{\circ}\text{C}$ test conditions.

In contrast to stage I crack growth, oxidation has a adverse effect on stage II crack growth behaviour. An attempt has been made to depict the influence of oxidation schematically in Fig. 8.33.

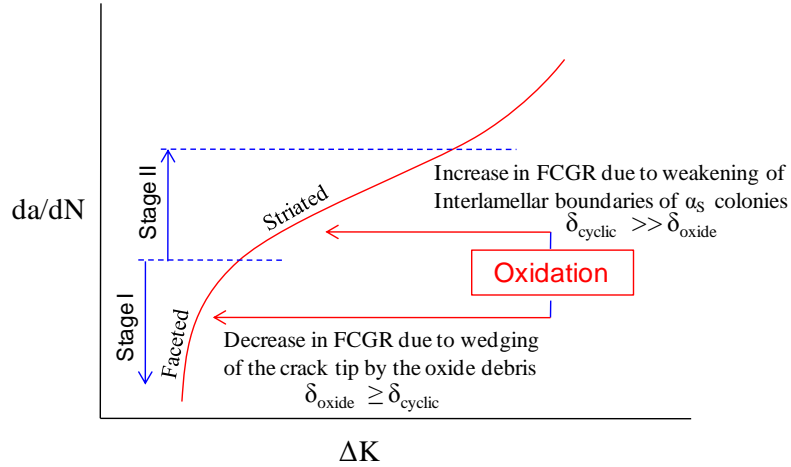


Fig. 8.33 A schematic plot of da/dN vs. ΔK illustrating the influence of oxidation in stage I and stage II TMFCG behaviour.

In stage II crack growth region, oxidation ceases to affect the crack growth rate through closure mechanism as the CTOD parameters are significantly higher than the characteristic values of crack closure. The higher crack growth rate exhibited by the alloy at $450^{\circ}\text{C} \leftrightarrow 600^{\circ}\text{C}$ TMFCG loading can be corroborated with larger spacing of striations (Fig. 8.11d and e) as compared to other test conditions. Oxide debris along the cracked striations can only be seen at this test condition. While average size of these striations corresponds to α lath size, it is surmised that the oxygen diffusion along the semicoherent boundary of $\alpha_{lath}/\beta_{retained}$ weakens the interlamellar regions [Mishra et al. 2005] which

offers easy path for crack propagation. In bi-model microstructure of this alloy, oxygen diffusion is much faster due to considerably higher grain boundary/grain ratio [Leyens et al. 1995]. It is thus interesting to summarize that oxidation reduces the effective ΔK by crack tip wedging during stage I crack growth regime on the one hand, and also to the increase in crack driving force by weakening the interlamellar regions during stage II crack growth regime on the other hand.

8.4.4 TMFCG Based on Micro Crack Tip TMF Process

It can be inferred from Figs. 8.15a-b that in the SENT specimens cyclic hardening occurs ahead of crack tip for both the temperature intervals for IP and OP-TMFCG test conditions. The question that arises is when did the hardening occur during test? Microhardness measurements ahead of the crack tip in fatigue crack growth tests carried out under isothermal conditions at 300°C, 450°C and 600°C revealed hardening only at 450°C while at 300°C and 600°C only softening was noticed (Fig. 7.9, chapter VII). Also the results of TMF tests carried out on smooth specimens described in results section 6.3.1 (Fig. 6.3) of chapter VI indicates that hardening occurs only at 450°C and softening at 300°C and 600°C irrespective of test conditions. On the basis of these evidences on isothermal fatigue crack growth measurements and TMF behaviour of smooth specimens, it is clear that hardening in the material is occurring only at 450°C. On the basis of above arguments it is reasonable to conclude that hardening observed ahead of the crack tip in SENT specimens in both temperature intervals has also occurred at 450°C. In the present work, amongst the TMFCG test conditions studied, the highest crack growth rate

observed at $450^{\circ}\text{C} \leftrightarrow 600^{\circ}\text{C}$ OP loading condition could be partly attributed to the gradual tensile cyclic hardening at 450°C . Since the peak tensile stress (maximum stress) increases significantly with strain cycling at 450°C which controls the mechanical environment of the crack tip (Fig. 8.34), the increase in stress acting at the head of the dislocation pile-up is expected to increase the crack growth rate during cyclic hardening [Antolovich and Armstrong 2014].

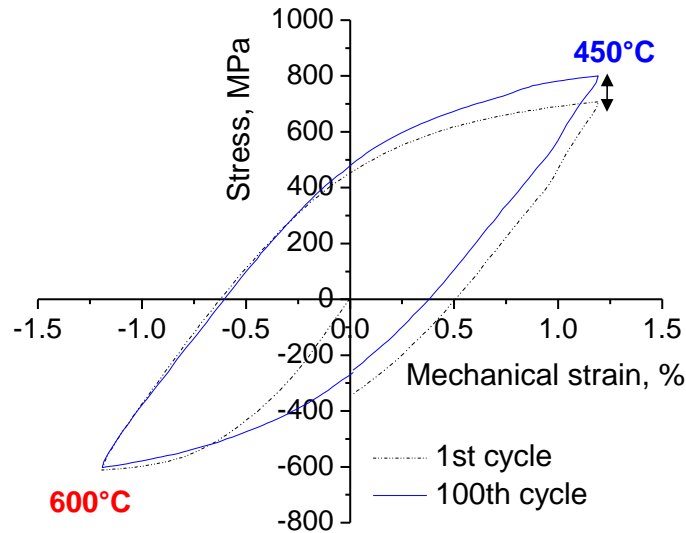


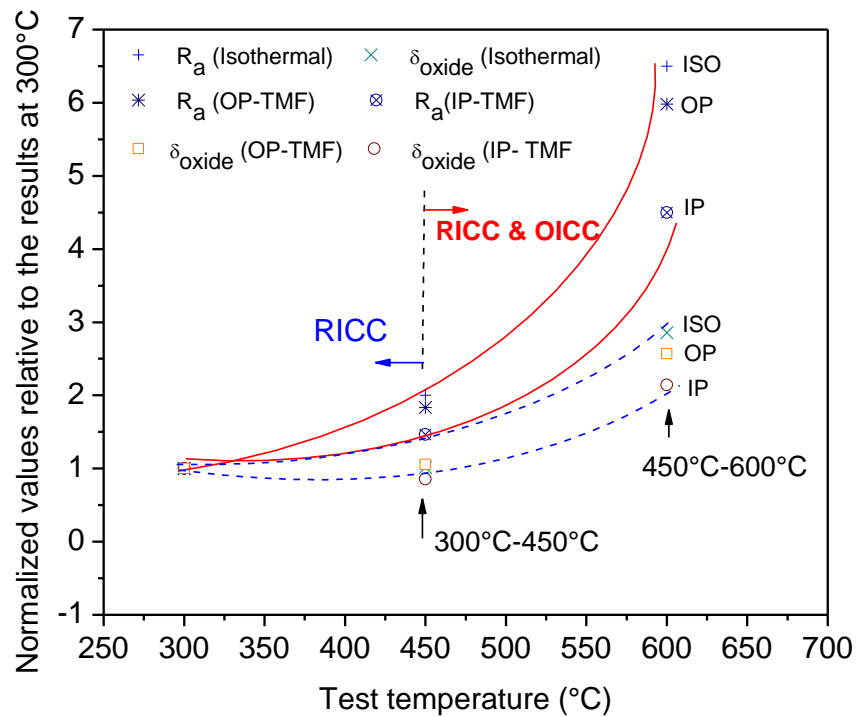
Fig. 8.34 Hysteresis loops at 1st and 100th cycle showing significant increase in peak tensile stress at 450°C as compared to 600°C .

Thus it can be concluded that oxidation as a primary effect in conjunction with DSA as a secondary effect increases the crack growth rate at $450^{\circ}\text{C} \leftrightarrow 600^{\circ}\text{C}$ OP-TMFCG

loading. Thus, stage II crack growth behaviour is accounted by CTOD per cycle in conjunction, crack closure mechanisms and cyclic hardening occurring at the crack tip.

8.5 Summary

In-phase and out-of-phase thermomechanical fatigue crack growth behaviour of a Timetal 834 near α titanium alloy have been studied in two temperature intervals viz. $300^{\circ}\text{C} \leftrightarrow 450^{\circ}\text{C}$ and $450^{\circ}\text{C} \leftrightarrow 600^{\circ}\text{C}$. Role of crack closure mechanisms and local crystallographic orientation have been critically assessed. It was found that the thermomechanical fatigue crack growth behaviour can be accounted by amalgamating crack closure mechanisms and crack tip opening displacement (CTOD) per cycle. At near threshold region, while fracture surface roughness induced crack closure (RICC) is the predominant closure mechanisms in the temperature interval of $300^{\circ}\text{C} \leftrightarrow 450^{\circ}\text{C}$, oxide induced crack closure strengthens the RICC in the temperature interval of $450^{\circ}\text{C} \leftrightarrow 600^{\circ}\text{C}$. These mechanisms reduce the crack driving force in near threshold region. In both the temperature intervals, the mechanical environment of the crack tip is controlled by the cyclic response of the alloy at 450°C . The alloy exhibited cyclic hardening at this test temperature. Apart from the influence of oxidation, higher crack growth rate at OP-TMFCG loading could be attributed to gradual increase in peak tensile stress at 450°C . Lower crack growth in IP-TMF loading could be attributed to larger plastic zone size as observed in this mode of loading as compared to OP-TMF loading.



Chapter IX

Comparative Assessment of Fatigue and Fracture Behavior

9.1 Introduction

As envisaged in chapter II (literature survey), material behavior is a function of test conditions. It has been out that the life limiting damage mode is low cycle fatigue in disc alloy and thermomechanical fatigue in case of bling alloy. In this thesis work, fatigue as well as fracture related studies as an input to safe and damage tolerant design, respectively, under both isothermal and non-isothermal test conditions have met these objectives. While the fatigue and fracture behavior of Timetal 834 under isothermal test conditions was thoroughly discussed in chapters V and VII, respectively, chapters VI and VIII dealt with fatigue and fracture behavior, respectively, under non-isothermal test conditions. Therefore, in this short chapter, we only discuss the comparative assessment of fatigue and fracture behavior of Timetal 834 under isothermal and non-isothermal conditions considering few of the key results obtained. This short chapter will highlight the specific conditions under which degradation of mechanical behavior of Timetal 834 is severe. While section 9.1 addresses the comparative assessment under safe life design (fatigue behavior), section 9.2 focuses the comparision of fracture behavior.

9.1.1 Comparative Assessment of Fatigue Behavior under Isothermal and Non-Isothermal Test Conditions.

In the present study, it is clear that while the primary mode of deformation remains planar slip irrespective of mode of loading (tensile, LCF and TMF loading), the fatigued microstructures in terms of dislocation substructure under TMF loading is observed to be similar as that of isothermal (LCF) loading. However, isothermal test conditions at 450°C appear to influence heavily to the dislocation substructure evolved under TMF (non-isothermal) loading. The severity of planar slip appears to be higher in case of 450°C isothermal (Fig. 5.11 of chapter V) and 450°C↔600°C OP-TMF loading (Fig. 6.10) as compared to other test conditions.

While the response of the alloy is unusual at 450°C in isothermal and 450°C↔600°C OP-TMF loading, an attempt has been made to compare the cyclic stress response curve (CSR) and cyclic stress – strain (CSS) curves considering these two test conditions. The CSR and CSS curves of the alloy at 450°C in these two test conditions are shown in Fig. 9.1a and b, respectively. It is evident from Fig. 9.1a that the 1st cycle stress is identical under both the test conditions, however, the alloy shows gradual hardening under TMF loading as compared to isothermal loading. It can also be inferred from Fig. 9.1b that the CSS curve of the alloy under TMF loading is above than that of isothermal loading. This shows that for design of such type of components which experiences TMF loading during service, CSS curves based on isothermal loading can underestimate the performance of the alloy.

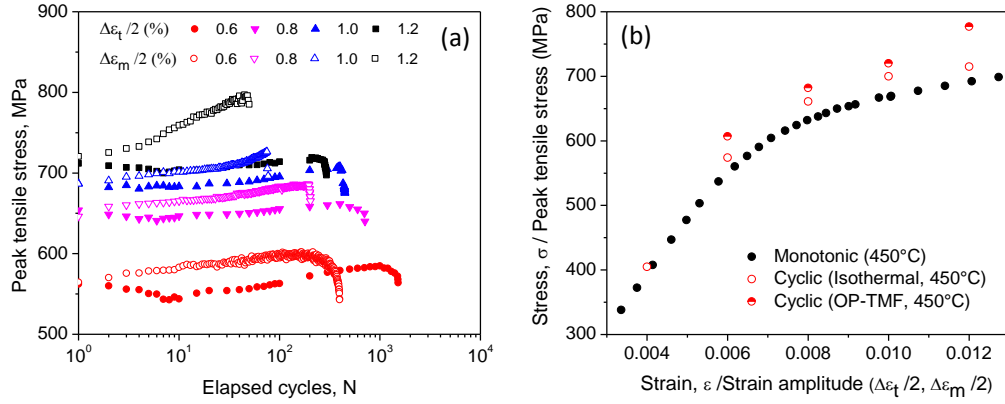


Fig. 9.1 (a) Comparison of hardening response of Timetal 834 at 450°C under isothermal and 450°C↔600°C OP-TMF loading and (b) comparison of stress – strain curves at 450°C under monotonic, isothermal and 450°C↔600°C OP-TMF loading.

The fatigue lives determined under isothermal and TMF loading is shown in Fig. 9.2. It is evident from Fig. 9.2 that fatigue lives are lower in TMF loading as compared to isothermal test conditions. While there is no significant difference observed in microstructural changes in fatigued Timetal 834 under isothermal and non-isothermal conditions, the variation in fatigue lives is primarily attributed to the development of mean stresses and effects of oxidation in TMF loading.

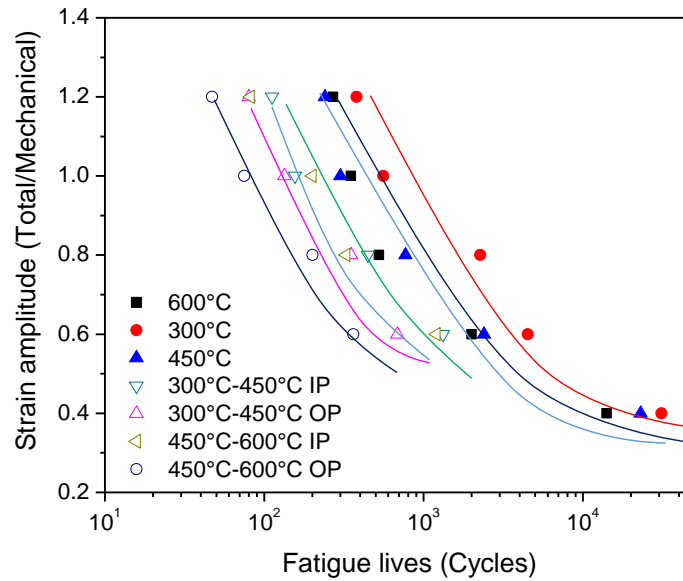


Fig. 9.2 Variation of fatigue lives of Timetal 834 under isothermal (LCF) and non-isothermal (TMF) loading.

9.2.2 Comparative Assessment of Fatigue Crack Growth Behavior under Isothermal and Non-Isothermal Test Conditions.

In order to rationalize the crack growth behavior under isothermal and thermomechanical test conditions, two key figures on fatigue crack growth namely, da/dN versus ΔK and da/dN versus $\Delta K_{eff}^2/(\sigma_y E)$ are considered. These curves under combined isothermal and TMF test conditions are shown in Figs. 9.3a and b, respectively.

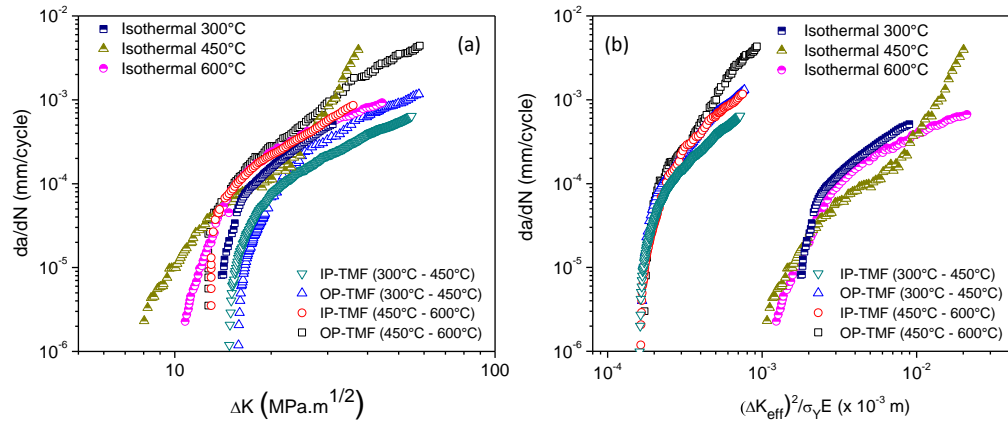


Fig. 9.3 (a) da/dN vs. ΔK curves and (b) da/dN versus $\Delta K^2/\sigma_y E$ at isothermal and TMF test conditions.

The Paris constants of the alloy under both modes of loading are also listed in Table 9.1. Considering the Paris constants of 1st slope region of all the curves, it can be seen from Fig. 9.3a and Table 9.1 that the alloy exhibits relatively higher crack growth rate at 450°C ↔ 600°C OP-TMF loading as compared to other test conditions. Fig. 9.3b shows that collapsing of fatigue crack growth data in near threshold region using $\Delta K_{eff}^2/(\sigma_y E)$ is achieved under both isothermal as well as thermomechanical fatigue loading. The range of ΔK required to attain a fixed range of crack growth rate between 10^{-5} and 10^{-3} mm/cycle under both isothermal and TMF loading has been compared qualitatively and is shown in Fig. 9.4.

Table 9.1: Paris constants under isothermal and non-isothermal test conditions.

Temperature	m	C	m	C
/Temperature Interval (°C)	(Closure corrected)			
300°	2.32	1.07×10^{-7}	2.12	5.17×10^{-7}
450°	2.27	1.32×10^{-7}	2.22	9.8×10^{-7}
	5.96	1.63×10^{-12}	5.90	1.43×10^{-11}
600°	1.92	8.81×10^{-7}	1.17	7.87×10^{-7}
300°C↔450°C IP-TMF	2.32	1.07×10^{-7}	2.12	5.17×10^{-7}
300°C↔450°C OP-TMF	2.50	2.67×10^{-7}	1.98	9.8×10^{-7}
450°C↔600°C IP-TMF	2.35	3.12×10^{-7}	2.08	7.87×10^{-7}
450°C↔600°C OP-TMF	3.2	1.27×10^{-8}	2.57	2.82×10^{-7}

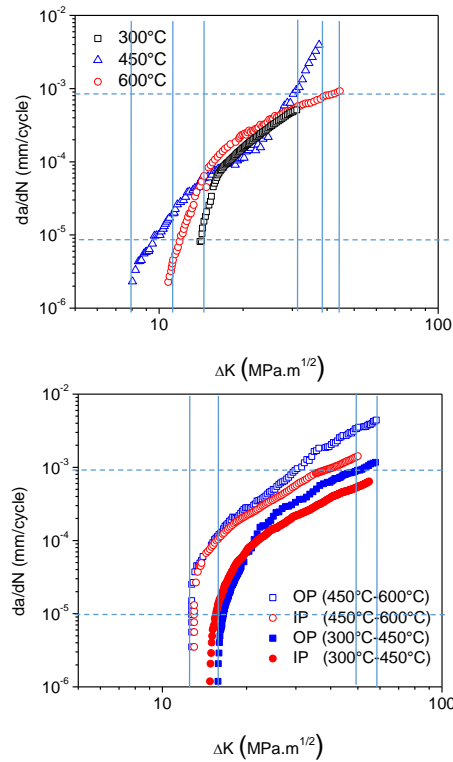


Fig. 9.4 Comparison of da/dN vs. ΔK curves of Timetal 834 under identical crack growth rates for both the modes of loading.

It can be inferred from Fig. 9.4 that the difference in ΔK for covering the same range of crack growth is marginally higher (~10%) under TMF loading as compared to isothermal test conditions.

Measurement of P_{cl} or P_{op} for quantification of crack closure effects through mechanical compliance using COD and physical compliance using ACPD or DCPD methods has drawn conflicting views on the merits of several experimental

methods [Halliday and Beevers 1981]. While the crack closure mechanisms has been studied using COD and ACPD under isothermal (chapter VII) and non-isothermal (chapter VIII) test conditions, respectively, an attempt has been made to compare the closure values determined using these techniques. The variation of closure parameters such as K_{cl} and K_{cl}/K_{max} as a function of K_{max} under both isothermal and non-isothermal modes of loading are shown in Figs. 9.5a and b, respectively. It is evident from Fig. 9.5a and b that the highest value of closure levels was determined using COD gauge at 600°C isothermal test conditions.

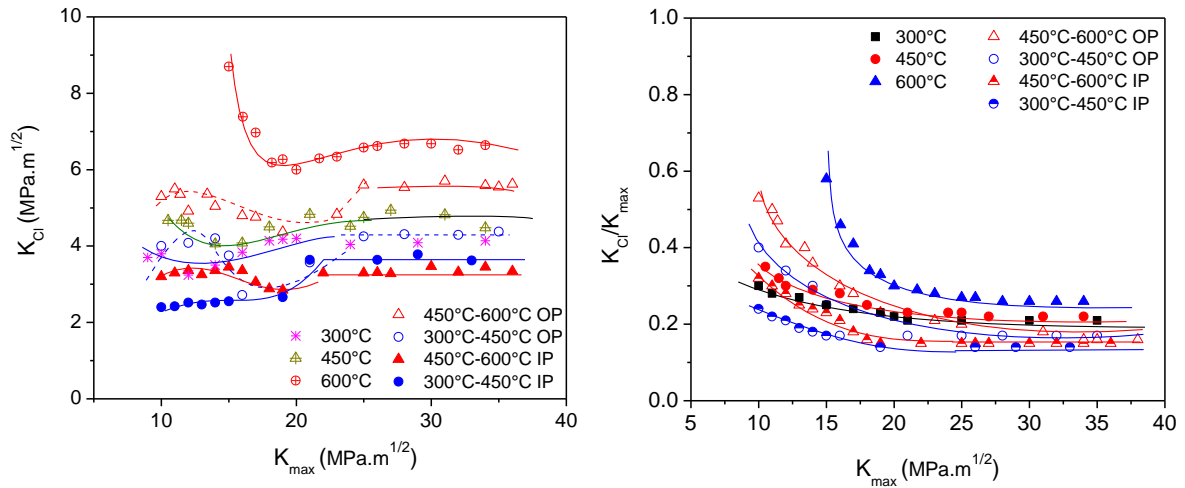


Fig. 9.5 Comparison of closure curves in (a) K_{cl} versus K_{max} and (b) K_{cl}/K_{max} versus K_{max} plots under isothermal and thermomechanical fatigue test conditions.

As mentioned in section 2.25 of chapter VIII, in order to find out whether COD and ACPD technique give the same closure load value or not, crack growth measurement was carried out on a CT specimen in an Instron machine (Instron 8500 plus with resistive heating furnace) at isothermal test temperature of 600° C using COD and ACPD technique. These results are shown in Fig. 9.6.

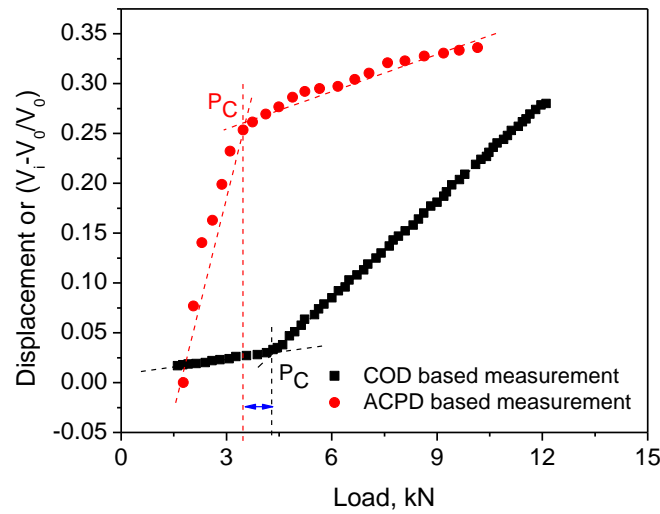


Fig. 9.6 Comparison of closure load determined using COD and ACPD at 600°C. ACPD based technique gives small reduction in closure load as compared to COD technique.

It is clear from Fig. 9.6 that the ACPD based technique gives a small reduction in the closure load by a value less than 0.5 kN. From these observations it is not unreasonable to assume that the ACPD gives a slightly lower value of K_{CI} but the trend of K_{CI} versus K_{max} remains unaffected. In order to study the influence of crack closure mechanisms under isothermal and TMF loading in a common space,

the characteristics value of crack closure mechanisms at all test conditions are normalized with respect to those at 300°C isothermal test conditions, as shown in Fig. 9.7.

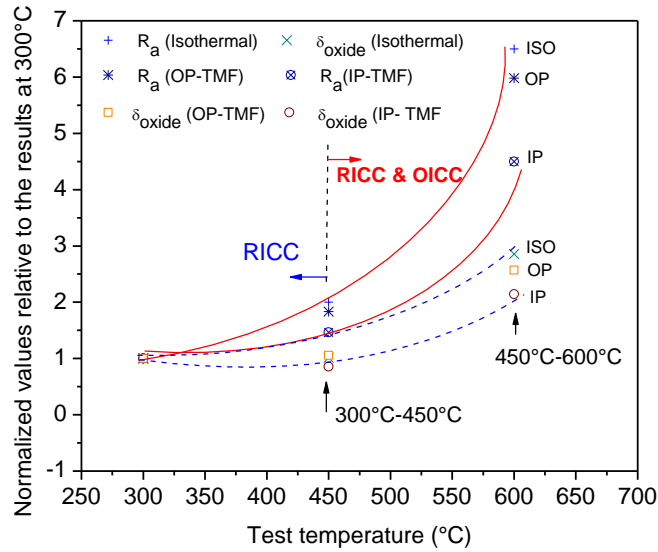


Fig. 9.7 Comparison of characteristic values of crack closure mechanisms under isothermal and thermomechanical fatigue test conditions.

Following inferences can be drawn from Fig. 9.7:

- (1) Crack closure has its pronounced effect at isothermal test conditions as compared to TMF test conditions.
- (2) The raising bound envelope of fracture surface roughness induced crack closure (RICC) is much steeper than oxide induced crack closure at all the test conditions. This shows that RICC is the main crack closure mechanism in Timetal 834 under both isothermal and non-isothermal test conditions.

- (3) The maximum effect of oxide induced crack closure has been observed at higher test temperature (600°C in case of isothermal loading) and at higher temperature interval (450°C↔600°C in case TMF loading).

9.2 Summary

The fatigue and fatigue crack growth behavior of Timetal 834 under isothermal and non-isothermal test conditions has been assessed. In smooth specimen based fatigue behavior, it has been observed that the fatigue lives under non-isothermal test conditions are lower as compared to isothermal test conditions. This is primarily attributed to the development of mean stresses, high degree of cyclic hardening and influence of oxidation under TMF loading. In fracture mechanics based fatigue crack growth behavior, it is revealed that in general, the fatigue crack growth rate is higher under non-isothermal and compared to isothermal test conditions. The was also attributed to the influence of oxidation and development of mean stresses in non-isothermal test conditions as compared to isothermal test conditions.

Chapter X

Conclusions and Suggestions for Future Work

10.1 Monotonic Tensile Behavior

Monotonic tensile deformation Behavior of a near α titanium alloy Timetal 834 developed for gas turbine compressor disc application has been studied. Tensile Behavior was assessed over a temperature range of 250°C - 600°C and at strain rates ranging from 10^{-6} s^{-1} to 10^{-3} s^{-1} (chapter IV). The manifestations of dynamic strain aging (DSA) exhibited by the alloy was characterized. The influence of dynamic strain aging on tensile properties was analysed. Salient features of this study are concluded below:

1. The serrated flow Behavior in the plastic region of stress – strain curves, temperature insensitivity of strength parameters (0.2% yield strength and ultimate tensile strength), decrease in ductility with increase in temperature in the temperature range of occurrence of serrated flow Behavior, increase in strain hardening exponent, negative strain rate sensitivity and increase in activation volume with increase in temperature in the temperature range of occurrence of serrated flow Behavior has been noticed and these observations led to the confirmation of occurrence of dynamic strain aging (DSA) in Timetal 834.
2. A complete map for the occurrence of different types of serrations (A, B, C and E type) as a function of strain rate and temperature exhibited by the alloy was established.

3. Activation energy was determined using tensile stress – strain data as per McCormick's model, Intercept method and Stress – drop method for identifying the solute/solutes responsible for causing DSA. The results indicated that Si as a substitutional solute is causing DSA in Timetal 834.
4. In order to study the role of interstitial solute elements (substitutional/interstitial or a combination of both) in DSA, a chemically and microstructurally similar alloy without Silicon has been developed.
5. Detailed TEM studies using analytical transmission electron microscope and elemental mapping using energy filtered transmission electron microscope on interrupted tensile specimens of alloy 834 without Si revealed that carbon and nitrogen formed atmosphere around mobile dislocations. This observation was further substantiated by the activation energy determined using tensile stress – strain data.
6. Similar to that of Timetal 834, the complete serration map of alloy 834 without Si in the intermediate temperature range over a temperature range of 250°C - 525°C and at strain rates ranging from 10^{-6} s^{-1} to 10^{-3} s^{-1} has also been established.
7. Micro-mechanisms responsible for appearance and disappearance of serrations at various test temperatures have been identified.

8. The temperature range of occurrence of DSA as evident from the serrations maps was found to be wider in alloy 834 without Si as compared to Timetal 834. Comparing the manifestations of DSA in both the alloys, it was found that not only Si increases the temperature range of occurrence of DSA, the severity of DSA is higher in Timetal 834 as compared to alloy 834 without Si.
9. Detailed TEM analysis on interrupted tensile specimens has revealed that deformation occurs through heterogeneous planar slip in both the alloys. It is revealed that strains are accommodated primarily by basal slip in Timetal 834 alloy.
10. Fractographic studies on tensile fractured specimens indicated that fracture mode remains quasi – cleavage during intermediate temperature range, which however, changes to ductile mode of fracture showing predominantly dimples at 600°C.

10.2 Cyclic Deformation Behavior

Cyclic deformation Behavior of Timetal 834 under isothermal (low cycle fatigue) and non-isothermal conditions (thermomechanical fatigue) have been studied. Low cycle fatigue (LCF) Behavior was assessed at three temperatures viz. 300°C,

450°C and 600°C under fully reversed constant total strain amplitudes ($\Delta\epsilon_t/2$) ranging from 0.4% to 1.2% (chapter V). LCF deformation Behavior was characterized using TEM studies on half-life fatigued specimens. Thermomechanical fatigue (TMF) Behavior was assessed in two temperature intervals viz. 300°C↔450°C and 450°C↔600°C under fully reversed constant mechanical strain amplitudes ($\Delta\epsilon_m/2$) ranging from 0.6% to 1.2% (chapter VI). TMF deformation Behavior was characterized using TEM studies on half-life fatigued specimens. Few unconventional fatigue tests have been conducted under LCF as well as under TMF loading to emphasize the occurrence of dynamic strain aging. While LCF studies were carried out on solid cylindrical specimens, tubular specimens were used for studying TMF Behavior. Salient features noted and gained from this study are concluded below:

LCF Behavior:

1. Amongst the temperature studied, the alloy exhibited initial cyclic softening followed by cyclic hardening at 450°C for total strain amplitude, $\Delta\epsilon_t/2 \geq 0.4\%$.
2. At 300°C and 600°C, initial cyclic softening followed by cyclic stability, the extent of which decreases with increase in $\Delta\epsilon_t/2$ was observed in the cyclic stress response curves for $\Delta\epsilon_t/2 > 0.4\%$.

3. Precipitate shearing was observed to be the micro-mechanism responsible for cyclic softening at all the temperatures. However, dislocation-dislocation and dislocation – solute interaction was observed to be the micro-mechanism responsible for cyclic hardening only at 450°C for $\Delta\epsilon_t/2 \geq 0.4\%$.
4. LCF results at 450°C revealed the effects of dynamic strain aging.
5. TEM observations revealed that planar slip is the major deformation mode which prevails up to 600°C. However, the severity of planar slip is found to be more at 450°C.
6. Low cycle fatigue lives were found to reduce with increasing strain amplitudes.
7. While the cyclic softening Behavior of the alloy at 300°C and 600°C leads to the cyclic stress – strain (CSS) curves to lie below that of monotonic curve, CSS curves lies above the monotonic curves at 450°C due to secondary cyclic hardening.

TMF Behavior:

1. Amongst the temperature interval studied, the alloy exhibited initial cyclic softening followed by cyclic hardening at 450°C in temperature interval of 300°C↔450°C. However, gradual hardening was observed at 450°C in 450°C↔600°C for mechanical strain amplitude, $\Delta\epsilon_m/2 \geq 0.6\%$.
2. At 300°C and 600°C, cyclic softening has been observed in the cyclic stress response curves in 300°C↔450°C as well as at 450°C↔600°C for mechanical strain amplitude, $\Delta\epsilon_m/2 \geq 0.6\%$.
3. The dislocation substructure was observed to be planar in both the modes of TMF loading, however, slip band spacing was observed to be higher in 300°C↔450°C as compared to 450°C↔600°C TMF loading.
4. Based on TEM microstructures and few unconventional fatigue tests, it has been revealed that the observed cyclic hardening at 450°C could be due to dynamic strain aging.
5. Amongst the TMF loading conditions studied, the alloy exhibited minimum fatigue life under 450°C↔600°C OP-TMF loading. This was attributed to the combined effect of cyclic hardening which leads to early

strain localization and crack initiation, oxidation and development of tensile mean stresses.

6. Considering the comparison of fatigue lives under isothermal (LCF) and non-isothermal (TMF) loading, it was noticed that the alloy exhibited reduced fatigue under TMF loading as compared to LCF loading. This was attributed to the development of mean stresses and severe effect of oxidation under TMF loading as compared to isothermal loading.
7. The cyclic stress strain (CSS) curve of thermomechanically fatigued alloy was found to lie above the CSS curve of the isothermal one on the basis of comparison of the cyclic stress response of the alloy at 450°C under 450°C↔600°C OP-TMF loading in which the alloy exhibits minimum fatigue life and 450°C LCF loading.

10.3 Fatigue Crack Growth Behavior

Fatigue crack growth Behavior of Timetal 834 has been studied at constant load amplitude cycling under isothermal (300°C, 450°C and 600°C) test conditions (chapter VII). Similarly, Fatigue crack growth Behavior has been studied at constant load amplitude cycling under non-isothermal (TMF) test conditions at two temperature intervals viz. 300°C↔450°C and 450°C↔600°C (chapter VIII). The thermomechanical fatigue crack growth Behavior was studied under in-phase

(IP) and out-of-phase (OP) TMF loading. While a high temperature crack opening displacement (COD) gauge was used to monitor the crack growth under isothermal test conditions, alternating current potential drop (ACPD) technique was used for crack monitoring under TMF loading. The intrinsic (processes which occurs ahead of the crack tip) and extrinsic (processes which occurs behind the crack tip) behavior of the crack growth under both isothermal as well as non-isothermal loading was characterized. While microhardness measurements and electron back scattered diffraction technique were used to characterize the intrinsic Behavior, load vs. COD curves under isothermal loading and load vs. ACPD voltage curves under non-isothermal loading were used to characterize the crack closure as an extrinsic Behavior. Crack closure mechanisms which are operational under isothermal as well as non-isothermal loading were also reported. Salient features noted and gained from this study are concluded below:

Fatigue Crack Growth under Isothermal Loading:

1. Amongst the temperature range studied, the alloy exhibited higher fatigue crack growth rate at 450°C as compared to 300°C and 600°C.
2. Microhardness measurements revealed that cyclic softening occurs at the crack tip at 300°C and 600°C, whereas, cyclic hardening occurs at the crack tip at 450°C. The observation of cyclic hardening occurring at the

crack tip as revealed by microhardness measurements was attributed to increase in the crack growth rate at 450°C.

3. The cyclic plastic zone size as revealed by microhardness measurements was found to be larger than monotonic plastic zone size at all the temperatures.
4. Surface roughness and oxide induced crack closure mechanisms were found to be operative in this alloy. Surface roughness induced crack closure as a predominant crack closure mechanism influences the stage I crack growth rates at all the temperatures. However, the effect of oxide induced crack closure as revealed by auger electron spectroscopy was found to be significant at 600°C as compared to 300°C and 450°C.
5. It is surmised that the oxide induced crack closure leads to significant increase in average surface roughness which eventually retards the crack growth rate at 600°C.
6. Analysis of fatigue crack growth data in crack growth vs. $\Delta K^2/(\sigma_y E)$ space showed that crack tip opening displacement per cycle and various types of crack closure mechanisms influences the fatigue crack growth Behavior in threshold regime.

7. Fractographic studies revealed that crack growth remains faceted in nature in threshold regime which changes to striated mode of crack growth in Paris regime of sigmoidal shaped fatigue crack growth (da/dN) vs. stress intensity factor (ΔK) curve.

Fatigue Crack Growth under Non-Isothermal (TMF) Loading:

1. In both the temperature intervals studied, the alloy exhibited higher fatigue crack growth rate under OP-TMF loading as compared to IP-TMF loading. However, amongst the test conditions studies, the alloy exhibited highest crack growth rate under $450^{\circ}\text{C} \leftrightarrow 600^{\circ}\text{C}$ OP-TMF loading.
2. Results of microhardness measurements and EBSD revealed that cyclic plastic zone size at the crack tip under IP-TMF loading is three times higher than OP-TMF loading. The reduced fatigue crack growth rate under IP-TMF loading was attributed to increased size of plastic zone at the crack tip.
3. At near threshold region, while surface roughness induced crack closure (RICC) was found to be the predominant closure mechanism in the temperature interval of $300^{\circ}\text{C} \leftrightarrow 450^{\circ}\text{C}$, oxide induced crack closure strengthens the RICC in the temperature interval of $450^{\circ}\text{C} \leftrightarrow 600^{\circ}\text{C}$.

4. The synergistic effects of oxidation and cyclic hardening occurring at the crack tip led to higher crack growth rate at $450^{\circ}\text{C} \leftrightarrow 600^{\circ}\text{C}$ OP-TMFCG loading.
5. It was found that the thermomechanical fatigue crack growth Behavior can be accounted by amalgamating crack closure mechanisms and crack tip opening displacement (CTOD) per cycle.
6. Oxidation was found to reduce the crack growth rate in threshold regime through crack closure mechanisms, whereas, it increases the crack growth rate by weakening the inter lamellar region of transformed β matrix.
7. EBSD studies revealed that irrespective of temperature intervals, crack tends to form branches when it enters a highly deformable secondary α colony favourably oriented for prismatic slip, however, deviation in direction has been observed when it encounters a grain which is either (a) favorably oriented to basal slip or pyramidal slip or (b) highly misaligned to each other.
8. Considering the effects of crack closure under isothermal and non-isothermal test conditions, crack closure has its pronounced effect at isothermal test conditions as compared to non-isothermal test conditions. The maximum effect of OICC was realized at higher test temperature

(600°C in case of isothermal loading) or higher temperature interval (450°C↔600°C in case TMF loading) of test conditions

10.4 Suggestions for Future Work:

1. The results presented in this thesis have identified interstitial carbon and nitrogen atoms as solutes responsible for serrated flow at lower temperatures. The solute atoms responsible for causing serrated flow at relatively higher temperatures have to be identified.
2. Low cycle fatigue Behavior was studied at only one strain rate in the present. Further detailed research work is necessary to understand the influence of strain rate on LCF Behavior of this alloy as a function of temperature.
3. In the present study, thermomechanical fatigue (TMF) Behavior was studied at a heating rate of 5°C/s. Another area that requires further investigation is to study the TMF Behavior of the alloy as a function of heating rate/cooling rate.
4. In the present study, fatigue crack growth Behavior was studied in mode I loading (tensile opening mode of loading). Further detailed research work is necessary to understand how the temperature affects the mixed mode

crack growth Behavior of the alloy under isothermal as well as non-isothermal loading.

5. EBSD studies were conducted only on specimens tested under thermomechanical fatigue crack growth conditions. The role of crystallographic orientation in affecting the fatigue crack growth rate under isothermal test conditions has to be studied in detail.

Bibliography

A

ASTM Standard E 8/8M-11: Standard test methods for tension testing of metallic materials. In: Annual book of ASTM standards, vol. 3.01, ASTM International, West Conshohocken (PA), 2012

ASTM Standard E 606/E606M-12: Standard test method for strain controlled fatigue testing, In: Annual book of ASTM standards, vol. 3.01, ASTM International, West Conshohocken (PA), 2012

ASTM Standard E 647-13: Standard test method for measurement of fatigue crack growth rates, In: Annual book of ASTM standards, vol. 3.01, ASTM International, West Conshohocken (PA), 2013

ASTM Standard E 2368-10: Standard practice for strain controlled thermomechanical fatigue testing, In: Annual book of ASTM standards, vol. 3.01, ASTM International, West Conshohocken (PA), 2010

Andres C, Gysler A, Lütjering G. Correlation between microstructure and creep behaviour of the high temperature Ti alloy IMI 834, *Z. Metallkd.*, 88 (1997) 197-202

Anken S and Margolin H. The role of elastic interaction stresses on the onset of plastic flow for oriented two ductile phase structures. *Metall. Trans. A*, 11 (1980) 963-972

Albrecht J. Comparing fatigue behaviour of titanium and nickel based alloys, *Mater. Sci. Eng. A*, 263 (1999) 176-186

Assadi ATK, Flower HM, West DRF. Creep resistance of certain alloys of the Ti-Al-Zr-Mo-Si system. *Metals Tech.*, 6 (1979) 16-24.

Ananthkrishna G. Current theoretical approaches to collective behaviour of dislocations. *Physics Reports*. 440 (2007) 113-259

Allison JE. In *Fracture Mechanics: Eighteenth Symposium*, Read DT and Reed RP (Eds.), ASTM STP 945, American Society for Testing and Materials, Philadelphia, PA, 1988, pp. 913-933

Antolovich SD and Armstrong RW. Plastic strain localization in metals: Origins and Consequences. *Prog. Mater. Sci.*, 59 (2014) 1-160.

B

Banerjee D and Williams JC. Perspectives on Titanium Science and Technology. *Acta Mater.*, 61 (2013) 844-879

Bania PJ and Antolovich SD. High temperature low cycle fatigue behaviour of a near alpha titanium alloy, In: Lützer G, Zwicker U, Bunk W. (Eds.), *Titanium'85 Science and Technology*, Germany, 1985, p. 2305-2312

Borchert B and Daeubler MA. Influence of microstructure of IMI 834 on mechanical properties relevant to jet engine. In: Lacombe P, Tricot R, Beranger G (Eds.), *Proceedings of 6th world conference on titanium*, Cannes, France, 1988, p. 467-472

Bate PS and Blackwell PL. Thermomechanical processing of titanium IMI 834, In: Lacombe P, Tricot R, Beranger G (Eds.), *Proceedings of 6th world conference on titanium*, Cannes, France, 1988, p. 287-292

Beranger AS, Feaugas X, Clavel M. Low cycle fatigue behaviour of an $\alpha+\beta$ titanium alloy : Ti 6246, *Mater. Sci. Eng. A*, 172 (1993) 31-41

Beukel VAN DEN A and Kocks UF. The strain dependence of static and dynamic strain aging. *Acta Metall.*, 30 (1982) 1027-1034

Beukel VAN DEN A. On the mechanism of serrated yielding and dynamic strain aging. 28 (1980) 965-969

Beukel VAN DEN A, Blonk J, VAN Haastert GH. The strain dependence of static strain aging in a gold-copper alloy, *Acta Metall.*, 31 (1983) 69-75

Bhanu Sanakara Rao K, Schiffers H, Schuster H, Halford GR. Temperature and strain rate effects on low cycle fatigue behaviour of alloy 800H. *Metall. Mater. Trans. A*, 27 (1996) 255-267

Bhanu Sankara Rao K, Schiffers H, Schuster H, Nickel H. Influence of time and temperature dependent processes on strain controlled low cycle fatigue behavior of alloy 617. *Metall. Trans. A*, 19 (1988) 359-371.

Biallas G and Maier HJ, In-situ fatigue in an environmental scanning electron microscope – potential and current limitations. *Int. J. Fatigue*. 29 (2007) 1413-1425

Biallas G and Maier HJ. In-situ studies of deformation behavior and damage evolution in high temperature titanium alloy IMI 834. In: Lütjering G, Albrecht J (Eds.). *Ti-2003 science and technology, Proceedings of the 10th World Conference on Titanium, Vol. III*. Weinheim: Wiley-VCH, 2004, p. 1949–56.

Baxter GJ, Rainforth WM, Grabowski L. TEM observations of fatigue damage accumulation at the surface of the near α titanium alloy IMI 834, *Acta Mater.*, 44 (1996) 3453-3463

Bannantine JA, Comer JJ, Handrock JL. *Fundamentals of Metal Fatigue Analysis*, Prentice Hall, Englewood Cliffs, New Jersey, 1990

Broek D. *Elementary Engineering Fracture Mechanics*, Martins Nijhoff Publishers, 3rd Edition, Netherlands, 1984

Brechet Y and Estrin Y. On the influence of precipitation on the Portevin Le Chatlier effect. *Acta Metall. Mater.*, 43 (1995) 955-963

Boyce MP: *Gas Turbine Engineering Handbook*. 4th edition. Butterworth-Heinemann, New York, NY, 2012, pp. 803 – 883.

Boyd JD and Hoagland RG, Slip in titanium aluminium alloys containing small Ti_3Al precipitates. In: Jaffee RI and Burte HM (Eds.), New York, TMS-AIME, 1973, pp. 1071-83

Brandes EA and Brook GB. *Smithells light metals handbook*, Butterworth Heinemann, Jordan Hill, Oxford, UK, 1998, p. 61

Blackburn MJ, The ordering transformation in titanium aluminium alloys containing up to 25 at. Pct aluminium, *Trans. Met. Soc. AIME*, 239 (1967) 1200-1208.

Bathias C and Pelloux R, Fatigue crack propagation in martensitic and austenitic steels. *Metall. Trans.*, 4 (1973) 1265-1273

Birosca S, Buffiere JY, Garcia-Paster FA, Karadge M, Babout L, Preuss M. Three-dimensional characterization of fatigue cracks in Ti-6246 using X-ray tomography and electron backscatter diffraction. *Acta. Mater.* 57 (2009) 5834-5847

Bantounas I, Lindley TC, Rugg D, Dye D. Effect of microtexture on fatigue cracking in Ti-6Al-4V. *Acta. Mater.*, 55 (2007) 5655-5665

C

Cottrell AH. *Dislocations and plastic flow in crystals*, Oxford university press, UK, 1953, p. 136

Cottrell AH. A note on the Portevin LeChatelier effect. *Phil Mag.*, 44 (1953) 829-832

Cope MT, Hill MJ. The influence of aging temperature on the mechanical properties of IMI 834, In: *Proc. Sixth World Conf. On Titanium*, P Lacombe, R. Tricot, G. Beranger (Eds.), France, 1988, pp. 153-158.

Christ HJ. Effect of environment on thermomechanical fatigue life. *Mater. Sci. Eng. A*, 468-470 (2007) 98-108

Curtin WA, Olmsted DL, Hector LG. A predictive mechanism for dynamic strain aging in aluminum-magnesium alloys. *Nature Mater.*, 5 (2006) 875

Chandra Rao BSS, Srinivas M, Kamat SV. The effect of volume fraction of primary α phase on fracture toughness behaviour of Timetal 834 under mode I and mixed mode I/III loading, *Mater. Sci. Eng. A*, 520 (2009) 29-35

Chandra Rao BSS, Srinivas M, Kamat SV. Effect of temperature on fracture toughness of Timetal 834 under mode I and mixed mode I/III loading, *Metall. Mater. Trans. A*, 39 (2008) 1340-1349

Chandra Rao BSS, Srinivas M, Kamat SV. The effect of mixed I/III loading on the fracture toughness of Timetal 834 titanium alloy, *Mater. Sci. Eng. A*, 476 (2008) 162-168

Cuddy LJ and Leslie WC. Some aspects of serrated yielding in substitutional solid solutions of Iron, *Acta Metall.*, 20 (1972) 1157-1167

Crossley FA, Kinetics of Ti_3Al grain boundary precipitation in Ti-Al binary and Ti-Al-X ternary alloys and correlation with mechanical properties, *Metal. Trans. A*, 1 (1970) 1921-1929

Calabrese C, Laird C. Cyclic stress strain response of two phase alloys part I: Microstructures containing particles penetrable by dislocations. *Mater. Sci. Eng.*, 13 (1974) 141-157

Castelli MG, Miner RV, Robinson DN, Thermomechanical fatigue deformation behaviour of a dynamic strain aging alloy, Hastelloy X, In: Thermomechanical fatigue behaviour of materials, Sehitoglu H (Ed.), ASTM STP 1186, Philadelphia (PA), 1993, pp. 107-125

Chesnutt JC, Williams JC, Thompson AW: In Fatigue 84, Beevers CJ, (Ed.), University of Birmingham, UK, 1984, pp. 341-350

Clair A, Foucault M, Calonne O, Lacroute Y, Markey L, Salazar M, Vignal V, Finot E. Strain mapping near a triple junction in strained Ni-based alloy using EBSD and biaxial nanogauges. *Acta Mater.*, 59 (2011) 3116-3123

Cheng J., Nemat-Nasser S. A model for experimentally observed high strain rate dynamic strain aging in titanium. *Acta Mater.*, 48 (2000) 3131-3144

D

Driver D, Hall DW, Meetham GW, The Gas Turbine Engine, In: Meetham G. W (Ed.), The Development of Gas Turbine Materials, Applied Science Publishers Ltd., London, UK, 1st Edition, 1981.

Donlon WJ, Allison JE, Laseki JV. The influence of thermal exposure on properties and microstructure of elevated temperature titanium alloys, In: Froes FH and Caplan I (Eds.), Titanium '92 Science and Technology, TMS, Warrendale, 1993, pp. 295-302

Dowsen AL, Hollis AC, Beevers CJ. The effect of alpha phase volume fraction and stress ratio on the fatigue crack growth characteristics of the near alpha IMI 834 Titanium alloy. *Int. J. Fatigue.* 14 (1992) 261-70.

Dieter GE. Mechanical Metallurgy, McGraw-Hill Book Co., London, UK, 1988

Doner M, Conrad H. Deformation mechanisms in commercial Ti-50A (0.5 at. pct O_{eq}) at intermediate and high temperatures ($0.3 - 0.6 T_m$). Metall. Trans., 4 (1973) 2809-2817.

Dowsen HI, Electrical resistivity and shear modulus of copper during cyclic stressing. J. App. Physics. 39 (1968) 3022-25

Dingley DJ, Randle V. Microtexture determination by electron back scattered diffraction. J. Mater. Sci., 27 (1992) 4545-4566

E

Evans WJ. Mechanical behaviour at elevated temperatures: cycle and time dependent effects. In: Blenkishop PA, Evans WJ, Flower HM (Eds.), Titanium'95 science and technology, Birmingham, UK, 1995, pp. 1065-1074.

Evans WJ, Bache MR, Multiaxial fatigue of near α Ti alloys, In: Blenkishop PA, Evans WJ, Flower HM (Eds.), Titanium'95 science and technology, Birmingham, UK, 1995, pp. 1339-1346

Evans WJ, Bache MR, Nicholas PJ, The prediction of fatigue life at notches in the near α Ti alloy Timetal 834, Int. J. Fatigue., 23 (2001) S103-S109

Evans RW, Hull RJ. Creep of IMI 834, In: Blenkishop PA, Evans WJ, Flower HM (Eds.), Titanium'95 science and technology, Birmingham, UK, 1995, pp. 1058-1064

Estrin Y and Kubin LP. Plastic Instabilities: Phenomenology and Theory, Mater. Sci. Eng. A, 137 (1991) 125-134

Elber W. Fatigue crack closure under cyclic tension. Eng. Frac. Mech., 2 (1970) 37-45

Elber W. Fatigue crack closure under cyclic tension. Eng. Frac. Mech., 2 (1970) 37-45

Embley GT and Russel ES: In Proc. of First Parsons Inter. Turbine Conference, Dublin, Ireland, 1984, pp. 157-164.

F

Francois D, Pineau A, Zaoui A, Mechanical Behaviour of Materials. Vol II: Fracture Mechanics and Damage, Springer, 2013

Flower HM, Lipscombe K, West DRF. The effect of silicon on the structure and mechanical properties of an $\alpha + \beta$ titanium alloy. J Mater Sci., 17 (1982) 1221-1231

Feaugas X and Clavel M. Cyclic deformation behaviour of an $\alpha + \beta$ Ti alloy. I: Micromechanisms of plasticity under various loading paths, Acta Mater., 45 (1997) 2685 – 2701

Feltner CE, Laird C. Cyclic stress strain response of FCC metals and alloys – II dislocations structures and mechanisms. Acta Metall., 15 (1967) 1633-1653

Fujita H, Tabata T, Discontinuous deformation in Al-Mg alloys under various conditions, Acta Metall., 25 (1977) 793-800

G

Gleiter H, Shape change of precipitates by diffusion in the stress field of dislocations. Acta Mater., 16 (1968) 455

Gopinath K, Gogia AK, Kamat SV, Balamuralikrishnan R, Ramamurty U, Low cycle fatigue behaviour of a low interstitiual Ni base superalloy. Acta Mater., 57 (2009) 3450-3459

Govrilov KL, Bennison SJ, Mikeska KR, Chabala JM, Setti RL. Silica and magnesia dopant distributions in alumina by high resolution scanning secondary ion mass spectroscopy. *J. Am. Ceramic Society*. 82 (1999) 1001-1008

Garde AM, Santhanam AT, Reed-Hill RE. The significance of dynamic strain aging in titanium. *Acta Metall.*, 20 (1972) 215-220.

Ghonem H, Foerch R. Frequency effects on fatigue crack growth behaviour in a near alpha titanium alloy. *Mater. Sci. Eng. A*, 138 (1991) 69-81.

Graff S, Forest S, Strudel J-L, Prioul C, Pilvin P, Bechade J-L. Finite element simulations of dynamic strain aging effects at V notches and crack tips, *Scripta Mater.*, 52 (2005) 1181-86.

Gray GT, Williams JC, Thompson AW. Roughness induced crack closure: An explanation for microstructurally sensitive fatigue crack growth. *Metall. Trans. A*, 14 (1983) 421-433.

Ghosal P, Prasad R, Ramchandra C. Microstructural stability of the ($\alpha + \beta$) solution treated and quenched Near α titanium alloy Ti-5.8Al-4Sn-3.5Zr-0.70Nb-0.50Mb-0.35Si-0.06C. *Metall. Mater. Trans. A*, 26 (1995) 2751-2755

Germain L, Gey N, Humbert M, Vo P, Jahaji M, Bocher P. Texture heterogeneities induced by subtransus processing of near α titanium alloy, *Acta Mater.*, 56 (2008) 4298-4308

Germain L, Gey N, Humbert M, Bocher P, Jahaji M, Texture and microtexture analysis of an IMI 834 alloy after thermo-mechanical processing, In: Lütjering G, Albrecht J (Eds.), *Ti – 2003 science & technology*, Proceedings of 10th world conference on Titanium, Germany, Hamburg, 2003, p. 1283-1290

Gysler A, Weissmann S, Effects of order in Ti_3Al particles and of temperature on the deformation behaviour of age hardened Ti-Al alloys, *Mater. Sci. Eng.*, 27 (1977) 181-193

H

Hasija V, Ghosh S, Mills MJ, Joseph DS. Deformation and creep modeling in polycrystalline Ti-Al alloys. *Acta Mater.*, 51 (2003) 4533-4549

Hardt S, Maier HJ, Christ HJ, High temperature fatigue damage mechanisms in near α titanium alloy IMI 834, *Int. J. Fatigue*. 21 (1999) 779-789

Hahner P, Affeldt E, Beck T, Klingelhoffer TH, Loveday M, Rinaldi C. Validated code-of-practice for strain-controlled thermo-mechanical fatigue testing. Joint research centre, European commission, June 2006

Halliday MD and Beevers CJ, Some aspects of fatigue crack closure in two contrasting titanium alloys. *J. Testing and Evaluation*, 9 (1981) 195-201.

Ham RK and Jaffery D. Dislocation multiplication, vacancy accumulation, and the onset of jerky flow during forward and reverse 1 strain in Cu-3.2at.%Sn, *Phil Mag.*, 15 (1967) 247-256

Hull D, Bacon DJ, Introduction to dislocations, 4th edition, Butterworth-Heinemann, 1984

Hintz M.B, Heldt LA, Clough SP, Moulder JF. Chemical state investigation of grain boundary segregated sulphur in polycrystalline nickel. *Scripta Metall.*, 17 (1983) 1415-1418

Hirabayashi M, Yamaguchi S, Asano H, Hiraga K. Order-Disorder Transformations of Interstitial Solutes in Transition Metals of IV and V Groups, In: Warlimont H (Ed.), *Order-Disorder Transformations in Alloys*, Springer Verlag, Berlin, 1974, p. 266.

Hono K. Atom probe microanalysis and nanoscale microstructures in metallic materials. *Acta Mater.*, 47 (1999) 3127-3145

Harrison PL, Winstone MR, Rawlings RD. Dynamic strain aging in titanium-aluminium alloys. *J. Less Common Metals*. 42 (1975) 137-140.

Huang ZY, Chaboche J-L, Wang QY, Wagner D, Bathias C. Effect of dynamic strain aging on isotropic hardening in low cycle fatigue for carbon manganese steel, *Mater. Sci. Eng. A*, 589 (2014) 34-40

Hu YM, Floer W, Krupp U, Christ H-J. Microstructurally short fatigue crack initiation and growth in Ti-6.8Mo-4.5Fe-1.5Al. *Mater. Sci. Eng. A*, 278 (2000) 170-180

J

Johnson EW and Johnson HH. Imprefection density of fatigued and annealed copper via electrical resistivity measurements. *Trans AIME*. 233 (1965) 1333

Joshi A, Stein DF. Auger spectroscopic analysis of bismuth segregated to grain boundaries in copper. *J. Inst. Metals.*, 99 (1971) 178-181.

K

Kordisch T, Nowack H. Creep-fatigue interaction and life behaviour of the titanium alloy IMI 834 at 600°C, In: Blenkishop PA, Evans WJ, Flower HM (Eds.), *Titanium'95 science and technology*, Birmingham, UK, 1995, p. 1179-1186

Kumar A, Singh, Singh V. Influence of stabilization treatment on low cycle fatigue behaviour of Ti alloy IMI 834, *Mater. Charact.* 51 (2003) 225-233

Kestler H, Mughrabi H, Renner H. Optimization of microstructure and mechanical properties of the hot forged titanium alloy IMI 834 by heat treatment, In:

Blenkishop PA, Evans WJ, Flower HM (Eds.), Titanium'95 science and technology, Birmingham, UK, 1995, p. 1171-1178

Koc R and Glatzmaier GC: Process for synthesizing titanium carbide, titanium nitride and titanium carbonitride. Midwest Research Institute, United States Patent, Patent No. 5417952, 1997, pp. 1

Kocks UF and Westlake DG, The importance of twinning for the ductility of CPH polycrystals. Trans. TMS-AIME, 239 (1967) 1107-09.

Klesnil M and Lukas P. In Proc. Second Int. Conf. on Fracture, Andrews EH, Frost NE, Nichols RW, Smith E, Pratt PL, (Eds.), Chapman and Hall, London, 1969, pp. 725.

Koul AK, Bellinger NC, Fahr A. Damage tolerance based life prediction of aeroengine compressor discs: I. A deterministic fracture mechanics approach. Int J Fatigue 12 (1990) 379-87.

Koul AK, Bellinger NC, Gould G. Damage tolerance based life prediction of aeroengine compressor discs: II. A probabilistic fracture mechanics approach. Int J Fatigue 12 (1990) 388-96.

Korbel A, Dybiec H. The problem of the negative strain rate sensitivity of metals under the Portevin-LeChatelier deformation conditions, Acta Metall., 29 (1981) 89-93

Kubin LP and Estrin Y. Evolution of dislocation densities and the critical conditions for the Portevin-LeChatelier effect, Acta Metall., 38 (1990) 697-708

Kale SS and Kashyap BP. Anomalous effect of temperature and strain rate on the strength of as-cast Al-Cu eutectic alloy. Scripta Metall., 26 (1992) 975-979

Kiessel WR, Sinnott WJ. Creep properties of commercially pure titanium. Trans. Metall. Soc., AIME. 197 (1953) 331-335.

Keast VJ, Williams DB. Quantitative compositional mapping of Bi segregation to grain boundaries in Cu. *Acta Mater.*, 47 (1999) 3999-4008

Keh AS, Nakada Y, Leslie WC. *Dislocation Dynamics*. McGraw-Hill, 1968

Kocks UF, Argon AS, Ashby MF. Thermodynamics and kinetics of slip. *Prog. Mater. Sci.*, 19 (1975) 110

L

Lütjering G, Williams JC. *Titanium*, 2nd Edition, Springer, 2007.

Leyens C, Peters M, Kaysser WA, In: *Proc. Eighth World Conf. on Titanium*, Blenkishop PA, Evans WJ, Flower HM, eds., Birmingham, UK, 1995, pp. 1935-1942.

Lenets TS, Nicholas T. Load history of fatigue crack growth thresholds for a Ti alloy, *Eng. Frac. Mech.*, 60 (1998) 187-203

Landgraf RW, Morrow J, Endo T. Determination of cyclic stress-strain curve. *J. Matell.*, 4 (1969) 176

Lütjering G, Weissmann S, Mechanical properties of age hardened titanium-aluminium alloys. *Acta Metall.* 18 (1970) 785-795

Liu HW and Iino N. In *Proc. Second Int. Conf. on Fracture*, Andrews EH, Frost NE, Nichols RW, Smith E, and Pratt PL (Eds.), Chapman and Hall, London, 1969, pp. 812.

Li S. Orientation stability in equal channel angular extrusion Part II: hexagonal close packed materials. *Acta Mater.*, 56 (2008) 1031-1043

M

Mulford RA and Kocks UF. New observations on the mechanisms of dynamic strain aging and jerky flow, *Acta Metall.*, 27 (1979) 1125-1134

Manson SS, Halford GR. *Fatigue and Durability of Structural Materials*, ASM International, Materials Park, Ohio, US, 2006

McCormick PG. A model for the Portevin-LeChatelier effect in substitutional alloys, *Acta Metall.*, 20 (1972) 351-354

McCormick PG, Theory of flow localization due to dynamic strain aging. 36 (1988) 3061-3067

Mannan SL. Role of dynamic strain aging in low cycle fatigue. *Bull. Mater. Sci.*, 16 (1993) 561-582

Marchand NJ, Pelloux RM. Thermal-mechanical fatigue crack growth in Inconel X-750. NASA Technical Report, NASACR-174835, 1984

Marchand NJ, Pelloux RM. A computerized testing system for thermal-mechanical fatigue crack growth. *J Testing Eval.*, ASTM. 14 (1986) 303-311

Marchand NJ, Pelloux RM, Ilschner B. A fracture mechanics criterion for thermal-mechanical fatigue crack growth of gas turbine materials. *Eng. Frac. Mech.* 31 (1988) 535-551

Mughrabi H. Cyclic slip irreversibilities and the evolution of fatigue damage. *Metall Mater Trans. B*, 40 (2009) 431-453.

Madsen A and Ghonem H. Separating the effects of Ti_3Al and silicide precipitates on the tensile and crack growth behaviour at room temperature and 593°C in a near alpha Ti alloy, *J. Mat. Eng. Perform.*, 4 (1995) 301-307

Maier HJ, Christ HJ. Modeling of cyclic stress-strain behaviour and damage mechanisms under thermomechanical fatigue conditions. *Int. J. Fatigue*. 19 (1997) S267-S274

McDowell DL, Dunne FPE. Microstructure-sensitive computational modeling of fatigue crack formation. *Int J Fatigue* 32 (2010) 1521-1542

Mishra H, P. Ghosal, Nandy TK, Sagar PK. Influence of Fe and Ni on creep of near α Ti alloy IMI 834. *Mater. Sci. Eng. A*, 399 (2005) 222-231

Mishra H, Satyanarayana DVV, Nandy TK, Sagar PK. Effect of trace impurities on the creep behaviour of a near α titanium alloy, *Scripta Mater.*, 59 (2008) 591 – 594

Madsen A, Andrieu E, Ghonem H, Microstructural changes during aging of a silicon bearing near α titanium alloy, *Mater. Sci. Eng.* 171 (1993) 191-197

Mitchell MR. *Fatigue and Microstructure*, ASM, Metals Parl, 1979, pp. 385

Moskalenko VA, Pusptsova VN. Dispersed barrier hardening and thermally activated deformation in α -titanium. *Mater. Sci. Eng.*, 16 (1974) 269-276.

Meyers MM, Chawala KK. *Mechanical Behavior of MATERIALS*, 2nd edition, Cambridge University Press, UK, 2009

Markandeya R, Nagarjuna S, Satyanarayana DVV, Sarma DD. Correlation of structure and flow behaviour of Cu-Ti-Cd Alloys, *Mater. Sci. Eng. A*, 428 (2006) 233

Miner RV, Castelli MG, Hardening mechanisms in a dynamic strain aging alloy, Hastelloy X, during isothermal and thermomechanical cyclic deformation, *Metall. Trans. A*, 23 (1992) 551-561.

Mitchell MR. In: *Fatigue and Microstructure*, ASM, Metals Park, US, 1979, p. 385

Mecking H, Estrin Y, The effect of vacancy generation on plastic deformation, *Scripta Metall.*, 14 (1980) 815-819

Minakawa K and McEvily AJ. On crack closure in the near threshold region. Scripta Metall., 15 (1981) 633-636

N

Neal DF. Development and evaluation of high temperature titanium alloy IMI 834, In: Lacombe P, Tricot R, Beranger G (Eds.), Proceedings of 6th world conference on titanium, Cannes, France, 1988, p. 253-258

Neal DF and Fox SP. The influence of Silicon and Silicides on the properties of Near Alpha Titanium Alloys, In: Froes F. H and Caplan I (Eds.), Titanium 92 Science and Technology, The Minerals, Metals & Materials Society, 1993, pp. 287-294.

Nambodhiri TKG, McMahon CJ Jr, Herman H, Decomposition of the α phase in titanium rich Ti-Al alloys. Metall. Trans. A, 4 (1973) 1323-1331

Naka S, Lasalmonie A, Costa P, Kubin LP. The low temperature plastic deformation of α titanium and the core structure of a-type screw dislocations. Phil Mag. A, 57 (1988) 717-740.

Newman JA, Piaschik RS. Interactions of plasticity and oxide crack closure mechanisms near the fatigue crack growth threshold. Int. J. Fatigue. 26 (2004) 923-927

Nabarro FRN. Report on strength of solids, Physical Society, 1948, p. 38

Nakada Y and Keh AS. Serrated flow in Ni-C Alloys, Acta Metall., 18 (1970) 437-443

Neu RW, Sehitoglu H. Thermomechanical fatigue, oxidation and creep: part I. Damage Mechanisms, Metall. Mater. Trans. A, 20 (1989) 1755

Nagalaxmi G, Hari Krishna E, Vikram G. B, Gogia AK, Kumar V. High temperature fatigue crack growth characterization of IMI 834 Near α Ti alloy for aeroengine compressor disk application – Part I. DMRL TR 2005 371, 2005

Nicholas T, Heil M, Haritos GK. Predicting crack growth under thermo-mechanical cycling. *Int J Fracture* 41 (1989) 157-176

Newman JA, Piaschik RS. Interactions of plasticity and oxide crack closure mechanisms near the fatigue crack growth threshold. *Int. J. Fatigue*. 26 (2004) 923-927

O

Omprakash CM, Satyanarayana DVV, Kumar V. Effect of primary α content on creep and creep crack growth behaviour of near α Ti alloy, *Mater. Sci. Techn.*, 27 (2011) 1427

Okazaki M, Koizumi T. Relationship of crack growth between thermal-mechanical and isothermal low cycle fatigue at elevated temperatures. *J. Eng. Mater. Technol.* 109 (1987) 114.

Okazaki M, Koizumi T. Crack propagation of steels during low cycle thermal-mechanical and isothermal fatigue at elevated temperatures. *Metall. Trans. A*, 14 (1983) 1641.

P

Pilchak AL, Bhattacharjee A, Rosenberger AH, Williams JC. Low ΔK faceted crack growth in titanium alloys. *Int. J. Fatigue*, 31 (2009) 989-994

Prasad K, Varma VK. Serrated flow behaviour in a near alpha titanium alloy IMI 834. *Mater. Sci. Eng. A*, 486 (2008) 158 – 166.

Prasad K, Kamat SV. Effect of strain rate on tensile behaviour and fracture toughness of Timetal 834 titanium alloy at ambient temperature. *J. Advanced Mater.*, 41 (2009) 64-73

Prasad K, Kamat SV. Transient flow behaviour in a near alpha titanium alloy in the dynamic strain aging regime, *Mater. Sci. Eng. A*, 490 (2008) 477-480

Prasad K. Influence of dynamic strain aging on plastic instability behaviour of near α titanium alloy Timetal 834, *Mater. Sci. Technology*, 26 (2010) 1068-1072

Prasad K and Kumar V. A novel test method to study the simultaneous creep-fatigue interaction, *Mater. Sci. Eng. A*, 551 (2012) 293-295

Prasad K, Sarkar R, Ghosal P, Varma VK. The influence of dynamic strain ageing on the low cycle fatigue behaviour of titanium alloy IMI 834, *Mater. Sci. Eng. A*, 494 (2008) 227-31.

Prasad K, Kumar V. Effect of temperature and hold time on internal hardening behaviour of near alpha titanium alloy IMI 834 under cyclic deformation. *Mater. Design*, 31 (2010) 2716-2724.

Prasad K, Kumar V. Effects of strain waveform on low cycle fatigue behaviour of near alpha Timetal 834 Titanium alloy. *Mater Design*, 32 (2011) 1710-15.

Prasad K, Kamat SV. Dynamic fracture toughness of a near alpha titanium alloy Timetal 834, *J. Alloys and Comp.*, 491 (2010) 237-241

Penning P. Mathematics of the Portevin-LeChatelier effect, *Acta Metall.*, 20 (1972) 1169-1175

Pink E and Grinberg A. Stress drops in serrated flow curves of AL5Mg. *Acta Metall.*, 30 (1982) 2153-2160

Pink E, Leoben. Grinberg A, Mexico F. Practical aspects of the Portevin Le Chatelier effect (1). Aluminium, 60 (1984) E601-E605

Paris P, Erdogan F, A critical analysis of crack propagation laws. J. Basic Eng., 85 (1963) 528-534

Petarra DP, Beshers DN. Cold-work internal friction peak in iron. Acta Metall., 15 (1967) 791-800

Pototzky P, Maier HJ, Christ HJ. Thermomechanical fatigue behaviour of the high temperature titanium alloy IMI 834, Metall. Mater. Trans. A, 29 (1998) 2995-3004

Pototzky P, Maier HJ, Christ HJ, Behaviour of the high temperature titanium alloy IMI 834 under thermomechanical and isothermal fatigue conditions. In: Third symposium on thermo-mechanical fatigue behaviour of materials, H Sehitoglu and H J Maier (Eds.), ASTM STP 1371, West Conshohocken (PA): 1999, pp. 18-35

Peters M, Hemptenmacher J, Kumpfert J, Leyens C. Structure and Properties of Titanium and Titanium Alloys, In: Leyens C, Peters M (Eds.), Titanium and Titanium Alloys: Fundamentals and Applications, Wiley – VCH GmbH & Co. KGaA, 2003.

Polmear IJ. Light Alloys. 4th edition, Butterworth-Heinemann, 2006

R

Rugg D, Dixon M, Dunne FPE. Effective structural unit size in titanium alloys. The J Strain Analysis for Eng. Design. 42 (2007) 269-279

Ramchandra C, Singh AK, Sarma GMK. Microstructural characterisation of near α titanium alloy Ti-6Al-4Sn-4Zr-0.70Nb-0.50Mo-0.40Si. Metall. Trans. A, 24 (1993) 1273-1280

Renner H, Kestler H, Mughrabi H, Influence of heat treatment and microstructure on the low cycle fatigue properties of the hot forged near α titanium alloy IMI 834, In: Fatigue '96, Proc. Of the Sixth International Congress. G. Lütjering and H Nowack (Eds.), Oxford: Pergamo, 1996, pp. 935-940

Rogers PT, Nicholas T. Micro-mechanisms of crack growth in Inconel 718 under thermo-mechanical fatigue. TMS/AIME Annual Meeting, Phoenix, Ariz, 1988

Reed RC. The Superalloys: Fundamentals and Applications, Cambridge University Press, UK, 2006

Rosenberg HM, Vacancies and other point defects in metals and alloys, Institute of metals, London, 1958, pp. 206

Ritchie RO. Mechanisms of fatigue crack propagation in ductile and brittle solids, Int. J. Fracture. 100 (1999) 55-83

Rosi FD, Perkins FC. Mechanical properties and strain aging effects in titanium. Trans. Am. Soc Metals., 45 (1953) 972-992.

Reed-Hill RE, Abbaschian R, Abbaschian L. Physical metallurgy principles. 3rd edition. Thomson Asia (P) Ltd., Singapore. 2003. pp. 288.

Robinson JM and Shaw MP. Microstructural and mechanical influenced on dynamic strain aging phenomena. Int. Mater. Rev., 39 (1994) 113-122

S

Santhanam AT and Reed-Hill RE. The influence of strain rate dependent work hardening on the necking strain in α titanium at elevated temperatures. Metall. Trans., 2 (1971) 2619-2622

Shamblen CE, Redden TK, Creep resistance and high temperature metallurgical stability of titanium alloys containing Gallium, *Metal. Trans.* 3 (1972) 1299-1305

Soares C, *Gas Turbines: A Handbook of Air, Land and Sea applications.* Butterworth-Heinemann, New York, NY, 2008, pp. 679-716

Suresh S and Ritchie R. O. Propagation of short fatigue cracks. *Int. Met. Reviews.* 29 (1984) 445-476

Suresh S, Zamiski GF, Ritchie RO. Oxide induced crack closure: An explanation for near threshold corrosion fatigue crack growth behaviour. *Metall. Trans. A*, 12 (1981) 1435-1443

Schijve J, *Fatigue of Structural Materials*, 2nd edition, Springer, The Netherlands, 2009

Schijve J. Fatigue crack closure: Observations and Technical Significance, In: Newman J. C, Elber W (Eds.), *Mechanics of Fatigue Crack Closure*, ASTM STP 982, 1988, pp. 5-34

Spera DA, what is thermal fatigue?: In *Thermal fatigue of materials and components*; D. A. Spera and D. F. Mowbray (Eds.), American Society for Testing and Materials, STP 612, 1975, pp. 3-9.

Suresh S. *Fatigue of Materials*, 2nd edition, Cambridge University Press, UK, 2004

Sundararaman M, Chen W, Singh V, Wahi RP. TEM investigations of γ' free bands in Nimonic PE16 under low cycle fatigue loading at room temperature. *Acta Metall. Mater.*, 38 (1990) 1813-1822

Sundararaman M, Chen W, Wahi RP. Interpretation of fatigue softening at room temperature in a superalloy. *Scripta Metall.*, 23 (1989) 1795-1800

Spence SH, Evans WJ, Medwell N. Crack growth response of IMI 834 under variable amplitude loading. *Int. J. Fatigue*, 19 (1997) 33-41

Saxena A and Antolovich SD. Low cycle fatigue, fatigue crack propagation and substructure in a series of polycrystalline C-Al alloys. Metall. Trans. A., 6 (1975) 1809-1828

Soare MA, Curtin W. A. Solute strengthening of both mobile and forest dislocations: The origin of dynamic strain aging in fcc metals. Acta Mater., 56 (2008) 4046-4061

Shewmon PG. Diffusion in Solids. 2nd edition. McGraw-Hill. 1963.

Shankar V, Valsan M, Bhanu Sankara Rao K, Mannan S. L. Effects of temperature and strain rate on tensile properties and activation energy for dynamic strain aging in alloy 625. Metall. Mater. Trans. A, 35 (2004) 3129-3139

Schlipf J. Collective dynamic aging of moving dislocations. Mater. Sci. Eng. A, 137 (1991) 135-140

Sehitoglu H. Constraint effects in thermomechanical fatigue. J. Eng. Mater. Techn., 107 (1985) 221-226

Singh N, Singh V. Effect of temperature on tensile properties of near α alloy Timetal 834, Mater. Sci. Eng. A, 485 (2008) 130-139

Singh N, Prasad N, Singh V. On the occurrence of dynamic strain aging in near alpha alloy Ti-5.8Al-4Sn-3.5Zr-0.7Nb-0.5Mo-0.35Si. Metall. Mater. Trans. A, 30 (1999) 2547-2549

Smallman RE, Bishop RJ. Modern Physical Metallurgy and Materials Engineering, 6th Edition, Butterworth Heinemann, UK, 1999

Sai Srinadh KV, Singh N, Singh V. Role of Ti₃Al/Silicides on tensile properties of Timetal 834 at various temperatures. Bull. Mater. Sci. 30 (2007) 595-600

Singh N, Gouthama, Singh V. Low cycle fatigue behaviour of Ti alloy IMI 834 at room temperature, Mater. Sci. Eng. A, 325 (2002) 324-332

Singh N, Gouthama, Singh V. Low cycle fatigue behaviour of Ti alloy IMI 834 at 873K. *Int. J. Fatigue*. 29 (2007) 843-851

Specht J, Crack propagation of titanium alloys for compressor discs, In: Lacombe P, Tricot R, Beranger G (Eds.), *Proceedings of 6th world conference on titanium*, Cannes, France, 1988, pp. 229-234

Sounim ES. Creep behaviour and creep microstructures of a high temperature titanium alloy Ti – 5.8 Al – 4.0 Sn – 3.5 Zr – 0.7 Nb – 0.35 Si – 0.06 C (Timetal 834) Part I : Primary and steady state creep, *Mater. Charact.*, 46 (2001) 365 – 379

Sounim ES. Creep deformation behaviour of three high temperature near alpha Ti alloys: IMI 834, IMI 829, and IMI 685, *Metall. Mater. Trans. A*, 32 (2001) 285-293

Satyanarayana DVV, Omprakash CM, Sridhar T, Kumar V. Effect of microstructure on creep crack growth behaviour of a near α Ti alloy IMI 834, *Metall. Mater. Trans. A*, 40 (2008) 128-137

T

Torster F, Gysler A, Lütjering G, Effect of microstructure and test temperature on fatigue properties of IMI 834, In: Blenkishop P. A, Evans W. J, Flower H. M (Eds.), *Titanium'95 science and technology*, Birmingham, UK, 1995, pp. 1395-1402

Truax DJ, McMahon Jr. Plastic deformation of titanium-aluminium alloys, *Mater. Sci. Eng. A*, 13 (1974) 125

Tsuzaki K, Hori T, Maki T, Tamura I. Dynamic strain aging during fatigue deformation in type 304 austenitic stainless steel, *Mater. Sci. Eng. A*, 61 (1983) 247-260

Tsuzaki K, Matsuzaki Y, Maki T, Tamura I. Fatigue deformation accompanying dynamic strain aging in a pearlitic eutectoid steel. *Mater. Sci. Eng. A*, 142 (1991) 63-70

Tabata T, Fujita H, Nakajima Y. Behaviour of dislocations in Al-Mg single crystals observed by high voltage electron microscopy, *Acta Metall.*, 28 (1980) 795-805

Tang F, Gianola DS, Moody MP, Hemkar KJ, Cairney JM. Observations of grain boundary impurities in Nanocrystalline Al and their influence on microstructural stability and mechanical behaviour. *Acta Mater.*, 60 (2012) 1038-1047.

Turner N. G, Roberts W. T. Dynamic strain aging in titanium. *J. Less Common Metals.*, 16 (1968) 37-44

U

Uta E, Humbert M, Gey N, Hazotte A, Bocher P, Jahazi M, Description and characterization of texture heterogeneities in Titanium alloy Timetal 834 with a bimodal microstructure, In: Niinomi M, Akiyama S, Ikeda M, Hagiwara M, Maruyama K (Eds.), *Ti – 2007 science & technology*, p. 263 – 266

V

Viswanathan R. *Damage Mechanisms and Life Assessment of High Temperature Components*, ASM International, 2nd Edition, Ohio, US, 1993

Vander Velde GP and D. A Koss. In *Fatigue 84*, Beevers CJ (Ed.), University of Birmingham, UK, 1984, pp. 411-421

Verbeeck J, Van Dyck D, Van Tendeloo G. Energy-filtered transmission electron microscopy: an overview. *Spectrochimica Acta B*, 59 (2004) 1529-1534.

W

Wang X, Jahazi M, Yue S. Substructure of high temperature compressed titanium alloy IMI 834, *Mater. Sci. Eng. A*, 434 (2006) 188-193

Wei RP. *Fracture Mechanics: Integration of Fracture Mechanics, Material Science, and Chemistry*. Cambridge University Press, 2010, pp. 50.

Woodfield AP, Postans PJ, Loretto MH, Smallman RE, The effect of long term high temperature exposure on the structure and properties of the titanium alloy Ti 5331S, *Acta Metall.* 36 (1988) 507-515

Wen YR, Hirata A, Zhang Z. W, Fujita T, Liu C. T, Jiang J. H, Chen M. W. Microstructure characterization of Cu rich nanoprecipitates in a Fe-2.5Cu-1.5Mn-4.0Ni-1.0Al multicomponent ferritic alloy. *Acta Mater.*, 61 (2013) 2133-2147.

White J, Loretto MH, Smallman RE, Winstone MR. In: Lütjering G, Zwicker U and Bunk W (Eds.), *Proc. Fifth World Conf. on Titanium*, Munich, Germany, Vol. IV, 1985, pp. 2297-2304

Williams DB, Carter CB, *Transmission electron microscopy*, 2nd edition, Springer Science & Business Media, 2009

Winstone MR, Rawlings RD, West DRF. Dynamic strain aging in some titanium-silicon alloys. *J. Less Common Metals*. 31 (1973) 143-150

Williams JC, Baggerly RG, Paton NE., Deformation behaviour of HCP Ti-Al alloy single crystals. *Metall. Mater. Trans. A*, 33 (2002) 837-850

Wei RP and Brazil RL. In: Fatigue Crack Growth Measurement and Data Analysis, Hudak SJ Jr., and R. J. Bucci RJ (Eds.), ASTM STP 738, American Society for Testing and Materials, 1981, pp. 103-119

Y

Yuan H, Kalkhof D. Effects of temperature gradients on crack characterisation under thermal-mechanical loading conditions. *Int. J. Fracture*. 100 (1999) 355-377

Yoo MH, Slip, twinning and fracture in hexagonal close packed metals. *Metall. Trans. A*, 12 (1981) 409-18.

Yoder GR, Cooley LA, Crooker TW. Observations on microstructurally sensitive fatigue crack growth in a widmanstatten Ti-6Al-4V alloy, *Metall. Trans. A*, 8 (1977) 1737-1743

Z

Zhang XD, Wiezorek JMK, Baeslack WA III, Evans DJ, Fraser HL. Precipitation of ordered α_2 phase in Ti-6-22-22 alloy. *Acta Mater.*, 46 (1998) 4485-4495.

Crack Closure Measurements

In this thesis work, closure load (P_{cl}) was determined from load versus COD plot and load versus ACPD plot under isothermal and non-isothermal test conditions, respectively. The procedure adopted for determining P_{cl} was same in both the test conditions. Hence, the procedure used under one of the isothermal test conditions (fatigue crack growth test carried out at 600°C) is summarized in this section. A typical load-displacement trace obtained with the COD technique is shown in Fig. 1 under $R = 0.1$ loading at a frequency of 1 Hz at 600°C. Approximately 500 data points shown were acquired during the fatigue cycle. The total crack opening displacements measured under maximum load was approximately 2.8 μm (Fig. 1).

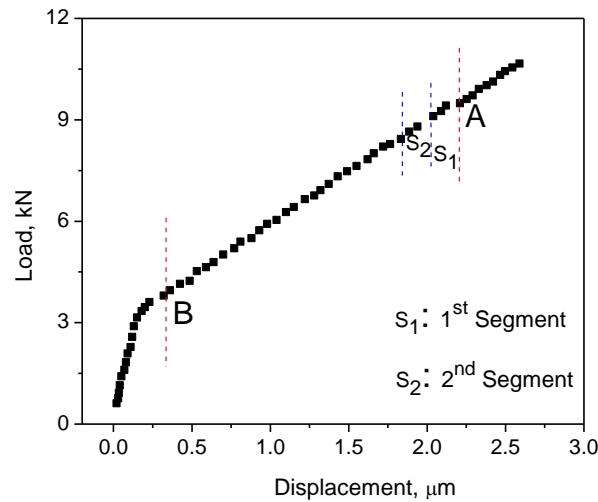


Fig. 1 Load versus COD plot at 600°C showing slope segments for crack closure level dterminations

The closure load was determined by reduced displacement method which involved the following steps:

- (1) As shown in Fig. 1, least square fit of the load-displacement data using segments with a range in load of 10% was computed. Segment 1 ranges from 90% (as indicated by A in Fig. 1) to 80% of P_{\max} , Segment 2 ranges from 80% to 70 % of P_{\max} and so on. These segments were illustrated in Fig. 1. The data points beyond the point B (as indicated in Fig. 1) were considered for this analysis. The slope of each segment was determined.
- (2) The percent change in slope of each segment was computed. Starting with the first slope in the array, the slope segments corresponding to a deviation in slope (offset) of greater than 1, 2 and so on with respect to point A and B were noted.
- (3) The offset of subsequent slope segments was compared. If a subsequent slope segment has less offset than the previous one, the new segment is substituted in place of old one.
- (4) The plot of load versus corresponding segments of slope offset is shown in Fig. 2. The load value corresponding to 1.0% slope offset (ASTM Standard E 647-13) is taken as closure load.

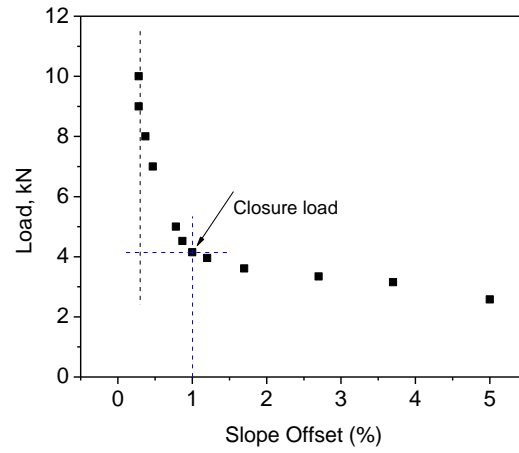


Fig. 2 Plot of load versus percent offset determined from the slope segments of Fig. 1 for determination of closure load.

Theoretically, the closure load is defined as the point where the reduced displacement data becomes zero. However, it is extremely difficult to find out the point where the reduced data displacement is exactly zero because mostly the original data are not perfectly linear. In the present investigation, amongst all the test conditions, the load value corresponding to reduced data displacement beyond 21 μm is considered for measuring closure load.